

Air Force Institute of Technology

AFIT Scholar

Theses and Dissertations

Student Graduate Works

3-2021

Shock Migration on an Oscillating Straked Delta Wing Using an Unsteady Euler Solver

Alexander J. Brown

Follow this and additional works at: <https://scholar.afit.edu/etd>



Part of the [Aerospace Engineering Commons](#), and the [Mechanics of Materials Commons](#)

Recommended Citation

Brown, Alexander J., "Shock Migration on an Oscillating Straked Delta Wing Using an Unsteady Euler Solver" (2021). *Theses and Dissertations*. 4972.

<https://scholar.afit.edu/etd/4972>

This Thesis is brought to you for free and open access by the Student Graduate Works at AFIT Scholar. It has been accepted for inclusion in Theses and Dissertations by an authorized administrator of AFIT Scholar. For more information, please contact AFIT.ENWL.Repository@us.af.mil.



SHOCK MIGRATION ON AN
OSCILLATING STRAKED DELTA WING
USING AN UNSTEADY EULER SOLVER

THESIS

Alexander J. Brown, 1st Lt, USAF

AFIT-ENY-MS-21-M-290

DEPARTMENT OF THE AIR FORCE
AIR UNIVERSITY

AIR FORCE INSTITUTE OF TECHNOLOGY

Wright-Patterson Air Force Base, Ohio

DISTRIBUTION STATEMENT A. APPROVED FOR PUBLIC RELEASE;
DISTRIBUTION UNLIMITED.

The views expressed in this thesis are those of the author and do not reflect the official policy or position of the United States Air Force, Department of Defense, or the United States Government.

AFIT-ENY-MS-21-M-290

SHOCK MIGRATION ON AN
OSCILLATING STRAKED DELTA WING
USING AN UNSTEADY EULER SOLVER

THESIS

Presented to the Faculty

Department of Aeronautics and Astronautics

Graduate School of Engineering and Management

Air Force Institute of Technology

Air University

Air Education and Training Command

In Partial Fulfillment of the Requirements for the
Degree of Master of Science in Aeronautical Engineering

Alexander J. Brown, B.S.M.E.

1st Lt, USAF

March, 2021

DISTRIBUTION STATEMENT A. APPROVED FOR PUBLIC RELEASE;
DISTRIBUTION UNLIMITED.

AFIT-ENY-MS-21-M-290

SHOCK MIGRATION ON AN
OSCILLATING STRAKED DELTA WING
USING AN UNSTEADY EULER SOLVER

Alexander J. Brown, B.S.M.E.
1st Lt, USAF

Committee Membership:

Donald L. Kunz, Ph.D
Chair

Mark F. Reeder, Ph.D
Member

Lt Col Brian T. Bohan, Ph.D
Member

Abstract

In support of the Air Force Office of Scientific Research, this project seeks to contribute to the understanding of Shock Induced Trailing Edge Separation (SITES) as the driver of Limit Cycle Oscillations (LCO) by performing a computational investigation of nonlinear aerodynamic phenomena on a transonic straked delta wing oscillating in pitch. Many works, to include flight tests, wind tunnel tests, and computational methods, have aimed to determine the drivers of LCO on the F-16 fighter aircraft. Interest has been focused on SITES behavior on an oscillating wing as a potential primary driver of LCO. The investigations presented in this report aim to expand the understanding of unsteady, nonlinear aerodynamics by studying flow around an oscillating straked delta wing using an aeroelastic Euler-based solver, ZEUS, with a boundary layer coupling scheme capable of estimating viscous flow effects within the boundary layer.

A delta wing model was used in ZONA's Euler Unsteady Aerodynamics Solver (ZEUS) for this analysis. Parameters such as trim angle of attack (AoA), amplitude, and Mach were varied to create 71 unique test cases. Out of the 71 cases, only 52 cases resulted in a solution due to either ZEUS' limitations in solving complex boundary layer interactions and large flow separation regions, or the grid's influence on the transient analysis. Pressure data from ZEUS was collected at four stations along the semispan for a full cycle of oscillation.

Results demonstrate that the same single shock systems at low AoA and two shock systems at moderate to high AoA that were observed by Cunningham in his wind tunnel tests were also present using ZEUS. Patterns of significant shock migration and disappearance were observed within the transonic flow region. A hysteresis was also found to be present. These findings support the theories that shock migration and SITES may play significant roles in driving LCO.

Table of Contents

	Page
Abstract	iv
List of Figures	viii
List of Tables	xx
List of Symbols	xxi
List of Abbreviations	xxii
 I. Introduction	 1
1.1 Background and Motivations	1
1.2 Research Objectives	3
 II. Literature Review	 5
2.1 Introduction	5
2.2 Aeroelastic Phenomena	5
2.3 Flight Testing Methodology	8
2.3.1 LCO Testing	9
2.4 Computational Aeroelastic Analysis	10
2.4.1 Classical Linear Flutter Analysis	10
2.4.2 Nonlinear LCO Analysis	11
2.4.3 Nonlinear Aerodynamics	12
2.4.4 Nonlinear Structural Damping	15
2.5 Wind Tunnel Experiments by Cunningham	16
2.5.1 Straked Delta Wing Model	16
2.5.2 Wind Tunnel Test Matrix	17
2.6 Delta Wing CFD using Euler and Navier-Stokes	21
2.7 Chapter Summary	25
 III. Methodology	 26
3.1 Introduction	26
3.2 Computational Model with ZEUS	26
3.2.1 Structural Finite Element Model	26
3.2.2 Aerodynamic Model	27
3.2.3 Mesh Generation	30
3.2.4 Transient Analysis	31
3.3 Grid Studies	35
3.3.1 Static Convergence Study by Dylan Hope	36

	Page
3.3.2 Comparison Criteria	38
3.3.3 Model Improvements	41
3.3.4 Dynamic Grid Sensitivity Study	43
3.3.5 Oscillatory Motion Study	46
3.3.6 Grid Study Conclusions	48
3.4 Computational Analysis	49
3.5 Post-Processing of Data	51
IV. Results and Analysis	52
4.1 Introduction	52
4.2 Numerical Analysis	53
4.3 Comparison to Hope's and Pung's results	58
4.4 Convergence Issues	61
4.4.1 Oscillation Study	62
4.5 General Observations	64
4.6 Inviscid vs Viscous Solutions	72
4.7 Low Transonic Cases	75
4.8 Trim Sweep	77
4.9 Amplitude Sweeps	85
4.10 Mach Number Sweeps	95
4.11 Maximum and Minimum AoA Comparisons	102
V. Conclusions and Recommendations	106
5.1 Results Summary	106
5.1.1 Shock Formations	106
5.1.2 Moment	106
5.1.3 Lift	107
5.1.4 Hysteresis	107
5.1.5 Convergence	107
5.1.6 Comparing to Hope's and Pung's Research	108
5.1.7 Inviscid vs Boundary Layer Coupled	108
5.1.8 Comparison to Cunningham's Results	109
5.2 SITES and LCO	109
5.3 Future Research Areas	110
5.3.1 Convergence	111
5.3.2 Friction Coefficient	111
Appendix A. C_p Data for Wing Station 1	112
Appendix B. C_p Data for Wing Station 2	132

	Page
Appendix C. C_p Data for Wing Station 3	152
Appendix D. C_p Data for Wing Station 4	172
Appendix E. C_m Data for Wing Station 1-4	192
Appendix F. C_l Data for Wing Station 1-4	212
Bibliography	232
Vita	235

List of Figures

Figure		Page
2.1	Schematic of the field of aeroelasticity [19, p.2].	6
2.2	First Antisymmentric Bending and Torsional Modes for the F-16 [18].	8
2.3	Shock development and flow separation on an airfoil [1].	12
2.4	SITES induced LCO at a contant angle of attack [7].	14
2.5	Dimensions of the staked NACA 64A-204 wing modell (in mm) [9].	17
2.6	SiS model with station numbers 1-7 (in mm) [9].	18
2.7	Mach 0.9 test matrix for Cunningham’s wind tunnel tests [9]. . . .	19
2.8	Time trace of the wind tunnel test maneuver sequence [9].	20
3.1	Planform Dimensions for the ZEUS SiS Model (in mm) [20].	28
3.2	SiS model in ZEUS with Stations 1-4 in black, located at 209mm, 274mm, 336mm, and 395mm from the centerline [20].	29
3.3	Automated 3D mesh of the ZEUS SiS Model [20].	31
3.4	Top View of the ZEUS SiS model 3D mesh and surface grid [20]. .	32
3.5	Flow Chart of the Euler Solver in ZEUS [33].	34
3.6	Planform of the evenly distributed 35 spanwise x 40 chordwise panel surface grid [20].	37
3.7	Grid sensitivity study by Hope. Plot is trim angle of attack vs number of panels [20].	38
3.8	Pressure coefficient vs chord location. Mach = 0.95, trim AoA = 7°, amplitude = 2°, and frequesncy = 5.7 Hz.	39
3.9	Moment coefficient vs chord location. Mach = 0.95, trim AoA = 7°, amplitude = 2°, and frequesncy = 5.7 Hz.	41
3.10	Comparison between original grid (a) and refined grid (b).	42
3.11	Comparison between the original mesh (a) and the refined mesh (b) at the leading edge of the wing.	43
3.12	Dynamic grid study. Mach = 0.95, trim AoA = 7°, amplitude = 2°, frequency = 5.7 Hz. Grid densities are a factor of the original density used by Hope.	45

Figure		Page
3.13	Cycle study at Station 2 with Mach number = 0.95, trim AoA = 7° , amplitude = 2° , frequency = 5.7 Hz, ran for 4 cycles.	48
4.1	Pressure coefficient vs chord location showing shock movement and shock slope calculations.	55
4.2	Example of lift plots for a single chord on the wing.	56
4.3	Example of lift plots for a single chord on the wing.	57
4.4	Pressure Coefficient vs Chord Location at Station 2.	59
4.5	Pressure Coefficient vs Chord Location at Station 2.	60
4.6	Pressure Distributions at Station 2.	64
4.7	Pressure Distributions with $T = 0^\circ$, $A = 0.5^\circ$ at Station 2.	66
4.8	Pressure Distributions for $T = 4^\circ$, $A = 12^\circ$ at Station 2. $M = 0.3$ (top), 0.6 (middle), & 0.9 (bottom).	69
4.9	Moment and Lift Coefficients vs AoA at Station 2.	70
4.10	Model planform with the pitching axis location in relation to Stations 1-4.	71
4.11	Pressure Coefficient vs Chord Location. $T = 4^\circ$, $A = 12^\circ$, & $M = 0.9$	72
4.12	Pressure Coefficient Contour Plot: Cycle Time vs Chord Location. $T = 4^\circ$, $A = 12^\circ$, & $M = 0.9$. The supersonic flow region is outlined by a dashed line.	73
4.13	Moment Coefficient vs Chord Location for Stations 1-4. $T = 4^\circ$, $A = 12^\circ$, & $M = 0.9$	74
4.14	Lift Coefficient vs Chord Location for Stations 1-4. $T = 4^\circ$, $A = 12^\circ$, & $M = 0.9$	75
4.15	Pressure Coefficient vs Chord Location for Increasing Amplitudes. $M = 0.6$ & $T = 0^\circ$	77
4.16	Trim Sweep Pressure Coefficient vs Chord Location at Station 2. $M = 0.9$, $A = 2^\circ$	79
4.17	Trim Sweep Pressure Coefficient vs Chord Location at Station 3. $M = 0.9$, $A = 2^\circ$	80
4.18	Trim Sweep Pressure Coefficient vs Chord Location Contour Plot at Station 2. $M = 0.9$, $A = 2^\circ$	82

Figure		Page
4.19	Trim Sweep Pressure Coefficient vs Chord Location Contour Plot at Station 3. $M = 0.9$, $A = 2^\circ$	83
4.20	Moment Coefficient vs AoA for Increasing Trim AoA. $M = 0.9$, $A = 2^\circ$	84
4.21	Pressure Coefficient vs Chord Location at Station 2. $M = 0.9$. A spike in negative pressure at leading edge develops as AoA increases.	85
4.22	Pressure Distribution at Stations 1-4. $M = 0.9$, $T = 0^\circ$ & $A = 12^\circ$.	86
4.23	Amplitude Sweep Pressure Distributions at Station 3. $M = 0.9$ & $T = 4^\circ$).	91
4.24	Amplitude Sweep Pressure Distributions at Station 2. $M = 0.9$ & $T = 0^\circ$	92
4.25	Pressure Distributions at Station 2. $M = 0.9$, $T = 0^\circ$, & $A = 12^\circ$.	93
4.26	Amplitude Sweep Pressure Distributions at Station 2. $M = 0.9$ & $T = 4^\circ$	94
4.27	Mach Number Sweep Pressure Distributions at Station 2. $T = 0^\circ$ & $A = 2^\circ$	98
4.28	Mach Number Sweep Pressure Distributions at Station 2. $T = 0^\circ$ & $A = 12^\circ$	99
4.29	Mach Number Sweep Moment Coefficient vs AoA. $T = 0^\circ$ & $A = 12^\circ$	100
4.30	Mach Number Sweep Moment Coefficient vs AoA at Station 3. $T = 0^\circ$	101
4.31	Pitch Up Pressure Distributions, $t^* = 1$. All cases have the same AoA at pitch up. $M = 0.9$	103
4.32	Pitch Down Pressure Distributions, $t^* = 0.5$. All cases have the same AoA. $M = 0.9$	105
A.1	Pressure distributions at Mach number 0.3. Frequency = 5.7 Hz, trim = 0° , amplitude = 0.5° , 2° , & 12°	112
A.2	Pressure distributions at Mach number 0.3. Frequency = 5.7 Hz, trim = 4° , amplitude = 0.5° , 2° , & 12°	113

Figure		Page
A.3	Pressure distributions at Mach number 0.3. Frequency = 5.7 Hz, trim = 8°, amplitude = 0.5°, 2°, & 12°	114
A.4	Pressure distributions at Mach number 0.3. Frequency = 5.7 Hz, trim = 12°, amplitude = 0.5° & 2°	115
A.5	Pressure distributions at Mach number 0.6. Frequency = 5.7 Hz, trim = 0°, amplitude = 0.5°, 2°, & 4°	116
A.6	Pressure distributions at Mach number 0.6. Frequency = 5.7 Hz, trim = 0°, amplitude = 8°, 10°, & 12°	117
A.7	Pressure distributions at Mach number 0.6. Frequency = 5.7 Hz, trim = 4°, amplitude = 0.5°, 2°, & 12°	118
A.8	Pressure distributions at Mach number 0.6. Frequency = 5.7 Hz, trim = 8°, amplitude = 0.5° & 2°	119
A.9	Pressure distributions at Mach number 0.75. Frequency = 5.7 Hz, trim = 0°, amplitude = 2° & 12°	120
A.10	Pressure distributions at Mach number 0.85. Frequency = 5.7 Hz, trim = 0°, amplitude = 2° & 12°	121
A.11	Pressure distributions at Mach number 0.85. Frequency = 5.7 Hz, trim = 0°, amplitude = 2°. Top used -cosine function, and bottom used +cosine function.	122
A.12	Pressure distributions at Mach number 0.9. Frequency = 5.7 Hz, trim = 0°, amplitude = 0.5°, 2°, & 4°	123
A.13	Pressure distributions at Mach number 0.9. Frequency = 5.7 Hz, trim = 0°, amplitude = 8°, 10°, & 12°	124
A.14	Pressure distributions at Mach number 0.9. Frequency = 5.7 Hz, (Top) trim = 2° & amplitude = 2°, (middle & bottom) trim = 4°, amplitude = 0.5° & 2°	125
A.15	Pressure distributions at Mach number 0.9. Frequency = 5.7 Hz, trim = 4°, amplitude = 4°, 8°, & 10°	126
A.16	Pressure distributions at Mach number 0.9. Frequency = 5.7 Hz, trim = 4°, amplitude = 12°. Top used BLC solver, and bottom used fully inviscid solver.	127

Figure		Page
A.17	Pressure distributions at Mach number 0.9. Frequency = 5.7 Hz, trim = 6°, amplitude = 2°. The Bottom plot used a +cosine function.	128
A.18	Pressure distributions at Mach number 0.9. Frequency = 5.7 Hz, Top and middle plots had trim = 8°, amplitude = 0.5° & 2°. Bottom plots had trim = 12°, amplitude = 0.5°, & used a +cosine function.	129
A.19	Pressure distributions at Mach number 0.95. Frequency = 5.7 Hz, trim = 0°, amplitude = 2° & 12°	130
A.20	Pressure distributions at Mach number 0.95. Frequency = 5.7 Hz, trim = 10°, amplitude = 2°, 2°, & 4°. Middle plots used a +cosine function.	131
B.1	Pressure distributions at Mach number 0.3. Frequency = 5.7 Hz, trim = 0°, amplitude = 0.5°, 2°, & 12°	132
B.2	Pressure distributions at Mach number 0.3. Frequency = 5.7 Hz, trim = 4°, amplitude = 0.5°, 2°, & 12°	133
B.3	Pressure distributions at Mach number 0.3. Frequency = 5.7 Hz, trim = 8°, amplitude = 0.5°, 2°, & 12°	134
B.4	Pressure distributions at Mach number 0.3. Frequency = 5.7 Hz, trim = 12°, amplitude = 0.5° & 2°	135
B.5	Pressure distributions at Mach number 0.6. Frequency = 5.7 Hz, trim = 0°, amplitude = 0.5°, 2°, & 4°	136
B.6	Pressure distributions at Mach number 0.6. Frequency = 5.7 Hz, trim = 0°, amplitude = 8°, 10°, & 12°	137
B.7	Pressure distributions at Mach number 0.6. Frequency = 5.7 Hz, trim = 4°, amplitude = 0.5°, 2°, & 12°	138
B.8	Pressure distributions at Mach number 0.6. Frequency = 5.7 Hz, trim = 8°, amplitude = 0.5° & 2°	139
B.9	Pressure distributions at Mach number 0.75. Frequency = 5.7 Hz, trim = 0°, amplitude = 2° & 12°	140
B.10	Pressure distributions at Mach number 0.85. Frequency = 5.7 Hz, trim = 0°, amplitude = 2° & 12°	141

Figure		Page
B.11	Pressure distributions at Mach number 0.85. Frequency = 5.7 Hz, trim = 0°, amplitude = 2°. Top used -cosine function, and bottom used +cosine function.	142
B.12	Pressure distributions at Mach number 0.9. Frequency = 5.7 Hz, trim = 0°, amplitude = 0.5°, 2°, & 4°	143
B.13	Pressure distributions at Mach number 0.9. Frequency = 5.7 Hz, trim = 0°, amplitude = 8°, 10°, & 12°	144
B.14	Pressure distributions at Mach number 0.9. Frequency = 5.7 Hz, (Top) trim = 2° & amplitude = 2°, (middle & bottom) trim = 4°, amplitude = 0.5° & 2°	145
B.15	Pressure distributions at Mach number 0.9. Frequency = 5.7 Hz, trim = 4°, amplitude = 4°, 8°, & 10°	146
B.16	Pressure distributions at Mach number 0.9. Frequency = 5.7 Hz, trim = 4°, amplitude = 12°. Top used BLC solver, and bottom used fully inviscid solver.	147
B.17	Pressure distributions at Mach number 0.9. Frequency = 5.7 Hz, trim = 6°, amplitude = 2°. The Bottom plot used a +cosine function.	148
B.18	Pressure distributions at Mach number 0.9. Frequency = 5.7 Hz, Top and middle plots had trim = 8°, amplitude = 0.5° & 2°. Bottom plots had trim = 12°, amplitude = 0.5°, & used a +cosine function.	149
B.19	Pressure distributions at Mach number 0.95. Frequency = 5.7 Hz, trim = 0°, amplitude = 2° & 12°	150
B.20	Pressure distributions at Mach number 0.95. Frequency = 5.7 Hz, trim = 10°, amplitude = 2°, 2°, & 4°. Middle plots used a +cosine function.	151
C.1	Pressure distributions at Mach number 0.3. Frequency = 5.7 Hz, trim = 0°, amplitude = 0.5°, 2°, & 12°	152
C.2	Pressure distributions at Mach number 0.3. Frequency = 5.7 Hz, trim = 4°, amplitude = 0.5°, 2°, & 12°	153
C.3	Pressure distributions at Mach number 0.3. Frequency = 5.7 Hz, trim = 8°, amplitude = 0.5°, 2°, & 12°	154

Figure		Page
C.4	Pressure distributions at Mach number 0.3. Frequency = 5.7 Hz, trim = 12°, amplitude = 0.5° & 2°	155
C.5	Pressure distributions at Mach number 0.6. Frequency = 5.7 Hz, trim = 0°, amplitude = 0.5°, 2°, & 4°	156
C.6	Pressure distributions at Mach number 0.6. Frequency = 5.7 Hz, trim = 0°, amplitude = 8°, 10°, & 12°	157
C.7	Pressure distributions at Mach number 0.6. Frequency = 5.7 Hz, trim = 4°, amplitude = 0.5°, 2°, & 12°	158
C.8	Pressure distributions at Mach number 0.6. Frequency = 5.7 Hz, trim = 8°, amplitude = 0.5° & 2°	159
C.9	Pressure distributions at Mach number 0.75. Frequency = 5.7 Hz, trim = 0°, amplitude = 2° & 12°	160
C.10	Pressure distributions at Mach number 0.85. Frequency = 5.7 Hz, trim = 0°, amplitude = 2° & 12°	161
C.11	Pressure distributions at Mach number 0.85. Frequency = 5.7 Hz, trim = 0°, amplitude = 2°. Top used -cosine function, and bottom used +cosine function.	162
C.12	Pressure distributions at Mach number 0.9. Frequency = 5.7 Hz, trim = 0°, amplitude = 0.5°, 2°, & 4°	163
C.13	Pressure distributions at Mach number 0.9. Frequency = 5.7 Hz, trim = 0°, amplitude = 8°, 10°, & 12°	164
C.14	Pressure distributions at Mach number 0.9. Frequency = 5.7 Hz, (Top) trim = 2° & amplitude = 2°, (middle & bottom) trim = 4°, amplitude = 0.5° & 2°	165
C.15	Pressure distributions at Mach number 0.9. Frequency = 5.7 Hz, trim = 4°, amplitude = 4°, 8°, & 10°	166
C.16	Pressure distributions at Mach number 0.9. Frequency = 5.7 Hz, trim = 4°, amplitude = 12°. Top used BLC solver, and bottom used fully inviscid solver.	167
C.17	Pressure distributions at Mach number 0.9. Frequency = 5.7 Hz, trim = 6°, amplitude = 2°. The Bottom plot used a +cosine function.	168

Figure		Page
C.18	Pressure distributions at Mach number 0.9. Frequency = 5.7 Hz, Top and middle plots had trim = 8°, amplitude = 0.5° & 2°. Bottom plots had trim = 12°, amplitude = 0.5°, & used a +cosine function.	169
C.19	Pressure distributions at Mach number 0.95. Frequency = 5.7 Hz, trim = 0°, amplitude = 2° & 12°	170
C.20	Pressure distributions at Mach number 0.95. Frequency = 5.7 Hz, trim = 10°, amplitude = 2°, 2°, & 4°. Middle plots used a +cosine function.	171
D.1	Pressure distributions at Mach number 0.3. Frequency = 5.7 Hz, trim = 0°, amplitude = 0.5°, 2°, & 12°	172
D.2	Pressure distributions at Mach number 0.3. Frequency = 5.7 Hz, trim = 4°, amplitude = 0.5°, 2°, & 12°	173
D.3	Pressure distributions at Mach number 0.3. Frequency = 5.7 Hz, trim = 8°, amplitude = 0.5°, 2°, & 12°	174
D.4	Pressure distributions at Mach number 0.3. Frequency = 5.7 Hz, trim = 12°, amplitude = 0.5° & 2°	175
D.5	Pressure distributions at Mach number 0.6. Frequency = 5.7 Hz, trim = 0°, amplitude = 0.5°, 2°, & 4°	176
D.6	Pressure distributions at Mach number 0.6. Frequency = 5.7 Hz, trim = 0°, amplitude = 8°, 10°, & 12°	177
D.7	Pressure distributions at Mach number 0.6. Frequency = 5.7 Hz, trim = 4°, amplitude = 0.5°, 2°, & 12°	178
D.8	Pressure distributions at Mach number 0.6. Frequency = 5.7 Hz, trim = 8°, amplitude = 0.5° & 2°	179
D.9	Pressure distributions at Mach number 0.75. Frequency = 5.7 Hz, trim = 0°, amplitude = 2° & 12°	180
D.10	Pressure distributions at Mach number 0.85. Frequency = 5.7 Hz, trim = 0°, amplitude = 2° & 12°	181
D.11	Pressure distributions at Mach number 0.85. Frequency = 5.7 Hz, trim = 0°, amplitude = 2°. Top used -cosine function, and bottom used +cosine function.	182

Figure		Page
D.12	Pressure distributions at Mach number 0.9. Frequency = 5.7 Hz, trim = 0°, amplitude = 0.5°, 2°, & 4°	183
D.13	Pressure distributions at Mach number 0.9. Frequency = 5.7 Hz, trim = 0°, amplitude = 8°, 10°, & 12°	184
D.14	Pressure distributions at Mach number 0.9. Frequency = 5.7 Hz, (Top) trim = 2° & amplitude = 2°, (middle & bottom) trim = 4°, amplitude = 0.5° & 2°	185
D.15	Pressure distributions at Mach number 0.9. Frequency = 5.7 Hz, trim = 4°, amplitude = 4°, 8°, & 10°	186
D.16	Pressure distributions at Mach number 0.9. Frequency = 5.7 Hz, trim = 4°, amplitude = 12°. Top used BLC solver, and bottom used fully inviscid solver.	187
D.17	Pressure distributions at Mach number 0.9. Frequency = 5.7 Hz, trim = 6°, amplitude = 2°. The bottom plot used a +cosine function.	188
D.18	Pressure distributions at Mach number 0.9. Frequency = 5.7 Hz, Top and middle plots had trim = 8°, amplitude = 0.5° & 2°. Bottom plots had trim = 12°, amplitude = 0.5°, & used a +cosine function.	189
D.19	Pressure distributions at Mach number 0.95. Frequency = 5.7 Hz, trim = 0°, amplitude = 2° & 12°	190
D.20	Pressure distributions at Mach number 0.95. Frequency = 5.7 Hz, trim = 10°, amplitude = 2°, 2°, & 4°. Middle plots used a +cosine function.	191
E.1	Moment time histories at Mach number 0.3. Frequency = 5.7 Hz, trim = 0°, amplitude = 0.5°, 2°, & 12°	192
E.2	Moment time histories at Mach number 0.3. Frequency = 5.7 Hz, trim = 4°, amplitude = 0.5°, 2°, & 12°	193
E.3	Moment time histories at Mach number 0.3. Frequency = 5.7 Hz, trim = 8°, amplitude = 0.5°, 2°, & 12°	194
E.4	Moment time histories at Mach number 0.3. Frequency = 5.7 Hz, trim = 12°, amplitude = 0.5° & 2°	195
E.5	Moment time histories at Mach number 0.6. Frequency = 5.7 Hz, trim = 0°, amplitude = 0.5°, 2°, & 4°	196

Figure		Page
E.6	Moment time histories at Mach number 0.6. Frequency = 5.7 Hz, trim = 0°, amplitude = 8°, 10°, & 12°	197
E.7	Moment time histories at Mach number 0.6. Frequency = 5.7 Hz, trim = 4°, amplitude = 0.5°, 2°, & 12°	198
E.8	Moment time histories at Mach number 0.6. Frequency = 5.7 Hz, trim = 8°, amplitude = 0.5° & 2°	199
E.9	Moment time histories at Mach number 0.75. Frequency = 5.7 Hz, trim = 0°, amplitude = 2° & 12°	200
E.10	Moment time histories at Mach number 0.85. Frequency = 5.7 Hz, trim = 0°, amplitude = 2° & 12°	201
E.11	Moment time histories at Mach number 0.85. Frequency = 5.7 Hz, trim = 0°, amplitude = 2°. Top used -cosine function, and bottom used +cosine function.	202
E.12	Moment time histories at Mach number 0.9. Frequency = 5.7 Hz, trim = 0°, amplitude = 0.5°, 2°, & 4°	203
E.13	Moment time histories at Mach number 0.9. Frequency = 5.7 Hz, trim = 0°, amplitude = 8°, 10°, & 12°	204
E.14	Moment time histories at Mach number 0.9. Frequency = 5.7 Hz, (Top) trim = 2° & amplitude = 2°, (middle & bottom) trim = 4°, amplitude = 0.5° & 2°	205
E.15	Moment time histories at Mach number 0.9. Frequency = 5.7 Hz, trim = 4°, amplitude = 4°, 8°, & 10°	206
E.16	Moment time histories at Mach number 0.9. Frequency = 5.7 Hz, trim = 4°, amplitude = 12°. Top used BLC solver, and bottom used fully inviscid solver.	207
E.17	Moment time histories at Mach number 0.9. Frequency = 5.7 Hz, trim = 6°, amplitude = 2°. The bottom plot used a +cosine function.	208
E.18	Moment time histories at Mach number 0.9. Frequency = 5.7 Hz, Top and middle plots had trim = 8°, amplitude = 0.5° & 2°. Bottom plots had trim = 12°, amplitude = 0.5°, & used a +cosine function.	209
E.19	Moment time histories at Mach number 0.95. Frequency = 5.7 Hz, trim = 0°, amplitude = 2° & 12°	210

Figure		Page
E.20	Moment time histories at Mach number 0.95. Frequency = 5.7 Hz, trim = 10°, amplitude = 2°, 2°, & 4°. Middle plots used a +cosine function.	211
F.1	Lift time histories at Mach number 0.3. Frequency = 5.7 Hz, trim = 0°, amplitude = 0.5°, 2°, & 12°	212
F.2	Lift time histories at Mach number 0.3. Frequency = 5.7 Hz, trim = 4°, amplitude = 0.5°, 2°, & 12°	213
F.3	Lift time histories at Mach number 0.3. Frequency = 5.7 Hz, trim = 8°, amplitude = 0.5°, 2°, & 12°	214
F.4	Lift time histories at Mach number 0.3. Frequency = 5.7 Hz, trim = 12°, amplitude = 0.5° & 2°	215
F.5	Lift time histories at Mach number 0.6. Frequency = 5.7 Hz, trim = 0°, amplitude = 0.5°, 2°, & 4°	216
F.6	Lift time histories at Mach number 0.6. Frequency = 5.7 Hz, trim = 0°, amplitude = 8°, 10°, & 12°	217
F.7	Lift time histories at Mach number 0.6. Frequency = 5.7 Hz, trim = 4°, amplitude = 0.5°, 2°, & 12°	218
F.8	Lift time histories at Mach number 0.6. Frequency = 5.7 Hz, trim = 8°, amplitude = 0.5° & 2°	219
F.9	Lift time histories at Mach number 0.75. Frequency = 5.7 Hz, trim = 0°, amplitude = 2° & 12°	220
F.10	Lift time histories at Mach number 0.85. Frequency = 5.7 Hz, trim = 0°, amplitude = 2° & 12°	221
F.11	Lift time histories at Mach number 0.85. Frequency = 5.7 Hz, trim = 0°, amplitude = 2°. Top used -cosine function, and bottom used +cosine function.	222
F.12	Lift time histories at Mach number 0.9. Frequency = 5.7 Hz, trim = 0°, amplitude = 0.5°, 2°, & 4°	223
F.13	Lift time histories at Mach number 0.9. Frequency = 5.7 Hz, trim = 0°, amplitude = 8°, 10°, & 12°	224

Figure		Page
F.14	Lift time histories at Mach number 0.9. Frequency = 5.7 Hz, (Top) trim = 2° & amplitude = 2°, (middle & bottom) trim = 4°, amplitude = 0.5° & 2°	225
F.15	Lift time histories at Mach number 0.9. Frequency = 5.7 Hz, trim = 4°, amplitude = 4°, 8°, & 10°	226
F.16	Lift time histories at Mach number 0.9. Frequency = 5.7 Hz, trim = 4°, amplitude = 12°. Top used BLC solver, and bottom used fully inviscid solver.	227
F.17	Lift time histories at Mach number 0.9. Frequency = 5.7 Hz, trim = 6°, amplitude = 2°. The bottom plot used a +cosine function. .	228
F.18	Lift time histories at Mach number 0.9. Frequency = 5.7 Hz, Top and middle plots had trim = 8°, amplitude = 0.5° & 2°. Bottom plots had trim = 12°, amplitude = 0.5°, & used a +cosine function.	229
F.19	Lift time histories at Mach number 0.95. Frequency = 5.7 Hz, trim = 0°, amplitude = 2° & 12°	230
F.20	Lift time histories at Mach number 0.95. Frequency = 5.7 Hz, trim = 10°, amplitude = 2°, 2°, & 4°. Middle plots used a +cosine function.	231

List of Tables

Table		Page
2.1	Hope's test matrix [20].	22
2.2	Summary of Hope's results at station 1 [20].	22
2.3	Pung's test matrix [28].	24
3.1	C_p and C_m for improved surface grid and mesh configurations. . .	44
3.2	Test Matrix. Frequency = 5.7 Hz, "I" = fully inviscid, & "+" = + <i>cosine</i> function.	50
4.1	Critical pressure coefficient vs Mach using standard air properties at sea level.	54
4.2	Converged (green) vs non-converged (red) cases. A "+" = + <i>cosine</i> function & "I" = fully inviscid solution.	62
4.3	Amplitude sweep with trim AoA = 0°, Mach number = 0.6 & fre- quency = 5.7 Hz.	76
4.4	A trim sweep with amplitude = 0° Mach number = 0.9, & frequency = 5.7 Hz.	78
4.5	Amplitude sweeps with Mach number = 0.9 & frequency = 5.7 Hz.	88
4.6	Amplitude sweep clockwise (CW) moment vs AoA curves. Mach number = 0.9 & frequency = 5.7 Hz. Green indicates a CW twist, and AoA values show the moment curve intersection point.	89
4.7	Mach number sweep with trim AoA = 2° & frequency = 5.7 Hz. . .	95
4.8	A comparison of pitch up pressure distributions ($t^* = 1$) for cases with the same AoA. Mach number = 0.9 & frequency = 5.7 Hz. . .	102
4.9	A comparison of pitch up pressure distributions ($t^* = 0.5$) for cases with the same AoA. Mach number = 0.9 & frequency = 5.7 Hz. . .	104

List of Symbols

Symbol		Page
t^*	Cycle Time	36
$C_{p_{min}}$	Minimum Sectional Pressure Coefficient	38
C_p	Sectional Pressure Coefficient	38
C_m	Sectional Moment Coefficient	38
$ C_p _2$	2-norm of the Sectional Pressure Coefficient	39
α	Angle of Attack	40
$ C_m _2$	2-norm of the Sectional Moment Coefficient	40
(x/c)	Location within the Local Chord	43
T	Trim AoA	52
A	Amplitude	52
M	Mach	52
F	Frequency	52
C_l	Sectional Lift Coefficient	55
C_{l_α}	Lift Curve Slope	56
C_{l_0}	Zero Lift AoA	56

List of Abbreviations

Abbreviation		Page
USAF	The United States Air Force	1
LCO	Limit Cycle Oscillation	1
AFSEO	Air Force Seek Eagle Office	1
SITES	Shock Induced Trailing Edge Separation	2
AoA	Angle of Attack	3
ZEUS	ZONA Technologies Euler Unsteady Solver	3
V-g	Velocity-Damping	10
N-S	Navier-Stokes	11
CFD	Computational Fluid Dynamics	11
NLR	National Aerospace Laboratory	16
3D	Three Dimensional	22
FEM	Finite Element Model	26
JST	Jameson-Schmidt-Turkel	33

SHOCK MIGRATION ON AN OSCILLATING STRAKED DELTA WING USING AN UNSTEADY EULER SOLVER

I. Introduction

Aircraft have taken on many roles since their conception over 100 years ago, when the Wright brothers first took flight in 1903. Only a few short years after, aircraft found their first military role in World War I for surveillance and reconnaissance. As aircraft became safer, they started to be used for transportation and travel. These aircraft have evolved into highly technical tools designed to fill specific roles. The United States Air Force (USAF) has many aircraft to fill unique needs. As our threats evolve, so does the complexity of those needs. In order to keep up with the advancing threats of modern technology in the hands of our adversaries, there is an increasing need to expand our capabilities to match. One of the most versatile aircraft of the US military is the multi-role F-16. Designed to be a lightweight fighter, the F-16 has thin, light wings in order to be fast and agile. The thin wings of the F-16 are sensitive to aeroelastic phenomena like flutter and limit cycle oscillations (LCO) within the standard operating flight envelope, particularly when carrying stores on its wings. Each store configuration is susceptible to flutter and LCO at different flight conditions. This presents significant danger to the pilot and the aircraft and must be tested. To fill this need, the Air Force Seek Eagle Office (AFSEO) is charged with certifying each load configuration before it can become operational. Through analysis and testing, AFSEO ensures pilots can safely perform their mission.

1.1 Background and Motivations

One aeroelastic phenomenon of great interest to AFSEO is flutter, which has influenced aircraft design since World War I. It is characterized as a self-sustaining oscillatory instability that propagates when the aerodynamic forces on a flexible body

coupled with its natural modes of vibration. In flutter, the oscillation amplitude will continue to increase until there is either a change in flight conditions or the structure fails. Faster aircraft with thin, flexible wings like a fighter aircraft designed for maneuverability and speed are more susceptible to flutter. When the oscillation amplitude does not change, the phenomenon is called LCO. Like flutter, LCO is an oscillatory motion, except the forces acting on/within the wing structure are nonlinear, which limits the amplitude to a maximum constant value.

For the F-16, LCO is seen to be an antisymmetric oscillation of its wings and a lateral motion of the fuselage that can adversely affect the pilot's performance, target accuracy, and cause structural fatigue that increases maintenance costs and decreases the lifespan of the aircraft. Fighter aircraft like the F-16 often carry external stores like missiles, bombs, and fuel tanks under its wings and fuselage which inherently change the inertial, aerodynamic, and elastic forces on the aircraft in flight. This can increase the airframe's susceptibility to LCO and makes understanding when LCO will occur and the severity of the oscillation when it does very important. AFSEO certifies each external store configuration before it can become operational, ensuring they are both safe and effective. Flight testing is often used to determine the LCO onset Mach number and amplitude for specific flight conditions within the flight envelope, but it is expensive, time consuming, and requires a lot of manpower. Using nonlinear computational analysis can be less costly than flight test and can predict amplitude as well as LCO onset, but can also be time consuming. For this reason, linearized models are being explored to shorten computation time. Some linear analysis techniques have been shown to predict LCO onset conditions fairly accurately but have not yet been shown to predict the severity.

There is general consensus among aeroelasticians that LCO is a result of the interaction between nonlinear aerodynamic and structural forces, but there is disagreement on which is the more significant contributor. One phenomenon thought by some to be the primary driver is shock induced trailing edge separation (SITES). As a shock develops on the upper surface of the wing, separation of the flow from the wing

can occur behind the shock, which decreases the lift force generated by the wing. The dynamic response of the aircraft can cause the shock to move and the flow to separate further or reattach behind the shock. This would once again change the aerodynamic forces, possibly triggering the cyclical pattern required for oscillation of the wing. In order to understand the impact of SITES on LCO, we must first understand the shock movement as the wing oscillates to determine if the changes in aerodynamic forces have the potential to drive this oscillation.

1.2 Research Objectives

In order to understand the true impact of SITES, this research aims to expand the tested envelope completed by Hope [20] with his delta wing model created to replicate the half-span straked delta wing used in Cunningham’s wind tunnel experiments. LCO testing is performed throughout the whole flight envelope for a fighter aircraft. The expanded test envelope will improve characterization of shock movement by simulating cases with Mach number between 0.3 and 0.95, trim angle of attack (AoA) between 0° and 12° , and oscillation amplitude between 0.5° and 12° . By changing one variable at a time, the impact of each individual variable’s impact on shock development and motion can be better understood.

Another objective of this research is to demonstrate the use of ZONA Technologies Euler Unsteady Aerodynamic Solver (ZEUS), an Euler solver, as a useful tool in predicting shock movement on a pitching wing. Comparisons of flow developments such as shock development, movement and separation were made to those observed in Cunningham’s wind tunnel tests, Hope’s CFD analysis using ZEUS, and Pung’s CFD analysis using a Navier-Stokes solver. By improving Hope’s ZEUS model and comparing flow developments to Cunningham and Pung, the usefulness of ZEUS’ results can be discussed. Because ZEUS has shown limited success in predicting separation, a development necessary for SITES, inaccuracies are expected when separation is present, and so comparisons to Cunningham and Pung are primarily qualitative.

The broader test envelope will be used to aid future flight tests in predicting shock development and motion under LCO conditions. These flight tests will help determine if ZEUS is a valuable tool for the AFSEO to better understand LCO and alleviate flight testing.

II. Literature Review

2.1 *Introduction*

The F-16 is a multi-role fighter aircraft that is more susceptible to limit cycle oscillations (LCO) than most aircraft because of the variety and number of payloads it can carry under its thin wings. It has nine traditional stations that allow it to perform a dynamic range of missions. Each store configuration requires testing to determine safe and effective operation. The need to alleviate the extensive flight testing that is required is the fundamental issue which drives continued research into LCO for the F-16. This chapter will first provide a basic understanding of aeroelasticity and linear flutter analysis before narrowing focus to the specific issue of LCO. This chapter will also provide an overview of store aerodynamics, flight testing by AFSEO, as well as computational methods that have been used to understand and predict characteristics of LCO. Finally, wind tunnel experiments performed by Cunningham [8] and research completed by Dylan Hope [20] are summarized, which form the foundation for the author's own research.

2.2 *Aeroelastic Phenomena*

Aeroelasticity is the study of the interaction between the elastic forces of a deforming structure, aerodynamic forces of the fluid around the structure, and the inertial forces of the aircraft in motion [19]. Hodges separates aeroelasticity into three categories of interaction shown in Figure 2.1. A wide spectrum of aeroelastic phenomena can develop as a result of complex aircraft design ranging from unnoticeable perturbations to instability and catastrophic failure.

Aeroelastic phenomena have played a major role in powered flight since the very beginning. The Wright brothers' use of wing warping to overcome instability gave them the advantage they needed to achieve flight before Samuel Langley, who's attempts in 1903 failed due to torsional divergence, when the lifting surface deforms such that the aerodynamic loads increase, causing more deformation and even higher loads until the structure fails [19]. Stability and control is a major concern aeroe-

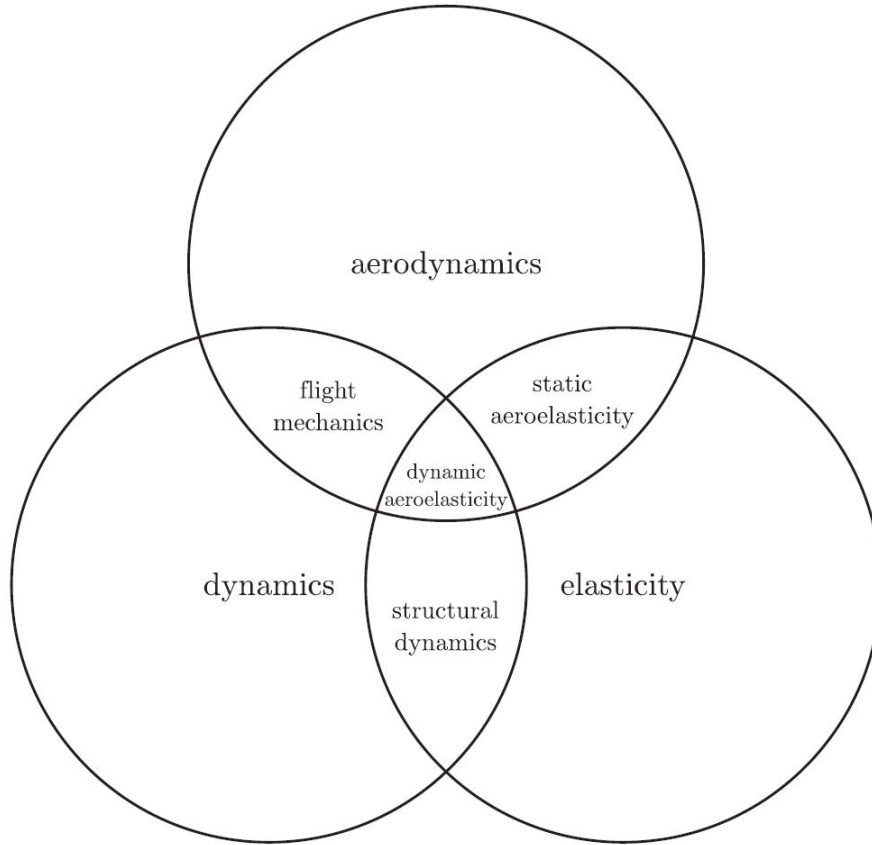


Figure 2.1: Schematic of the field of aeroelasticity [19, p.2].

lasticians face when designing new aircraft. The coupled relationship between elastic deformation and aerodynamic loads can cause unexpected results like torsional divergence or control reversal. An example of control reversal is called aileron reversal, where the deflection of the ailerons results in the opposite motion than was intended. These are two of the most common static instabilities, and can severely limit the flight envelope if not designed out of the aircraft.

When dynamics are added into the equation, other instabilities like flutter may occur. Also known as dynamic divergence, flutter is a self-excited motion which, like divergence, increases in structural deformation until structural failure. Unlike static divergence, flutter is oscillatory in nature, where the aerodynamic forces pair with the structure's natural modes of vibration to produce sinusoidal motion with continuously increasing amplitude. Fighter aircraft like the F-16 have thin, stubby

wings designed for high maneuverability. This makes these aircraft more susceptible to flutter than classical aircraft. In highly dynamic maneuvers and in the transonic regime, a nonlinear phenomenon known as LCO can occur [24]. LCO is similar to flutter except for the presence of nonlinear forces that limit the oscillation amplitude, creating a sustained, sinusoidal motion that will continue at a constant amplitude until flight conditions change [5]. Because the amplitude is limited, LCO is considered neutrally stable and typically does not lead to catastrophic failure, but it often causes pilot discomfort, degrades mission performance, interferes with sensors, and fatigues the structure of the aircraft.

LCO is grouped into two categories, typical and non-typical. Typical LCO develops for a specific flight condition when the onset Mach number is reached. As the Mach number increases further, so does the amplitude of the oscillation. For non-typical LCO, the amplitude increases with Mach number, but once a certain Mach number is reached, the amplitude begins to decrease. Because of this, non-typical LCO is sometimes referred to as a hump mode. Some natural vibration modes are symmetrical, but LCO usually develops when the first antisymmetric bending and torsion modes coalesce at the same frequency [17].

Due to its nonlinear properties, LCO is not easy to predict. Many methods of analysis are being studied in the effort to quickly and efficiently determine LCO onset and severity. The presence of LCO is a recurring problem for certain fighter aircraft, particularly those with external store configurations like the F-16 that are predicted to be flutter sensitive [13]. Each store configuration can change the onset and severity of LCO, so it is essential to verify the aircraft can safely operate within its entire flight envelope for each store configuration.

Figure 2.2 shows the first antisymmetric bending and torsional modes for the F-16 which have proven to be susceptible to LCO. This figure also shows the nine traditional store locations for an F-16; one at each wing tip, three under each wing, and one under the centerline of the forebody. Each station is compatible with a variety

of stores of varying size, shape, and weight. This means that there are thousands of possible configurations, each with unique vibration modes that output just as unique of a response when excited. One configuration may experience classical flutter where another configuration experiences typical LCO at a slightly different frequency.

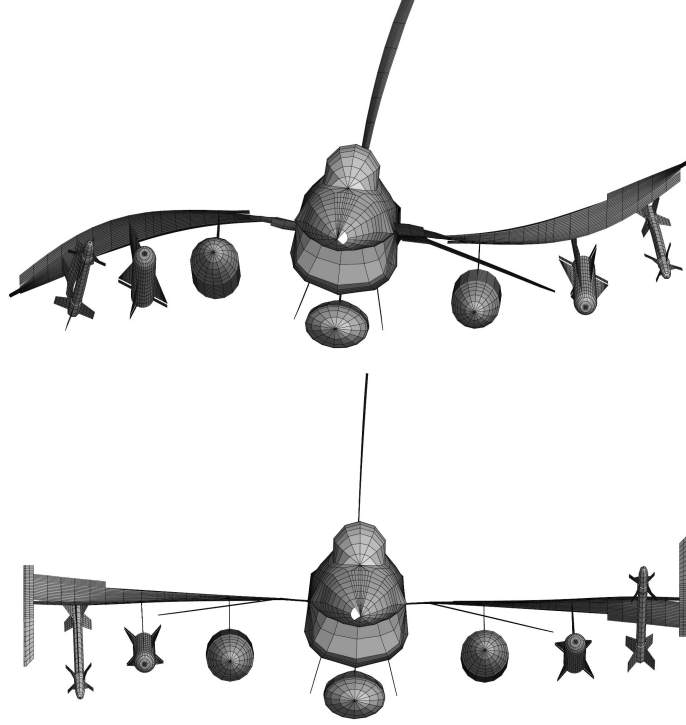


Figure 2.2: First Antisymmetric Bending and Torsional Modes for the F-16 [18].

2.3 *Flight Testing Methodology*

Due to its nonlinear properties, LCO is not easy to predict, so it is essential to verify the aircraft can safely operate within its entire flight envelope. Since different store configurations respond to inputs differently, the USAF investigates each configuration to ensure safe flight for the pilots. The Air Force Seek Eagle Office (AFSEO) is the organization within the USAF responsible for verifying that each store configuration for the F-16 is operationally acceptable. To do this, they examine a variety of factors, including electromagnetic compatibility, safe payload separation from the aircraft, structural strength, and flutter/LCO [17]. With the thousands of

store configurations currently available for the F-16 and new payloads added every year that must be certified with each prior configuration, one can picture the ever expanding task AFSEO is responsible for completing. Delays in certification leave gaps in our war fighter’s capabilities. LCO and flutter testing are time consuming and labor intensive, so it is not feasible to test each flight condition for every store configuration. To reduce the amount of testing needed, analytical tools are used to down-select which configurations need flight testing.

2.3.1 LCO Testing. Both flutter and LCO behavior are dependent on the external stores on the aircraft. The F-16 can easily reach LCO within its normal operational envelope when carrying external stores. In flight test, the pilot intentionally inputs a small motion to the flaperon at a predetermined frequency [12]. This small input excites the vibration modes in the aircraft structure resulting in LCO. The pilot will vary Mach number, altitude, and input frequency as needed to certify the flight envelope for that load configuration. Through this test method, Charles Denegri of AFSEO was able to excite classical flutter, typical, and non-typical LCO, and found that the wingtip launcher’s aerodynamics had a significant influence on the instability onset speed [12]. Safety limits are put in place to terminate the test if the motion becomes too risky to continue. Denegri notes that classical flutter occurred during this test series, terminating the test due to the divergent nature of the response. To reduce the amount of testing AFSEO must complete, simulations and clearance by similarity are already used, but this introduces a different kind of risk. As explained by Tauer, qualification by similarity has resulted in unexpected vibrations during operational flight in the past when aeroelastic characteristics are overlooked or misunderstood [29]. With good computational analysis, fewer flight tests will be required and the tests that remain will have lower risk if the type of response and severity can be estimated with reasonable certainty. A good balance of model fidelity and processing time must be acquired before analysis can significantly reduce testing requirements without unnecessary risk.

2.4 *Computational Aeroelastic Analysis*

In order to alleviate extensive flight testing, aeroelastic analysis must be quick, accurate, and able to predict the Mach number onset speed, frequency, and discern between flutter, typical, and non-typical LCO. If LCO is predicted, knowing the amplitude is also necessary to determine the severity. Linear flutter analysis has been used to predict frequency [12] as well as Mach onset with varying success [17], but linear analysis is unable to determine the severity of LCO when present. This is due to the nonlinear characteristics that distinguish LCO from classical flutter which is linear.

2.4.1 Classical Linear Flutter Analysis. Classical linear flutter analysis has been used by many researchers in order to bring understanding to LCO on the F-16. Charles Denegri of AFSEO used the doublet-lattice method to determine that linear flutter analysis can be used to identify oscillation frequency, and showed a strong correlation between flight test behavior and modal composition analysis [12]. Though most have been unsuccessful in using linear analysis to predict onset Mach number, Gabbard had some success but found that his analysis was very dependent on altitude [17]. This suggests that dynamic pressure plays a significant role in the development of LCO. Thomas [30] used a harmonic balance approach and was able to correlate LCO amplitude to flight tests with some accuracy. He discovered that small changes in the aircraft's natural frequency modes had a significant impact on the flutter onset Mach number. This is particularly significant for the F-16 because of the vast variation found between wing structures from one aircraft to another due to the structural upgrades required to keep the aging aircraft operational. Toth [32] and Chen [6] each examined various store configurations for the F-16 using ZAERO, the predecessor of ZEUS by ZONA. Furthering his research, Toth used the ZTAIC solver by ZONA and discovered that one could distinguish between classical flutter, typical LCO, and non-typical LCO by looking at the velocity-damping (V-g) plots. The accuracy of classical linear flutter analysis is limited due to the nonlinear phenomena

that characterize LCO. Though linear analysis is not enough on its own to alleviate testing requirements, it has proven to give good indication of configurations that are expected to develop oscillatory instabilities in flight [23].

2.4.2 Nonlinear LCO Analysis. The nonlinear phenomenon that drives LCO is a topic debated by experts in the field of aeroelastic analysis. Nonlinear aerodynamics are present at transonic speeds above the critical Mach number when a normal shock develops on the top surface of the wing. In addition, complicated flows around wing-stores can excite other aerodynamic nonlinearities. Nonlinear structural damping can also occur due to movement within the structure when large deflections occur. Based on their research, some experts are of the opinion that LCO is a result of the relationship between nonlinear aerodynamics and nonlinear structural elasticity. Regardless of their opinions, high fidelity models can be compared to flight tests to determine accuracy, but are only as accurate as the data inputted into them. Navier-Stokes (N-S) equations are highly accurate due to their ability to include viscous effects and other aerodynamic nonlinearities. Researchers like Dowell [14], Thomas [30], and Melville [25] used Navier-Stokes equations in their analysis of the F-16. Thomas found that including viscous effects in the Computational Fluid Dynamics (CFD) model are crucial for computing the finite amplitude of LCO. N-S equations have given a lot of insight to the complicated issue of LCO, but the computational time required to achieve a solution is substantial, so a quicker analysis is desired for AFSEO to certify F-16 store-configurations. For this reason, the Euler equations have been studied. These equations are simplified versions of the more general Navier-Stokes equations and so are both less accurate and less time-consuming to compute. Viscous effects in the fluid are not captured in the Euler equations, so nonlinearities like flow separation cannot be predicted accurately. Tauer also found that these simplified equations made his analysis overly-sensitive to altitude changes [29]. Despite their limitations, Euler equations have the ability to predict characteristics

of the overarching issues of LCO which can be utilized to predict onset Mach number and amplitude.

2.4.3 Nonlinear Aerodynamics. Through wind tunnel experiments in 1986, Cunningham observed shock development and shock motion on a wing, and concluded that nonlinear aerodynamics provide the forces that drive the principal motion of LCO [24]. In order to understand how a shock can drive LCO, a basic understanding of how shocks form is necessary. A standard wing has a curved surface from its leading edge to its trailing edge. As the flow passes over the wing, the streamlines must diverge from their linear paths. This divergence decreases the local pressure and increases the local Mach number such that some of the flow around the wing is moving faster than the free stream flow [21]. As can be seen in Figure 2.3, when the critical Mach number is reached, a singular point on the upper surface of the wing reaches a Mach number of one. As speed is increased along the upper surface of

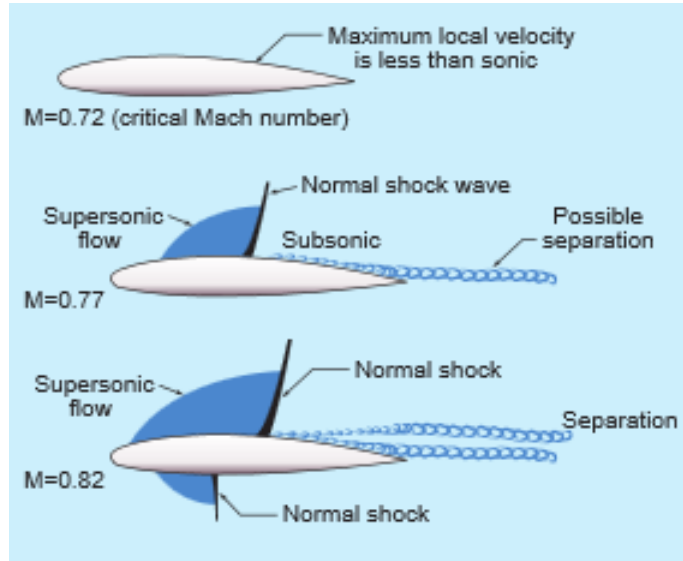


Figure 2.3: Shock development and flow separation on an airfoil [1].

the wing, the supersonic region expands. The low pressure in the supersonic region causes the local boundary layer to thicken. A weak family of compression waves forms and join to create a near-normal shock at the aft end of the supersonic region. The formation of a shock on the top of the wing is a nonlinear singularity that rapidly

increases pressure behind the shock. As pressure is increased, the boundary layer thins behind the shock. This thinning can sometimes cause enough expansion to create a smaller supersonic region and weak near-normal shock called a subsidiary shock [21]. By observing wind tunnel tests, researchers saw that for small angles of attack, an increase in angle of attack or Mach number strengthens the shock and moves the shock aft [3]. As the main shock strengthens, the subsidiary shocks weaken and/or disappear. A further increase in angle of attack or Mach number can strengthen the shock enough to locally separate the boundary layer. Though local separation is not typically seen in turbulent flow since turbulent flow is less susceptible to disturbances than laminar flow, if the boundary layer separates locally around the shock, the motion of the shock will reverse and move forward with an increase in angle of attack. If the local separation moves ahead of the shock, an oblique shock can occur in front of and joint the main shock some distance above the surface. This shock formation is called a lambda shock [21]. When a lambda shock formation occurs, the boundary layer is unlikely to reattach and is associated with shock stall. Another typical shock development is the presence of an oblique shock towards the leading edge of the wing.

Shocks can move, disappear, and reappear when flight conditions change or in response to wing motion like oscillations. Tijdeman concluded from his research that shocks can disappear for portions of the oscillation [31]. Parker et al [27] agreed with Tijdeman's findings, naming shock disappearance and reappearance as the nonlinearity responsible for LCO, which has the potential to excite and self-sustain oscillatory motion. Shock induced trailing edge separation (SITES) is one leading explanation behind LCO. With the presence of a normal shock, flow can separate aft of the shock where the flow is subsonic. Further increase in Mach number or angle of attack will increase the supersonic region further, pushing the normal shock wave back and increasing the likelihood of flow separation behind the shock. A normal shock can also appear on the bottom surface of the wing, but this is less common due to the geometric shape and angle of attack needed to create lift for the wing.

When a shock interacts with the boundary layer and removes energy, the flow can separate from the surface of the wing. This separation phenomenon gives a small shock movement the potential to drive large nonlinear changes in aerodynamic forces [17]. SITES was the particular nonlinearity that Cunningham indicated played the dominant role in LCO development at transonic speeds in his wind tunnel tests [24]. This concept is illustrated in Figure 2.4. When a change in flight conditions initiates SITES, a sudden nose-down pitching moment develops as a result of the reduced pressure on the top trailing edge of the wing. This pitching moment reduces wing incidence until a delayed reattachment follows and the nose down moment disappears [7].

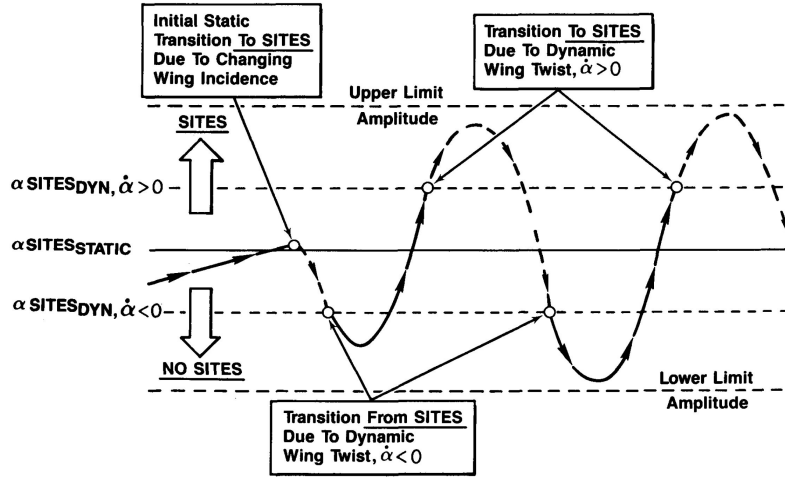


Figure 2.4: SITES induced LCO at a constant angle of attack [7].

Further research by Melville, who synchronized a Navier-Stokes model with an Euler model to retain some accuracy from the N-S equations and benefit from the speed of the Euler method, concluded that instabilities were linear when no SITES was observed, and nonlinear when SITES was present [25]. Some research does not support this theory, such as Gabbard who had mixed results [17]. Gabbard used ZONA Technologies Euler Unsteady Aerodynamic Solver (ZEUS) and found in his steady Euler analysis that shocks did not form on his F-16 model until Mach number .95, much higher than LCO has been recorded in flight. Gabbard also determined through flight tests that onset Mach number varied little with altitude compared to

his ZEUS analysis with structural damping included, suggesting that LCO is driven more by compressible flow effects.

2.4.4 Nonlinear Structural Damping. The topic of this research explores flow characteristics surrounding SITES. Contrary to Cunningham [10] and Melville [25] who believe SITES alone can cause LCO, many experts have the opinion that LCO is a result of the interaction of nonlinear aerodynamics and nonlinear structural elements. This view is not explored further in this study, but a brief summary of the prior research surrounding nonlinear structural damping will give the reader a view of the breadth of the issue of LCO analysis. One supporter of nonlinear structural force involvement in LCO is Meijer, who concluded that static deformations have a significant effect on response level during LCO and is therefore critical in determining LCO severity [24]. Amplitude-dependent frictional damping can limit the growth amplitude seen in flutter resulting in steady state oscillations if the damping is drastically increased around the neutral stability point [6]. In analysis by Mignolet, Liu and Chen [26], LCO was seen to occur at speeds below the transonic region where aerodynamic nonlinearities like shocks do not occur, suggesting that structural nonlinearities are likely present.

Dowell found that uncertainties in the structural natural frequencies could result in significant variations in the aeroelastic analysis [14]. Due to the ongoing life extension program for the F-16, periodic reinforcement parts are added to the structure. This makes every F-16 unique, which makes it difficult to validate analytical methods by comparing to flight tests. For this reason, Ferguson, in his project HAVE LCOcho, tuned his structural modes with static deflection data off a particular F-16, refined his model to match the data he gathered, and then compared his analytical result to flight test data from the same F-16 [16]. This model, named “AFIT07”, was later used by Masset [22], Hanson [18], and Tauer [29] in their individual studies.

2.5 *Wind Tunnel Experiments by Cunningham*

Wind tunnel tests were completed in 1986 by Lockheed Fort Worth Company at the National Aerospace Laboratory (NLR) in Amsterdam on a full span, straked wing model which represented the delta wing design of a modern aircraft [4, 11, 20]. The purpose of these tests were to oscillate the model in pitch to mimic dynamic flight maneuvers and observe the development and collapse of vortices. Then in 1991, more wind tunnel tests were completed to better understand unsteady transonic vortex flow about a simple semispan straked delta wing model, as well as to investigate the unsteady pressures and forces for typical LCO [8]. This test series expanded the test envelope of 1986 tests by testing the model at higher incidence angles as well up to transonic speeds. One of the objectives of these tests was to develop a prediction method for full scale LCO characteristics of an elastic aircraft [20].

2.5.1 Straked Delta Wing Model. The wind tunnel tests were conducted in NLR's $2.0 \times 1.6 \text{ m}^2$ high-speed tunnel. The wing was a cropped NACA 64A-204 airfoil with a -3° washout at the wingtip, the same airfoil used on the F-16. The wing had a sweep angle of 40° and was blended to the fuselage/wall with a strake which had a sweep angle of 76° . This model, referred to as the SiS model, was constructed of an aluminum alloy to decrease the weight and inertial loads on the wing and its support structures. Dimensions for the cropped wing are shown in Figures 2.5 and 2.6.

The straked delta wing model was mounted to a hydraulic actuated turntable within the sidewall of the test section of the wind tunnel [9]. This provided the oscillatory pitching motion of the wing during tests. Accelerometers and pressure transducers were attached to the model to measure motion and pressure distribution along the wing. The sensors were located along 4 chordwise Stations (1-4) of the wing and 3 spanwise Stations (5-7) of the wing as shown in Figure 2.6. The chordwise pressure Stations 1-4 measure 209.1, 274.0, 336.1, and 395.3 mm from the wind tunnel wall. These chordwise stations were later used by Dylan Hope to compare a computational model to the wind tunnel data [20].

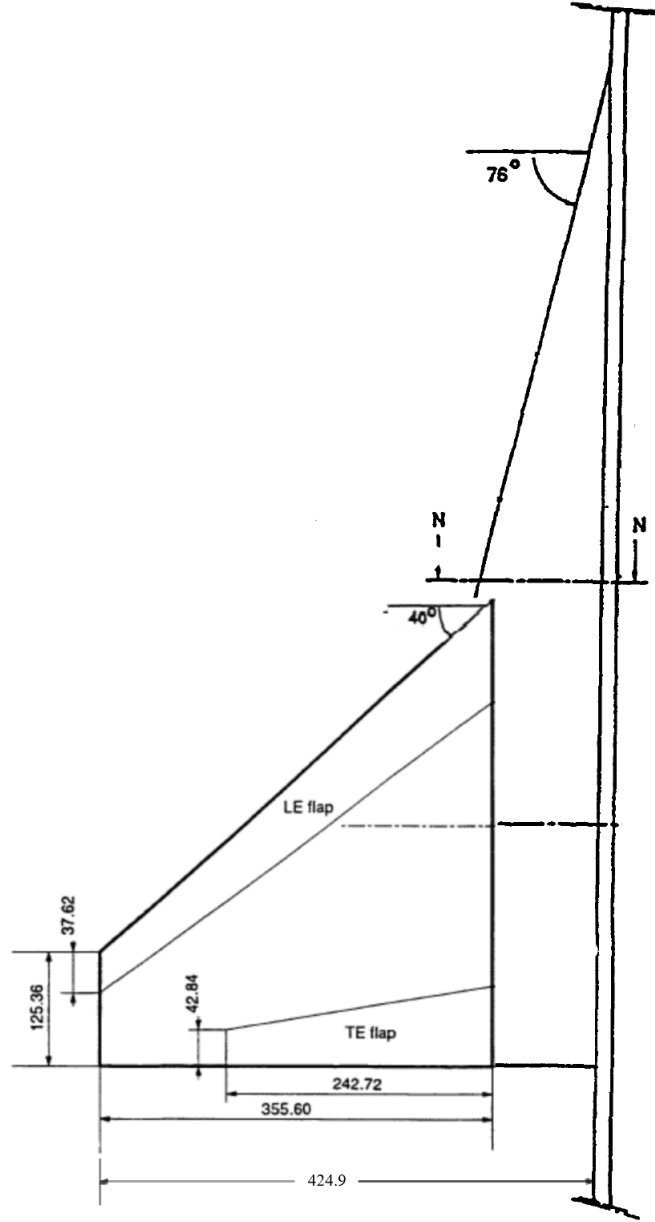


Figure 2.5: Dimensions of the staked NACA 64A-204 wing modell (in mm) [9].

2.5.2 Wind Tunnel Test Matrix. Cunningham used three test matrices, each testing the same model at different Mach numbers; $M = 0.225$, 0.6 , and 0.9 [9]. Figure 2.7 shows the test matrix for all Mach number 0.9 test points. Each Mach number was tested at a Reynolds number of 8×10^6 calculated based on the root chord. At Mach number 0.225 , a Reynolds number of 3.8×10^6 was also used to compare to the full

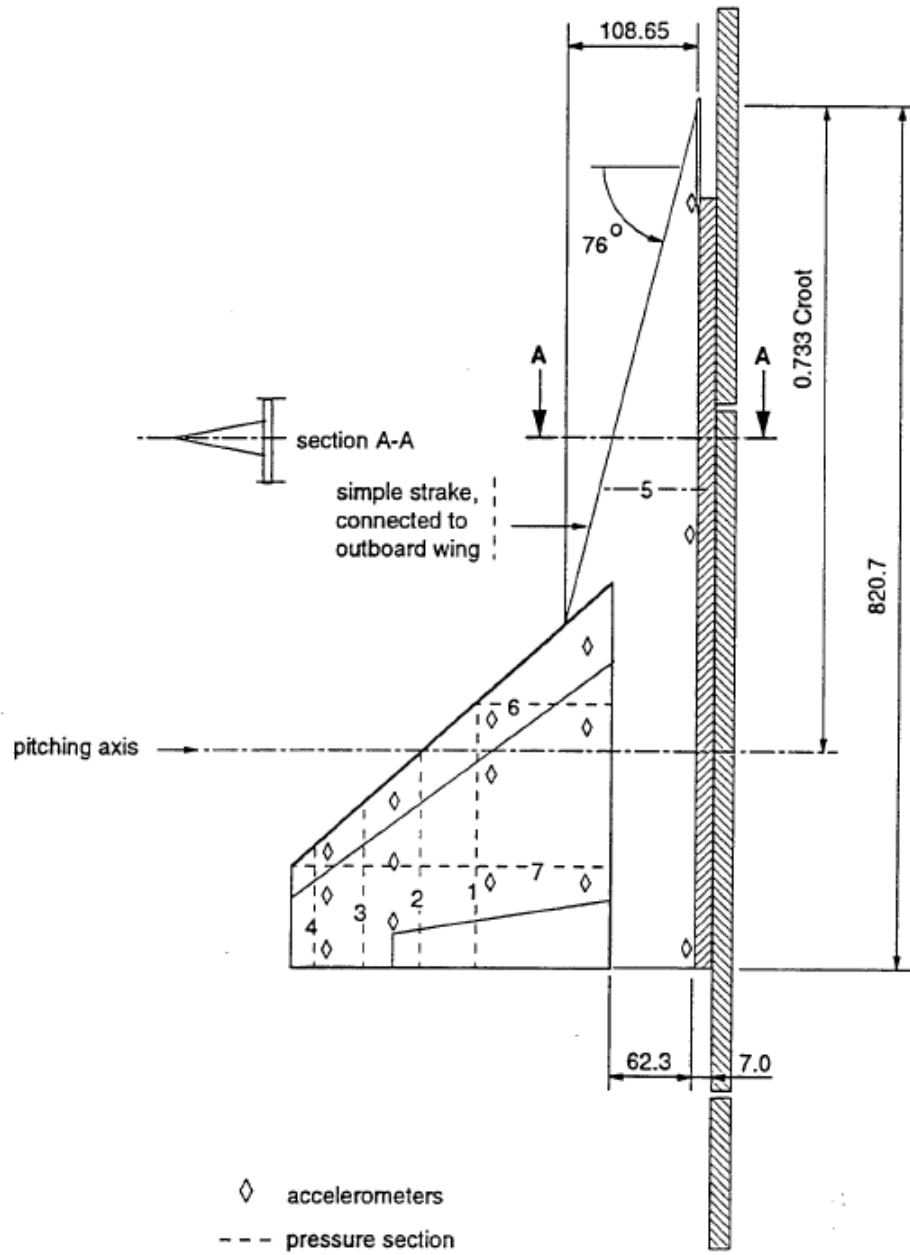


Figure 2.6: SiS model with station numbers 1-7 (in mm) [9].

span model used in the 1986 wind tunnel tests. The results from this comparison were not exact matches but similar enough to indicate that the important flow mechanisms were preserved. Four different frequencies were used, ranging from 5.7 to 15.2 Hz.

Three different oscillation amplitudes, $\Delta\alpha$ in the test matrix, were used; 0.5° , 4.0° , and 8.0° . At each test point, the wing was swept from 6° to 48° of mean incidence, depicted as α in the test matrix.

Mach	0.900								
Re*10 ⁻⁶	= 8.0								= 14.0
freq.	5.7			7.6			11.4	15.2	5.7
dalpha	0.5	4.0	8.0	2.0	4.0	8.0	2.0	2.0	0.5
alpha									
4.0	499								527
5.0	500								528
6.0	501	566	574	584	592	601	609	617	529
7.0	502								530
8.0	503								531
9.0	504								533
10.0	505	567	575	585	593	602	610	618	534
10.5									535
11.0	506								536
11.5									537
12.0	507								538
12.5									539
13.0	508								540
14.0	509	568	576	586	594 595	603	611	619	541
15.0	510								542
16.0	511								543
17.0	512								544
18.0	513	569	579	587	596	604	612	620	545
19.0	514								548
20.0	515								547
21.0	516								549
22.0	517	570	580	588	597	605	613	621	526 550
23.0	518								551
24.0	519	565		583	591	600	608	616	
25.0	520								553
26.0	521	571	581	589	598	606	614	622	554
27.0	522								555
28.0	523								556
29.0	524								557
30.0	525	572	582	590	599	607	615	623	558
32.0	559								
34.0	560								
36.0	561								
38.0	562								
40.0	563								
42.0	564								
44.0									
46.0									
48.0									

Figure 2.7: Mach 0.9 test matrix for Cunningham's wind tunnel tests [9].

For each test point, Cunningham oscillated the wing model in four distinct patterns to mimic dynamic flight maneuvers. Each pattern followed the same oscillation amplitude and frequency, but the starting and ending positions were unique. The first pattern started at the bottom of the oscillation, or the minimum angle of incidence, oscillated to the highest point at the peak incidence, then back down to the minimum incidence angle completing one cycle. The second pattern repeated the first,

but ended at the maximum incidence angle instead of continuing down, therefore only completing 1/2 of a cycle. The third pattern was the opposite of pattern 1 and started and ended at the maximum incidence angle. Finally, the fourth pattern started at the maximum angle of incidence and ended at the minimum angle of incidence. These four patterns were run in this order with a small pause in between so that flow from the previous pattern would not influence the next. The full maneuver sequence is illustrated in Figure 2.8.

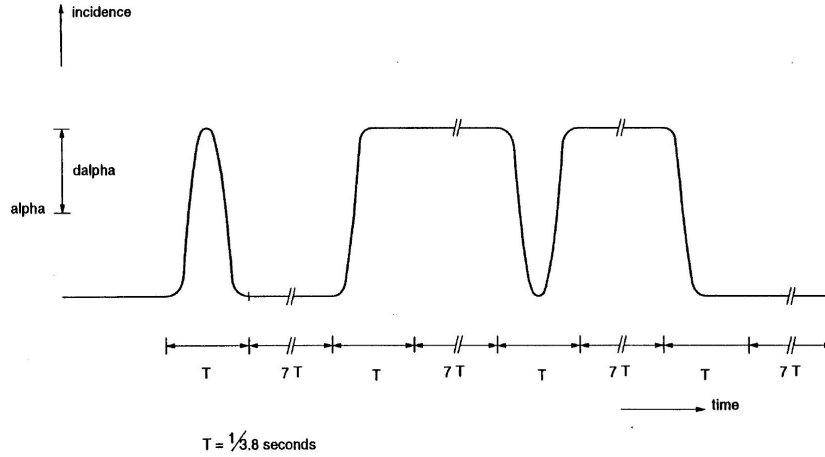


Figure 2.8: Time trace of the wind tunnel test maneuver sequence [9].

Following the tests in 1991, Cunningham completed his test series on the straked delta wing model in 1996 with flow visualization tests [10]. These tests were conducted using steady flow with a stationary wing and unsteady flow for a pitching wing to demonstrate a lag of flow behind the motion of the wing. For the stationary tests, flow was accelerated to Mach number 0.9. His results show that incidence angles below 10.5° are dominated by shock systems. Two main shocks were observed, a forward shock and an aft shock. The forward shock moved aft until it merged to the aft shock in the wing tip region [8]. Between 10.5° and 11° , the aft shock was seen to move considerably forward and SITES was found to form. Above 11° of steady incidence angle, leading edge separation was observed.

Since the SiS model tests were scaled to maintain flow dynamic pressure and viscous characteristics, an accurate model structure could not be maintained. This

resulted in a more rigid structure than an aircraft would experience. Mignolet observed that where Cunningham’s wind tunnel tests resulted in flutter, flight test data resulted in LCO [26]. This observation suggests the involvement of Coulomb friction effects on the more complicated aircraft structure which are not present in the simplified model structure.

2.6 Delta Wing CFD using Euler and Navier-Stokes

Hope’s research aimed to recreate the wind tunnel test model in a series of time-accurate Euler analyses to gather data on potential shock migration on the straked delta wing [20]. In order to relate to Cunningham’s wind tunnel tests, Hope mimicked the SiS model, and matched the Reynolds and Mach numbers for his data points. Due to the constraints in geometry input in ZEUS, the boundary between the strake and airfoil was pushed 46.35 mm towards the wingtip. This change did not affect the total span, chord length, and planform area which all matched the wind tunnel model.

Hope’s test points concentrated around the Mach number 0.9 wind tunnel tests performed by Cunningham for comparison [20]. Table 2.1 shows Hope’s test matrix, where x and o indicate an oscillation frequency of 5.7 and 7.4 Hz respectively. The symbol, I, indicates fully inviscid tests where boundary layer coupling was turned off. This was done to compare to the boundary layer coupled solutions to the fully inviscid solutions. Hope first ran all points in his test matrix with an oscillation amplitude of 2° , then again for 4° , giving a total of 32 unique tests. Hope’s test matrix concentrated on the high transonic region, and tested points with relatively low mean incidence angles compared to the wind tunnel tests. Hope’s analysis did not copy the maneuver sequence from the wind tunnel tests. Insead, he started at a trim AoA and oscillated through two sinusoidal cycles instead of the one cycle and 1/2 cycle maneuvers used by Cunningham [9]. This change was necessary to capture harmonic response and transient effects. Measurements were made at the same locations along the span used in the wind tunnel tests for direct comparison, labeled as Stations 1-4 by Hope.

Table 2.1: Hope’s test matrix [20].

Mach	Trim, (deg)		
	4	7	10
	0.85	x	x
	0.90	xoI	xoI
	0.95	xo	xo

Table 2.2 shows Hope’s tabulated results for position 1 on the delta wing [20]. The shock movement is reported in percent of local chord, and the percent change in C_p for the shock migration is reported as $(C_{p,max} - C_{p,min})/C_{p0}$. Station 2 and 3 show similar results to station 1. Since station 4 is close to the wing tip, the results were less consistent and difficult to assess due to three dimensional (3D) effects such as vortex flow circulating the wing.

Table 2.2: Summary of Hope’s results at station 1 [20].

				Frequency = 5.7 Hz		Frequency = 7.4 Hz	
Mach	ω	Trim	$\Delta\alpha$	% Movement	% Cp change	% Movement	% Cp change
0.9	5.7/7.4	4	2	5.0%	35%	5.0%	35%
0.9	5.7/7.4	4	4	7.5%	79%	7.5%	76%
0.9	5.7/7.4	7	2	7.5%	33%	7.5%	34%
0.9	5.7/7.4	7	4	15.0%	67%	15.0%	71%

				M = 0.90		M = 0.95	
Mach	ω	Trim	$\Delta\alpha$	% Movement	% Cp change	% Movement	% Cp change
0.9/0.95	5.7	4	2	5.0%	35%	5.0%	23%
0.9/0.95	5.7	4	4	7.5%	79%	10.0%	38%
0.9/0.95	5.7	7	2	7.5%	33%	5.0%	30%
0.9/0.95	5.7	7	4	15.0%	67%	7.5%	53%
0.9/0.95	5.7	10	2	10.0%	31%	5.0%	23%
0.9/0.95	5.7	10	4	2.5%	41%	5.0%	43%

				M = 0.90, BLC		M = 0.9, Inviscid	
Mach	ω	Trim	$\Delta\alpha$	% Movement	% Cp change	% Movement	% Cp change
0.9	5.7	4	2	5.0%	35%	2.5%	27%
0.9	5.7	4	4	7.5%	79%	5.0%	60%
0.9	5.7	7	2	7.5%	33%	2.5%	30%
0.9	5.7	7	4	15.0%	67%	7.5%	57%
0.9	5.7	10	2	10.0%	31%	5.0%	23%
0.9	5.7	10	4	2.5%	41%	7.5%	54%

As seen in the top box of this table, Hope observed that both tested frequencies experienced the same amount of shock migration and only showed small differences in % C_p change. Hope saw a slight reduction in shock movement and % C_p change as Mach number was increased. This is shown in the middle box of the table. He also observed that an increase in mean incidence angle or oscillation amplitude led to an increase in shock migration with one exception: Increasing the trim for the Mach number 0.95 case with 4° oscillation amplitude actually reduced the shock movement along the wing. In the last box in this figure, Hope showed compared the results of cases using ZEUS' boundary layer coupling scheme which includes some viscous effects to fully inviscid cases. In this comparison, Hope saw higher shock movement and % C_p change when viscous effects in the boundary layer were included in the simulation. For most comparisons completed by Hope, a correlation was observed between an increase in shock movement and an increase in % C_p change. Hope's setup and results were used for comparison for this study and will be discussed more in Chapter 4.

Pung recreated Hope's simulations using Kestrel, a fluid dynamics N-S solver and analyzed his results against ZEUS and the wind tunnel tests [28]. For his simulations, Pung used a Reynolds number of 1.55×10^7 instead of 8×10^6 used by Hope and Cunningham. This increase changed the viscous and dynamic pressure properties of the flow influence the thickness and growth of the boundary layer as well as the pressures on the wing's surface. Because of differences in the simulation setups between Hope and Pung, I direct quantitative comparison is not beneficial unless they are normalized by the differences in flow properties. For this reason, a qualitative comparison between the work of Hope, Pung, and the work in this thesis is more appropriate. Table 2.3 shows the test matrix run by Pung. A few of Pung's cases match Hope's and were compared in Pung's thesis [28].

One variable varied by Pung was frequency. Pung saw no change in shock migration as a result of a change in frequency just as Hope observed. He did, however, see an increase in % C_p change when frequency was increased from 5.7 to 7.6. Pung

Table 2.3: Pung’s test matrix [28].

ID Number	Maneuver	Mach	Trim (°)	Amplitude (°)	Frequency (Hz)
101	Sin	0.90	4	2	5.7
103	Sin	0.90	4	2	7.6
107	Sin	0.90	4	4	7.6
117	Sin	0.90	7	4	5.7
119	Sin	0.90	7	4	7.6
120	Sin	0.95	7	4	7.6
123	Sin	0.90	7	8	7.6
131	Sin	0.90	10	4	7.6
201	1 - Cos	0.90	6	32	3.8

observed larger changes as a result of frequency at higher trim AoAs. The two shock system seen observed by Cunningham was also observed in Pung’s analysis.

For all cases comparable between Pung and Hope, Pung noted having less but similar shock migration more change in shock strength as it dissolved for portions of the cycle. This seems to be due in part to a difference in interpretation of the furthest forward position of the shock, the point where the adverse pressure gradient can no longer be called a shock. Because of this, a direct comparison between the two could be misleading, but trends seen between cases can be compared qualitatively.

With increases in amplitude, Pung saw an increase in shock movement and shock strength similar to Hope, but differences in surface pressure between Hope and Pung became more prominent. Pung saw SITES in most cases, even in some with lower trim AoA and amplitudes. He also saw large regions of flow separation for larger trim AoA cases. Hope’s analysis did not see these regions of separation due to limitations in ZEUS’ ability to calculate separation and its ability to provide data in a form that can determine separation such as velocity and Mach plots. In Pung’s case with 10° trim AoA, the wing was dominated primarily by separation. He observed separation over the entire wing for the majority of the oscillation cycle, with a small period of reattached flow and shock formation at the leading edge in the pitched down position. This is vastly different than the fully attached flow observed by Hope. The large regions of separation minimized the the shock movement Hope observed for this

test case. Pung's observed flow separation is supported by Cunningham's findings for high AoA cases where he observed flow dominated by vortices and separation above 10° AoA.

2.7 Chapter Summary

In Chapter 2, the author has given the reader a foundation in LCO theory by presenting research relevant to the author's own research. First, a brief introduction to aeroelasticity and LCO theory were discussed. A broad picture of LCO testing for operational certification was introduced, specifically for the F-16. Starting the review of computational analysis, classical linear flutter analysis was discussed before complicating the discussion with the involvement of nonlinear forces. Various forms of nonlinear forces were explained as well as their potential involvement in LCO. Finally, Cunningham's wind tunnel tests [8, 10] on a straked delta wing and Hope's computational analyses using ZEUS [20] on the same straked delta wing were summarized in greater detail due to their relationship with the author's own research.

III. Methodology

3.1 *Introduction*

The work completed in this study expands on the research completed by Dylan Hope [20] and his analysis of a pitch oscillating delta wing using an Euler aerodynamic solver to investigate characteristics of shock movement on the wing. This chapter details the methods used for this analysis by first discussing the ZEUS software used to analyze various wing oscillation patterns. Next, this chapter describes the setup of the ZEUS model and the grid studies done to optimize the aerodynamic model. Finally, an overview of the test matrices and the processes used to analyze the test results are presented.

3.2 *Computational Model with ZEUS*

ZONA's Euler Unsteady Aerodynamic Solver (ZEUS) is an aeroelastic analysis software that couples a structural finite element model with an aerodynamic model to investigate aeroelastic phenomena such as flutter and dynamic loading due to store ejection, wind gusts, and maneuvering. It uses a Cartesian grid system with time-stepping algorithms to calculate unsteady solutions to complex problems. ZEUS uses a bulk data input format similar to NASTRAN and includes a Finite Element Model (FEM), aerodynamic model, automated mesh generation capability, and control over many parameters that allow the user to shape the interaction between these elements and the surrounding flow [33]. This section details the elements and parameters used by Dylan Hope [20] in his research efforts which form the foundation for the work in this study.

3.2.1 Structural Finite Element Model. The first element included in the ZEUS input file is the structural FEM. ZEUS imports the modal data from the free vibration or mode solutions developed by other commercially available software. The external FEM output file is read by ZEUS to obtain structural grid point locations that relate the structural model to the aerodynamic model. ZEUS can pull a variety

of information from the structural models such as modes, natural frequencies, and generalized mass & stiffness matrices. The user also has the option to input these parameters directly. A nonlinear analysis can be also completed if the structural model includes nonlinearities.

Since Cunningham’s model did not replicate inertial properties of the F-16 [9], Dylan Hope [20] did not use a FEM for his model. For the wind tunnel tests, Cunningham measured the natural frequencies of the model, and found that the model could be considered rigid below 8 Hz. For this reason, Dylan Hope was able to use a “dummy” FEM model which contained a single point at the intersection of the strake root and pitching axis, where $x=0.733 \cdot C_{root}$. This point contained an eigenvector which defined the rotational pitch mode of the wing. All other degrees of freedom were constrained except the rigid body rotation in pitch. Because of these constraints, this model can only demonstrate aerodynamics’ influence in LCO.

3.2.2 Aerodynamic Model. The SiS model used in Cunningham’s wind tunnel experiments was recreated in ZEUS by Dylan Hope [20]. The model consisted of a cropped NACA 64A-204 airfoil with a strake as detailed in Figure 2.5. ZEUS develops the aerodynamic model by taking a series of leading edge points and chord lengths provided by the user and creates a flat plate with the desired wing planform. The planform created by Hope and used for the entirety of this study can be seen in Figure 3.1.

Next, the user can add thickness and camber to the wing by direct tabular input or by referencing the directory of common airfoils. The strake used on the SiS model was built by direct input and consisted of a diamond shaped airfoil with a max thickness of 2.5% of the chord. The max thickness was located at 85% of the chord. Since the thickness and thickness location were dependent on the chord length, these dimensions hold true for every chord along the span of the strake. The strake flowed nicely into the NACA airfoil which had a slight twist which resulted in a 3° washout (-3° incidence) at the wingtip. The right wing was scripted into the input file and

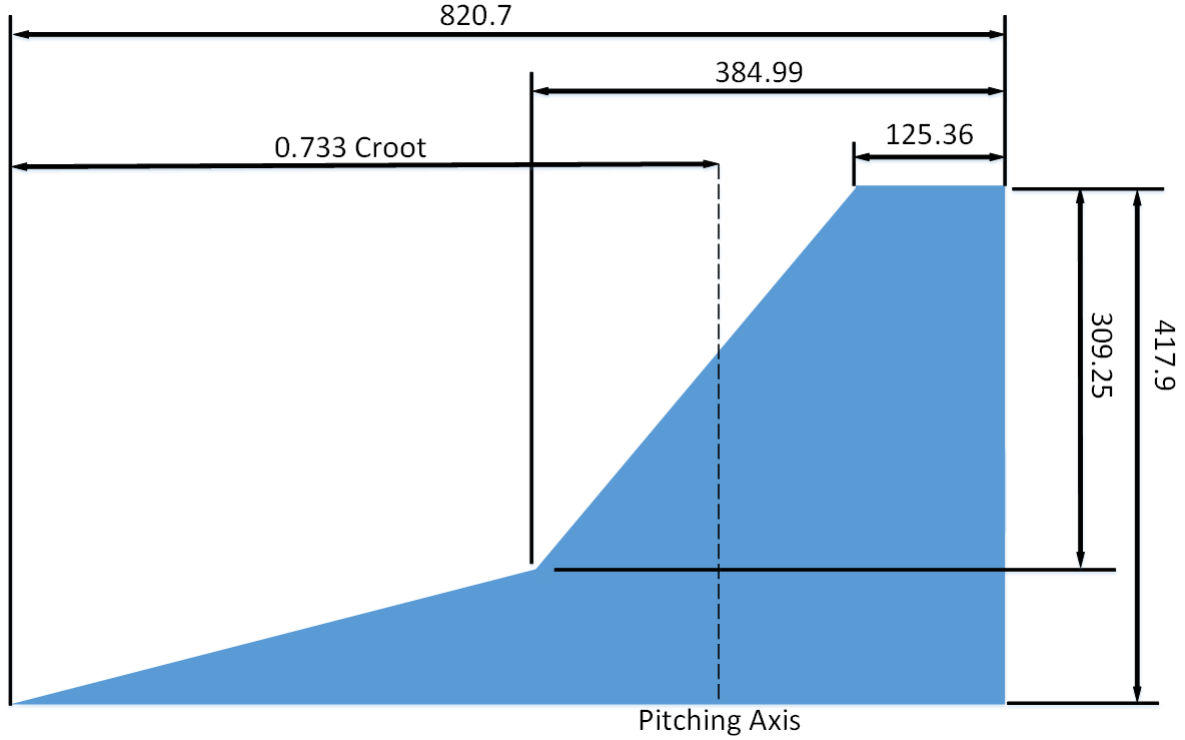


Figure 3.1: Planform Dimensions for the ZEUS SiS Model (in mm) [20].

mirrored by ZEUS to the left wing. Figure 3.2 shows the complete aerodynamic model with lines designating the spanwise stations, designated as Stations 1 through 4 with Station 1 being closest to the wing root. These stations were chosen to match those used by Cunningham who gathered pressure and accelerometer data on his physical SiS model.

Because of limitations within ZEUS' modeling capability, the SiS model required a slight modification in order to integrate with ZEUS [20]. To accommodate the basic geometry input capability of ZEUS, the boundary between the strake and NACA wing was moved 46.35mm outboard. This change was made in order to maintain accuracy for more critical characteristics such as wing span, chord length throughout the wing, and planform area of the wing.

Once the 3D model is created in ZEUS, a surface grid is formed which consists of a flat sheet of trapezoidal panels that divide the wing surface. The surface grid

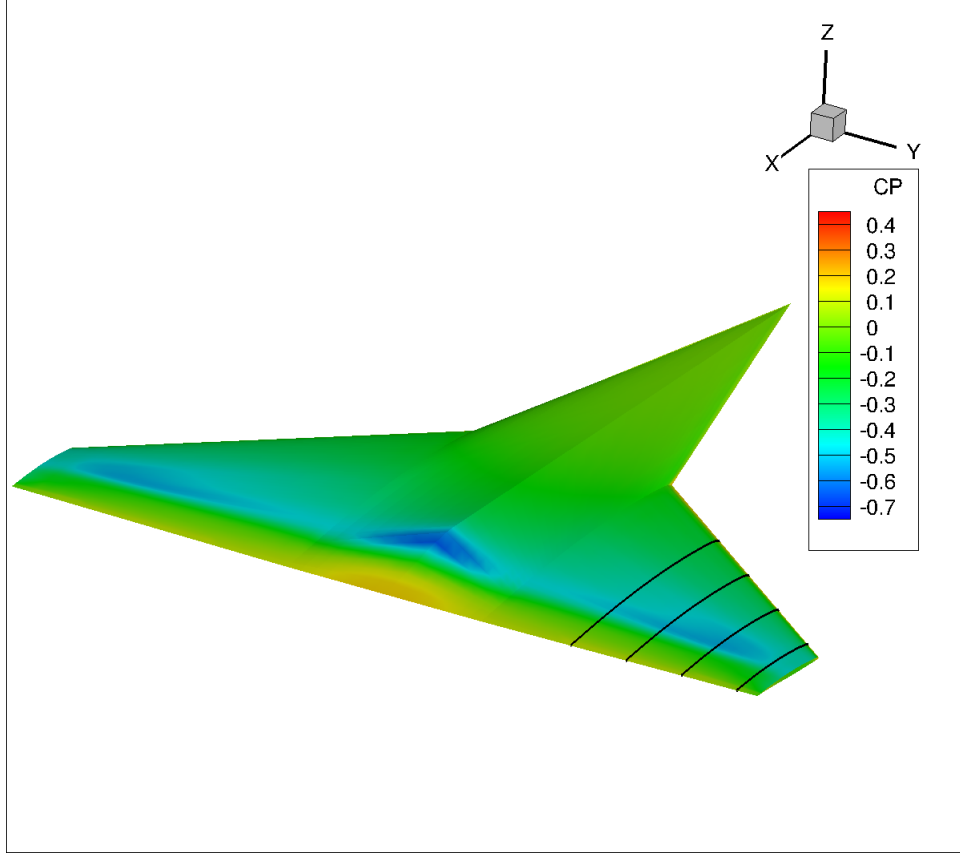


Figure 3.2: SiS model in ZEUS with Stations 1-4 in black, located at 209mm, 274mm, 336mm, and 395mm from the centerline [20].

is overlaid onto the 3D model to complete the aerodynamic model used by ZEUS. For the SiS model, two separate surface grids were created for the strake and the NACA wing. The user has control over the number of grid lines that divide the surface. With more grid lines, the grid density increases which inherently increases the number of points where ZEUS calculates forces and displacements. This improves accuracy but also drives up computation time, so a balance of speed and accuracy requires a reasonable grid density.

With a complete aerodynamic model and external structural model, ZEUS mates these models by a spline module, which matches the coordinates of the models and binds them together. This method establishes the displacement and force transmission between models. Since the structural model used for this analysis is a

singular point and the wing is assumed to be rigid, the spline fixes the aerodynamic model to the singular point. This allows the wing to rotate in pitch about the fixed point, but constrains all other degrees of freedom and deformations.

3.2.3 Mesh Generation. In order to accurately calculate the flow field around the wing, ZEUS generates a volumetric (3D) mesh to a size specified by the user. This mesh is automatically created by growing the 3D mesh from the aerodynamic surface mesh to create a seamless transition. Figure 3.3 shows the mesh for the SiS model in ZEUS. The automated mesh used for this analysis is 6.5 meters deep (x direction in the figure), 2 meters wide (y direction) and 1.6 meters tall (z direction). This equates to 5 root chord lengths downstream, 2 wingspans wide, and a chord length above and below. This mesh is undersized compared to standard CFD practices, follows the suggested flow field sizing recommended in the ZEUS manual [33].

In order to grow the 3D mesh from the surface mesh, the user has the ability to designate which surface meshes to use for different spanwise locations within the 3D mesh. Since separate surface meshes were made for the strake and the wing, the automated mesh scheme grows from both surface meshes into a rectangular 3D mesh. Figure 3.4 shows a top view of the mesh to illustrate the grid growth around the surface meshes.

In some scenarios, the automated mesh does a poor job in creating a mesh that can accurately calculate flow characteristics. The most noticeable examples are between the wing and tail surfaces when both are included in a model, and above and below a wing when a fuselage is modeled as well. Both of these examples generate low grid densities as a result of multiple aerodynamic surfaces whose meshes clash. Illustrations of this can be found in the ZEUS User’s Manual [33]. ZEUS allows the user to manually control characteristics of the mesh growth from the aerodynamic surfaces to eliminate these issues.

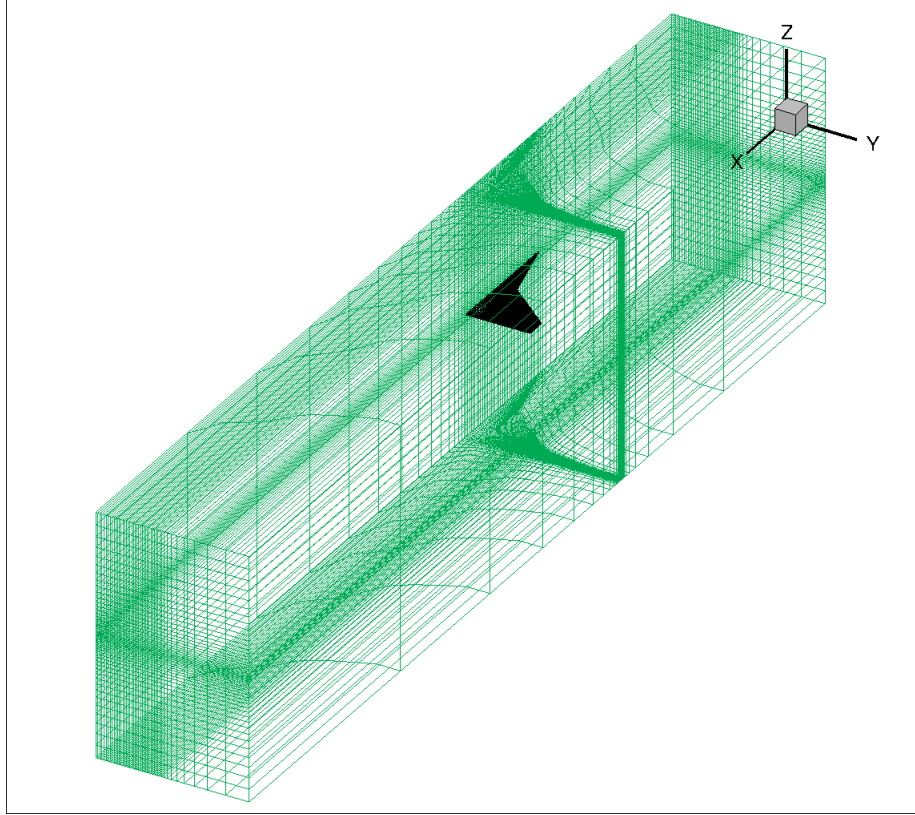


Figure 3.3: Automated 3D mesh of the ZEUS SiS Model [20].

3.2.4 Transient Analysis. Once the aerodynamic model and structural model are paired through a spline and the flow field mesh is created, the computational model is complete. What is left before simulations can begin is to choose which analysis methods to use and set flow parameters. ZEUS includes a number of modules that allow the user to choose what transient analysis they would like to complete, and provides control over numerous computational parameters to tailor the simulation to the user's needs. The modules used in this analysis were MLOADS and FLUTTER. Before beginning any transient response analysis, ZEUS first computes the steady, static aeroelastic solution. For this analysis, 100 time steps were used to ensure convergence of the static solution before initiating the transient analysis.

The MLOADS module allows the user to analyze transient maneuver loads resulting from a pilot's input to a control surface. In order to move the wing in oscillation to mimic the wind tunnel tests, the entire SiS model was treated as a

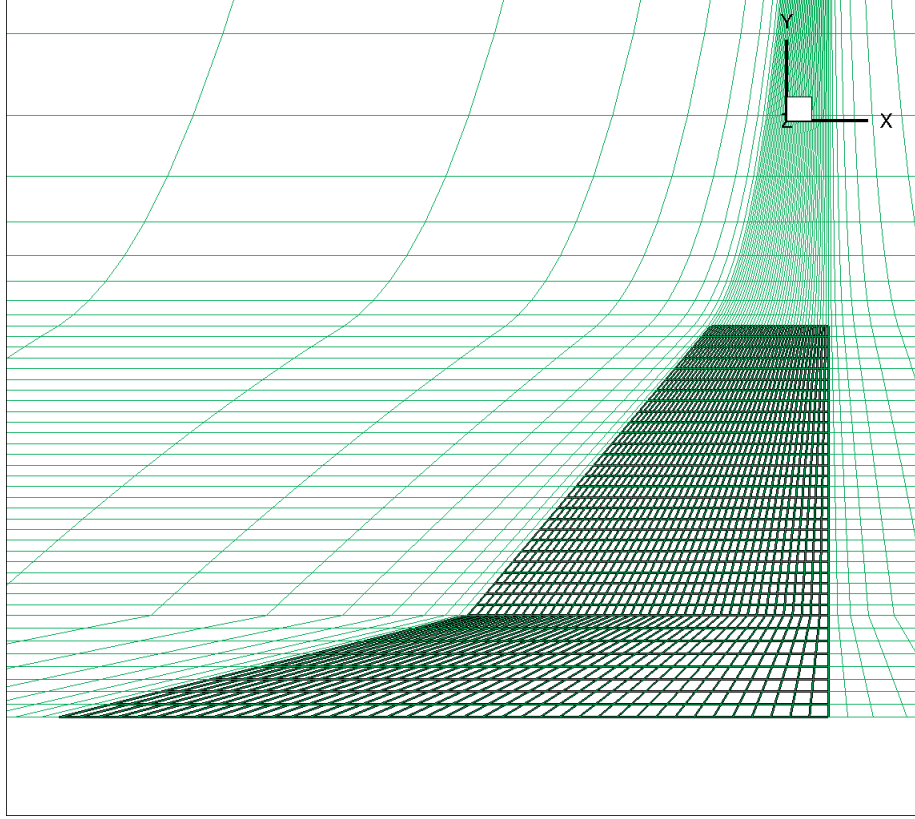


Figure 3.4: Top View of the ZEUS SiS model 3D mesh and surface grid [20].

control surface. With this method, ZEUS can perform transient response analysis by specifying the time history of the wing's deflection. For the SiS model, the period of the oscillation was split into 24 time steps tabulated along with the relating change in angle of attack in order to build an array of data readable by ZEUS. For each frequency analyzed, a new table was required. The MLOADS module generally uses this table to compute structural loads on the wing by solving a state space equation created from the generalized mass and stiffness matrices provided by the structural model or by matrix form from the user, as well as by the aerodynamic forces generated by the flow field around the wing. Since the SiS model in ZEUS is rigid, this part of MLOADS was not utilized. However, the MLOADS module uses the FLUTTER module which allows the user to specify flight conditions and parameters used by the Euler-Solver module.

3.2.4.1 Unsteady Euler Solver. The Euler-Solver module is essentially an unsteady aerodynamic force generator based on a stationary Cartesian grid that solves time-accurate Euler equations. It uses a cell-centered central-differencing finite-volume method along with a Jameson-Schmidt-Turkel (JST) artificial dissipation scheme to stabilize the flow solver [33, 6.1]. For Hope’s analysis and the work completed in this study, the time accurate Euler method was used [20]. At each time step, the Euler-Solver module is coupled with the structural state space equations. The state space solution is then applied to the boundary conditions of the Euler equations to calculate the unsteady aerodynamic forces to be used by the Euler-Solver module in the next time step. Many parameters of the Euler-Solver can be set by the user to control how the solver iterates through the time steps. ZEUS’ user manual [33] gives extensive details on these parameters and how they are used by the solver to influence convergence to an acceptable solution.

To determine convergence ZEUS calculates residuals at each time step within the simulation. If the residuals do not drop by a few orders of magnitude, the case is determined to have not converged. For extreme cases, ZEUS will fail in the middle of a simulation which also results in a non-converged case. It is important to note residuals alone are not the preferred measure for convergence, but was the best option due to the limited outputs available from ZEUS.

3.2.4.2 Time Steps and Loops in ZEUS. ZEUS’ Euler-Solver module uses a dual-time marching scheme. In this scheme, a pseudo-time stepping loop marches within the physical time stepping loop. Figure 3.5 shows the full time marching scheme used by ZEUS, where loop 1 and loop 2 complete the pseudo-time march and loop 3 completes the physical time march calculations.

In loop 1, which is the innermost loop, ZEUS uses a five-stage Runge-Kutta pseudo-time marching scheme to solve the series of ordinary differential equations derived from the 3D Euler equations. These calculations assume that the fluid flow is adiabatic and inviscid. Within the boundary layer around the wing, the fluid

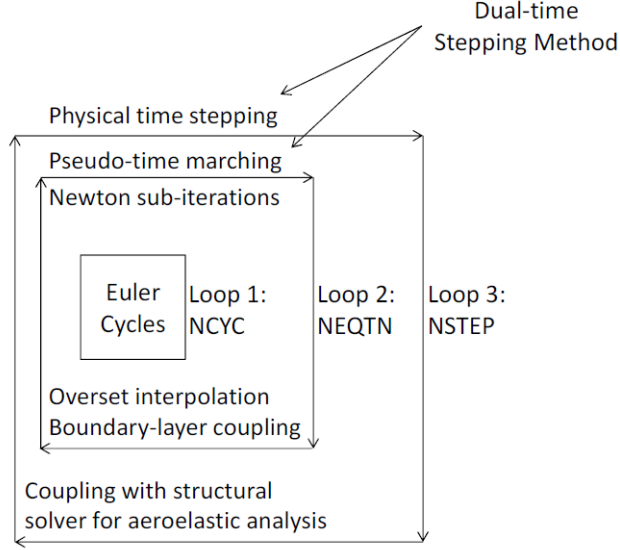


Figure 3.5: Flow Chart of the Euler Solver in ZEUS [33].

flow is likely to develop turbulent flow which can have very large Reynolds numbers. With Reynolds numbers in the millions, viscous effects cannot be ignored. For this reason, ZEUS offers a boundary-layer coupling capability where viscous flow within the boundary layer are computed separately from the flow field. This gives a good compromise between the speed of Euler solvers and the accuracy of RANS solvers. In loop 2 of the Euler-Solver module, the boundary layer solution is computed then coupled with the inviscid flow outside of the boundary layer. In the final outer loop, loop 3, the Euler-Solver couples the solution from loop 2 with the structural model. For this study, the pressure forces acting on the wing are computed at each panel along the surface mesh. For each loop, the user can specify the number of sub-iterations within each loop before continuing to the next loop. For this analysis, the number of Euler cycles per Newton sub-iterations (loop 1/loop 2) was set to 3, and the number of Newton sub-iterations per physical time step (loop 2/loop 3) was 12. The pseudo-time step size is also defined by the user, though ZEUS will decrease the time step size in order to achieve numerical stability and solution convergence. The physical time step size was specified to be 0.0005 seconds.

3.2.4.3 Pressure Data From ZEUS. ZEUS does not automatically store data for the entire simulation. Instead, the user specifies starting and ending times, and how often within that time to store data. For this analysis, one full cycle of data was stored with time steps of 0.005, 10 times the physical time step within the ZEUS solver scheme. ZEUS can store the generalized aerodynamic forces output from the MLOADS module in different forms such as force, elastic deformation, pressure, and friction. This analysis required ZEUS to convert the aerodynamic forces to pressure coefficients for further analysis.

3.2.4.4 Matching of Reynolds Number and Other Flow Properties. Another flow parameter specified by the user is the Reynolds number. For this study, the Reynolds number was set at 8×10^6 to match the flow characteristics of the wind tunnel tests. Since Reynolds number is a function of density, velocity, chord length, and viscosity, each of these parameters must also match the wind tunnel test setup with the exception of the flow velocity which is a control variable. All of Hope's flow parameters were used in this study for direct comparison [20]. Hope's setup was then used to determine the optimal grid setup that would achieve grid independence.

3.3 Grid Studies

This section summarizes efforts to determine the optimal grid to be used for this analysis of the oscillating delta wing, SiS model. First the static convergence analysis completed by Dylan Hope is reviewed, where a trim analysis was used to compare the resulting trim AoA for various grid densities [20]. It is likely that the optimal grid density for a static trim analysis is not the same as the optimal grid density for the unsteady aerodynamic forces surrounding the dynamic motion of an oscillating wing so a dynamic study was performed. To build on Hope's grid study, one flight condition from Hope's test matrix was evaluated, which had a Mach number of 0.95, an angle of attack of 7° , an oscillation frequency of 5.7 Hz, and an amplitude of 2° . This data point was chosen for comparison because of its high transonic speed and

moderate angle of attack that would ensure shock presence without approaching stall characteristics. As used by Hope, the non-dimensional time variable (t^*) was used to split a cycle into 9 equal time steps from 0 to 1.

The first grid study targeted the optimal setting for controllable characteristics of the surface grid and 3D mesh that were found to likely influence the solution. A dynamic convergence study was also completed where the effects of grid density on the coefficients of pressure and pitch moment were analyzed. This study determined an optimal grid density that would minimize computation time without sacrificing solution accuracy. Finally, an oscillatory motion study was completed to realize the models dependence on the oscillation function and the number of cycles. In the oscillatory motion study, the starting point within the oscillation was changed and was also ran for additional cycles to compare flow behavior between cycles.

3.3.1 Static Convergence Study by Dylan Hope. Dylan Hope completed a grid sensitivity study prior to his analysis by performing a trim analysis at various grid densities to determine the trim angle of attack [20]. To vary density, Hope changed the number of spanwise and chordwise grid lines on the wing, which are used by ZEUS to create divisions on the wing. ZEUS automates the panel creation by evenly distributing the grid lines. Figure 3.6 shows Hope’s uniform grid set up by ZEUS’ automated panel setup.

In his analysis, Hope compared the trim angle of attack to a variety of surface panel densities increasing from a 10 spanwise x 10 chordwise grid (100 panels) to a 45 x 55 grid (2,475 panels). This comparison can be seen in Figure 3.7. The smallest grid density of 10 x 10 is drastically different from the rest of the densities ran by Hope. This shows the minimum density that is required by ZEUS to get a reasonable result. It is also work noting that the inclusion of this point changes the perspective of the plot so that the differences from the remaining grid densities appear much smaller. Convergence may have looked very different if the y-axis scale had a minimum value of 8.7° instead of 8.3° .

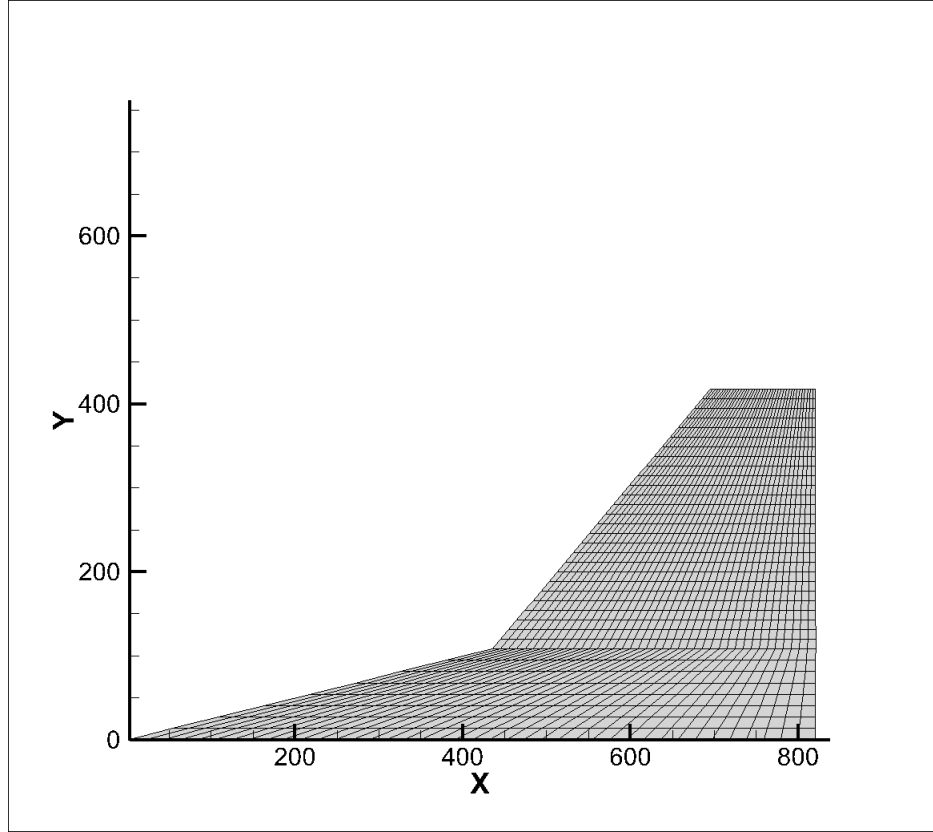


Figure 3.6: Planform of the evenly distributed 35 spanwise x 40 chordwise panel surface grid [20].

From this plot, it can be seen that the angle of attack appears to converge to a final value as grid density is increased. The ideal grid density is a balance of computational time and accuracy. It is important to note that ZEUS' automated mesh generator surrounding the wing uses the surface panel mesh to extrapolate into its 3-D mesh, so a small increase in density can greatly increase the number of mesh cells. From his grid study, Hope chose a final wing density of 35 spanwise and 40 chordwise divisions, which equals a total of 1,400 aerodynamic panels on the surface of the wing. The automated mesh for the chosen density was composed of over 83,000 cells. Hope determined that the 0.18% difference in trim AoA when compared to the highest density solution (45x55) was acceptable for his unsteady analysis on the oscillating delta wing.

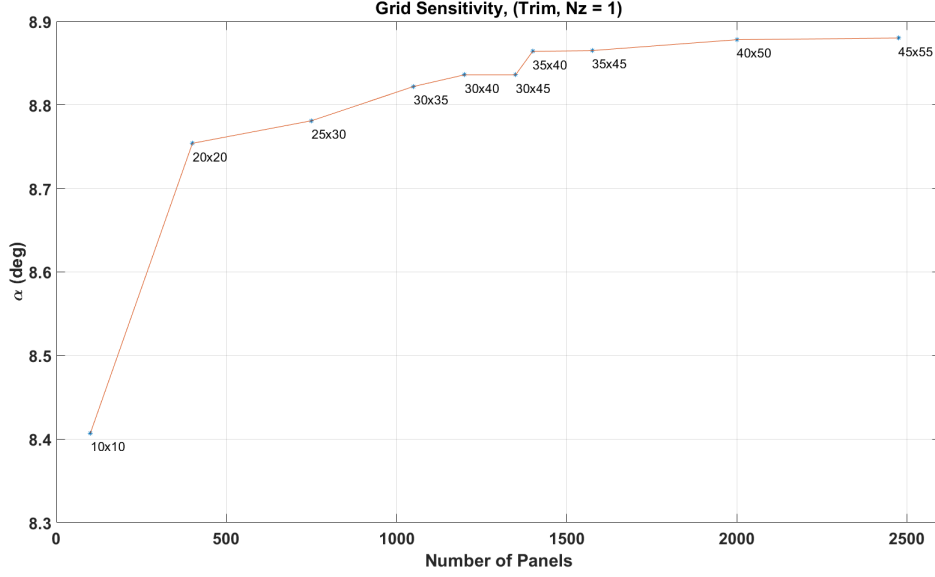


Figure 3.7: Grid sensitivity study by Hope. Plot is trim angle of attack vs number of panels [20].

3.3.2 Comparison Criteria. Since this study uses transient analysis, it is likely that only a dynamic grid convergence study will capture transient effects. For this reason, instead of comparing the trim angle of attack, characteristics of the dynamic motion of the wing were calculated for comparison to determine the optimal grid density. These characteristics included the magnitude and location of the minimum coefficient of pressure ($C_{p_{min}}$), the 2-norm of the pressure coefficient (C_p) along a length of the wing chord for an entire cycle, and the 2-norm of the moment coefficient (C_m) along a wing chord. The ZEUS PLTTIME card was set to output pressure at every grid point for the wing from the beginning to the end of the second oscillation cycle.

3.3.2.1 Pressure Coefficient. ZEUS uses a PLTTIME card to output C_p for a user defined time interval. Figure 3.8 shows a typical plot of the sectional pressure coefficient C_p along the chord for the upper surface of the wing at various cycle times. Each plot represents one spanwise location, or station, along the wing.

The times shown in the plot were normalized by the cycle period so that one full cycle is shown.

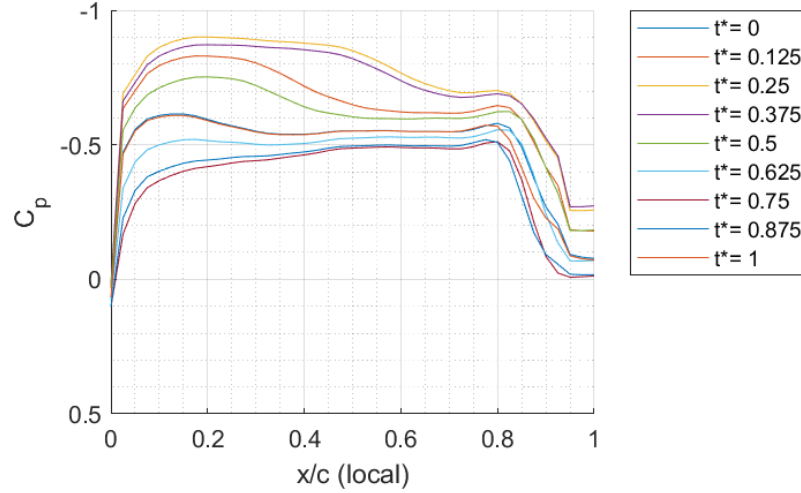


Figure 3.8: Pressure coefficient vs chord location. Mach = 0.95, trim AoA = 7°, amplitude = 2°, and frequency = 5.7 Hz.

First, the C_{pmin} magnitude and location along the chord were extrapolated from the PLTTIME output from ZEUS. The minimum pressure point was found when the wing was fully pitched up to its peak AoA where $t^* = 0.25$. The 7° mean incidence (trim AoA) and 2° amplitude for the case chosen for the grid studies has a peak AoA of 9°.

Next, the 2-norm of the C_p ($\|C_p\|_2$) in order to total differences in pressure across the entire chord. This calculation used Equation 3.1, where n_{chord} is the location of each C_p along the chord and n_{time} is the normalized time within the cycle for each C_p calculation.

$$\|C_p\|_2 = \sqrt{\sum_{n_{time}=0}^1 \left(\sqrt{\sum_{n_{chord}=0}^1 C_p^2} \right)^2} \quad (3.1)$$

This equation gives a difference in C_p along the whole chord and for the entire cycle to understand the overall impact of any changes in the grid or mesh on C_p .

3.3.2.2 Moment Coefficient. Lastly, sectional moment coefficient, C_m , was calculated to understand what effects the changes in pressure have on the pitching moment of the wing as it oscillates. To calculate C_m for each spanwise position, the C_p from the upper surface of the wing was subtracted from the lower surface of the wing for each point along the chord. This calculation assumed a flat wing, meaning all of the C_p values for the upper and lower wing surfaces were acting on and perpendicular to the chord. Each ΔC_p was then multiplied by its distance from the pitching axis, creating a vector of moment coefficients for the chord being analyzed. A vector-valued function was created, which allowed the data to be integrated over and normalized by the chord length. The result of this calculation is the coefficient of pitching moment for one chord, and for one moment in time. This process was repeated for each time step within the cycle and at each spanwise location along the wing as dictated by the analysis.

C_m was plotted vs cycle time (t^*) as well as AoA (α). Figure 3.9 shows a typical plot of the sectional moment coefficient vs angle of attack as the wing pitches up and down in oscillation. The “+” symbol indicates the starting point of the cycle. Like the pressure coefficient, each plot represents just one chord along the wing. The gap between the starting and ending points suggests that the flow has not yet reached a dynamically steady flow such that the subsequent cycle to this plot will likely have noticeable differences in C_m values that were visually unnoticeable by simply plotting C_p .

From the moment coefficient data, the 2-norm ($\|C_m\|_2$) was calculated using Equation 3.2, where n_{time} is the normalized time within the cycle for each C_m .

$$\|C_m\|_2 = \sqrt{\sum_{n_{time}}^1 C_m^2} \quad (3.2)$$

This calculation was used to quantify the impact of the grid and mesh on the resultant moment on the wing throughout one cycle of oscillation.

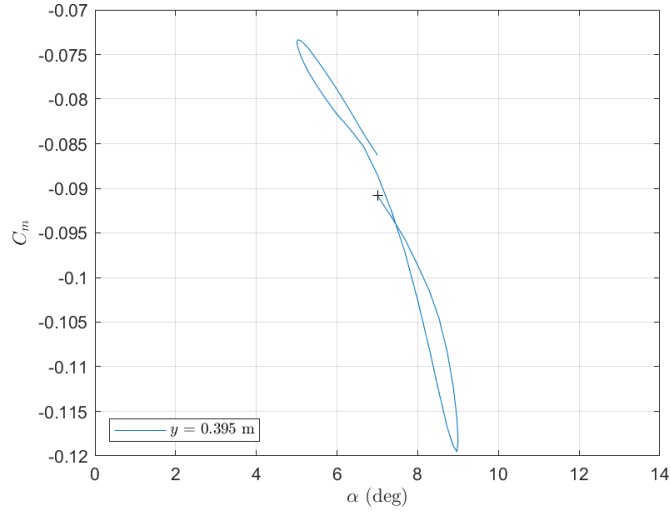


Figure 3.9: Moment coefficient vs chord location. Mach = 0.95, trim AoA = 7°, amplitude = 2°, and frequency = 5.7 Hz.

3.3.3 Model Improvements. By specifying the number of spanwise and chordwise divisions, ZEUS is capable of automating the creation the surface mesh as well as the mesh surrounding the wing. This automated process does not always produce a mesh refined enough to give optimal solutions, so ZEUS provided the capability to manually control some of the grid/mesh setup. Two such manual control options were used to bring further fidelity to the surface grid and the mesh generation. A comparison was done with and without the addition of these two manual control options.

3.3.3.1 Surface Mesh Study. The first manual control option used was to manually select each grid line's location on the surface of the wing. One of Hope's objectives was to compare the ZEUS analysis to the four spanwise stations where Cunningham gathered acceleration and pressure data in his wind tunnel tests [20]. Since ZEUS evenly distributes grid lines, interpolation is required to get data at a specific point. By manually choosing the grid line locations, the exact location of the spanwise stations could be specified, which eliminated the need to interpolate between grid points. With four grid lines specified at the four spanwise stations from the wind

tunnel tests and Hope’s analysis, the remaining grid lines were evenly distributed along the wing without regard to those wind tunnel stations. Figure 3.10 shows a comparison between the uniform grid used by Hope (3.10a) and the modified grid (3.10b) with Stations 1-4 shown in red. The modified grid in Figure 3.10a has a uniform spanwise grid spacing with four fewer grid lines, and the addition of the four lines on top of the wind tunnel stations so that the total spanwise grid density is the same.

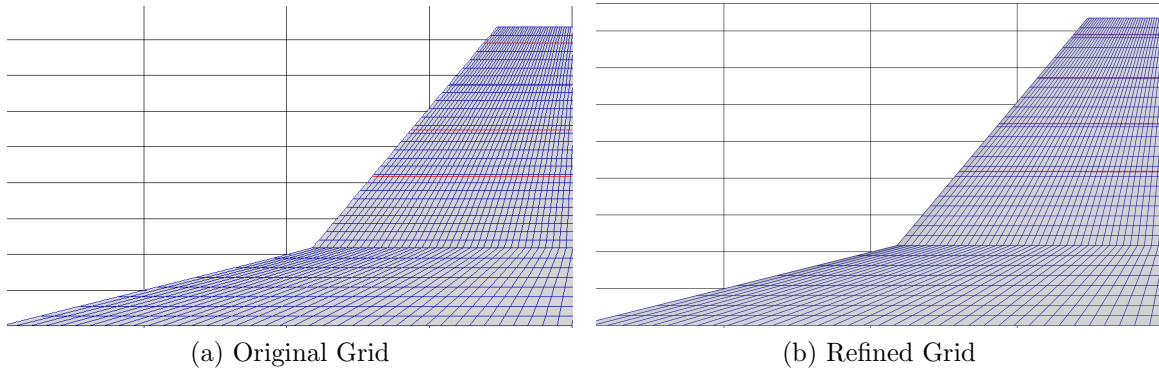


Figure 3.10: Comparison between original grid (a) and refined grid (b).

3.3.3.2 GAP Card Study. When a model has a heavily tapered wing, or two aerodynamic surfaces fairly close to one another such as a canard and wing or a wing and tail, the mesh in between the aerodynamic surfaces can be too large using ZEUS’ automated mesh generation to give accurate results. In the case of a tapered wing such as in this analysis, it can be useful to manually smooth the transition from a rectangular mesh pattern to the taper of the wing’s leading edge. The GAP card in ZEUS allows the user to specify the grid density of any area in the mesh similar to the setup of the surface grid itself. Figure 3.11 shows the original mesh (3.11a) vs the refined mesh (3.11b) which includes a GAP card to control the mesh density in front of the wing.

It can be seen here that the inclusion of the GAP card greatly increases the density of the mesh in front of the wing, which improves ZEUS’ ability to calculate

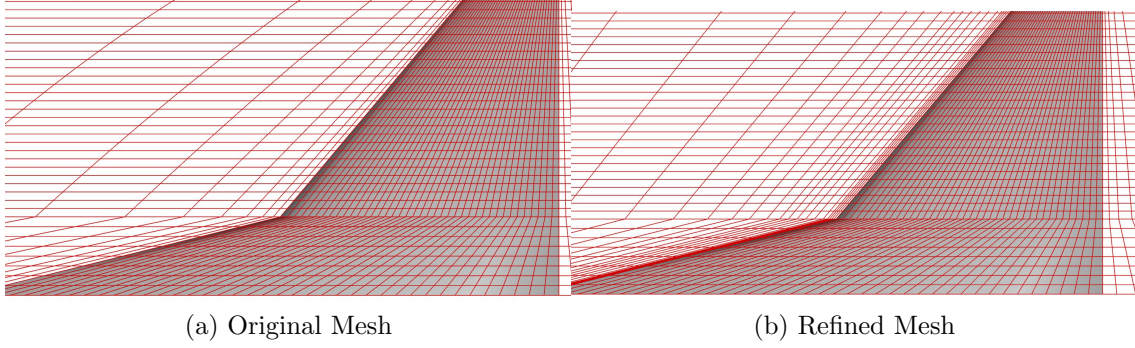


Figure 3.11: Comparison between the original mesh (a) and the refined mesh (b) at the leading edge of the wing.

flow over the leading edge of the wing, particularly at supersonic speeds and high angles of attack.

3.3.3.3 Results. Table 3.1 summarizes the results of the changes to the surface grid and mesh generation that were discussed in this section. These changes were made for the same final grid density used by Hope as the result of his grid independence study [20]. From this table, it can be seen that matching the surface grid to the wind tunnel stations had negligible changes to the C_{pmin} magnitude and location, but had a noticeable impact on $\|C_m\|_2$. In the case with a GAP card added, the opposite was seen. C_{pmin} magnitude changed by up to 1.7%, with a noticeable movement in location as well. The change in chord location ((x/c)) of C_{pmin} reflects one grid point movement and so is likely trivial. A higher density model would need to be used to evaluate the effects of the GAP card and station match on $(x/c)_{C_{pmin}}$. The combined case which included both GAP cards and station matches showed results somewhere in between those seen in each individual case. The largest change seen for the combined case was in $\|C_m\|_2$ at Station 4, which saw a change of 1.98% from the original grid used by Hope.

3.3.4 Dynamic Grid Sensitivity Study. Similar to Hope’s grid sensitivity study, the study summarized here used the same methods to determine the optimal grid density to use for the remainder of the work outlined in this thesis. The one

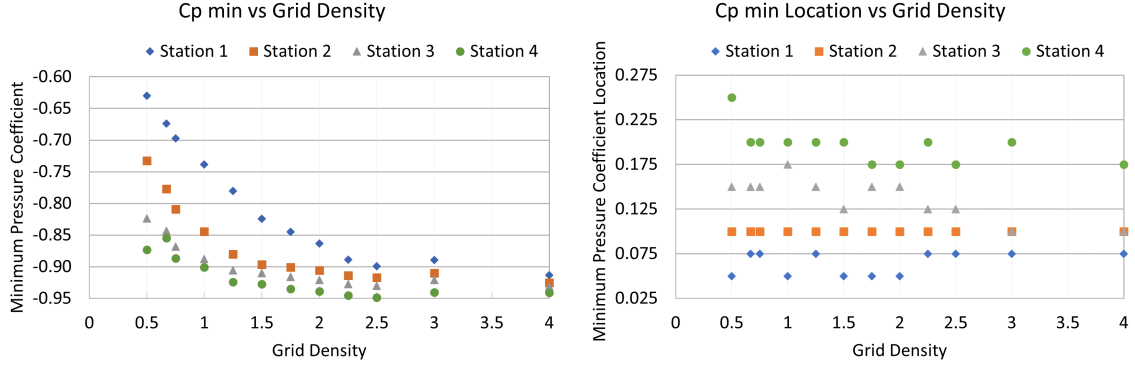
Table 3.1: C_p and C_m for improved surface grid and mesh configurations.

	Station	Original	w/ GAP	w/ Station Match	w/ GAP & Station Match
C_{pmin}	1	-0.7299	-0.7425	-0.7300	-0.7383
$(x/c)_{C_{pmin}}$	1	0.0750	0.0500	0.0750	0.0500
$\ C_p\ _2$	1	8.1978	8.2713	8.1703	8.2595
$\ C_m\ _2$	1	0.4867	0.4858	0.4807	0.4921
C_{pmin}	2	-0.8340	-0.8482	-0.8354	-0.8442
$(x/c)_{C_{pmin}}$	2	0.1000	0.1000	0.1000	0.1000
$\ C_p\ _2$	2	9.2634	9.3398	9.2460	9.3270
$\ C_m\ _2$	2	0.6171	0.6147	0.6119	0.6198
C_{pmin}	3	-0.8859	-0.8924	-0.8849	-0.8877
$(x/c)_{C_{pmin}}$	3	0.2000	0.1750	0.2000	0.1750
$\ C_p\ _2$	3	10.2560	10.3360	10.1870	10.2594
$\ C_m\ _2$	3	0.6070	0.6020	0.6013	0.6059
C_{pmin}	4	-0.8959	-0.9050	-0.8944	-0.9005
$(x/c)_{C_{pmin}}$	4	0.2000	0.2000	0.2000	0.2000
$\ C_p\ _2$	4	11.0760	11.1510	11.0570	11.1034
$\ C_m\ _2$	4	0.5797	0.5740	0.5690	0.5682

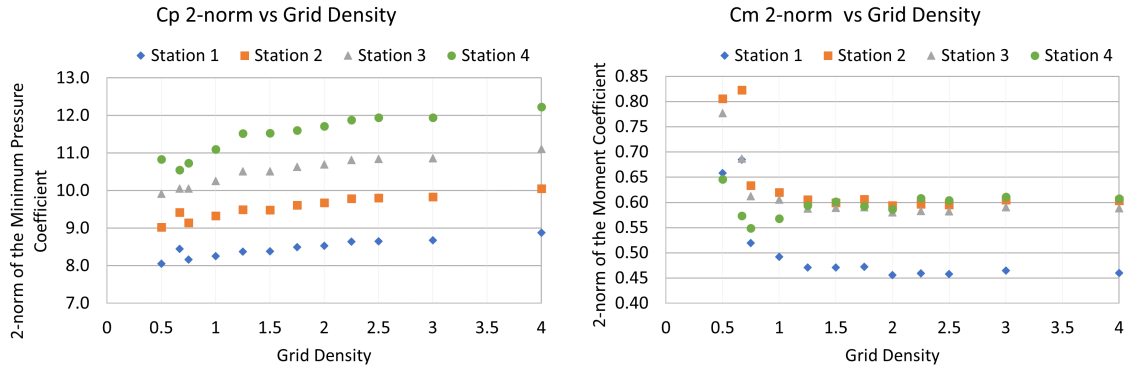
exception is the different criteria used. This grid study will compare the coefficients of pressure and moment for varying grid densities. For this study, each grid density was determined by multiplying Hope's optimal density by a factor, ranging from 0.5x to 4x. The smallest grid density of 0.5x has 21 spanwise and 18 chordwise grid lines, which equates to a total of 320 surface panel on the wing and strake. The mesh for this case has close to 36,000 cells. ZEUS completed the flutter analysis for this case in just over 4 minutes. Compare this to the largest grid density of 4x which has 164 spanwise and 144 chordwise grid lines which equates to over 23,000 surface panels and 890,000 cells in the 3D mesh. The computation time for the 4x density case was 3.5 hours, almost 60 times that of the 0.5x density case. This change in computation time is significant when running a large number of cases so it is important to choose the smallest grid density that does not sacrifice accuracy.

Figure 3.12a shows the minimum pressure coefficient found for the max pitch up position within the oscillation cycle. This plot shows all stations are converging to a steady value as grid densities are increased. Grid densities 0.67x and 3x show

variations from the general trend of all of the other grid densities. From Figure 3.12a, a grid density of 2.25x or greater was considered the converged region with acceptable grid densities. The previously chosen 1x density is outside of the converged region and shows a considerable difference in pressure coefficient to the high density cases, 4% at Station 4 and 16% at Station 1.



(a) Minimum pressure coefficient vs grid density. (b) Location of minimum pressure coefficient vs grid density.



(c) 2-Norm of the minimum pressure coefficient vs grid density. (d) 2-Norm of the moment coefficient vs grid density.

Figure 3.12: Dynamic grid study. Mach = 0.95, trim AoA = 7°, amplitude = 2°, frequency = 5.7 Hz. Grid densities are a factor of the original density used by Hope.

Figure 3.12b shows no noticeable trend toward convergence for the chord location of the minimum pressure coefficient. The location for the minimum pressure coefficient seems to settle on distinct chord locations independent of grid density.

This suggests that the solution requires smaller chordwise calculations of pressure on the wing which are done independent of the grid density or mesh. The tolerance of these location changes shown here are noted for future analysis. Figure 3.12c shows the 2-norm of C_p calculated as referred to in the subsection 3.3.2. The trends in this figure show a slight curve which suggests possible convergence at densities above 4x. A noticeable flattening at 2.25x can be seen, suggesting this density may be acceptable to meet the intent of the remaining work in this report. Figure 3.12d shows the 2-norm of C_m versus grid density for each wind tunnel station. This data does show convergence though a seemingly oscillatory behavior can be seen, particularly for Station 4. From this plot, convergence seems to develop just above 1x density where changes from one density to the next suggests C_m is influenced by another variable.

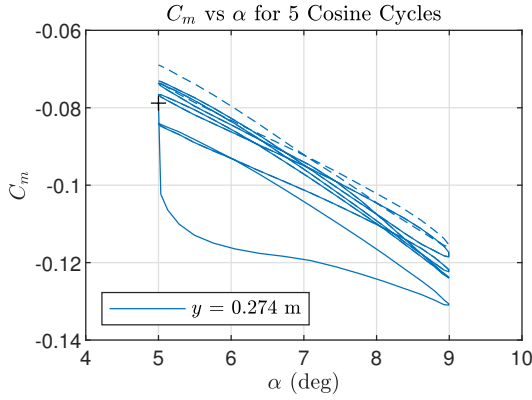
From Figure 3.12, a nominal grid density of 2.5x will be used for the work in Section 3.4 and Chapter IV of this thesis. From the density studies summarized above, the 2.5x density case appears to fall within the converged region for minimum pressure coefficient and the 2-norm of the moment coefficient. The other characteristics measured did not adequately demonstrate a converging trend, and so were not used to help determine the optimal grid for this grid convergence study.

3.3.5 Oscillatory Motion Study. The oscillatory motion used in Hope's analysis and the grid studies above was a sine function [20]. The ZEUS simulation was preset to record coefficients of pressure on the second of two cycles with the assumption that the second cycle would have reached a dynamically steady state response to the oscillation. This oscillation study tests that theory to determine the true effect of cycle count on the comparison criteria in 3.3.2. Since a sine function requires an instantaneous change in pitch rate from the steady state analysis completed by ZEUS to the start of the first cycle, this oscillation study compares the sine function to a negative cosine function which begins its oscillation at the lowest AoA, pitch down

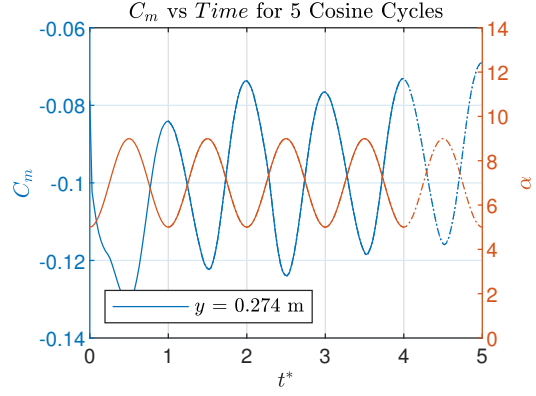
position. All calculations for this study will use the same Mach number, mean AoA, amplitude, and frequency for direct comparison.

The first simulation for this study changed the oscillatory function from sine to negative cosine and was run for a total of 5 cycles. Transient C_p data was recorded for individual cycles, cycles 1-4, and cycles 2-5 to determine any variation in data resulting from changing the starting position of the cycle. Next, the sine driven oscillation was run for 5 cycles with the C_p data for the first 4 cycles recorded for comparison against the negative cosine oscillation. Figure 3.13 shows these relationships at spanwise Station 2.

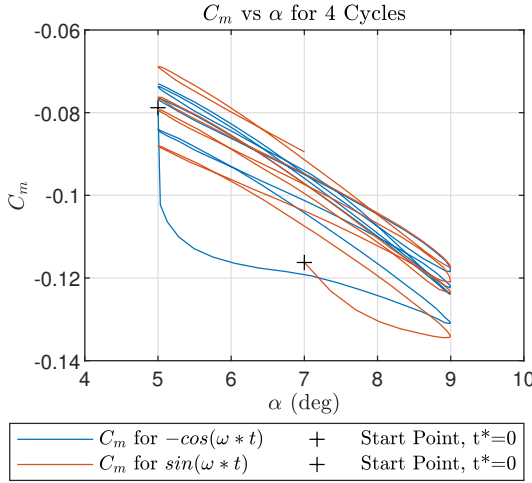
From Figures 3.13a and 3.13b which both show multiple negative cosine simulations for varying cycle counts, it can be seen that the simulations overlap exactly with one another with exception of the first and last data points which show slight error as a result of the interpolation inherent in the integrated function process that was used. It can also be seen from Figure 3.13a that the first cycle has significantly different moment coefficient values than the remaining cycles, suggesting that the flow has not fully developed around the oscillation. From Figure 3.13c where the negative cosine and sine simulations for the first 4 cycles are plotted together, it appears that both functions have initially more error within the first cycle, but less error in cycles 2 through 4. From this plot, it can also be seen that the maximum and minimum peaks are continually increasing throughout the 4 cycles for the sine oscillation pattern. The negative cosine function is also following this general trend as well, though at a lesser increase between cycles, and therefore was the oscillating pattern chosen for the remaining studies. When considering computation time, C_m appears to settle into an acceptable pattern by 1.5 cycles, and so the chosen setup for this report will gather cycle data from pitch up in the 2nd to pitch up in the 3rd cycle for the negative cosine oscillation pattern. It is possible that running this study for a higher cycle count would yield better results, however, the computation time needed was impractical when considering the quantity of simulations run to gather an effective mapping of the test envelope covered by this report. These changes to the



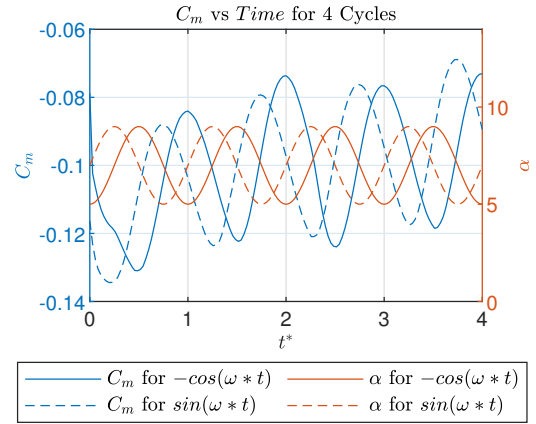
(a) Pitching moment coefficient vs AoA.



(b) Pitching moment coefficient and AoA vs cycle time.



(c) Pitching moment coefficient vs AoA comparing a sine curve vs a -cosine curve.



(d) Pitching moment coefficient and AoA vs cycle time comparing a sine curve vs a -cosine curve.

Figure 3.13: Cycle study at Station 2 with Mach number = 0.95, trim AoA = 7°, amplitude = 2°, frequency = 5.7 Hz, ran for 4 cycles.

setup of ZEUS' transient simulations attempt to minimize computation time without sacrificing accuracy of the analysis.

3.3.6 Grid Study Conclusions. Grid studies began with the addition of a GAP card to increase mesh fidelity in front of the tapered delta wing, and the alignment of the surface grid to the wind tunnel stations used by Cunningham [9] and

eliminate the interpolation completed by Hope [20]. Noticeable changes to the pressure and moment coefficient values were observed. The next study varied the surface grid density by factoring Hope's chosen optimal density to achieve grid independence for dynamic motion. Compared to Hope's static grid study where analysis showed a grid density of 35 x 40 was optimal, this dynamic study determined the accuracy of Hope's grid density for evaluating pressure forces around the oscillating delta wing in unsteady flow. Dynamic characteristics of pressure and moment were evaluated to determine a new optimal grid density. As a result of this study, it was determined that a density of 2.5x times that of Hope's choice, or 91 x 102 compared to Hope's 35 x 40, gave an optimal balance of computation time and grid independence for the dynamic motion that will be used for further analysis. This data suggested that though Hope's study found an adequate grid density for trim analysis, that grid density was inadequate for the dynamic analysis studied in this report. In the final optimization study, the oscillation function and cycle count were both varied. The change in oscillation function from sine to negative cosine was found to decrease variations between cycles. The cycle count study determined that a periodic flow does not seem to develop until almost 1.5 cycles into the transient analysis. For this reason, further analysis will use pressure coefficient data gathered from pitch up on the 2nd cycle to pitch up on the 3rd cycle, which is also a change from the full 2nd cycle used previously by Hope. The increase in the number of cycles and the denser surface grid will noticeably increase computation time, but these optimization studies have shown their impact on improving analysis moving forward. For these reasons, the extra computation time is necessary to ensure a more accurate simulation.

3.4 Computational Analysis

Once the optimization studies were complete, a test matrix was developed to capture the envelope of flight conditions to include in the analysis. The ZEUS SiS model was run for varying trim angles of attack, oscillation amplitudes, frequencies, and Mach numbers. The initial trim AoAs were 0°, 4°, 8°, and 12°, with oscillation

amplitudes 0.5° , 2° , and 12° . The frequency was held constant at 5.7 Hz. The initial envelope was run with Mach numbers 0.3, 0.6, and 0.9. The wide ranges of Mach number, trim, and amplitude were used to give a good visualization of flow characteristics along the wing. These data points were chosen to analyze general trends within the test envelope in order to determine specific regions to analyze specific flow development characteristics in more depth. More cases were added to capture development of these flow characteristics between the cases in the initial envelope. The final test matrix is shown in Table 3.2

Table 3.2: Test Matrix. Frequency = 5.7 Hz, “ I ” = fully inviscid, & “+” = $+cosine$ function.

Trim (deg)	Amplitude (deg)	Mach
0	0.5	0.3, 0.6, & 0.9
0	2	0.3, 0.6, 0.75, 0.85, 0.9, & 0.95
0	4	0.6, & 0.9
0	8	0.6, & 0.9
0	10	0.6, & 0.9
0	12	0.3, 0.6, 0.75, 0.85, 0.9, & 0.95
2	2	0.9
4	0.5	0.3, 0.6, & 0.9
4	2	0.3, 0.6, & 0.9
4	4	0.9
4	8	0.9
4	10	0.9
4	12	0.3, 0.6, 0.9, & 0.9^I
6	2	0.9 & 0.9^+
8	0.5	0.3, 0.6, & 0.9
8	2	0.3, 0.6, & 0.9
8	4	0.9
8	8	0.9
8	10	0.9
8	12	0.3, 0.6, & 0.9
10	2	0.75, 0.75^+ , 0.85, 0.85^+ , 0.9, 0.9^+ , 0.95, & 0.95^+
10	4	0.75, 0.85, 0.9, & 0.95
12	0.5	0.3, 0.6, 0.9, & 0.9^+
12	2	0.3, 0.6, & 0.9
12	12	0.3, 0.6, & 0.9

The improved grid and mesh from Section 3.3 were used for all cases run in the test matrix. Since these studies used a moderately trim AoA and high Mach number, the grid is expected to deliver fairly accurate results. This matrix has cases with high AoAs that were chosen to test the limit of ZEUS' convergence capabilities.

3.5 Post-Processing of Data

By outputting data from the transient response analysis, ZEUS allows the user to use other processing software for post-processing. For the time-accurate analysis used for this study, ZEUS outputs the normalized pressure data for every grid point on the wing's surface at each time step. The pressure data was output into a TECPLOT format that was then converted into a Matlab data structure for specialized post-processing. Analysis of the results concentrated solely on the four spanwise stations mentioned previously, and are similar to those used in the optimization studies in Section 3.3.

IV. Results and Analysis

4.1 Introduction

This chapter details the analysis of the oscillating delta wing using a time-accurate Euler solver known as ZEUS. The straked delta wing was partitioned by 93 spanwise and 103 chordwise grid lines. Simulation flight conditions varied in mean AoA or trim (T), oscillating amplitude (A), and Mach number (M), and aimed to capture the development of a wide range of aerodynamic phenomena as flight conditions changed. Pressure data were gathered for one full cycle from pitch up (nose up) in the second cycle to pitch up in the third cycle. Oscillations occurred about a fixed pitching axis at a frequency (F) of 5.7 Hz. The naming convention, T##A###F##M#, shows which numerical values were chosen for each motion parameter.

- T## shows what values was used for the mean AoA, also called trim. A case with a trim set at 2° would start its name with T02.
- A### shows the value assigned for amplitude. When three digits are shown, the third number is a decimal. The name of a case with an amplitude of 4° would include A040 in its name, and a case with an amplitude of 0.5° would include A005 in its name.
- F## shows the frequency value assigned to the case where the second number is a decimal. A case with a frequency of 5.7 Hz has F57 in its name.
- M# shows the Mach number used in each case. A case with Mach number of 0.9 would end in M9.

Special cases were also run which required additional changes to flow parameters. These changes did not fit within the standard naming convention. First, names to cases run with a fully inviscid solver began with an INV. Due to name length limits in ZEUS, the F## was dropped out of the name for these cases. Lastly, cases that used a positive cosine oscillation function instead of the standard negative cosine function begin with a P, for “positive”. The third digit in A### was dropped for these cases because of character limits in ZEUS’ file naming capacities.

A total of 71 unique cases were run and analyzed. Time was non-dimensionalized by the cycle period such that the start of the analyzed cycle was $t^* = 0$ and the end of the cycle was $t^* = 1$. Data were analyzed at 4 chords chosen to match the wind tunnel test data and analysis performed by Hope [20] on the same SiS model wing. These chord “Stations”, numbered 1-4, had spanwise measurements of $y = 0.209, 0.274, 0.336$, and 0.395 meters respectfully from the strake root. Since the wing has a -3° twist from wing root to wing tip, each station has a slightly different AoA. By interpolating the uniform twist along the wing, the washout for Stations 1 through 4 were found to be $-0.97^\circ, -1.6^\circ, -2.21^\circ$, and -2.78° respectfully. This equated to roughly 0.6° difference between each station.

Pressure, lift, and moment data were used to evaluate flow development that resulted from the different flight conditions outlined in the test matrix. First, A comparison was made to the results from Hope’s research to realize the effects of the grid studies detailed in Chapter 3. Next, some cases failed to converge to a solution, so analysis was completed in an attempt to determine the cause. After the convergence analysis, a general analysis of the testing envelope was completed to pinpoint and examine specific flow characteristics that were observed. Finally, further analysis was given to “sweeps”, where only one of either trim AoA, amplitude, or Mach number was varied and the other parameters were held constant. These sweeps help track the development of the flow characteristics of interest, such as a shock, as only one parameter was changed.

4.2 *Numerical Analysis*

For this analysis, pressure coefficient (C_p) was output from ZEUS and then plotted versus chord location at every 1/8th t^* interval for the full cycle. The critical pressure coefficient, which is the pressure at Mach number = 1.0, was also calculated using Equation 4.1 for each free stream Mach number used in this analysis. These critical pressure coefficients, shown in Table 4.1 [2], were then plotted as a dashed

line on the t^* vs x/c contour plots to outline the supersonic flow on the wing's upper surface.

$$C_{p,cr} = \frac{2}{\gamma M_\infty^2} \left[\left(\frac{1 + [(\gamma - 1)/2] M_\infty^2}{1 + (\gamma - 1)/2} \right)^{\gamma/(\gamma-1)} - 1 \right] \quad (4.1)$$

Table 4.1: Critical pressure coefficient vs Mach using standard air properties at sea level.

M_∞	$C_{p_{cr}}$
0.3	-6.95
0.6	-1.29
0.75	-0.59
0.85	-0.30
0.9	-0.19
0.95	-0.09

From these plots, shock movement and the slope of the shock were also calculated, along with the chordwise location of the shock(s). Figure 4.1 illustrates how the pressure data were used to calculate shock movement and the slope of the shock. Shock movement was calculated by differencing the local chord position, x/c , of the furthest forward and furthest aft shock position. The slope of the shock was found by dividing the change in C_p by the change in chord location between two points on the shock as shown in Equation 4.2. Since a shock is by definition a discontinuity, the shock slope is only used to indicate where the grid density is diffusing the result. When the shock slope is changing, compression waves are present but no shock. When the shock slope is at its greatest value and unchanging for a portion of the cycle, the pressure gradient is limited by the grid and a true shock is likely present. This assumption relies heavily on the use of a fine enough grid density. It is important to note the difficulty CFD solvers have with solving discontinuities like a shock. These difficulties can cause a solver to artificially smooth over a discontinuity to help with stability, a possible scenario that could impact these results.

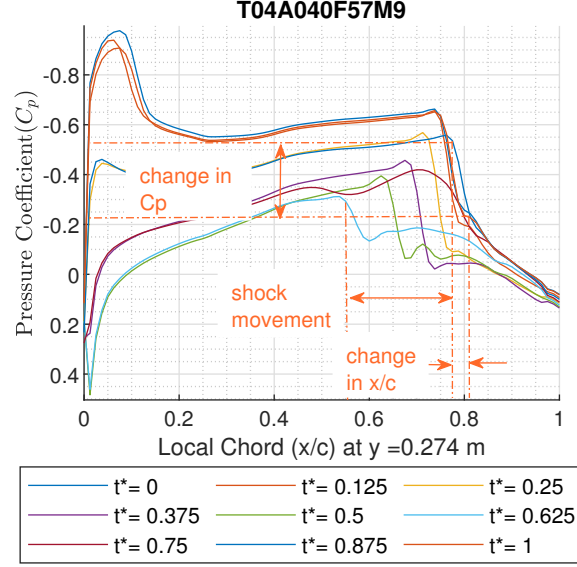


Figure 4.1: Pressure coefficient vs chord location showing shock movement and shock slope calculations.

$$Shock\ Slope = \frac{\Delta C_p}{\Delta x/c} \quad (4.2)$$

Sectional lift coefficient (C_l) and moment coefficient (C_m) were also calculated from the pressure coefficient data. To simplify calculations, it was assumed that the pressure coefficients acted perpendicular to the wing surface, and the thin airfoil was estimated as a flat plat. While this assumption added error to the lift and moment coefficients, it allowed the upper and lower surface pressure to be compared directly for each chordwise location. For lift calculations, the difference in upper and lower surface pressure coefficients along the chord were integrated them multiplied by cosine of the AoA. Equation 4.3 shows how the lift coefficient was derived from the pressure coefficient data.

$$C_l(t^*) = \left[\int_{x/c=0}^1 [C_{p,low}(t^*) - C_{p,up}(t^*)] d(x/c) \right] \times \cos(\alpha(t^*)) \quad (4.3)$$

Once calculated, the lift coefficient was plotted vs AoA and cycle time. Examples of lift plots are shown in Figure 4.2. The lift coefficient was also used to calculate

the lift curve slope (C_{l_α}) and zero lift AoA (C_{l_0}) at each station. For small to moderate angles of attack, the lift curve slope is expected to be linear, and taper off as the wing approaches stall conditions.

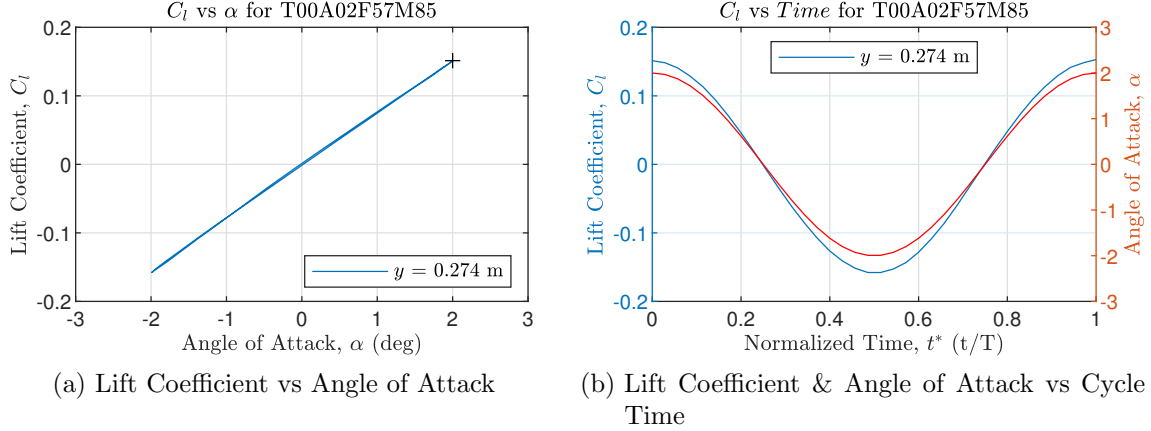


Figure 4.2: Example of lift plots for a single chord on the wing.

The moment coefficient was taken about the pitching axis. Since Hope's analysis took the moment about the quarter chord [20], these figures were not compared to Hope's moment coefficient plots. The moment coefficient was calculated similar to the lift coefficient by integrating the difference in pressure coefficients along the wing, except the ΔC_p was multiplied by its distance from the pitching axis for each point along the chord as shown in Equation 4.4.

$$C_m(t^*) = \int_{x/c=0}^1 (C_{p,low}(t^*) - C_{p,up}(t^*)) \times (x_{pitching\ axis} - x) d(x/c) \quad (4.4)$$

Like the lift coefficient, the moment coefficient was also plotted vs AoA and cycle time. Examples of these plots are shown in Figure 4.3. When the moment coefficient was plotted vs AoA, the rotational direction could be used to determine that chord's contribution to the stability/instability of the oscillation. In Figure 4.3a, the plus sign shows the starting point and the red star shows the curve's rotation direction. These symbols are included in all similar plots in this chapter. In this example, the

curve is rotating counterclockwise for the entire cycle. Typically, a counterclockwise rotation in moment coefficient signifies stable flight conditions such that the pitching moment acts to return the wing to an equilibrium state. A twist in the moment coefficient plot suggests a portion of the oscillation has unstable characteristics, where the pitching moment acts against a return to an equilibrium state. In this calculation, the location about which the moment is calculated plays a large roll in determining the stability/instability of an airfoil or wing. For this reason, an “unstable” result in this analysis may not translate to instability on a wing in flight test since the pitching axis location is dictated by the interaction of the bending and torsional natural frequencies of the wing instead of the fixed axis set perpendicular to the free stream flow, as in this analysis.

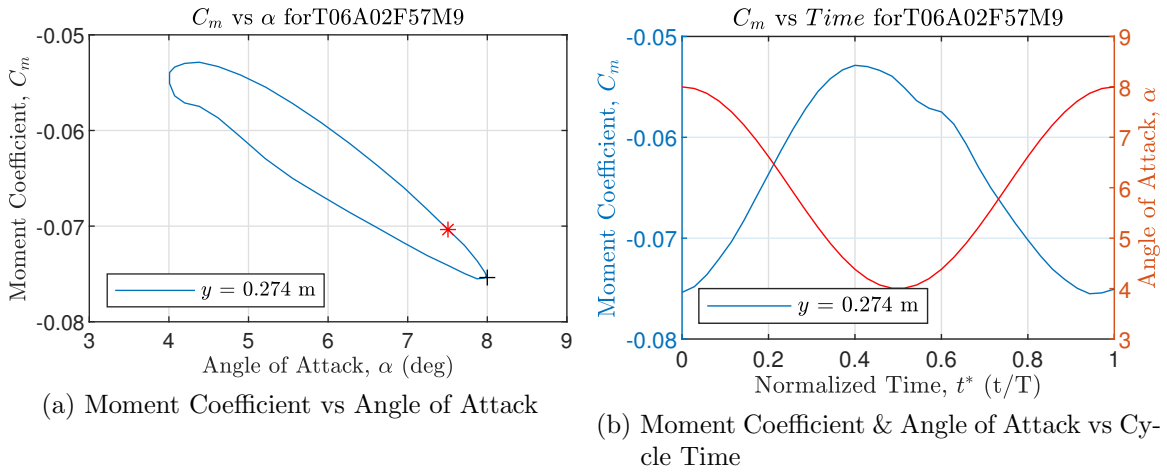


Figure 4.3: Example of lift plots for a single chord on the wing.

In analysis completed by Bendiksen, C_m vs α data from wind tunnel tests was compared to N-S and Euler models and concluded that both methodologies could predict the maximum and minimum C_m values accurately for a pitching wing in oscillation, but neither could predict the asymmetric “humps” between the two extremes that has been observed by many research investigations [3].

4.3 Comparison to Hope's and Pung's results

As detailed in the grid studies in Chapter 3, the grid density used in this analysis was 2.5x that used by Hope [20]. A 1/2 cycle delay in gathering transient data was also implemented from Hope's analysis. In order to best visualize a comparison, Hope's plots were reformatted in the same manner consistent with other plots from this analysis. First, cases with a trim AoA of 10° at 0.85, 0.9 and 0.95 Mach number were run with amplitudes 2° and 4° . The first notable observation was the non-convergence of $T = 10^\circ$, $A = 2^\circ$ & 4° , $M = 0.9$ cases which had resulted in converged solutions for Hope. The same cases that ran at $M = 0.85$ also did not converge for this analysis or for Hope. Pressure coefficient distributions for the 0.95 Mach number case at Station 2 are shown in Figure 4.4 where Hope's results are on the left for a side-by-side comparison with the results from his analysis on the right.

Due to a coarser grid density, Hope's results show more gradual changes in pressure. This is particularly noticeable around the forward and aft main shocks. This is likely the reason why Hope's study saw converged solutions where the denser grid did not. The coarse grid could not capture the rapid changes in pressure which result in complex shock boundary layer interactions. The denser grid allows sufficient data points to capture these abrupt changes in pressure. The higher shock strengths observed in this analysis matched more closely with Pung's observations in his N-S analysis. For cases that did not converge, it is likely that ZEUS struggled with the viscous boundary layer formation and the appearance of large regions of separation, resulting in non-convergence. It is possible that changing the boundary layer gain settings in ZEUS, which control boundary layer grow/shrinking rates, would be enough to achieve convergence. In the bottom left plot of Figure 4.4, a subsidiary shock can be seen immediately following the main aft shock. This shock is a result of the adverse pressure gradient causing a thinning of the boundary layer. The thinning of the boundary layer triggers an expansion of the mainstream flow, followed by an increase in pressure and another shock. This subsidiary shock was captured in Hope's plot

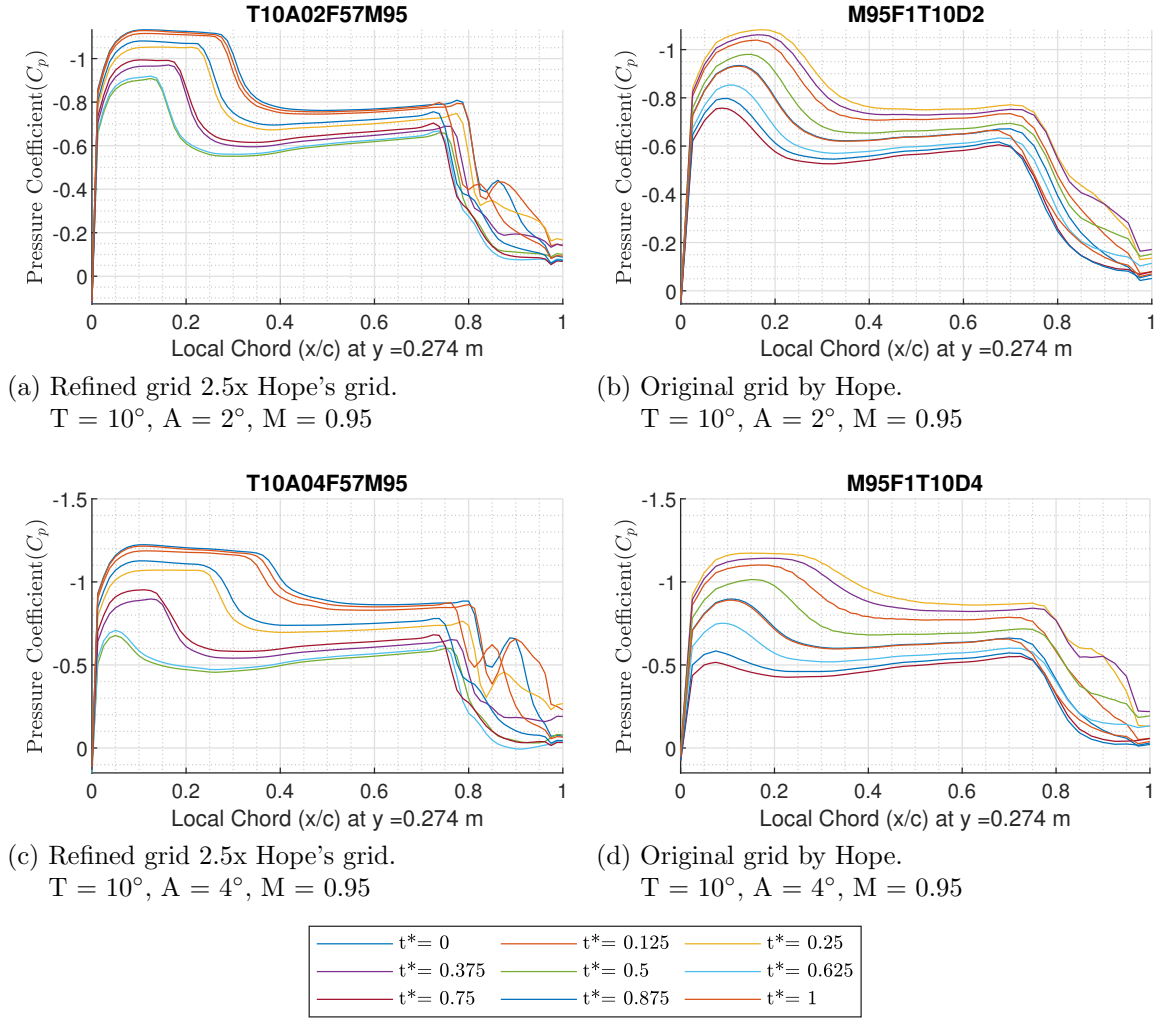


Figure 4.4: Pressure Coefficient vs Chord Location at Station 2.

seen on the right in the same figure, though it was not as detectable because of the coarse grid.

Next, the trim AoA was decreased to 4° and run with amplitudes of 2° and 4° at 0.9 Mach number. These cases are shown in Figure 4.5, where the left plots are from this analysis and the right plots are from Hope's analysis. Similar to the 10° cases, the changes in pressure are more gradual in Hope's analysis. This resulted in noticeable changes in overall C_p values, though general shape is very similar. Differences appear to occur around the adverse pressure gradients when the less dense grid of Hope's analysis cannot adequately react to the larger pressure changes of the

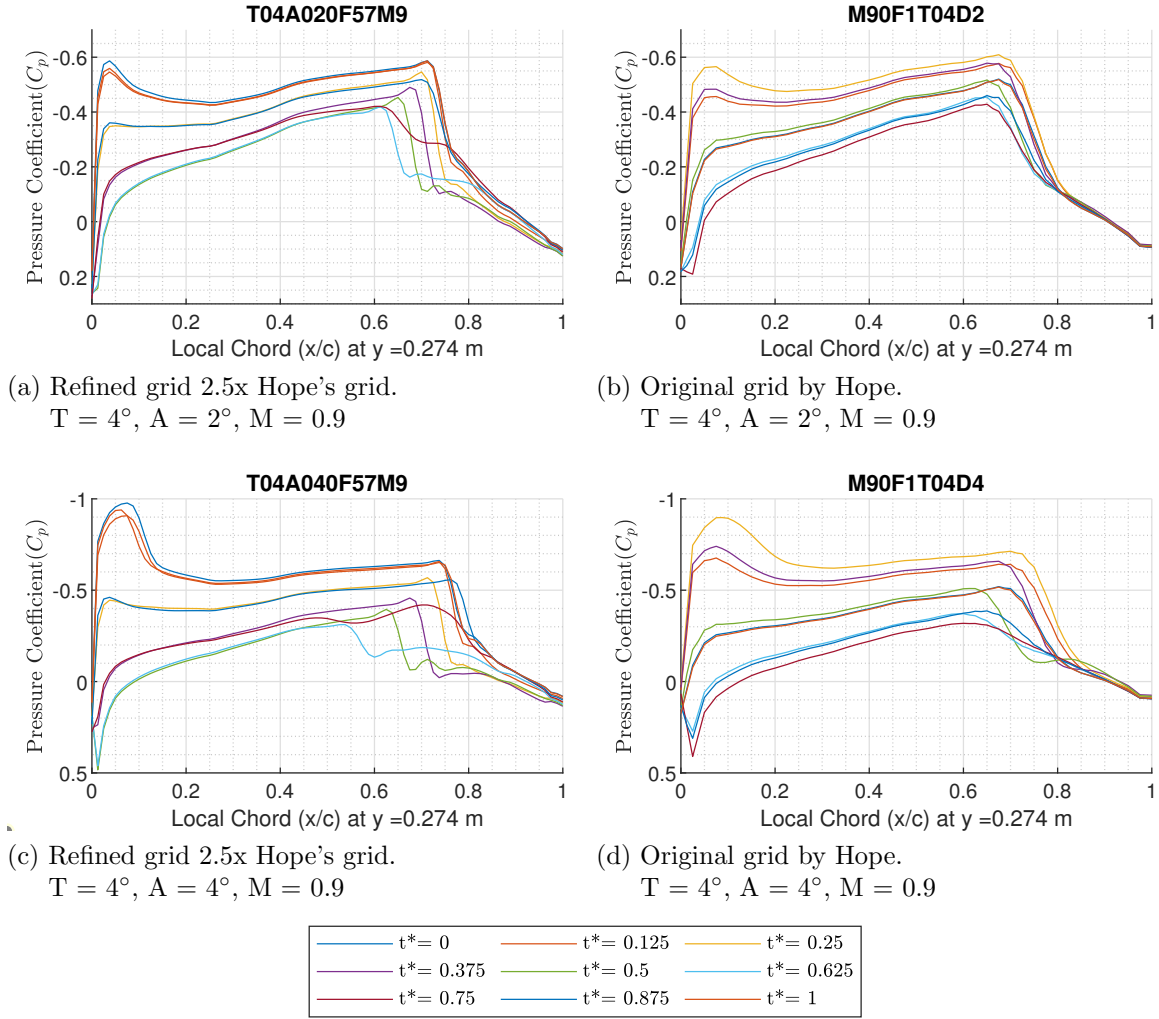


Figure 4.5: Pressure Coefficient vs Chord Location at Station 2.

flow. Unlike the previous comparison, these plots show a vast difference in shock movement. It appears that Hope's results showed less full shock movement and instead saw a changes in slope of the adverse pressure gradient. Though both analysis show possible shock disappearance when the amplitude was 4° , Hope's did not predict similar shock disappearance for the smaller amplitude of 2° like this analysis.

Due to the limited number of cases run by Pung and differences in flow characteristics such as Reynolds number, a direct comparison to Pung's results was not completed. Instead, a qualitative comparison was done by studying shock characteristics as wing motion parameters were varied. As amplitude was increased, Pung saw

increases in shock motion and shock strength. These observations were also noted in Hope’s results and seen in this analysis. Like Hope’s, this analysis did not distinctively observe SITES or large regions of separation that were observed by Pung and documented by Cunningham. These findings emphasize the limitation of ZEUS in predicting separation.

4.4 Convergence Issues

The convergence issues seen in the comparison to Hope’s analysis were not the only cases that did not converge. Table 4.2 highlights the 52 of the 71 total simulations which converged to solutions. The remaining 19 failed somewhere within the simulation and did not complete the transient analysis. The red cells show the cases that did not converge, and the green cells show where a converged solution was obtained. Simulations run with a positive cosine oscillation function are labeled with a “+” in the cell, and cases run using a fully inviscid solver are shown with an “I” in the cell. From this table, it can be seen that all cases where the AoA did not exceed 10° converged. For cases with a maximum AoA = 12° AoA and above, some converged and others did not. As can be seen from the 10° trim AoA cases, increasing Mach number results in some cases converging and others not converging. This shows that for a given trim AoA and amplitude, convergence is not determined by a Mach number threshold value where exceeding that value causes non-convergence. When looking at trends within each Mach number individually, there is a general trend towards non-convergence as maximum AoA is increased, though the trim AoA appears to have more influence on convergence than amplitude. A high trim AoA of 10 or 12 degrees is likely to not converge even with small amplitudes, but a case with a small trim AoA and a high amplitude of 10 or 12 degrees appears very likely to converge. Since convergence is often a function of the grid density, it is possible that a higher grid density would improve convergence for the high trim AoA cases that failed, though no additional grid variations were attempted to get the solutions for these cases to converge.

Table 4.2: Converged (green) vs non-converged (red) cases. A “+” = +*cosine* function & “I” = fully inviscid solution.

Trim (deg)	Amplitude (deg)	Max AoA (deg)	Mach number					
			0.3	0.6	0.75	0.85	0.9	0.95
0	.5	0.5						
0	2	2						
0	4	4						
0	8	8						
0	10	10						
0	12	12						
2	2	4						
4	.5	4.5						
4	2	6						
4	4	8						
4	8	12						
4	10	14						
4	12	16						
4	12	16					I	
6	2	8						
6	2	8					+	
8	.5	8.5						
8	2	8.5						
8	4	12						
8	8	16						
8	10	18						
8	12	20						
10	2	12						
10	2	12			+	+	+	+
10	4	16						
12	.5	12.5						
12	.5	12.5					+	
12	2	14						
12	12	24						

4.4.1 Oscillation Study. In order to determine the effect of the oscillation function on convergence, a few cases were run with a positive cosine oscillation instead of a negative cosine function. This study attempted to optimize the starting location within the sinusoidal oscillation to help ZEUS converge. By changing the starting point to the pitch up position, this allowed ZEUS to perform its trim analysis at the maximum AoA before the oscillations began. In order to best compare these results,

the data gathered from these cases was delayed by one half of a cycle so that the pressure data output from ZEUS began at pitch up for both functions. It can be seen in Table 4.2, shown by the cells with a “+”, that only 1 of 6 cases run with a positive cosine function had a result that varied from that of the negative cosine function. That case had an amplitude of only 0.5° , and shows that convergence is only very slightly affected by the sinusoidal type oscillation function used. Figure 4.6 shows pressure distributions for a couple of the cases with positive cosine cases shown on the right and negative cosine cases on the left. Ideally, these results would be identical. In reality, the results are very similar but not exact. The half a cycle difference in data needed to compare data with the same starting position most likely accounts for a majority of the differences as demonstrated by the cycle study detailed in Chapter 3.

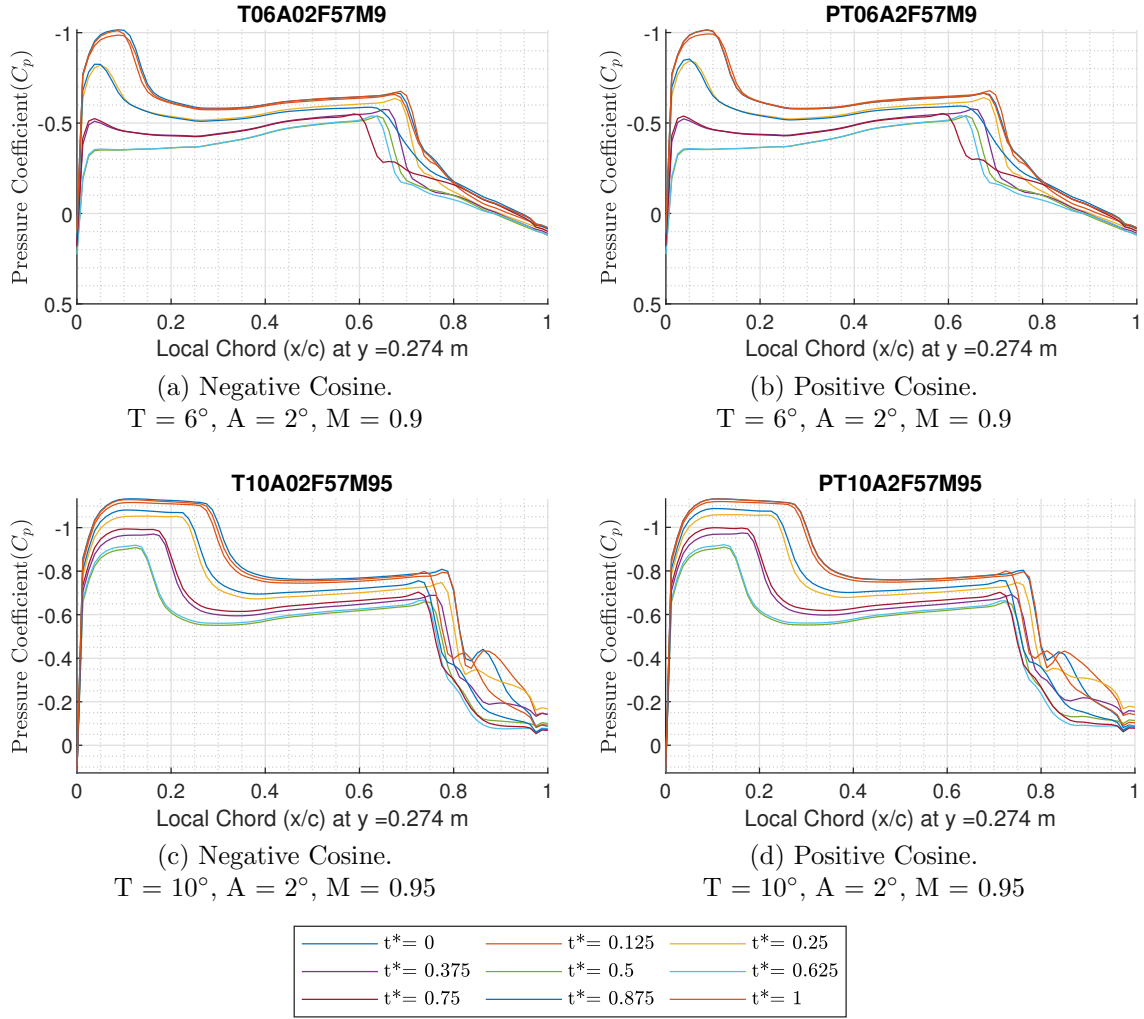


Figure 4.6: Pressure Distributions at Station 2.

4.5 General Observations

After the comparison to Hope's results [20] and the investigation into convergence issues, a general analysis of the testing envelope was completed to pinpoint and examine specific flow characteristics that were of interest. First, a forward main shock and an aft main shock developed with increases in AoA and Mach number. Once developed, a shock's movement appeared to increase with AoA. In some cases, the shock waves weakened back into compression waves for portions of the oscillation cycle. In high amplitude cases, smaller subsidiary shocks were seen aft of the main shock. Another observation that was studied in greater detail was a shock move-

ment hysteresis where the shock continued to move forward after the pitching motion changed direction. In the moment coefficient calculations, a “twist” or CW rotation in the C_m vs α curve developed in some cases. These observations are discussed in this section and further analyzed in the sections that follow.

When comparing the pressure data from all of the plots in the test matrix, the most drastic changes were seen at Station 4. However, these changes were heavily influenced by the 3D flow around the wing tip. This complex flow likely yields higher inaccuracies within an Euler solver such as ZEUS. A similar effect can also be seen at Station 1 due to vortex development off the leading edge of the strake. For these reasons, most the analysis outlined in this report concentrates on Stations 2 and 3, though Cunningham [10] found this vortex flow to influence these stations as well during various flight conditions.

Figure 4.7 and 4.8 show pressure distributions for a couple of cases that demonstrate some common flow characteristics seen in this analysis. Pressure coefficient versus chord location plots are on the left, and pressure contour plots of cycle time versus chord location are on the right. All of the pressure distribution plots show pressure data for the upper surface of the wing only. The left plot shows nine lines, each showing the pressure data along the chord at a time step within the cycle. The colors in the contour plot help visualize the pressure coefficient through the cycle. A dotted line outlines the supersonic region on the wing.

Mach number is increased from 0.3 in the top plots to 0.9 in the bottom plots. Figure 4.7 shows cases of increasing Mach number when trim AoA is held constant at 0° and amplitude is set to 0.5° , and Figure 4.8 shows cases of increasing Mach number when trim AoA is held constant at 4° and amplitude is set to 12° . When the Mach number is 0.3, the $C_{p_{cr}}$ is -6.95. For all converged cases at this Mach number, the flow never reaches this value, and therefore remains subsonic all the way around the upper surface. This is shown in the top right plot in these figures where no dotted line for the critical pressure is present. When the wing has a small or

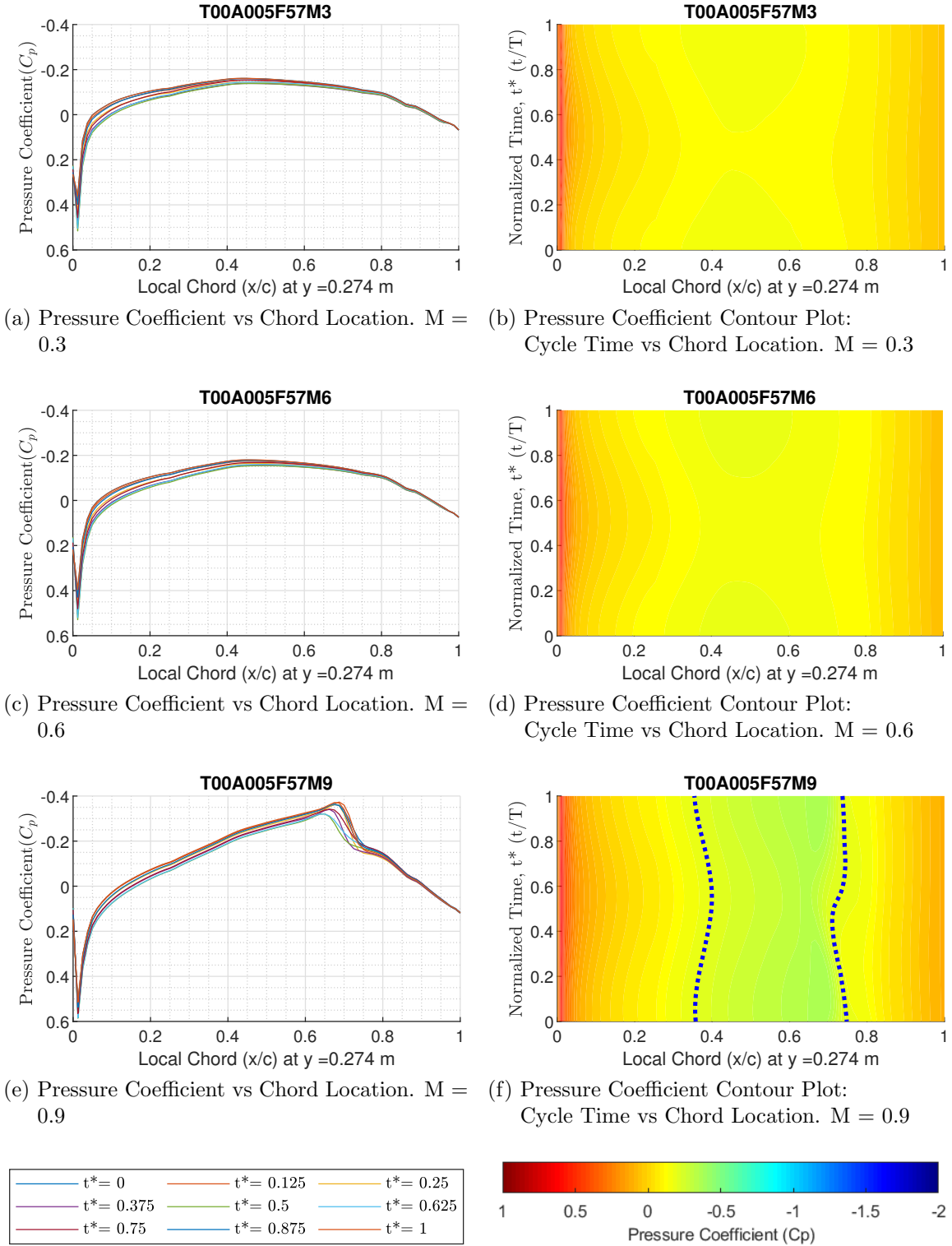


Figure 4.7: Pressure Distributions with $T = 0^\circ$, $A = 0.5^\circ$ at Station 2.

negative AoA such as in Figure 4.7, the flow at the leading edge on the upper surface experiences compression followed by expansion as the flow follows around the small radius of the leading edge. At higher AoAs like in Figure 4.8, the flow at the leading edge experiences the expansion fan first, then followed by compression. As the Mach number was increased to 0.6, the same patterns seen in the Mach number 0.3 cases are also seen, however, the $C_{p_{cr}}$ drops to -1.29. For cases with higher AoA, this results in the development of a supersonic region following the expansion fan at the leading edge as can be seen in the middle right plot of Figure 4.8. Compression waves follow the expansion fan, and begin to converge into shock waves when the strength of the pressure gradient is sufficient. As the flow velocity is increased further to 0.9 Mach number, shock waves develop at lower AoAs as seen in the bottom right plot of Figure 4.7. These shock waves are further aft on the wing than those found at the lower transonic speeds with higher AoA. The result is a potential two shock formation for high transonic, high AoA cases.

For some high amplitude cases, smaller subsidiary shocks can be seen aft of the main shock. The presence of a shock can thin the boundary layer immediately behind it creating an expansion zone for the mainstream flow. This expansion increases velocity and decreases pressure. In some cases, a small supersonic pocket can develop with a subsidiary shock on the trailing end to return flow to subsonic levels. As the main shock strengthens, strength is pulled from the subsidiary shocks, causing them to weaken and possibly disappear. The pressure distribution plots like the one in the bottom of Figure 4.8 show this phenomenon clearly. Many cases will see a small wave of expansion and compression behind the main shock, so the contour plot is useful in visualizing when flow regains supersonic speeds, a necessary condition for a shock to form.

Figure 4.9 shows moment and lift coefficient distributions for the 0.9 Mach number cases in Figures 4.7 and 4.8. In some cases such as in the top, left plot of Figure 4.7, the moment distribution shows a “twist” developed. This twist is uncommon and often suggests instability. Cases with the amplitudes greater than the

trim AoA saw positive moment values when pitched down. In the bottom plots, the lift coefficient develops an asymmetric oval shape instead of the almost linear path through the oscillation as the AoA is increased showing that the lift is not just a function of the AoA, but also the dynamic motion of the cycle.

One last critical observation was the asymmetrical pressure distribution through the cyclical motion, meaning that the pressure changes that were seen while pitching down were not reversed/mirrored while pitching up. It is likely that a hysteresis is present that is caused by the wing's motion into and away from the flow as it rotates about the pitching axis. Since the pitching axis of the wing is in front of most of the shock formations for Stations 1-4, the physical motion of the wing as a result of the rotation about the pitching axis can be significant, particularly on the aft portion of the wing that is furthest away from the axis of rotation. Figure 4.10 shows the location of the pitching axis with respect to Stations 1-4 on the wing.

This motion causes most of the wing to move into the flow as the wing pitches down, and away from the flow as the wing pitches up. When the wing surface moves into the flow, the effect is a compressive force which has the potential of thinning the boundary layer, increasing the pressure, and decreasing the speed. An expansion force is the result of the wing surface moving away from the flow. If great enough, this expansive force can decrease the pressure, increase the Mach number, and thicken the boundary layer. For cases with shocks, this hysteresis has the potential to impact the strength and migration of the shock. The observed result was asymmetrical migration of the shock wave, where the shock continues to move forward after the pitching motion change direction and has begun pitching up.

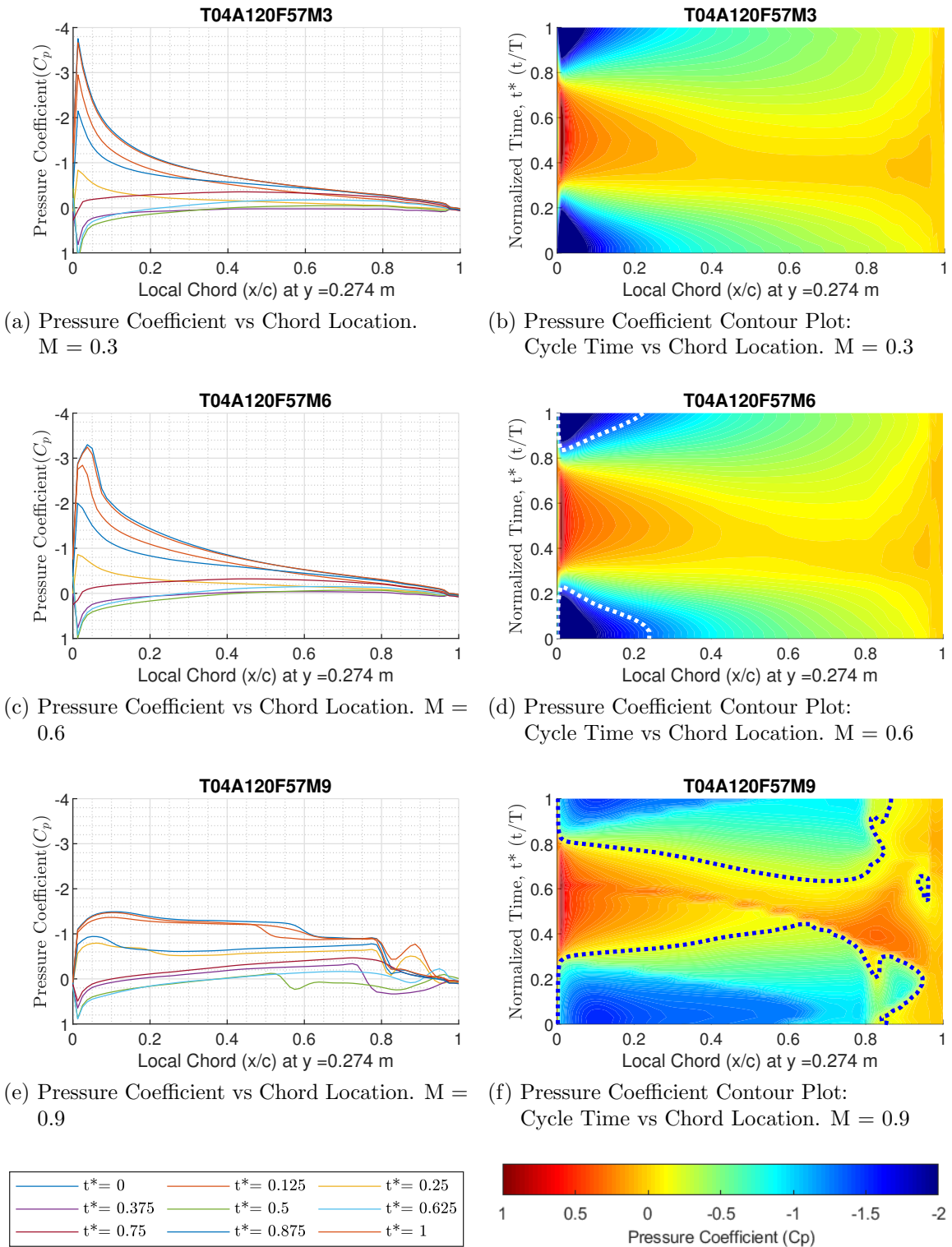
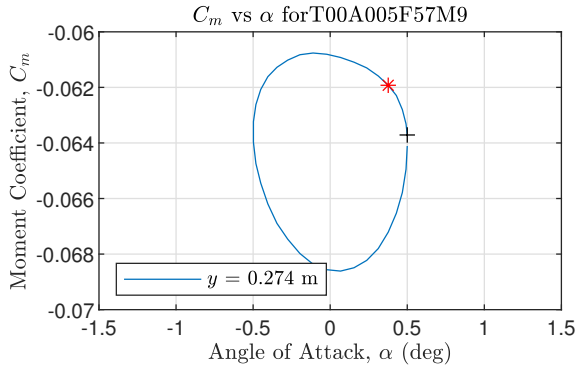
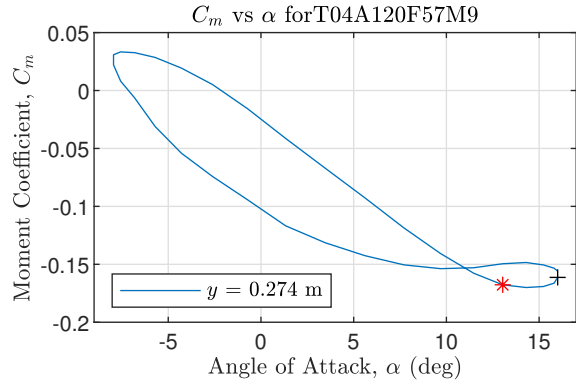


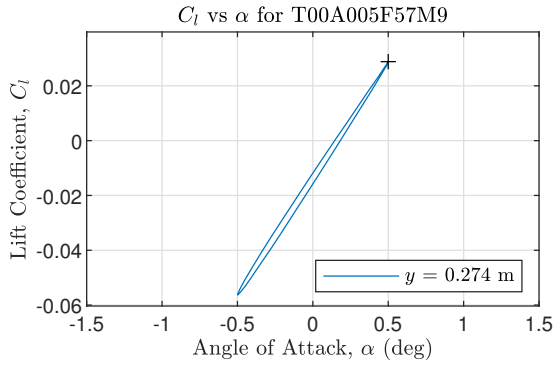
Figure 4.8: Pressure Distributions for $T = 4^\circ$, $A = 12^\circ$ at Station 2. $M = 0.3$ (top), 0.6 (middle), & 0.9 (bottom).



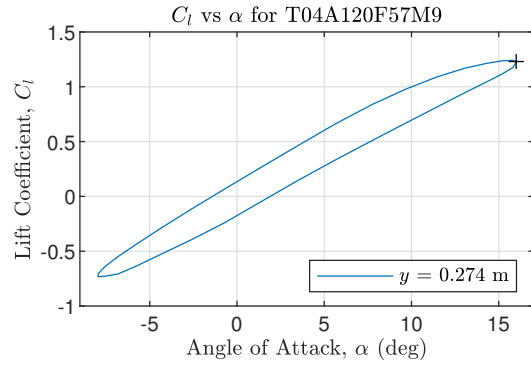
(a) Moment for $T = 0^\circ$, $A = 0.5^\circ$, $M = 0.9$ case.



(b) Moment for $T = 4^\circ$, $A = 12^\circ$, $M = 0.9$ case.



(c) Lift for $T = 0^\circ$, $A = 0.5^\circ$, $M = 0.9$ case.



(d) Lift for $T = 4^\circ$, $A = 12^\circ$, $M = 0.9$ case.

Figure 4.9: Moment and Lift Coefficients vs AoA at Station 2.

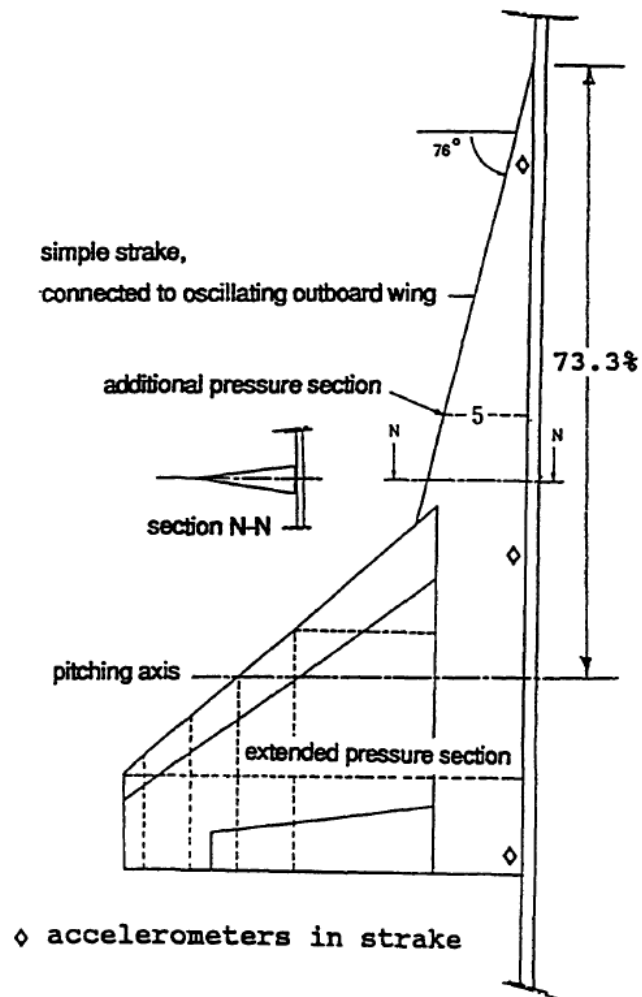


Figure 4.10: Model planform with the pitching axis location in relation to Stations 1-4.

4.6 Inviscid vs Viscous Solutions

In order to study the differences between the fully inviscid solution and the boundary layer coupling (BLC) solution, a case was run for each solver using the same motion parameters. Each case had $T = 4^\circ$ and $A = 12^\circ$ at $M = 0.9$. The pressure distributions at Stations 2 and 3 for these are shown in Figure 4.11, where the left plots use BLC and the right used the fully inviscid solver.

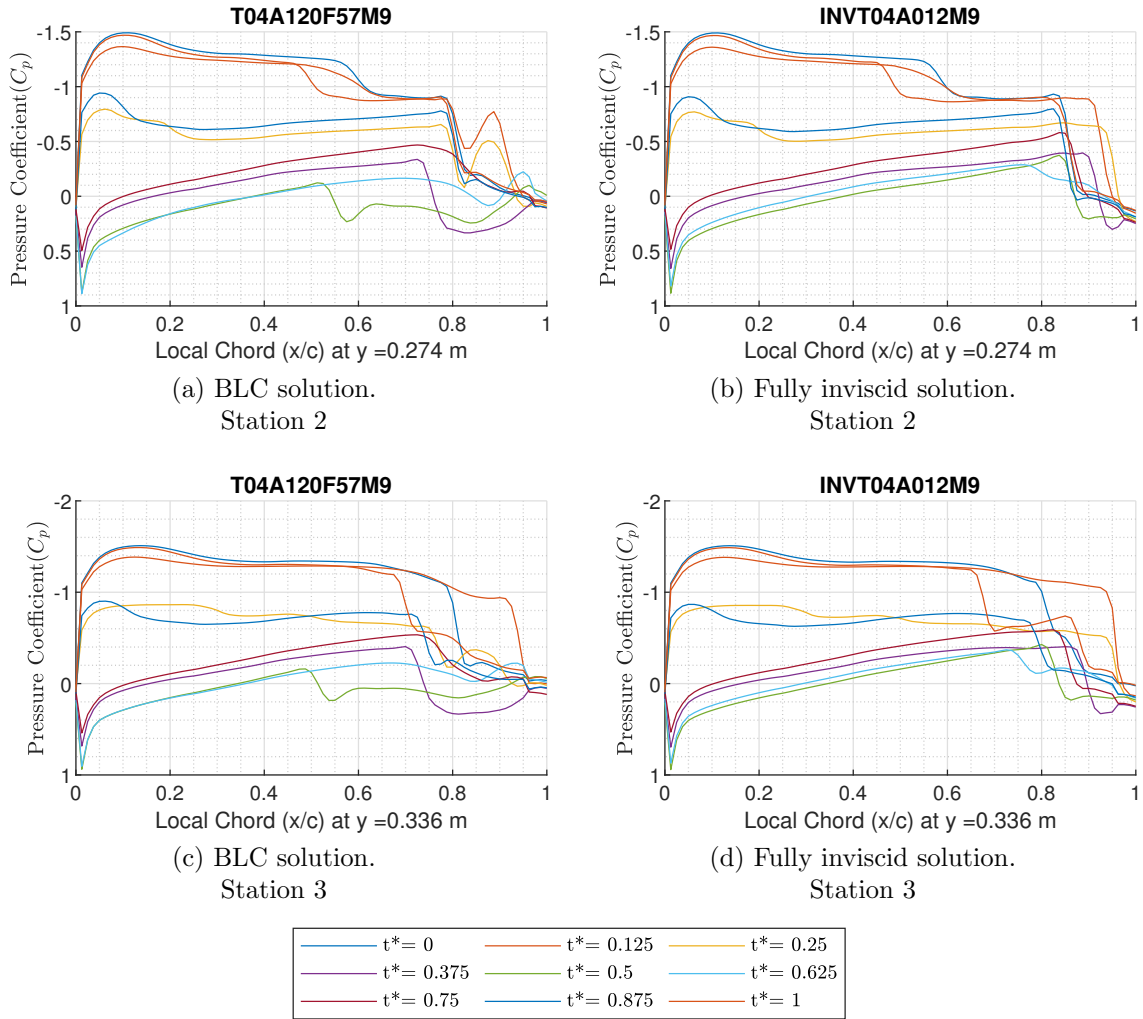


Figure 4.11: Pressure Coefficient vs Chord Location. $T = 4^\circ$, $A = 12^\circ$, & $M = 0.9$.

The top plots in this figure are Station 2 and the bottom plots are Station 3. When changes in pressure are small, the BLC and fully inviscid solutions compare closely. This can be seen by comparing the front half of each chord in Figure 4.11.

When shocks are present such as in the back half of each plot, significant differences are evident. The BLC solution at Station 2 shows subsidiary shocks aft of the main shock. The inviscid solution to the right of it fails to show subsidiary shocks, and instead shows the main shock further aft and with a larger rise in pressure. As seen in the contour plots in Figure 4.12, the BLC plots show a small supersonic region that matches the position of these subsidiary shocks.

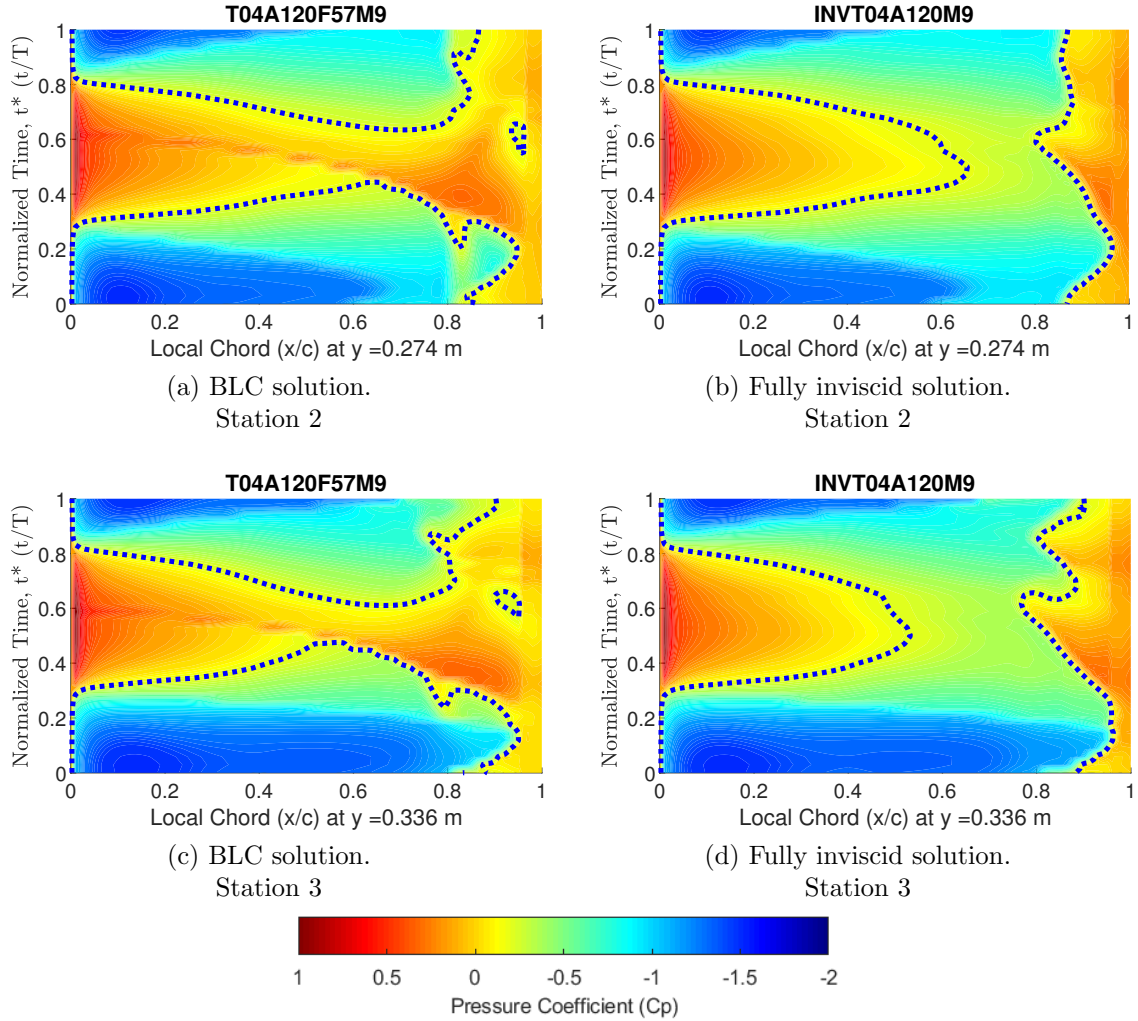


Figure 4.12: Pressure Coefficient Contour Plot: Cycle Time vs Chord Location. $T = 4^\circ$, $A = 12^\circ$, & $M = 0.9$. The supersonic flow region is outlined by a dashed line.

In Figure 4.11, the shock movement forward as the wing pitches down is shown to be considerably less in the inviscid plots. Where the BLC solution predicts the shock's disappearance at $t^* = 0.625$, the inviscid solution does not. This disappearance is matched by the contour plots which show the supersonic region disappearing for about 20 percent of the cycle when the wing is pitched down. These results match well to the results of the inviscid versus BLC study completed by Hope [20]. The differences are likely a result of the boundary layer's thickening/thinning responses reacting to changes in pressure in the mainstream flow and show the significant influence of boundary layer viscosity on the number of shocks present, the strength of each shock, and the location of each shock.

For the same cases shown in Figures 4.11 and 4.12, the moment coefficient was also analyzed. Figure 4.13 shows moment plots for these cases, where each station is represented by its own curve on each plot. As with the pressure data, the inviscid

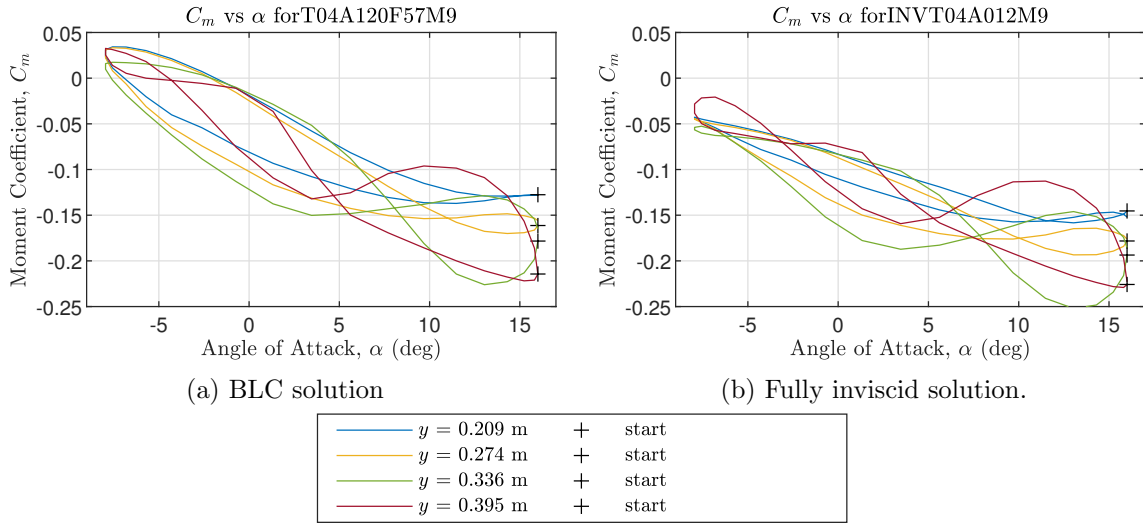


Figure 4.13: Moment Coefficient vs Chord Location for Stations 1-4. $T = 4^\circ$, $A = 12^\circ$, & $M = 0.9$.

case is on the right, and the BLC case is on the left. From these plots, the shape can be seen to be similar, even to the detail of the twist seen at Station 4 when the wing is pitch down, but the magnitudes of the moment coefficient are different. The moment in the BLC plot reaches positive values at all stations, which follows logic

if the wing pitches down past the zero lift AoA of the wing. When the wing is at a sufficiently negative AoA, the pitching moment acts to level the wing to a state of trim or equilibrium. The result of the inviscid case does not reach positive values at the minimum AoA of -8° like the BLC. Figure 4.14b shows lift distribution data that correlates with the pressure and moment plots. These plots show very similar looking curves, however, the lift in the pitch down position is more negative in the BLC case. Both cases have comparable lift in the pitch up position, but the inviscid case has a lower value for lift curve slope for all track stations. This can be seen in the plots where the lift at the pitched down position (AoA = -8°) for the inviscid case is close to -0.5 for all stations, and closer to -0.7 for all stations in the BLC case.

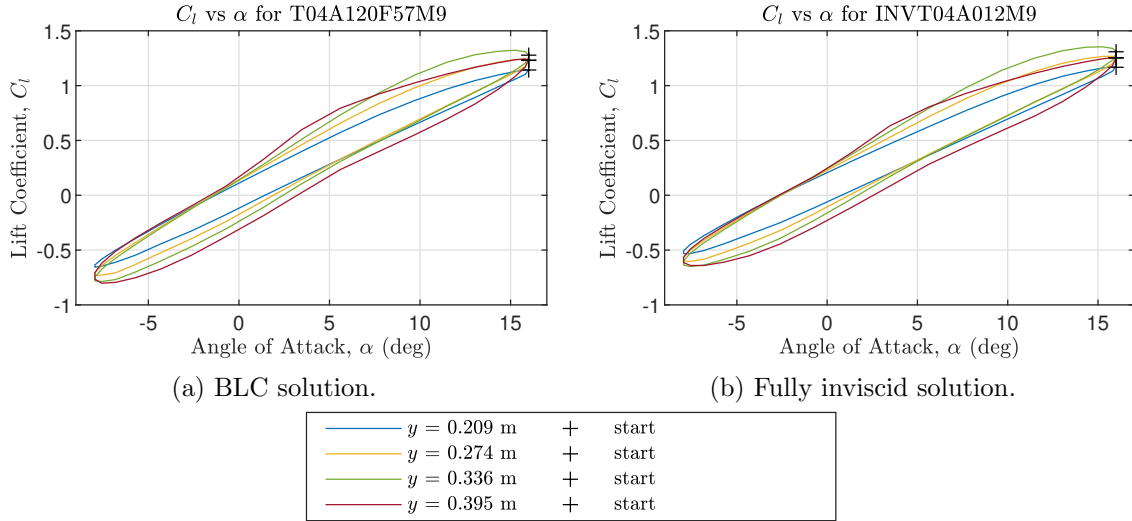


Figure 4.14: Lift Coefficient vs Chord Location for Stations 1-4. $T = 4^\circ$, $A = 12^\circ$, & $M = 0.9$.

4.7 Low Transonic Cases

To visualize the development of shock at lower transonic speeds, a sweep was completed holding at $M = 0.6$ and $T = 0^\circ$. The amplitude was increased from 0.5° to 12° . The minimum pressure C_{pmin} , chord location (x/c) at C_{pmin} , lift curve slope C_{l_α} , and lift at zero AoA C_{l_0} are all shown in Table 4.3 for Stations 2 and 3.

Table 4.3: Amplitude sweep with trim AoA = 0°, Mach number = 0.6 & frequency = 5.7 Hz.

Station	Amplitude	C_{pmin}	x/c of C_{pmin}	C_{l_α}	C_{l_0}
2	0.5°	-0.18	0.45	0.065	0.023
	2°	-0.22	0.43	0.065	0.022
	4°	-0.37	0.03	0.065	0.019
	8°	-1.37	0.01	0.066	0.010
	10°	-1.97	0.01	0.067	0.006
	12°	-2.54	0.03	0.067	0.002
3	0.5°	-0.18	0.45	0.067	0.007
	2°	-0.22	0.43	0.067	0.005
	4°	-0.36	0.04	0.067	0.002
	8°	-1.35	0.01	0.068	-0.010
	10°	-1.96	0.01	0.069	-0.016
	12°	-2.61	0.03	0.069	-0.020

The biggest change in C_{pmin} occurred between amplitudes of 2° and 4° where the pressure curve changes from a gradual arcing curve with the minimum around mid chord to rapid expansion and compression towards the leading edge which exceeds the negative pressure near the main shock. This can be seen in the table where the C_{pmin} at Station 2 migrates from $x/c = 0.43$ to $x/c = 0.03$ and in the pressure distribution plots for each case in Figure 4.15. At these amplitudes, the flow is still fully subsonic. As the amplitude increases to 8°, the pressure drops below -1.29 and a supersonic region develops for a short time while pitched up. This transition can be seen in the right plots of Figure 4.15. As the amplitude further increases, the minimum pressure continues to decrease and the compression region that returns the flow to subsonic speeds condenses to a shock. From the table, it can also be seen that C_{l_α} is consistently between 0.065 - 0.069 for Stations 2 and 3 and in all low transonic cases. Most of the differences in C_{l_α} between Stations 2 and 3 are due to the wing twist which equates to 0.6° difference in AoA. C_{l_0} is also seen to drop very slightly as amplitude is increased. This seems to be due to an increase in the hysteresis of pressure that is not a uniform lag for the entire cycle.

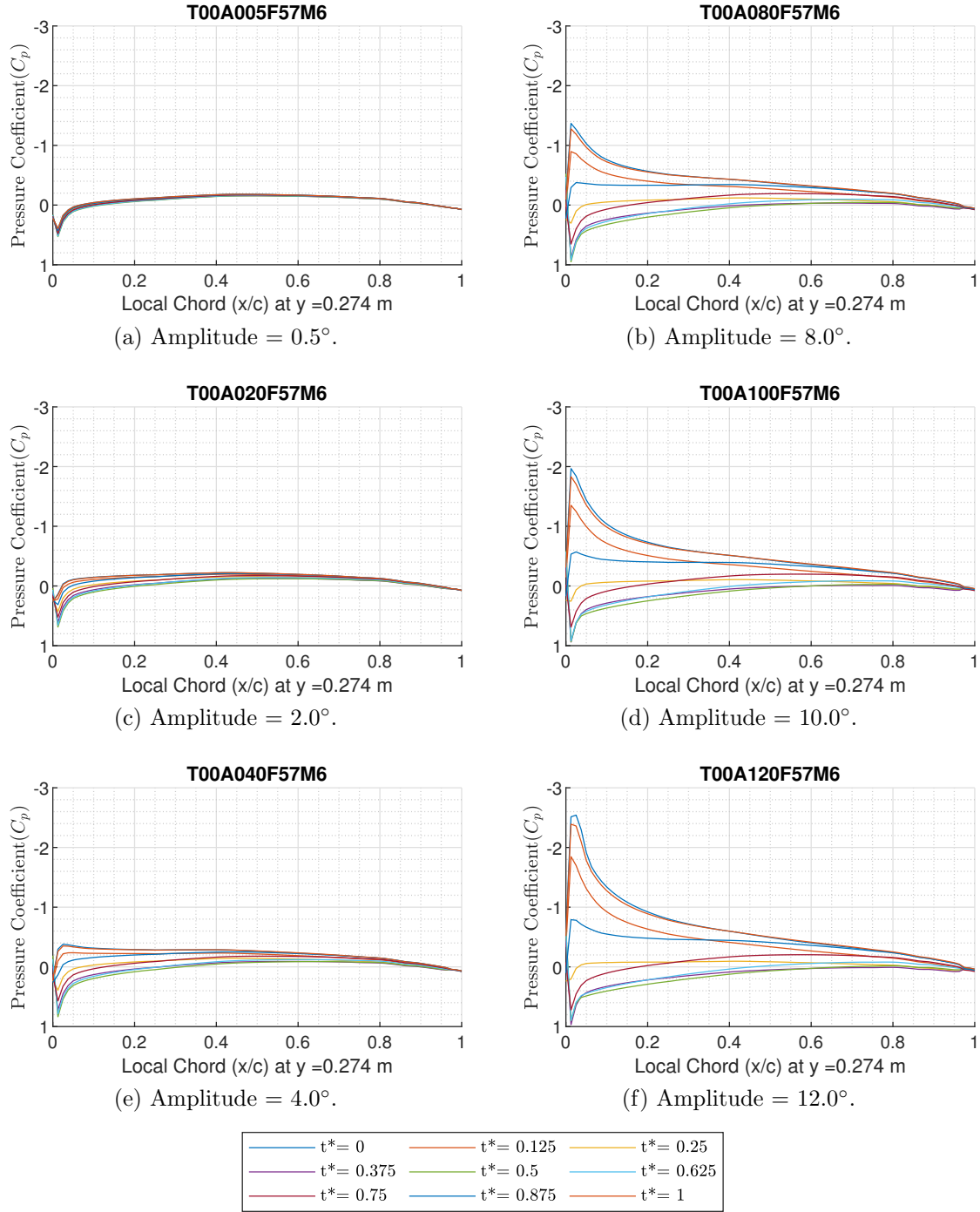


Figure 4.15: Pressure Coefficient vs Chord Location for Increasing Amplitudes. $M = 0.6$ & $T = 0^\circ$.

4.8 Trim Sweep

To better understand how shocks react to changes trim AoA as the wing oscillates, a trim sweep was completed using a moderate amplitude of 2° at 0.9 Mach

number. The trim increased from 0° to 12° . Cases with $T = 10^\circ$ and $T = 12^\circ$ did not converge. Figures 4.16 and 4.17 show pressure distribution for the converged cases at Stations 2 and 3 respectively. These figures are accompanied by Table 4.4, which shows shock slope, shock movement, lift curve slope, and lift at zero AoA.

Table 4.4: A trim sweep with amplitude = 0° Mach number = 0.9, & frequency = 5.7 Hz.

Station	Trim AoA	$\frac{\Delta C_p}{\Delta x/c}$	Shock Movement	C_{l_α}	C_{l_0}
2	0°	-23.98	0.14	0.085	-0.017
	2°	-29.93	0.11	0.082	-0.013
	4°	-24.53	0.10	0.080	-0.002
	6°	-32.44	0.09	0.080	0.011
	8°	-25.49	0.08	0.080	0.021
	10°		Did Not Converge		
	12°		Did Not Converge		
	0°	-13.46	0.13	0.088	-0.037
3	2°	-19.31	0.13	0.085	-0.030
	4°	-16.01	0.14	0.084	-0.020
	6°	-28.98	0.10	0.086	-0.013
	8°	-32.55	0.16	0.086	0.000
	10°		Did Not Converge		
	12°		Did Not Converge		
	0°	-13.46	0.13	0.088	-0.037
	2°	-19.31	0.13	0.085	-0.030

At both Stations 2 and 3, the point of minimum pressure slowly decreases as trim AoA increases from 0° to 4° . Within this range, the minimum pressure is located just before the shock on the aft part of the wing, referred to by Hope as the “knee” of the shock [20]. The shock seems to disappear in the pitched down portion of the cycle. As the trim AoA increases, the negative pressure builds toward the front of the wing and the shock motion lessens. At 4° , the negative pressure buildup results in a pressure at the loading edge equal to the pressure of the knee of the main shock. A large decrease in pressure then occurred between trim AoA of 4° and 6° , where a shock developed toward the front of the wing ahead of the main aft shock. This formation matched the two shocks observed by Cunningham [9] in the wind tunnel tests. When looking at the forward shocks location at each station, it is evident that the shock is swept. This also matched descriptions by Cunningham of the forward

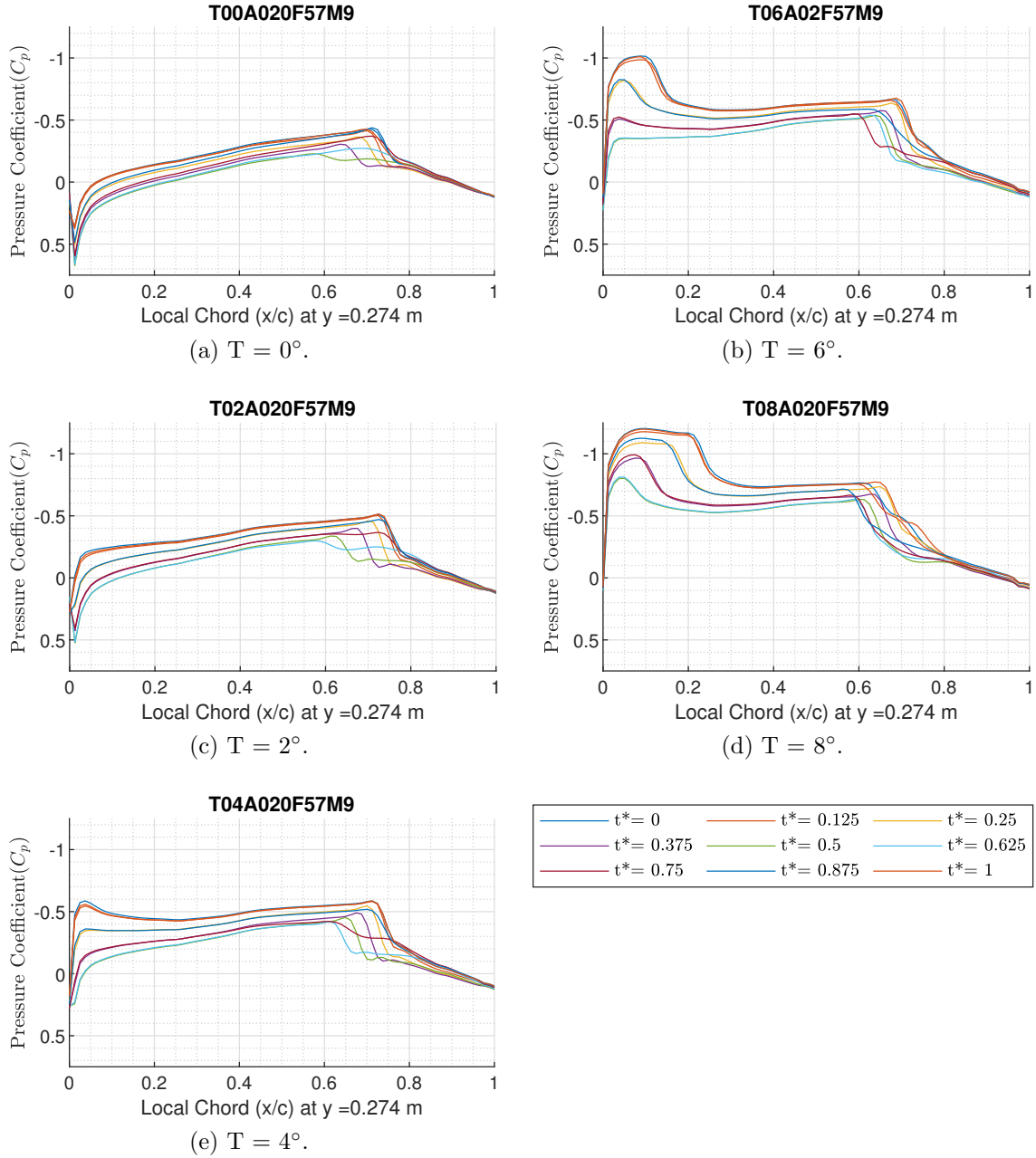


Figure 4.16: Trim Sweep Pressure Coefficient vs Chord Location at Station 2. $M = 0.9$, $A = 2^\circ$.

shock. It is likely that this swept shock formed in response to vortex flow off of the leading edge that is typical on delta wings at sufficient AoAs. Greater detail in the development of vortex flow on a delta wing can be found in [15] written by Elsenaar of the National Aerospace Laboratory. The forward shock appears to have little effect on

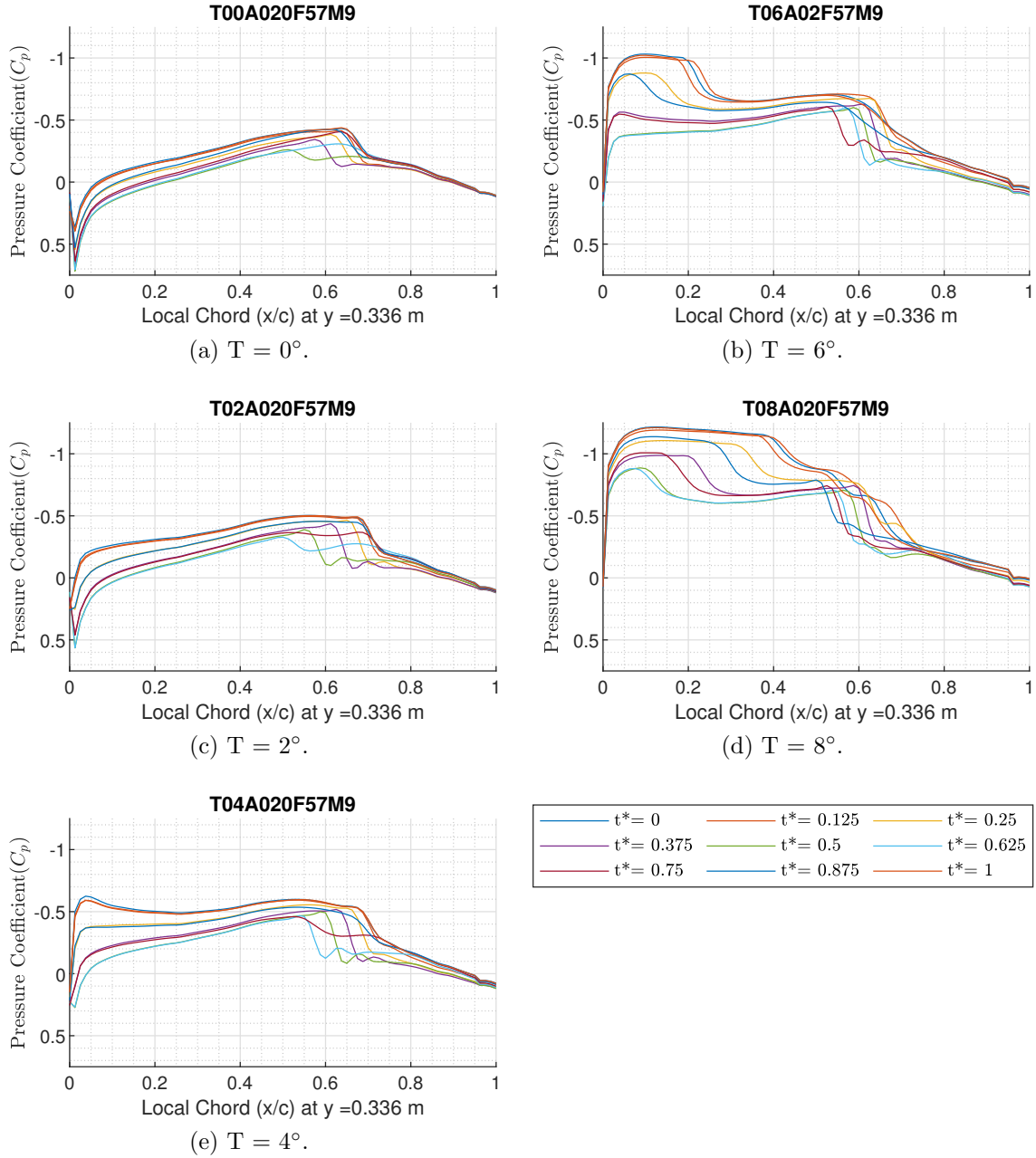


Figure 4.17: Trim Sweep Pressure Coefficient vs Chord Location at Station 3. $M = 0.9$, $A = 2^\circ$.

the aft shock in these flight conditions, likely due to the distance between the shocks. At 6° , the aft shock appears to remain intact throughout the full pitching cycle. It should also be noted that subsidiary shocks are absent in this analysis, which is likely a result of insufficient amplitude to complicate the flow around the shock formation.

At trim AoA increases to 8° , the two main shocks move towards each other with more motion seen from the front, weaker shock. Station 3 shows complex shock interaction as the front shock migrates very close to the aft shock. It is possible that the close vicinity of these shocks create a lambda shock formation which would likely result in flow separation. The motion of the front shock is considerable, about 30% of the chord. The motion of the aft shocks appears to decrease as a result of its proximity to the front shock. This decrease can be seen in Table 4.4. Station 2 does not show the shock in close proximity like Station 3, but does show some complex pressure changes on the trailing edge of the shock, possibly early stages of subsidiary shock development.

Figures 4.18 and 4.19 show contour plots for Stations 2 and 3 respectively that match the pressure distributions in Figures 4.16 and 4.17. The formation of the swept shock just aft of the darker blue sections first appear at $T = 6^\circ$ ($\text{AoA} = 8^\circ$) and become larger as trim AoA increases. What becomes very evident in these plots is the asymmetric nature, particularly of the aft shock. The main shock's location is right at the dotted line which shows where the flow decreases to subsonic speeds. These plots show the shock continuing to march forward past fully pitch down, $t^* = 0.5$, until about $t^* = 0.6$ where the shock rapidly jumps aft. The point where the shock is strongest slowly moves to later in the cycle as the trim AoA was increased. This drastic change was muted at Station 2 with the development of the swept shock. At Station 3, the contour plots clearly show the influence of the front shock on the aft shock, where the flow moves in and out of the supersonic region around fully pitch down. This development is possibly explained by similarity to the subsidiary shocks, where the proximity of the aft shock to the front shock results in a loss of strength and motion of the aft shock.

In the moment coefficient plots in Figure 4.20, cases with $T = 6^\circ$ and 8° at Stations 2 and 3 are shown. A twist can be seen to develop around the pitched down portion of the cycle as trim is increased from 6° to 8° . This correlates to the large negative pressure towards the front of the wing and the large motions of the

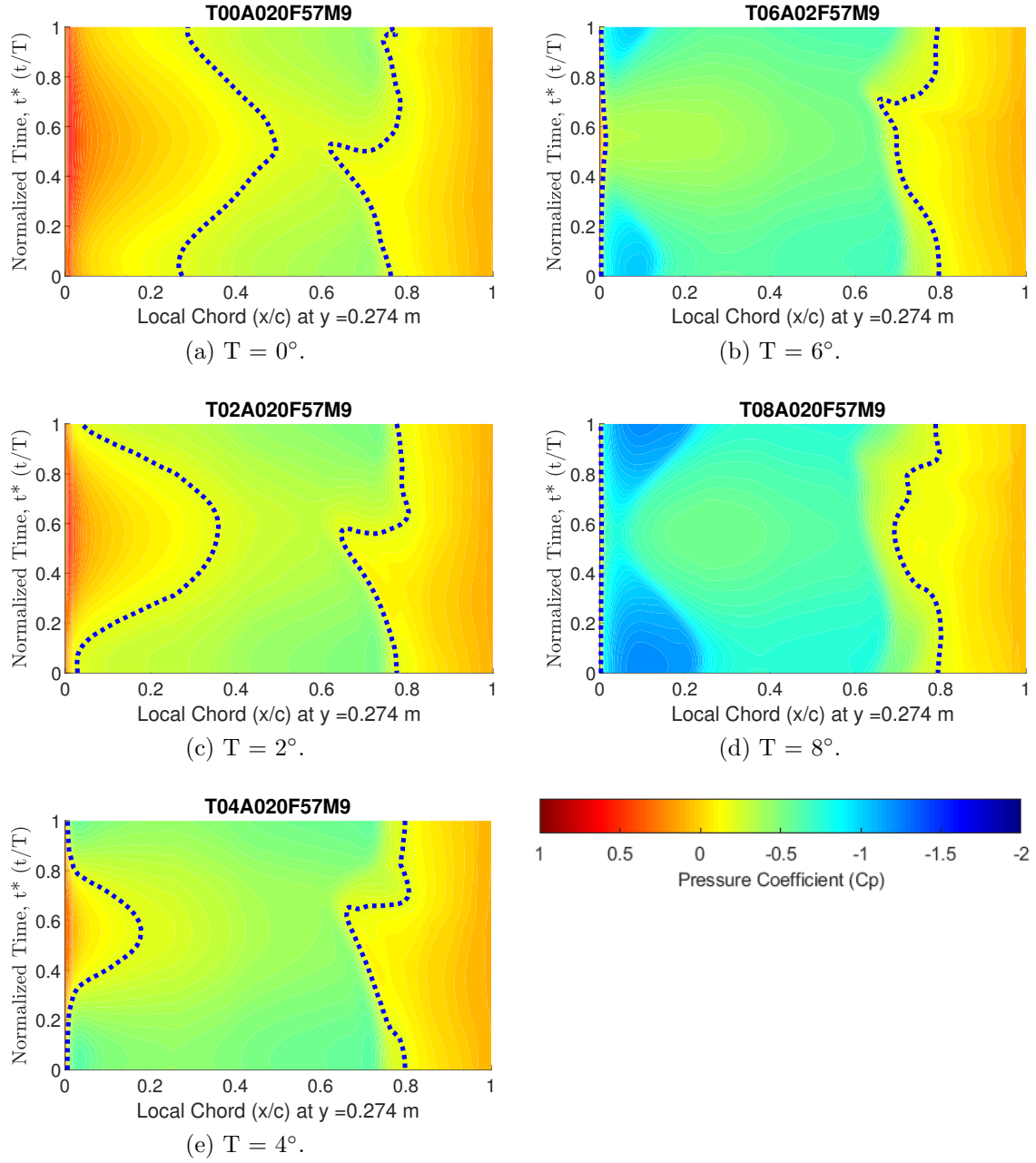


Figure 4.18: Trim Sweep Pressure Coefficient vs Chord Location Contour Plot at Station 2. $M = 0.9$, $A = 2^\circ$.

swept shock, demonstrating the influence of shock migration on the pitching moment. Because the wing does not pitch down past -2° for any of these cases, the moment never reaches positive values throughout the oscillation.

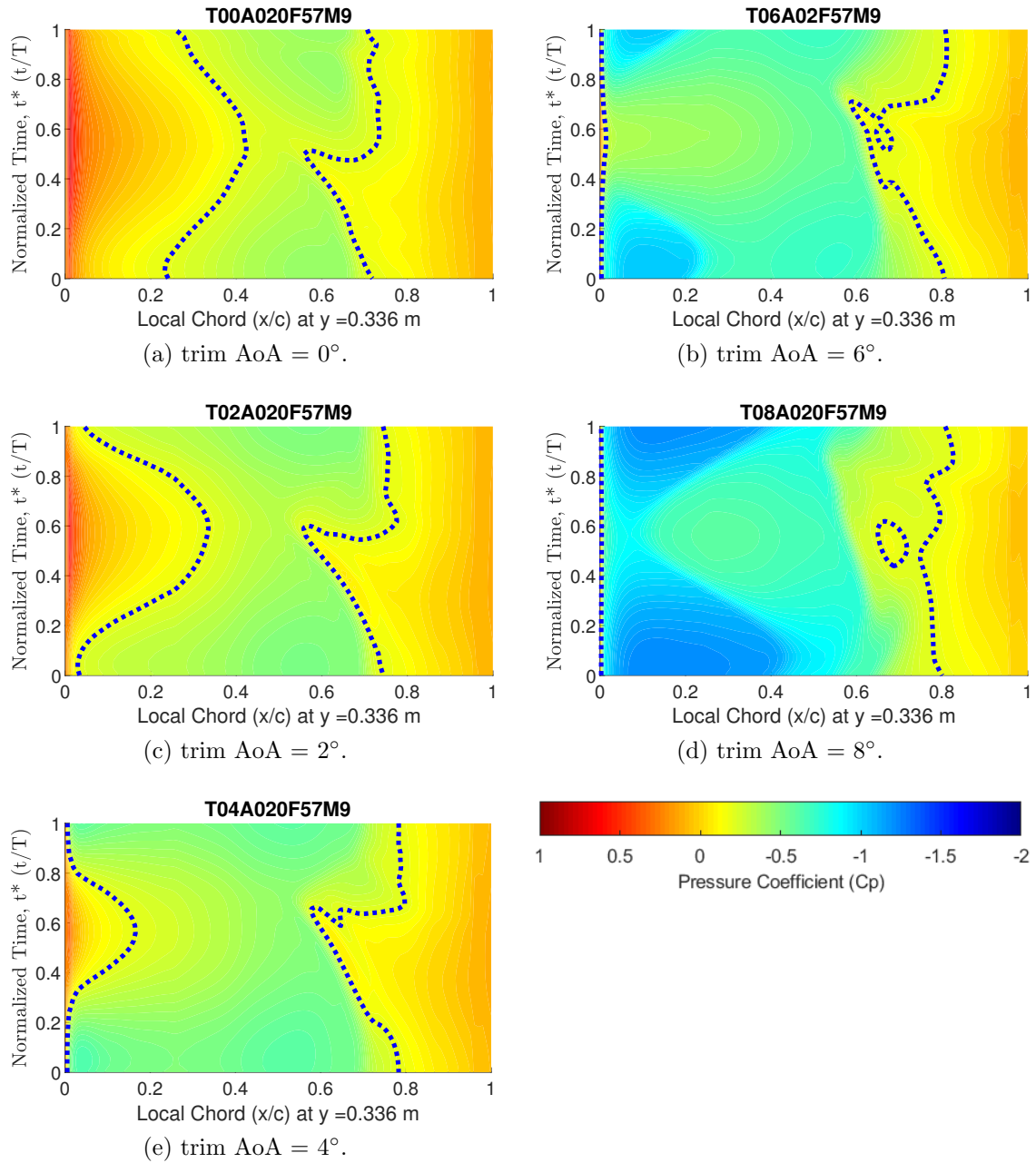


Figure 4.19: Trim Sweep Pressure Coefficient vs Chord Location Contour Plot at Station 3. $M = 0.9$, $A = 2^\circ$.

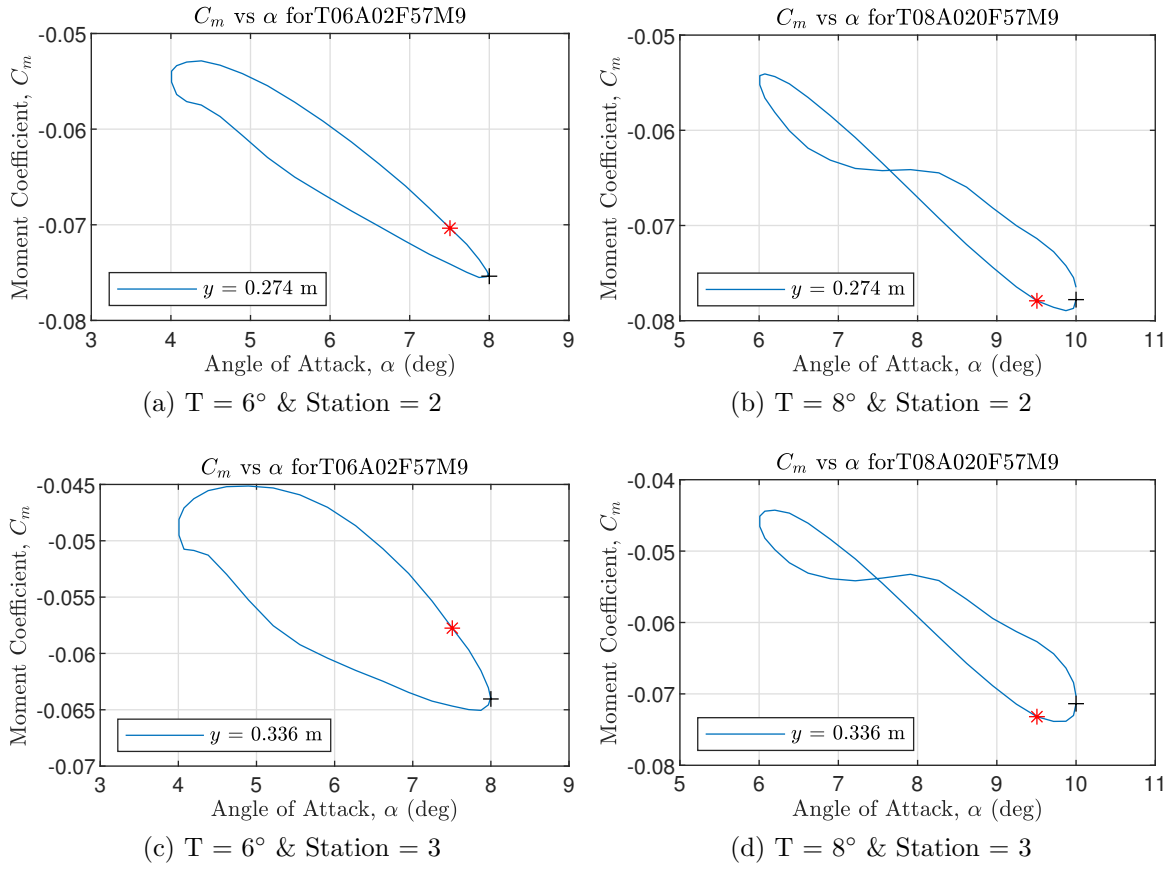


Figure 4.20: Moment Coefficient vs AoA for Increasing Trim AoA. $M = 0.9$, $A = 2^\circ$.

4.9 Amplitude Sweeps

Sweep of increasing oscillation amplitudes were run with $M = 0.9$ and $T = 0^\circ$ and 4° to better understand amplitudes' influence on shock formation and possible separation. In this sweep, amplitude was increased from 0.5° to 12° . For all cases in this analysis, a main aft shock is present. At low AoA, the point of minimum pressure is just in front of the shock. Just as with the trim sweep analysis, when the AoA exceeds a threshold, the minimum pressure point shifts toward the leading edge. That threshold is between 4.5° and 6° which matches the threshold seen in the trim sweep analysis. Figure 4.21 shows this transition for the two different amplitude sweeps.

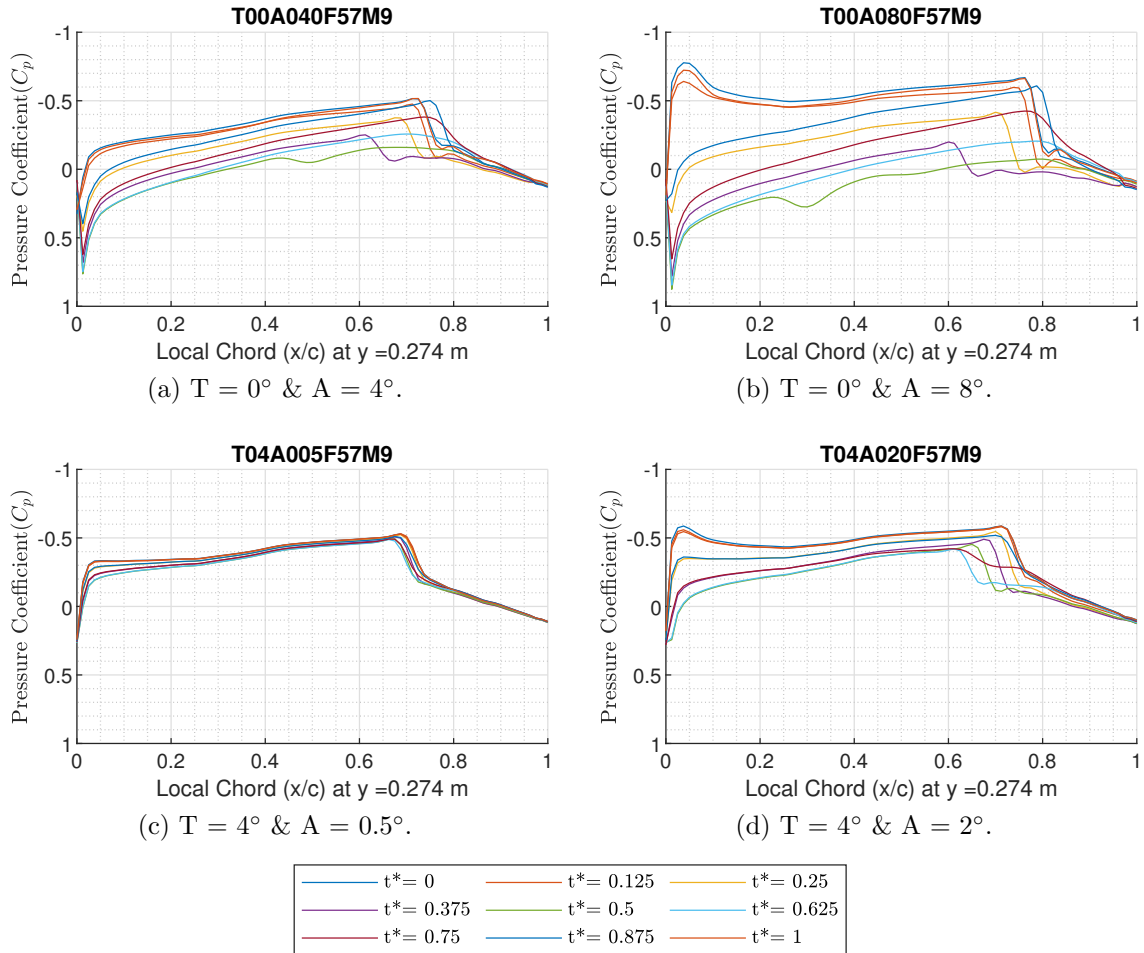


Figure 4.21: Pressure Coefficient vs Chord Location at Station 2. $M = 0.9$. A spike in negative pressure at leading edge develops as AoA increases.

As the AoA is increased further by trim or amplitude, a swept shock develops. Figure 4.22 shows the swept shock at Stations 1-4 for a trim AoA = 0° with an amplitude of 12°. The aft-ward sweep of the forward shock from wing root to wing tip supports the vortex theory presented earlier. As AoA is increased as shown in Figure 4.23 for $T = 4^\circ$, the front shock moves aft until the AoA is sufficient to cause interaction with the main aft shock. When trim AoA is 4°, shock interaction begins at Station 4 at $A = 8^\circ$ and moves inward to Station 3 as amplitude is increase to $A = 10^\circ$. For the amplitude sweep with $T = 0^\circ$, this interaction only appears at Station 4 with an amplitude of 12°.

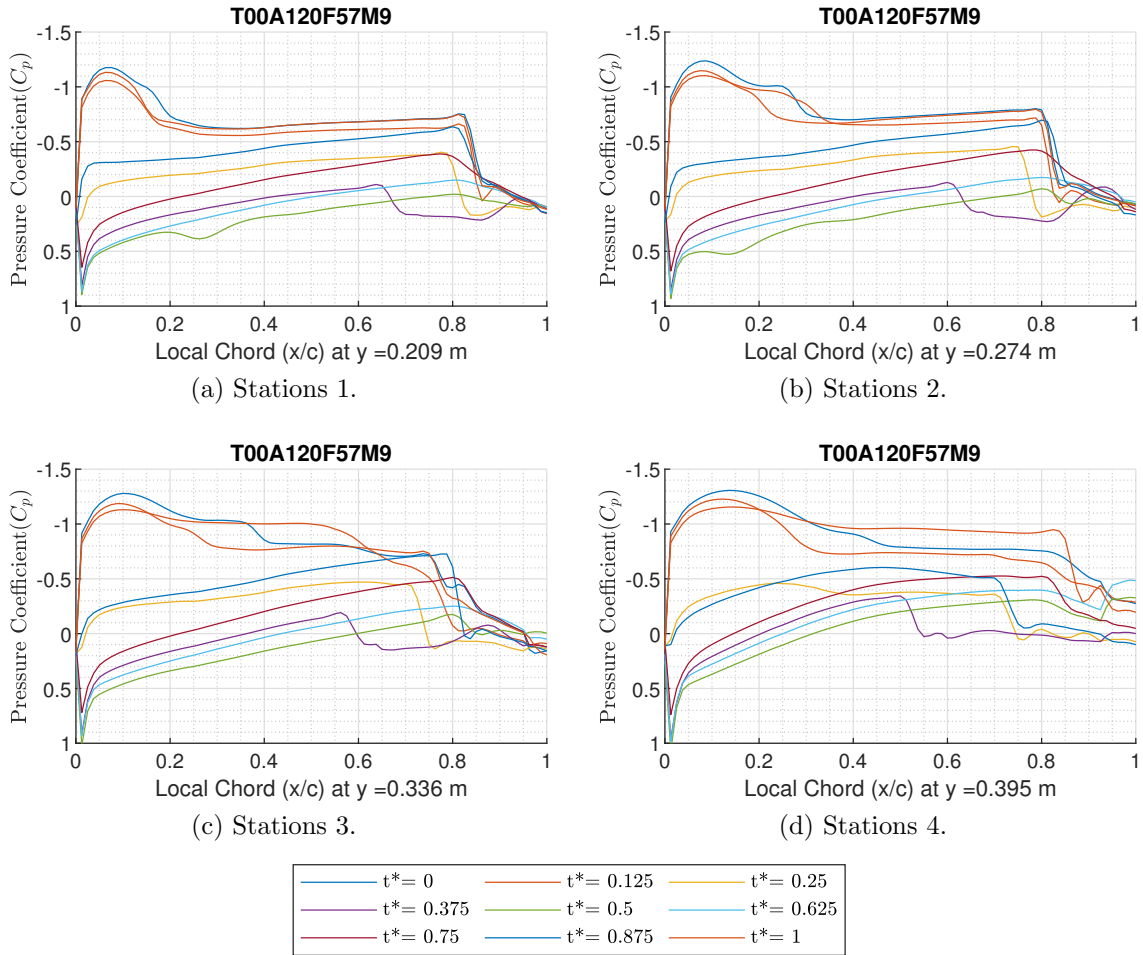


Figure 4.22: Pressure Distribution at Stations 1-4. $M = 0.9$, $T = 0^\circ$ & $A = 12^\circ$.

Another important observation, shown in Table 4.5, is the increase in shock migration of the main aft shock. An increase in shock movement from 5% of the chord to about 25% of the chord was observed for both trim AoAs at Stations 2 and 3. The forward migration is accompanied by a weakening of the shock as it dissolves into compression waves. This can be seen in the pressure contour plots in Figure 4.24 where the supersonic region breaks down at larger amplitudes which have negative AoAs when the wing is pitched down. At Station 3 ($y = 0.336$) for $T = 4^\circ$ and $A = 12^\circ$, shown in the bottom plot of Figure 4.23, the shock movement increased substantially to 43% of the chord. The main aft shock migrates aft-ward between $t^* = 0$ and $t^* = 0.2$. This downstream motion of the shock is not seen in the other cases. One viable theory that explains this movement is the influence of the vortex flow/ swept shock on the main shock. An increase in upstream motion of the main shock was also observed as the wing pitched down. This additional movement was expected because the higher amplitude drove a decrease in minimum AoA.

Like in the trim sweep analysis, subsidiary shocks were also observed in the amplitude sweep analysis. Figures 4.25 and 4.26 show this development at Station 2. The negative pressure was just sufficient enough in the $T = 0^\circ$ amplitude sweep for a subsidiary shock to form with $A = 12^\circ$ as shown in the contour plot on the right of Figure 4.25, but it did not last long enough to be captured by the pressure distribution plot on the left. Subsidiary shocks occurred for the $T = 4^\circ$ amplitude sweep when the amplitude reached 8° beginning in at $t^* = 0.5$ in the cycle. The subsidiary shocks strengthened with an increase in amplitude until the interaction of the front and aft shocks occurred. When the main shock moved aft at Station 3, the subsidiary shock disappeared. Since this shock movement and absence of a subsidiary shock closely resembles the fully inviscid case as already discussed, it is possible that the BLC solver was unable to more accurately predict pressure changes in this complex environment with the suggested solver parameters that were used.

Similar to the trim sweep, a hysteresis can be seen as asymmetric patterns in the contour plots in Figures 4.23, 4.24, 4.25, and 4.26. The motion of the front edge of

Table 4.5: Amplitude sweeps with Mach number = 0.9 & frequency = 5.7 Hz.

Station	Trim AoA	Amplitude	Shock Movement	C_{L_α}	C_{L_0}
2	0°	0.5°	0.05	0.085	-0.014
		2°	0.14	0.085	-0.017
		4°	0.14	0.085	-0.029
		8°	0.18	0.084	-0.044
		10°	0.20	0.083	-0.047
		12°	0.20	0.081	-0.052
	4°	0.5°	0.12	0.081	-0.005
		2°	0.10	0.080	-0.002
		4°	0.23	0.081	0.000
		8°	0.21	0.081	-0.005
		10°	0.25	0.082	-0.037
		12°	0.26	0.082	-0.078
3	0°	0.5°	0.05	0.089	-0.032
		2°	0.13	0.088	-0.037
		4°	0.15	0.088	-0.052
		8°	0.24	0.086	-0.067
		10°	0.25	0.086	-0.077
		12°	0.25	0.082	-0.089
	4°	0.5°	0.02	0.084	-0.023
		2°	0.14	0.084	-0.020
		4°	0.25	0.085	-0.014
		8°	0.26	0.085	-0.016
		10°	0.25	0.086	-0.049
		12°	0.43	0.086	-0.095

the supersonic region can be seen to follow a linear line of travel as the wing pitches. Furthermore, the slope of this line ($\frac{\Delta t^*}{\Delta x/c}$) is different between pitch up and pitch down. As amplitude is increased, these slopes decrease. As the wing pitches down, the shock at the back edge of the supersonic region moves forward in an exponential style curve until it dissolves to fully subsonic flow over the wing. The coloring of the contour plots show a continued forward motion of compression waves which continue to move forward as the wing continues its cycle. When the wing pitches back up, the shock does not reappear at the same AoA or chord location where it disappeared. For the general trends observed, the shock's reappearance was delayed and further aft on the wing.

Since the frequency is held constant between cases but the rotation angle increases, the angular velocity between cases must also increase. Because of this, the overlapping AoAs between two cases with different amplitudes will not look the same. this will be further demonstrated in Section 4.11. As the amplitude increases, the appearance of subsidiary shocks also increases. The middle contour plot in Figure 4.26 shows a supersonic region appearing at the trailing edge as the wing begins its pitch up motion. This shock appears to be similar to the subsidiary shocks in other cases, except that there is no supersonic region in front of it, and therefore no main shock until later in the cycle. An overall observation of these cases shows vastly different subsidiary shock formations between pitch up and pitch down. This demonstrates vast differences in shock formation due to the motion of the wing.

Just like in the trim sweep analysis, some cases show a clockwise “twist” in the moment vs AoA plots. Table 4.6 shows which cases that have a twist, whether the twists are near the pitch up or pitch down extremes, which spanwise stations saw the twist, and the AoA where the moment curve intersected itself. Where twists are present, the corresponding cells are colored green.

Table 4.6: Amplitude sweep clockwise (CW) moment vs AoA curves. Mach number = 0.9 & frequency = 5.7 Hz. Green indicates a CW twist, and AoA values show the moment curve intersection point.

Trim	AoA	Amplitude	CW at pitch up				CW at pitch down			
			1	2	3	4	1	2	3	4
0°	0.5°		No	No	No	No	No	No	No	No
	2°		No	No	No	No	No	No	No	No
	4°		No	No	No	No	No	No	No	No
	8°		No	No	No	No	No	No	No	-4°
	10°		No	No	No	+8.5°	No	No	-7.75°	-3°
	12°		No	No	No	+8°	No	-9.25°	-6.5°	-1.5°
4°	0.5°		No	No	No	No	No	No	No	No
	2°		No	No	No	No	No	No	No	No
	4°		No	No	No	No	No	No	No	No
	8°		No	No	No	+5.5°	No	No	No	No
	10°		No	No	+9.25°	+5°	No	No	No	No
	12°		+15°	+11.5°	+8°	+4.5°	No	No	No	-4.25°

A few trends were seen from this table. As amplitude increases, the first twists are seen at Station 4 for both amplitude sweeps with $T = 0^\circ$ and 4° . When amplitude is increased further, the twist moves inward and begins showing at the other stations in descending order. The clockwise rotation of the curve also takes over a larger portion of the curve as can be seen by the curve intersection AoA converging towards the trim AoA as amplitude is increased. For the $T = 0^\circ$ amplitude sweep, the twist develops in the pitch down position before the pitch up. This shows an asymmetry which could in part be explained by the cambered wing being asymmetrical. For the $T = 4^\circ$ amplitude sweep, the pitch up extreme develops a twist at a lower amplitude than the pitch down extreme. This contrasts the results in the $T = 0^\circ$ amplitude sweep. From this table, it appears that the pitch down twist at Station 4 developed at an AoA between 4° and 4.25° . A similar observation could not be made for the development of the pitch up twist, though that development may correlate to the aft-ward migration of the swept shocks that are present only at higher AoAs.

In the $T = 0^\circ$ amplitude sweep, the first positive moments appear at Station 4 when $A = 8^\circ$, and are seen at all stations when $A = 10^\circ$ and 12° . For the $T = 4^\circ$ amplitude sweep, the positive moment does not appear until $A = 10^\circ$ and is only seen at Stations 1 and 2. When amplitude increased to 12° , all stations showed positive moments for part of the cycle.

As seen in Table 4.5, the lift curve slope and lift at 0° AoA are very consistent between all cases in both amplitude sweeps. The differences seen are within calculation errors of the flat plate assumptions used to calculate lift from the pressure data. The asymmetrical aspect of the lift vs AoA curve increases as amplitude is increased. This is likely influenced by the strength and migration of the shocks throughout the cycle as seen in the contour plots.

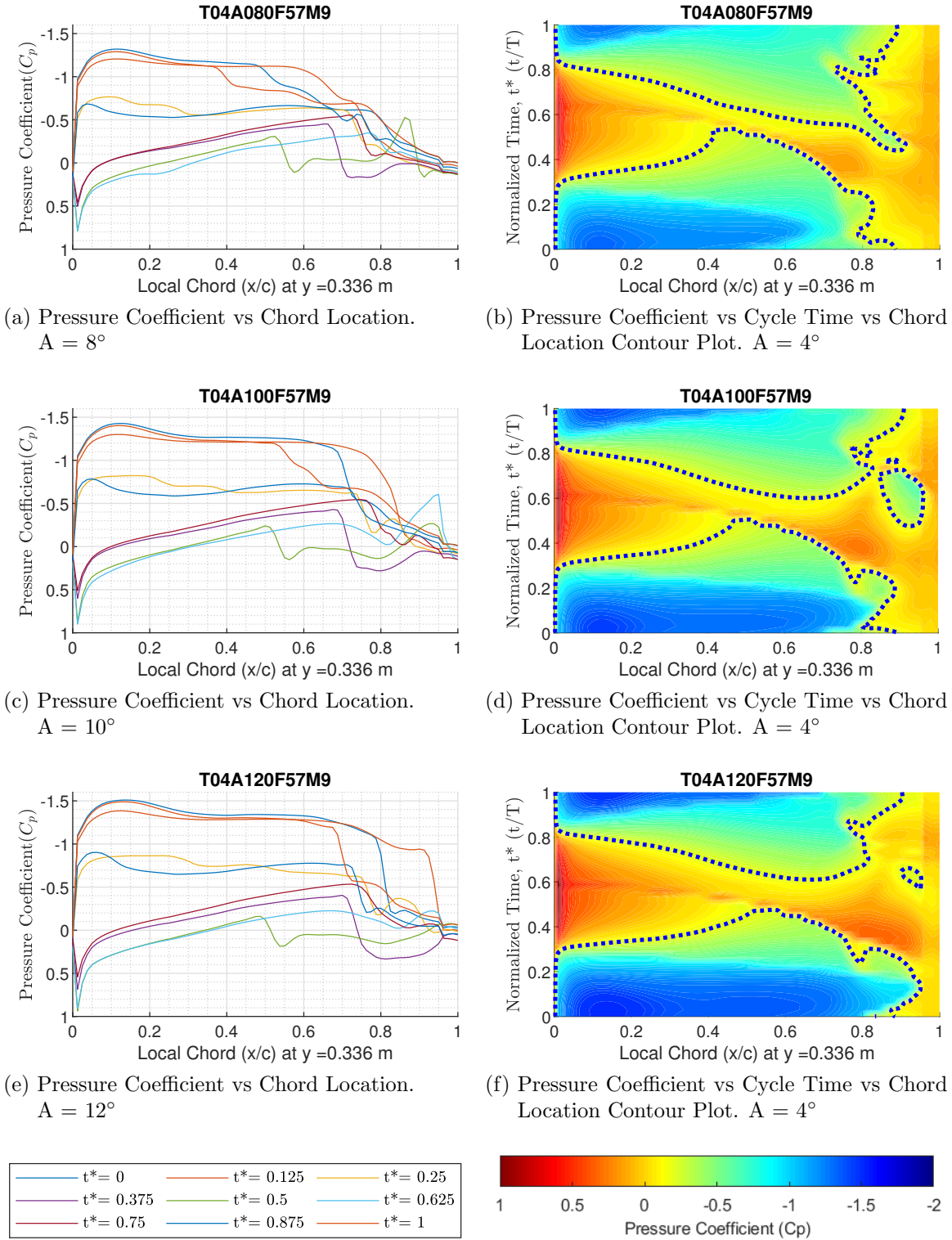


Figure 4.23: Amplitude Sweep Pressure Distributions at Station 3. $M = 0.9$ & $T = 4^\circ$.

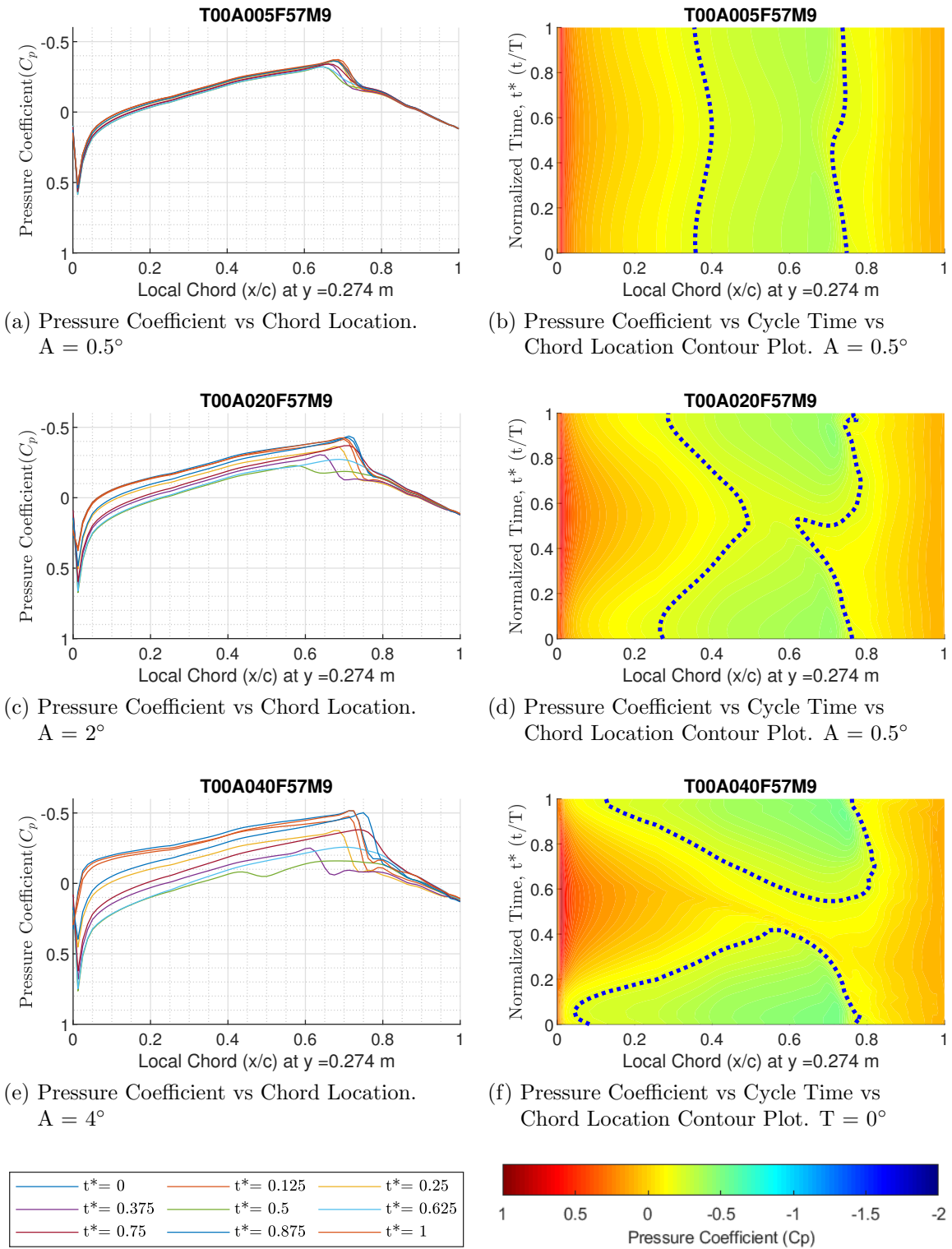
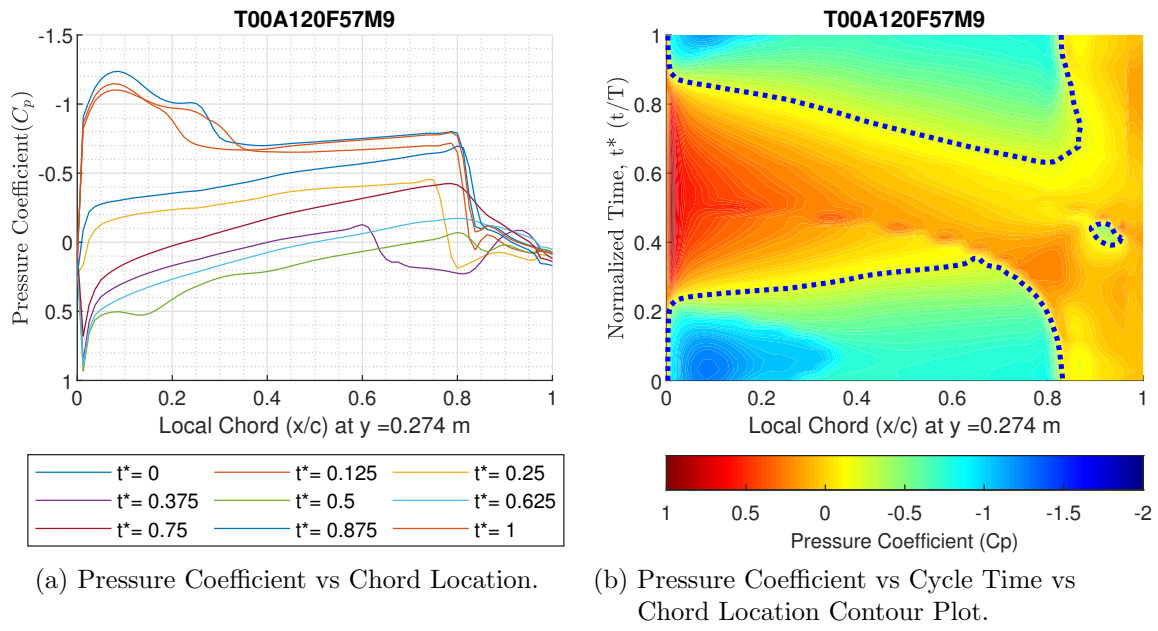


Figure 4.24: Amplitude Sweep Pressure Distributions at Station 2. $M = 0.9$ & $T = 0^\circ$.



(a) Pressure Coefficient vs Chord Location. (b) Pressure Coefficient vs Cycle Time vs Chord Location Contour Plot.

Figure 4.25: Pressure Distributions at Station 2. $M = 0.9$, $T = 0^\circ$, & $A = 12^\circ$.

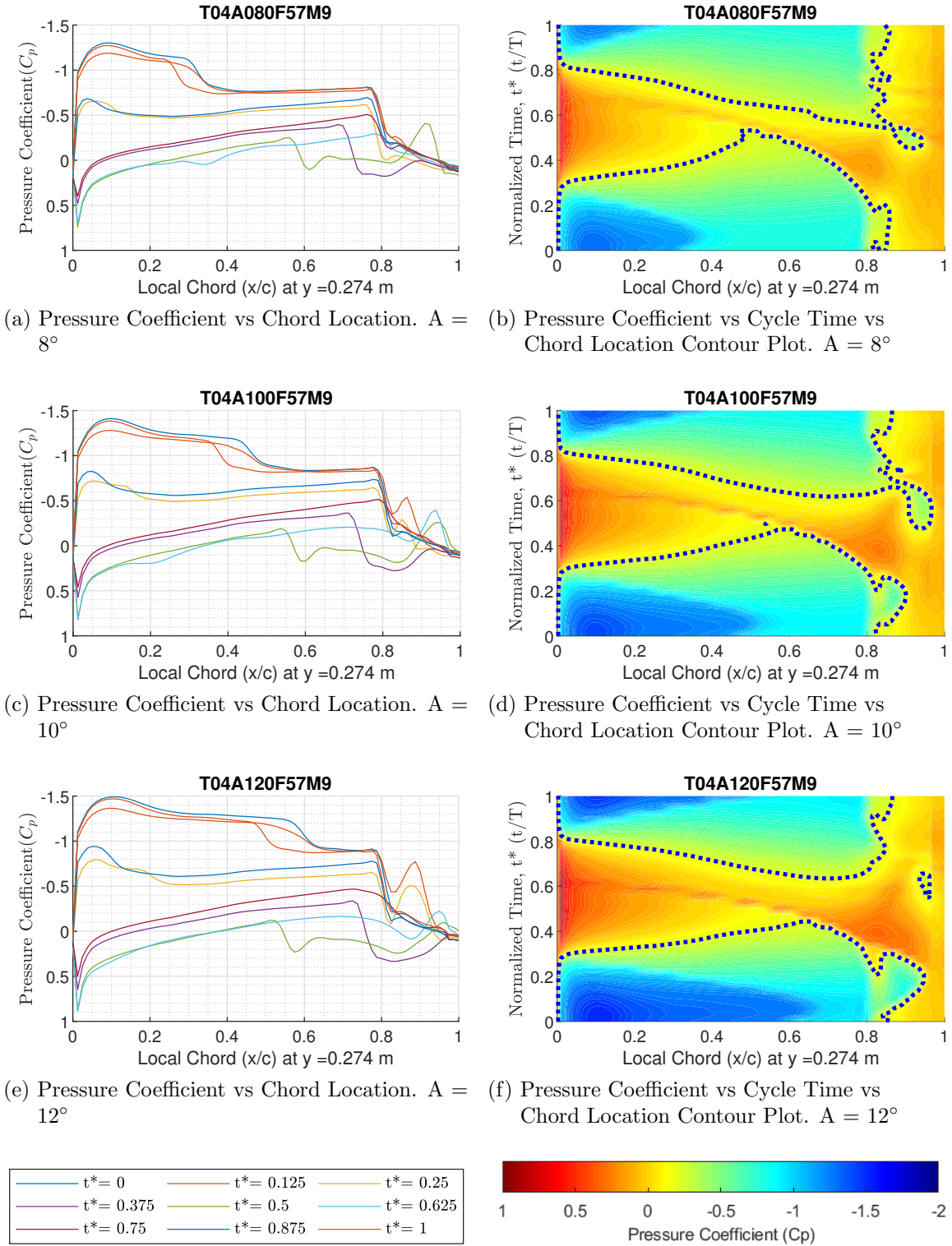


Figure 4.26: Amplitude Sweep Pressure Distributions at Station 2. $M = 0.9$ & $T = 4^\circ$.

4.10 Mach Number Sweeps

Two sweeps of increasing Mach number were run at $T = 0^\circ$ with $A = 2^\circ$ and 12° to visualize shock development and migration as a result of Mach number. In these sweeps, Mach number was increased from 0.6° to 0.95° . Table 4.7 shows all cases run in the Mach number sweep analysis and which cases observed shocks. Also seen in the table is the slope of the shock, shock movement, lift curve slope, and lift at 0° AoA for Stations 2 and 3 just like in the trim and amplitude sweep tables.

Table 4.7: Mach number sweep with trim AoA = 2° & frequency = 5.7 Hz.

Station	Amplitude	Mach number	$\frac{\Delta C_p}{\Delta x/c}$	Shock Movement	C_{l_α}	C_{l_0}
2	2°	0.6	No Shock	No Shock	0.065	0.022
		0.75	No Shock	No Shock	0.070	0.012
		0.85	No Shock	No Shock	0.077	-0.003
		0.90	-23.98	0.14	0.085	-0.017
		0.95	-63.23	0.02	0.085	-0.036
	12°	0.6	-91.73	0.00	0.067	0.002
		0.75	-71.94	0.04	0.073	-0.006
		0.85	-42.68	0.13	0.077	-0.031
		0.90	-65.63	0.20	0.081	-0.052
		0.95	-91.58	0.16	0.082	-0.083
3	2°	0.6	No Shock	No Shock	0.067	0.069
		0.75	No Shock	No Shock	0.072	-0.005
		0.85	No Shock	No Shock	0.080	-0.022
		0.90	-13.46	0.13	0.088	-0.037
		0.95	-59.92	0.04	0.088	-0.052
	12°	0.6	-79.86	0.00	0.005	-0.020
		0.75	-59.66	0.06	0.075	-0.022
		0.85	-46.47	0.11	0.081	-0.033
		0.90	-74.78	0.23	0.082	-0.089
		0.95	-118.24	0.14	0.086	-0.113

For the Mach number sweep with $A = 2^\circ$, the flow reaches supersonic conditions at 0.85 Mach number as the pressure exceeds the critical pressure around $x/c = 0.5$, but the pressure gradient is not strong enough to create a shock. As Mach number increased to 0.9, the pressure further decreased and a shock formed for the pitched up portion of the cycle, but dissolved into compression waves as the wing pitched down. As Mach number increased from 0.9 to 0.95, the slope of the shock increased and the

shock remained for the full cycle. This resulted in reduced shock migration. These developments are shown in Figure 4.27 for Station 2.

For the 12° amplitude Mach number sweep, the flow reached the critical pressure at 0.6 Mach number, and resulted in a shock wave for a short amount of time at pitch up. This shock, however, was the swept shock seen in the trim and amplitude sweep analyses. As Mach increased, this swept shock moved aft, but continued to disappear as a result of the large oscillation amplitude and zero trim AoA. The first main aft shock was seen to develop at 0.85 Mach number as shown in Figure 4.28 for Station 2. With its appearance, the swept shock weakened as the negative pressure region between the two shocks dropped. The aft shock continued to increase in strength and movement with an increase in Mach number up to 0.9. As the shock strengthened like in the lower amplitude Mach number sweep, the shock movement began to decrease as a result of the shock not dissolving for as much of the oscillation. At $t^* = 0.375$, the shock rapidly moved forward as it dissolved to compression waves. At this point in the cycle, the flow was no longer supersonic except for a small spike near the trailing edge where the flow expands then quickly compresses. This can be seen in the bottom contour plot in Figure 4.28. Between the compression zone and this supersonic region, the flow has positive pressure. It is possible that this region had some local separation.

The $A = 2^\circ$ Mach number sweep did not develop a twist in its C_m vs α curve for any case, however the higher amplitude Mach number sweep did see twist development. Figure 4.29 shows the development of twist at Station 2 and 3 for the Mach number sweep with an $A = 12^\circ$. The C_m twist first appears at Station 4 at 0.75 Mach number, then Station 3 at 0.85 Mach number, Station 2 at 0.9 Mach number, and Station 1 at 0.95 Mach number. This follows similar trends seen with an increase in trim or amplitude. Like the twist, the $A = 2^\circ$ Mach number sweep did not have a positive moment for part of the cycle, but the $A = 12^\circ$ did. When $M = 0.75$ and 0.85, the positive moment was present at positive AoA. As Mach number increased, the positive moment only occupied negative AoAs.

As seen with an increase in trim or amplitude, an increase in Mach number increases the lift curve slope of the oscillating wing and oddifies the lift from the linear trend of a steady, static wing. The oval shaped curves of the lift vs AoA of the oscillating wing can be seen in Figure 4.30. The curves appear to be largely symmetrical in the $A = 2^\circ$ Mach number sweep, but start developing a noticeable asymmetric curvature as Mach number increased in the $A = 12^\circ$ Mach number sweep.

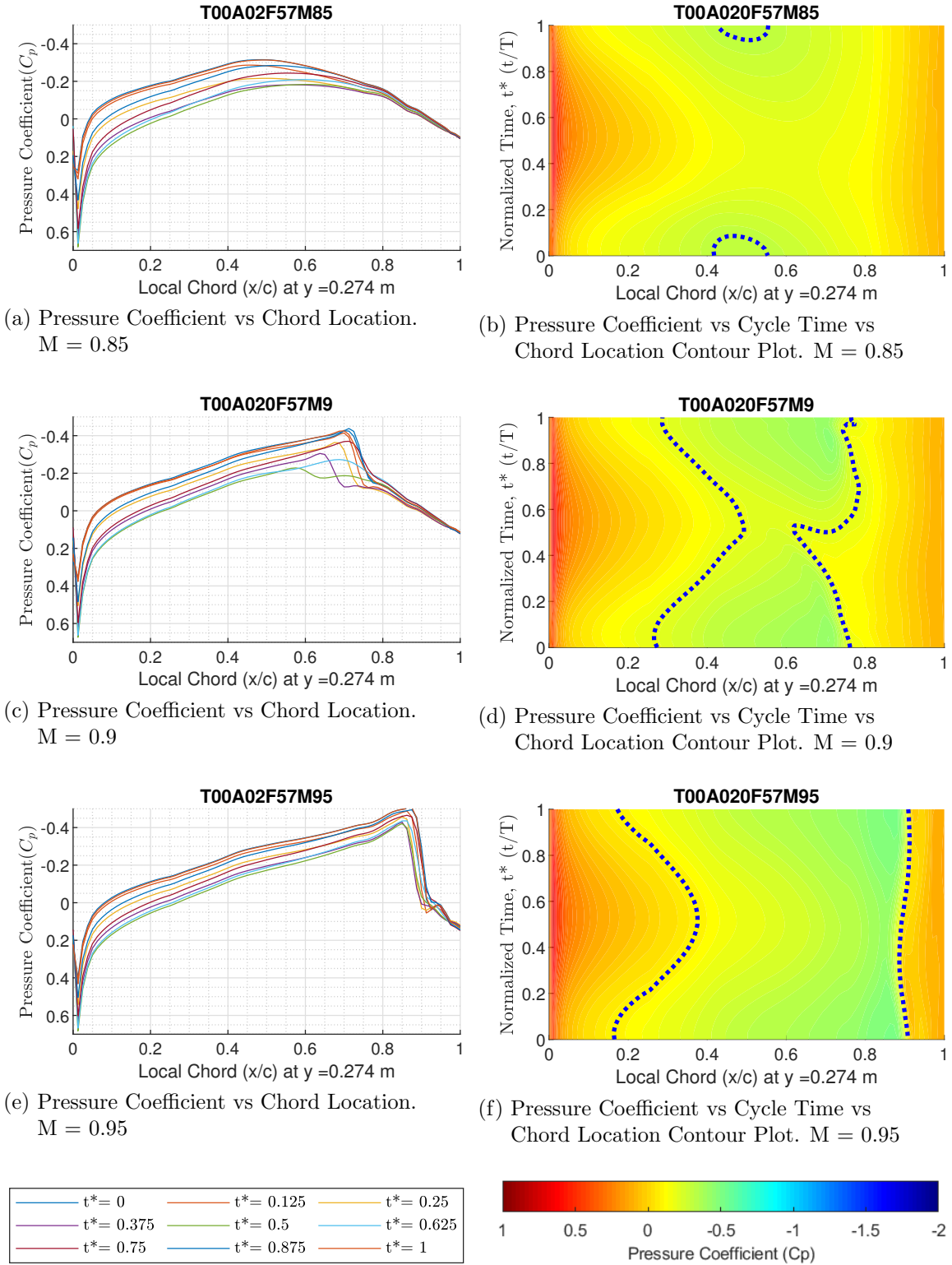


Figure 4.27: Mach Number Sweep Pressure Distributions at Station 2. $T = 0^\circ$ & $A = 2^\circ$.

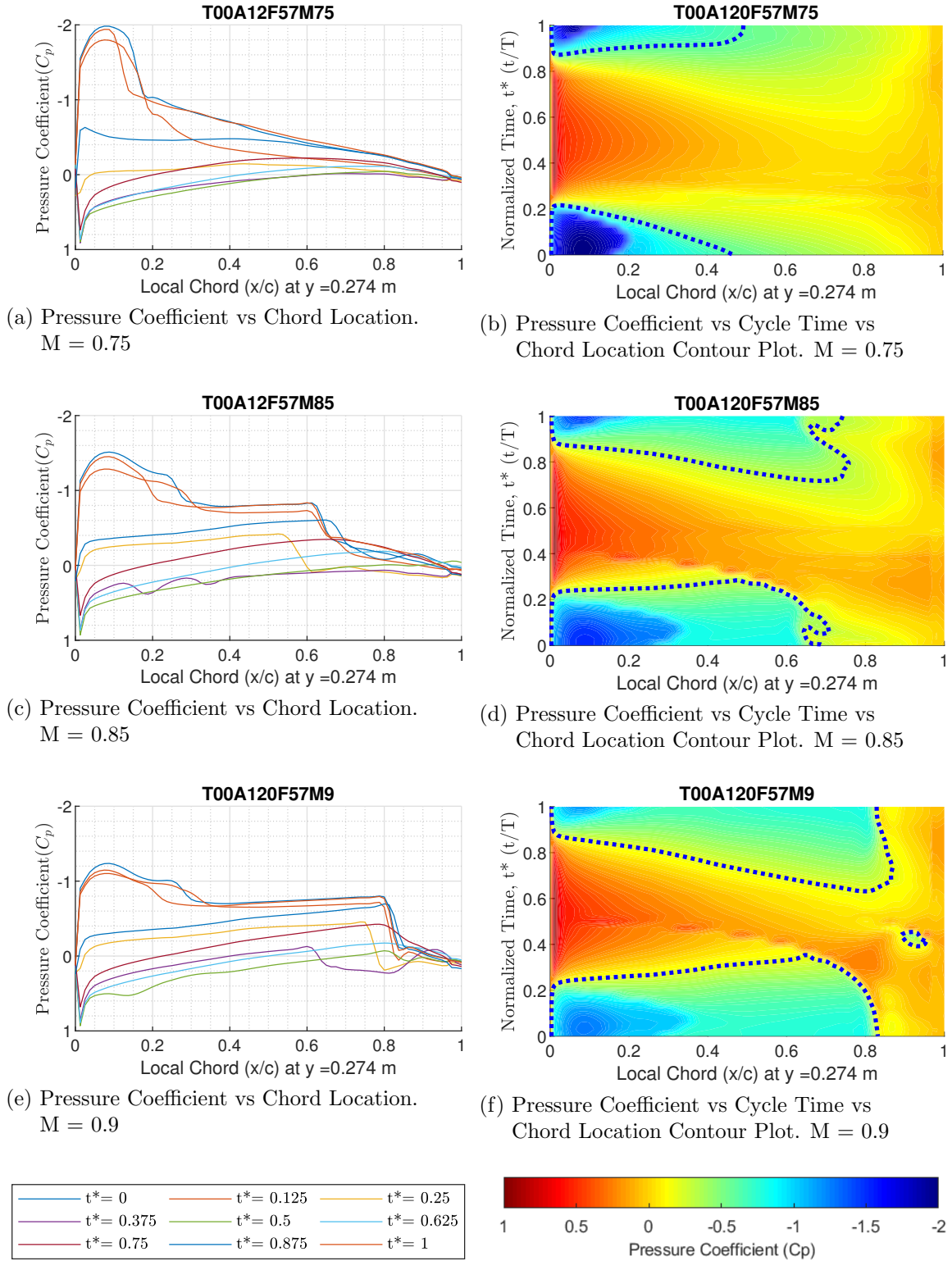


Figure 4.28: Mach Number Sweep Pressure Distributions at Station 2..T = 0° & A = 12°.

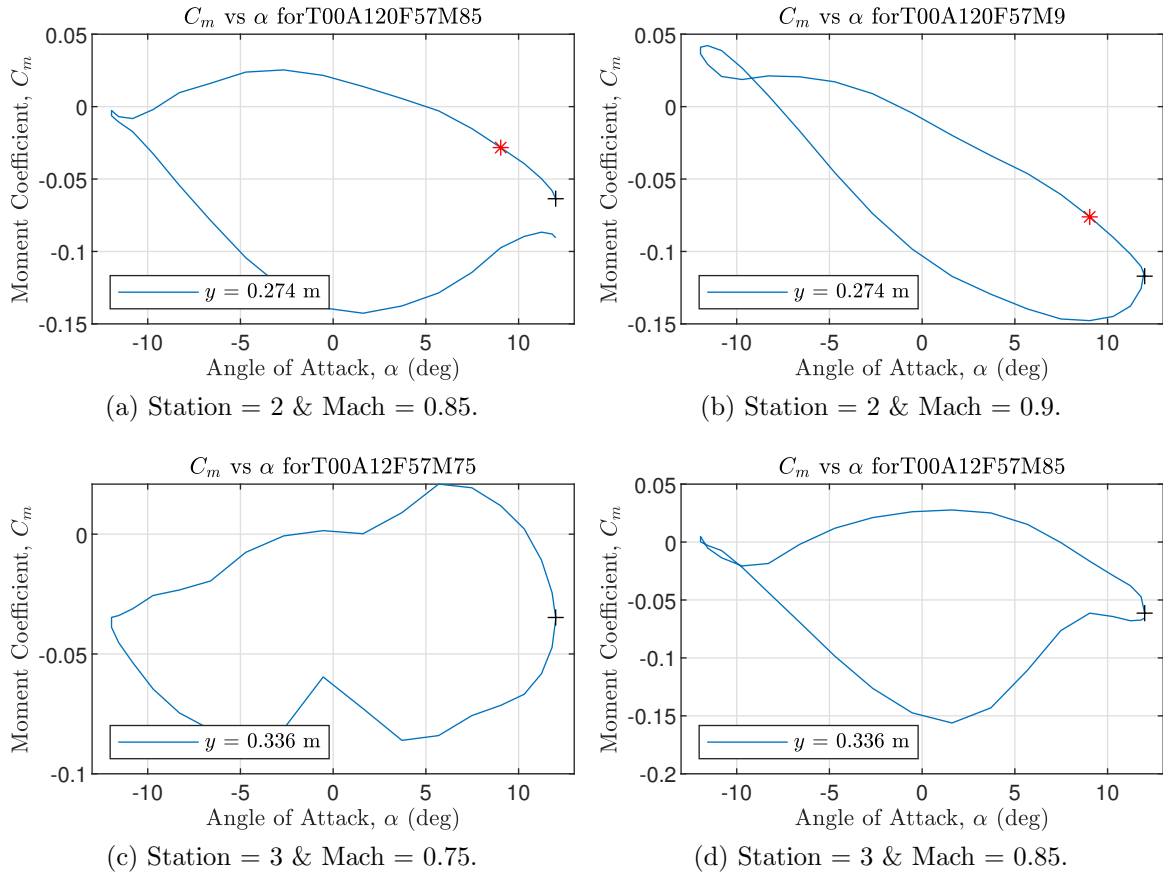
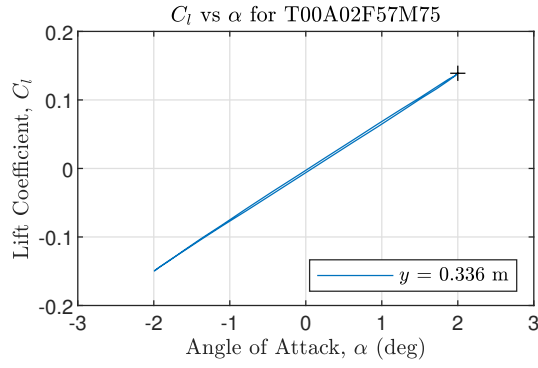
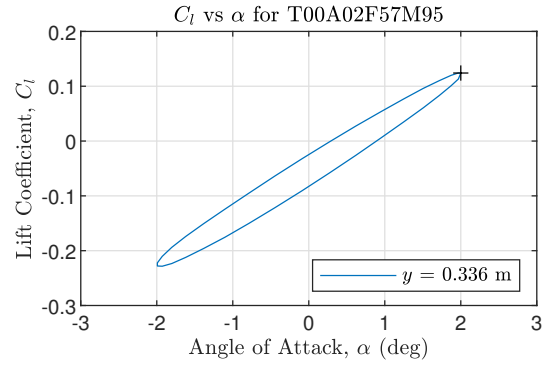


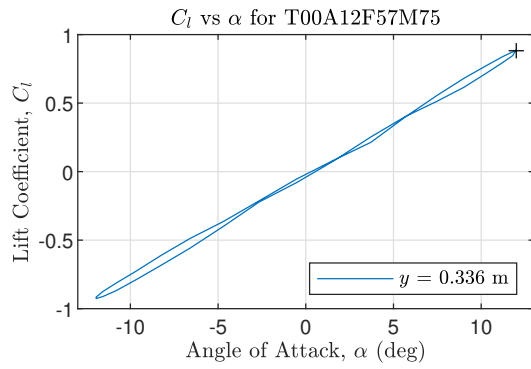
Figure 4.29: Mach Number Sweep Moment Coefficient vs AoA. $T = 0^\circ$ & $A = 12^\circ$.



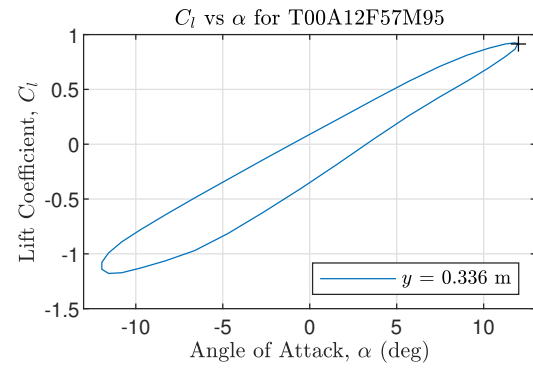
(a) Amplitude = 2° , & Mach = 0.75.



(b) Amplitude = 2° , & Mach = 0.95.



(c) Amplitude = 12° , & Mach = 0.75.



(d) Amplitude = 12° , & Mach = 0.95.

Figure 4.30: Mach Number Sweep Moment Coefficient vs AoA at Station 3. $T = 0^\circ$.

4.11 Maximum and Minimum AoA Comparisons

The final analysis discussed in this thesis compares cases with trim AoA and amplitude which result in the same AoA either at fully pitched up or fully pitched down. Pitch up is at $t^* = 0$ and $t^* = 1$, where the AoA is at its max, equal to $T + A$. $t^* = 1$ was chosen to compare between cases. Figure 4.31 shows pressure distributions at Station 2 and Table 4.8 shows moment and lift coefficients calculated for Stations 2 and 3 at pitch up ($t^* = 1$). In each plot in this figure, the higher trim AoA cases have a more negative leading edge pressure. Cases with higher amplitudes show small pressure oscillation not seen in the lower amplitude cases. Figures 4.31a and 4.31d show shocks with very similar strengths and chord locations. This is not the case for Figures 4.31b and 4.31c where the higher trim, lower amplitude cases show a gradual negative pressure gradient. The significant impact of pressure contributions due to the transient motion of the oscillating wing is demonstrated here.

Moment and lift coefficients look very similar across Stations 2 and 3 for each case, though a few outliers were observed. Cases $T=6^\circ, A=2^\circ$ and $T=8^\circ, A=2^\circ$ deviate from the pattern of moment decreasing as the lift increases. These deviations correlate with the differences in pressure around the shock seen in Figure 4.31.

Table 4.8: A comparison of pitch up pressure distributions ($t^* = 1$) for cases with the same AoA. Mach number = 0.9 & frequency = 5.7 Hz.

AoA	Trim AoA	Amplitude	Station 2		Station 3	
			C_m	C_l	C_m	C_l
4°	0°	4°	-0.07	0.31	-0.07	0.30
	2°	2°	-0.07	0.31	-0.07	0.31
8°	0°	8°	-0.09	0.62	-0.08	0.62
	4°	4°	-0.09	0.65	-0.08	0.66
	6°	2°	-0.08	0.65	-0.06	0.67
10°	0°	10°	-0.11	0.78	-0.08	0.78
	8°	2°	-0.08	0.82	-0.07	0.86
12°	0°	12°	-0.12	0.92	-0.08	0.90
	4°	8°	-0.11	0.96	-0.11	1.01

The same comparison at $t^* = 1$, pitch up was completed for cases with the same AoA at pitch down, $t^* = 0.5$. At pitch down, $AoA = T - A$. Figure 4.32 shows

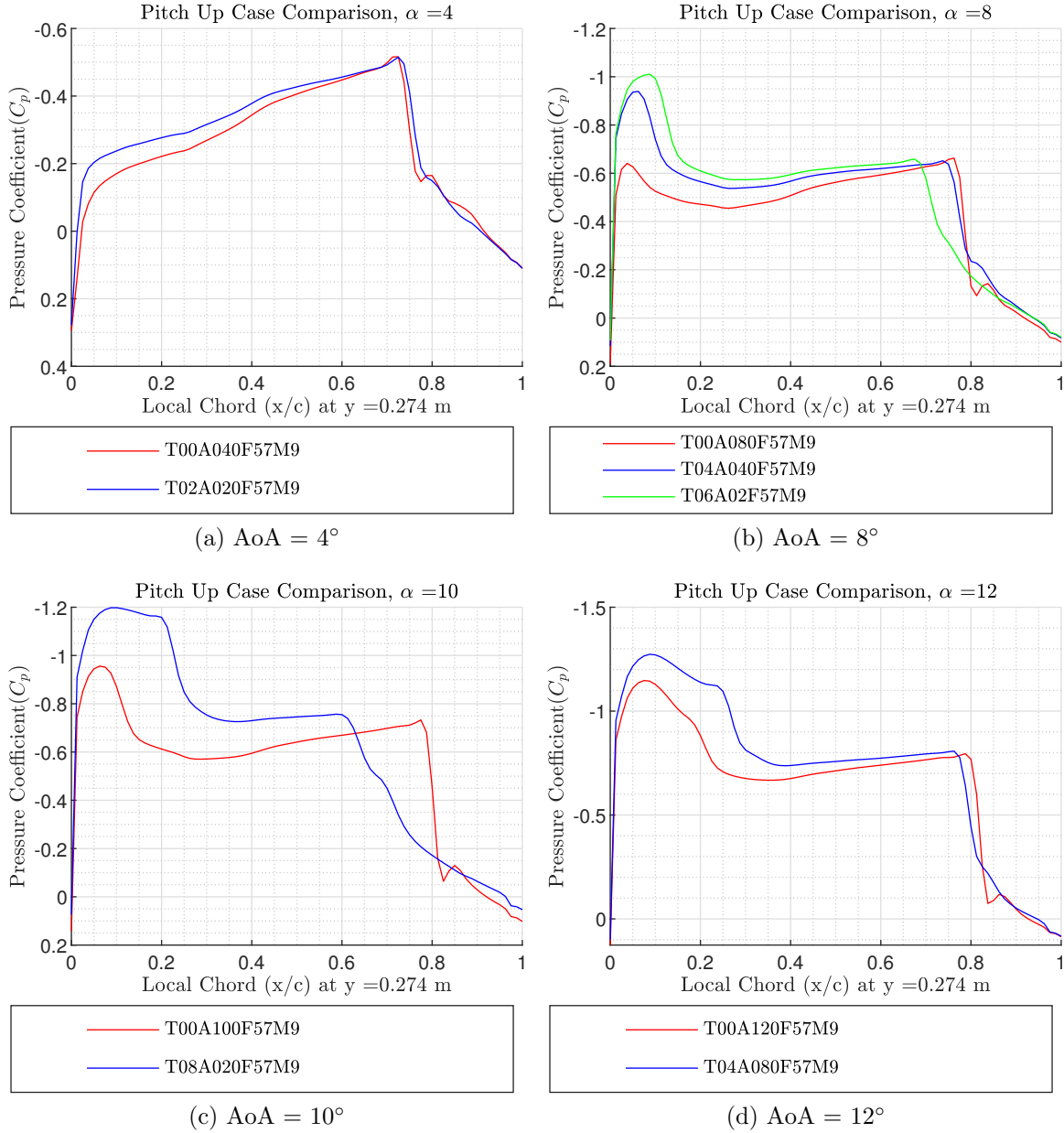


Figure 4.31: Pitch Up Pressure Distributions, $t^* = 1$. All cases have the same AoA at pitch up. $M = 0.9$.

pressure distributions at Station 2 and Table 4.9 shows moment and lift coefficients calculated for Stations 2 and 3 at pitch down. These plots show largely subsonic flow as a result of negative AoA. Figures 4.32a and 4.32b show largely different pressure distributions as a result of differences in transient motion as the wing oscillates. Areas of compression and expansion can be seen in these two plots that are largely residual

pressure formations from the wing's motion. Figure 4.32b shows the $T = 4^\circ$ and $A = 8^\circ$ case, which has two small regions of supersonic flow and a possible shock further aft. This section resembles pressures of a lambda shock formation where separation is more likely to occur. The difference in pressure at the trailing edge of Figure 4.32a suggests the possibility of trailing edge separation for the $T = 4^\circ$ and $A = 12^\circ$ case as well. Figure 4.32c shows cases where the pitch down AoA is 0° . The two cases in this plot show largely similar curves with slight differences that follow the same trends seen in the pitch up comparison where the higher trim case has more negative pressure towards the leading edge and the higher amplitude cases has a stronger shock with pressure oscillations more likely behind the shock. Moment and lift coefficient differences seem to reflect these differences in pressure. In particular, the $T = 4^\circ$, $A = 12^\circ$ case shows a positive moment coefficient. This suggests a change in direction of the resultant moment which further supports the presence of flow separation on the wing for this case.

Table 4.9: A comparison of pitch up pressure distributions ($t^* = 0.5$) for cases with the same AoA. Mach number = 0.9 & frequency = 5.7 Hz.

AoA	Trim AoA	Amplitude	Station 2		Station 3	
			C_m	C_l	C_m	C_l
-8°	0°	8°	-0.02	-0.71	-0.03	-0.76
	4°	12°	0.03	-0.73	0.02	-0.78
-4°	0°	4°	-0.04	-0.37	-0.04	-0.40
	4°	8°	-0.04	-0.33	-0.06	-0.36
0°	2°	2°	-0.05	-0.01	-0.06	-0.03
	4°	4°	-0.05	0.00	-0.05	-0.01

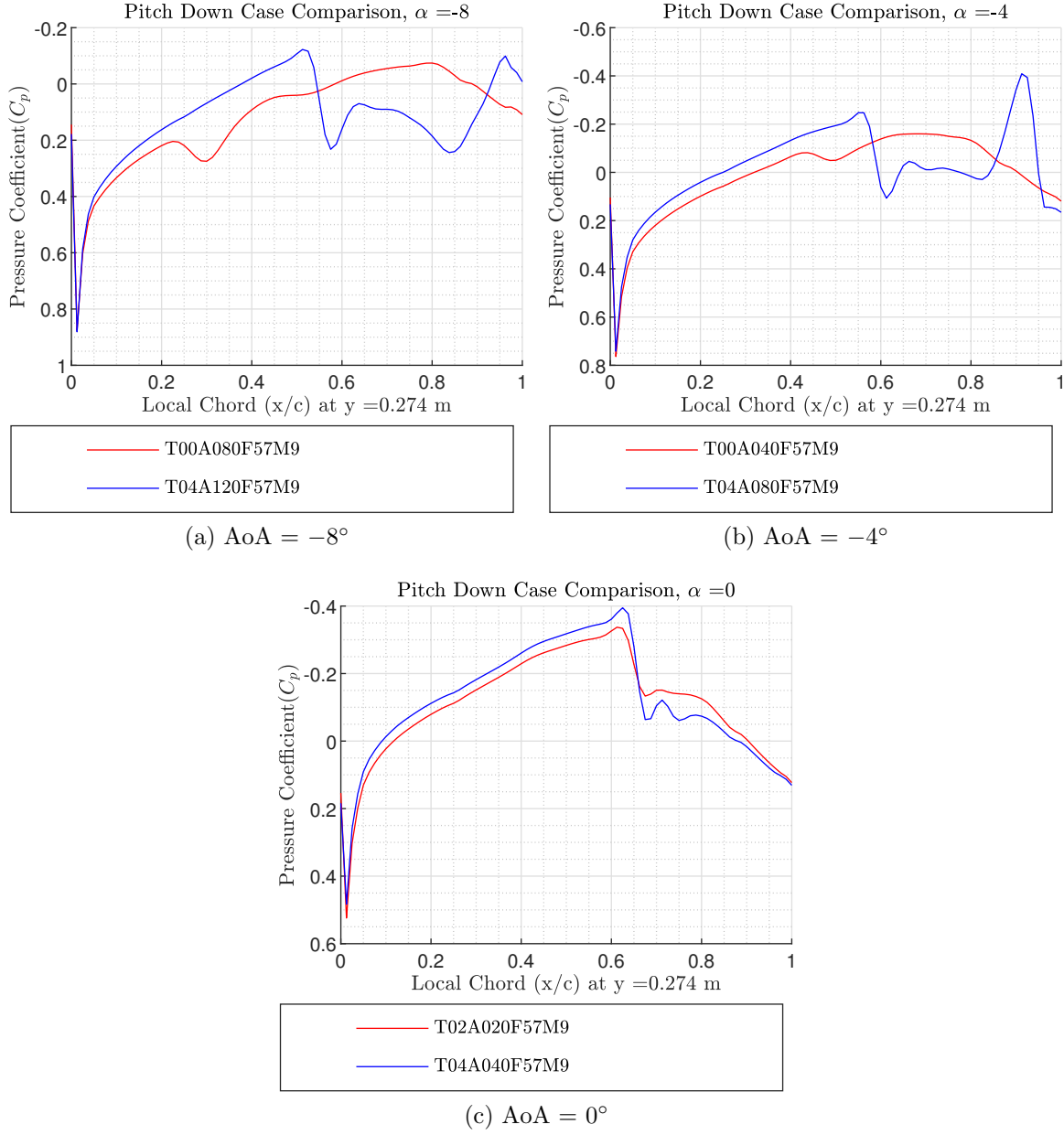


Figure 4.32: Pitch Down Pressure Distributions, $t^* = 0.5$. All cases have the same AoA. $M = 0.9$.

V. Conclusions and Recommendations

5.1 Results Summary

This research sought to increase fidelity and expand the test envelope researched by Hope [20]. A rigid, straked, delta wing modeled after Cunningham’s wind tunnel SiS model [9] was oscillated in pitch at various flight conditions using ZEUS, an Euler-based unsteady aeroelastic solver. The test envelope contained cases with trim AoAs ranging from 0° to 12° , amplitudes from 0.5° to 12° , and Mach from 0.3 to 0.95. For each simulation, pressure data was recorded for one full cycle of oscillation. The pressure data showed vastly different flow formations develop for different regions of the test envelope. The primary concentration of this research was the nonlinear flow surrounding shock wave formations.

5.1.1 Shock Formations. At a low transonic speed of 0.6 Mach, negative pressure on the upper surface of the wing remained largely subsonic. With AoA reaching 8° , a highly negative pressure development at the leading edge reached supersonic speeds. Compression waves converged to create shock waves to return flow to subsonic speeds. The formation of an swept shock formed as a result of vortex flow at sufficient AoA which became clearer at slightly higher Mach numbers. Along with an increase in Mach came the formation of a normal shock near the 75% chord. When the normal shock was present, higher amplitudes resulted in subsidiary shocks as the pressure oscillations behind the shock gained strength. With high transonic conditions and high AoA, shock wave interaction between the swept and main shock was observed. This interaction increases the likelihood of separation.

5.1.2 Moment. Sectional moment coefficients were calculated from the pressure data to support the analysis on shock formations. A twist in the moment vs AoA curve was observed where the typical counterclockwise (CCW) curve transitioned to a clockwise (CW) curve for a portion of the oscillation. When the AoA at pitch down became sufficiently negative, a CW portion formed. Positive moments were also seen at highly negative angles of attack. Some combinations of trim AoA and

amplitude resulted in a CW twist in the pitch up position. In these cases, a high trim AoA had greater influence on the presence of a pitch up twist than did a high amplitude.

5.1.3 Lift. As with the moment plots, lift data was calculated from the pressure data. At subsonic speeds and low to moderate AoA, the lift vs AoA plots showed largely linear oscillation curves. As the trim AoA increased, a hysteresis became prominent as demonstrated by the developing elliptical shape to the lift vs AoA curve. With increased amplitude, an asymmetrical pattern to the curve became visible.

5.1.4 Hysteresis. Due to the transient environment of the oscillating wing, a lag or hysteresis in the flow was observed. Observations suggest an asymmetrical nature to the hysteresis, not a uniform lag across the entire cycle. The hysteresis seemed more prominent around the fully pitched down position in the cycle. It is theorized that the flow formations that built up during the pitch down motion continued to develop into the pitching up motion resulting in hysteresis.

5.1.5 Convergence. Of the 71 cases run through ZEUS in this research, 19 cases did not converge to a solution. All non-converged cases contained AoAs equal to or greater than 12° . This result was expected in some cases where flow separation is expected to dominate regions outside of the boundary layer where ZEUS cannot calculate viscous effects. The test matrix includes AoAs where stall characteristics would begin to propagate on the wing.

When looking at trends that influenced convergence, unique AoA thresholds appeared to be a function of Mach, though not linearly dependent. To check the influence of the wing's position at the initiation of the oscillation, the starting point of the simulation was changed from pitch down (negative cosine) to pitch up (positive cosine). The recording of pressure data was delayed 1/2 of a cycle to keep the data's starting point at pitch up. A total of 6 cases were run using both functions. Of these

6, 2 cases converged and 4 did not using the negative cosine function. The positive cosine function saw 3 cases converge and 3 that did not. While this change resulted in one previously non-converged case to converge, the 5 remaining positive cosine cases saw the same results as the negative cosine cases. The two cases which converged with the negative cosine function showed very similar results with the positive cosine function.

5.1.6 Comparing to Hope's and Pung's Research. For the case comparisons to Hope's research [20], the same two shock system was seen. The increased grid density 2.5 times that used by Hope elevated the solver's ability to calculate rapid pressure changes particularly around shock strength, movement, and subsidiary shock formation. The cases with lower trim AoA of 4° showed greater shock movement than Hope's simulations, particularly with the dissolving of the main aft shock into compression waves. The cases with trim AoA of 10° show very similar shock migration, but with more fidelity around subsidiary shocks. Cases with $T = 10^\circ$, $A = 2^\circ$ and 4° , $M = 0.9$, which converged for Hope, did not converge with the higher density grid. Since Hope saw some of these cases converge to a solution that this analysis did not, and Hope's grid was less refined, the non-converged results were thought to be due to large regions of separation which were not compatible with ZEUS' boundary growth parameters. Pung found these cases to be dominated by separation which supports this theory [28]. When flow was attached, Pung saw the same main shock at low AoA and two shock system at higher AoA. He also saw increases in shock movement and shock strength when amplitude was increased which matches Hope and this analysis.

5.1.7 Inviscid vs Boundary Layer Coupled. Since large variations were observed as a results of the increased grid density from Hope's analysis, one fully inviscid case was run to compare to the boundary layer coupled method used for the other 70 cases run in this analysis. While the observations in Hope's similar analysis were confirmed, the increased grid density did not change the inviscid solution as severely as in the BLC cases. It was found that the leading edge flow and flow around

the swept shock were largely not impacted by the inviscid boundary layer, but vast differences surrounding the main aft shock were observed. The fully inviscid solution failed to produce subsidiary shocks, and instead predicted aft-ward migration of the main shock. The inviscid solution also failed to capture the forward motion of the pressure wave as the shock dissolved into compression waves. When comparing the moment calculations, the BLC case predicted a switch in moment from positive to negative at pitch down which the inviscid case did not.

5.1.8 Comparison to Cunningham's Results. Since Hope based his analysis on comparisons with Cunningham's results [10], an attempt was made in this analysis as well. Since access to Cunningham's data and his data processing techniques was not available, direct comparison of results was not possible, however, comparisons between general flow developments could be made. First, like in Hope's analysis, the two primary shock system seen by Cunningham was observed, where the front shock was swept aft-ward with vortex flow off of the wing's swept leading edge. This vortex development matches the transition from linear flow to nonlinear flow between 8° and 10° AoA noted by Cunningham. Just as Cunningham's reports detail, a lag of flow behind the wing motion was observed as a result of the pitching of the wing. Above 8° AoA, the wind tunnel tests saw the development of SITES on the stationary wing, starting at the wing tip. This conclusion was based off of a change in negative pressure at the trailing edge [10]. The same conclusion could not be made in this analysis. With the dynamic motion of an oscillating wing, a change in pressure at the trailing edge is not sufficient to confirm the existence of SITES.

5.2 *SITES and LCO*

This research sought to improve characterization of shock movement with changes in Mach number, trim, and amplitude. Sweeps were run while changing a single variable at a time. Through this method, relationships were found with shock formation and movement. The characterization completed here will influence full F-16 LCO

simulations using ZEUS which will then be flight tested to observe shock movement of the physical wing at various flight conditions. This future comparison between flight test and the F-16 ZEUS model that will be based on the findings in the present research will hopefully show the validity of ZEUS for this type of analysis.

Another goal of this research was to demonstrate the fidelity of ZEUS as an accurate tool in predicting shock movement on a pitching wing. An adequate grid density was found to be extremely important to achieving this objective. With a refined grid, this analysis showed the same shock systems as seen in the wind tunnel experiments [8]. Details surrounding the shocks were captured that went undetected in Hope's results. Qualitative comparisons were made to Pung's results which showed agreement until AoA was sufficient for separation to occur.

In this analysis, an asymmetrical lag or hysteresis was observed as a result of the transient pressure distribution along the wing. The presence of a lag can by its nature drive an ordinary linear system towards instability. It was hypothesized through observation that the hysteresis was heavily influenced by the presence of shocks on the wing. With complex shock formations, such as the presence of subsidiary shocks and interactions between the swept shock and the main aft shock, comes an increased probability of pockets of flow separation within the pitching cycle. These findings support the possibility of SITES having a significant role in some flight conditions which result in LCO. Since the presence of the swept shock exists at higher AoA, its involvement for LCO at steady level flight is not likely, but could have influence in LCO in high gain maneuvers such as g-loaded turns.

5.3 Future Research Areas

While this research sheds some light on shock movement on a pitching wing, a few areas of future research remain necessary to demonstrate shock movement and SITES' ability to drive oscillations.

5.3.1 Convergence. The ability for ZEUS to accurately simulate boundary layer growth and shrinking is largely dependent on gain parameters within the BLC setting that characterize the viscous flow properties. For highly nonlinear formations such as complex shock interactions and large areas of separation, higher boundary layer growth rates are necessary to converge to a solution. Further studies should be completed to research the impact of each of these parameters, and changing these in an attempt to achieve convergence for a few of the 19 cases in this analysis that did not converge. Recommended cases for this research include the two cases run by Pung [28] which compared directly to Hope's test cases. One of Pung's cases was run in this analysis and did not converge. Once this is accomplished, a verification of cases in this analysis that did converge should be completed to determine the differences between solutions that are a direct result of these viscous flow properties. The ZEUS User's Manual contains references to reports written that analyzed these parameters, and is a good starting point for this research. To achieve the most accurate simulation results, grid studies should be completed for each individual case. This could also have an impact on case convergence.

5.3.2 Friction Coefficient. Because this analysis used a wing in motion, pressure data alone is not sufficient in determining areas of separation. ZEUS has the ability to also output friction forces on the surface of the wing that can be used to help determine these areas of separation. Cunningham observed SITES start around 10° AoA and leading-edge separation beginning at 10.5° at the wing tip for the stationary wing. This supports the possibility of SITES and other forms of flow separation within the envelope tested in this analysis. The use of friction data may be able to link Cunningham's observation with this analysis.

Appendix A. C_p Data for Wing Station 1

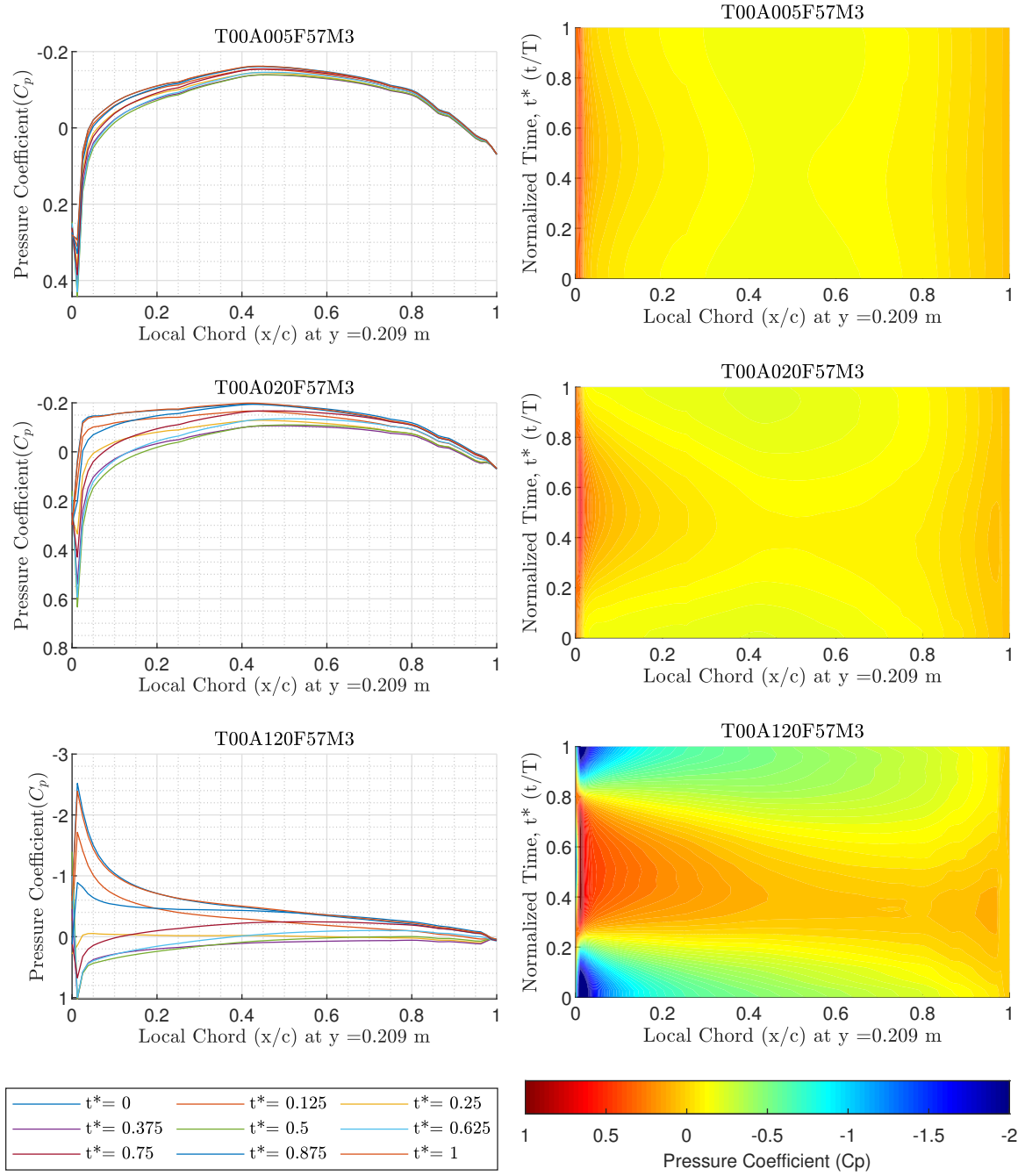


Figure A.1: Pressure distributions at Mach number 0.3. Frequency = 5.7 Hz, trim = 0°, amplitude = 0.5°, 2°, & 12°

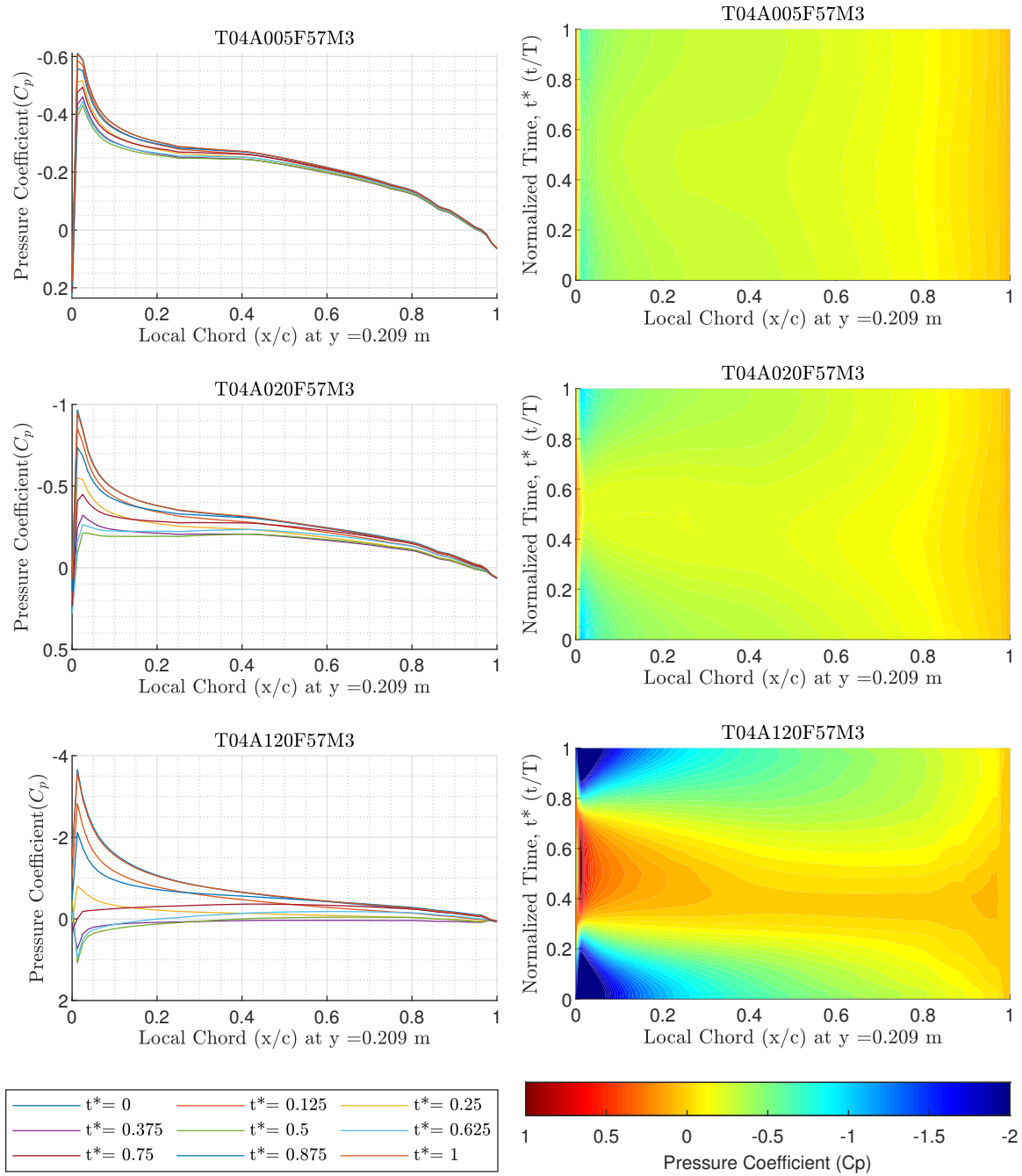


Figure A.2: Pressure distributions at Mach number 0.3. Frequency = 5.7 Hz, trim = 4°, amplitude = 0.5°, 2°, & 12°

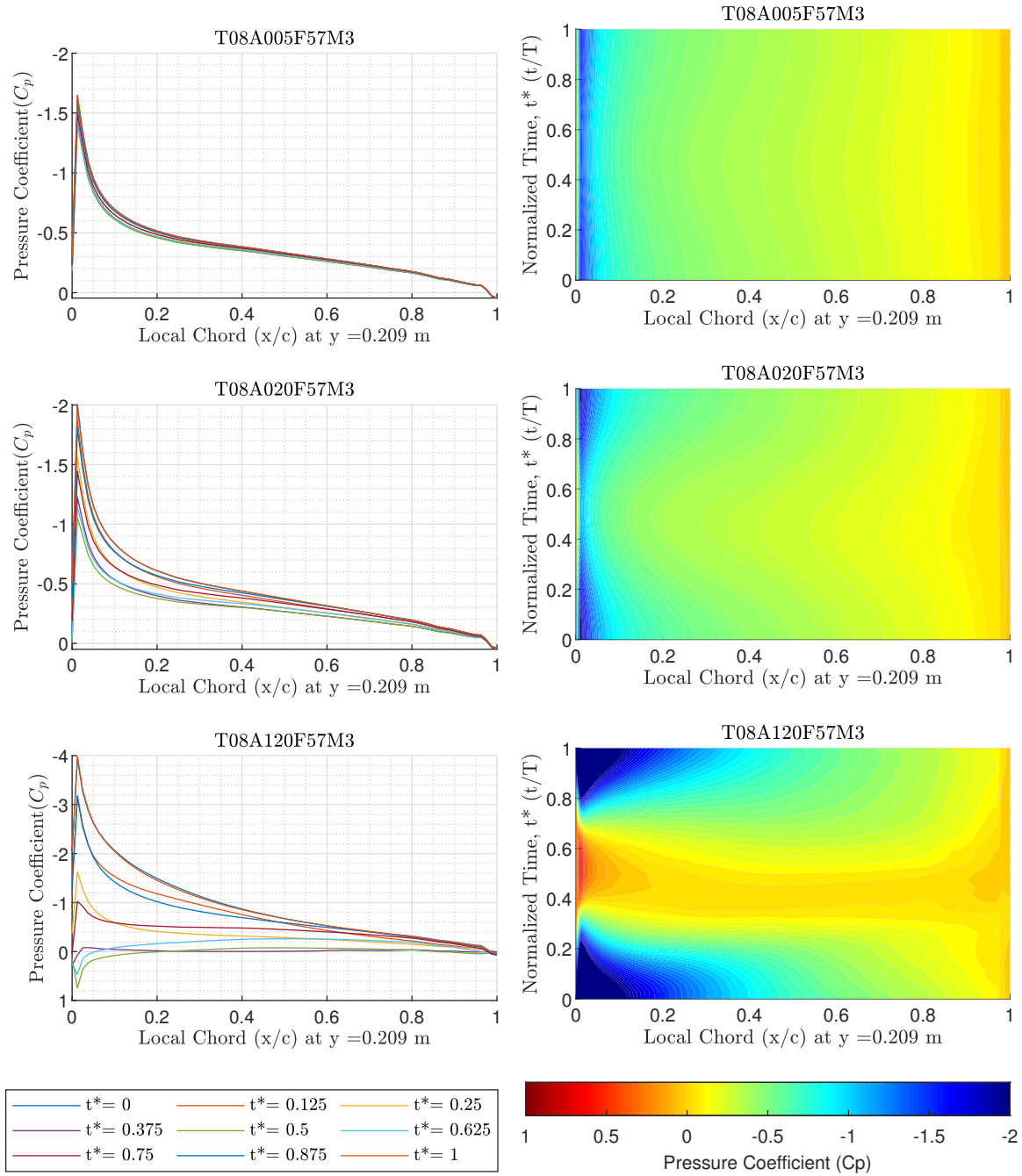


Figure A.3: Pressure distributions at Mach number 0.3. Frequency = 5.7 Hz, trim = 8° , amplitude = 0.5° , 2° , & 12°

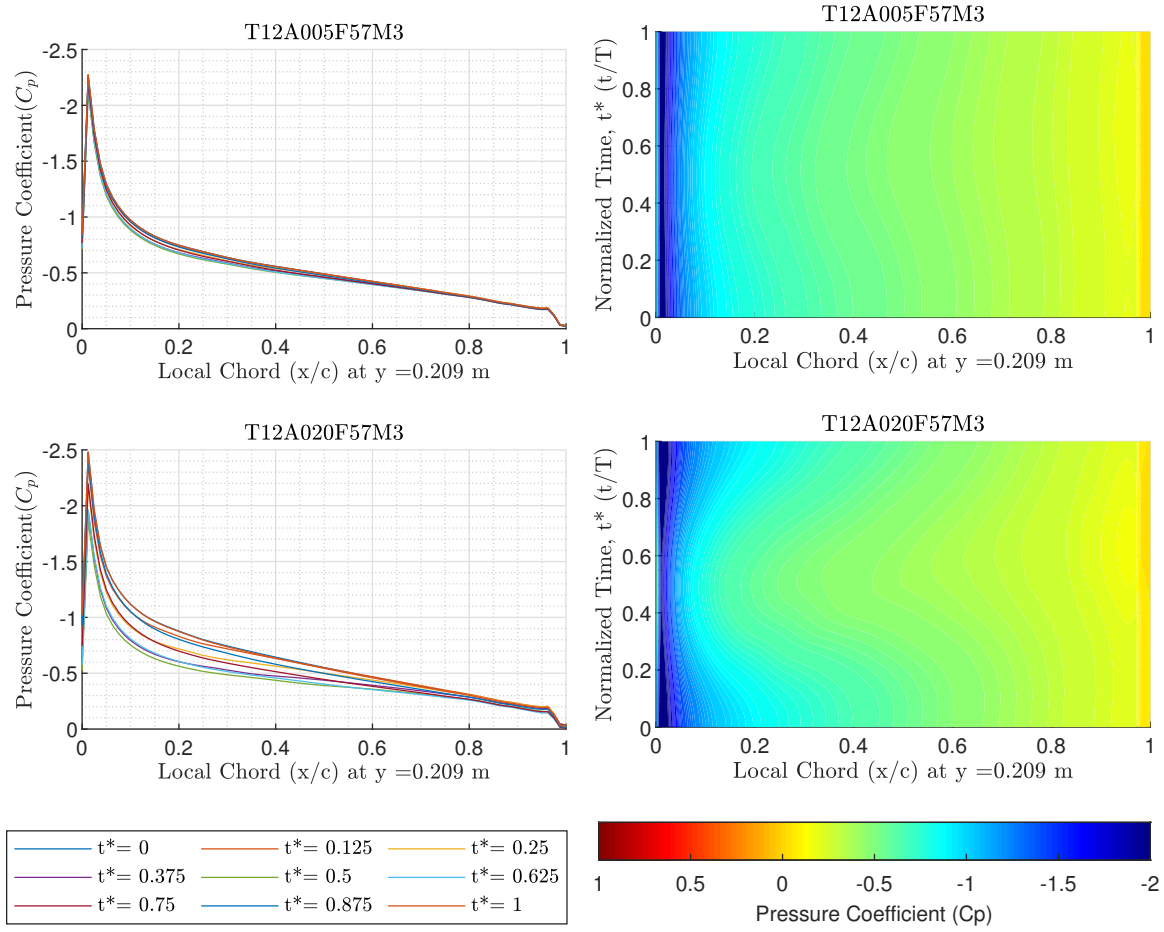


Figure A.4: Pressure distributions at Mach number 0.3. Frequency = 5.7 Hz, trim = 12°, amplitude = 0.5° & 2°

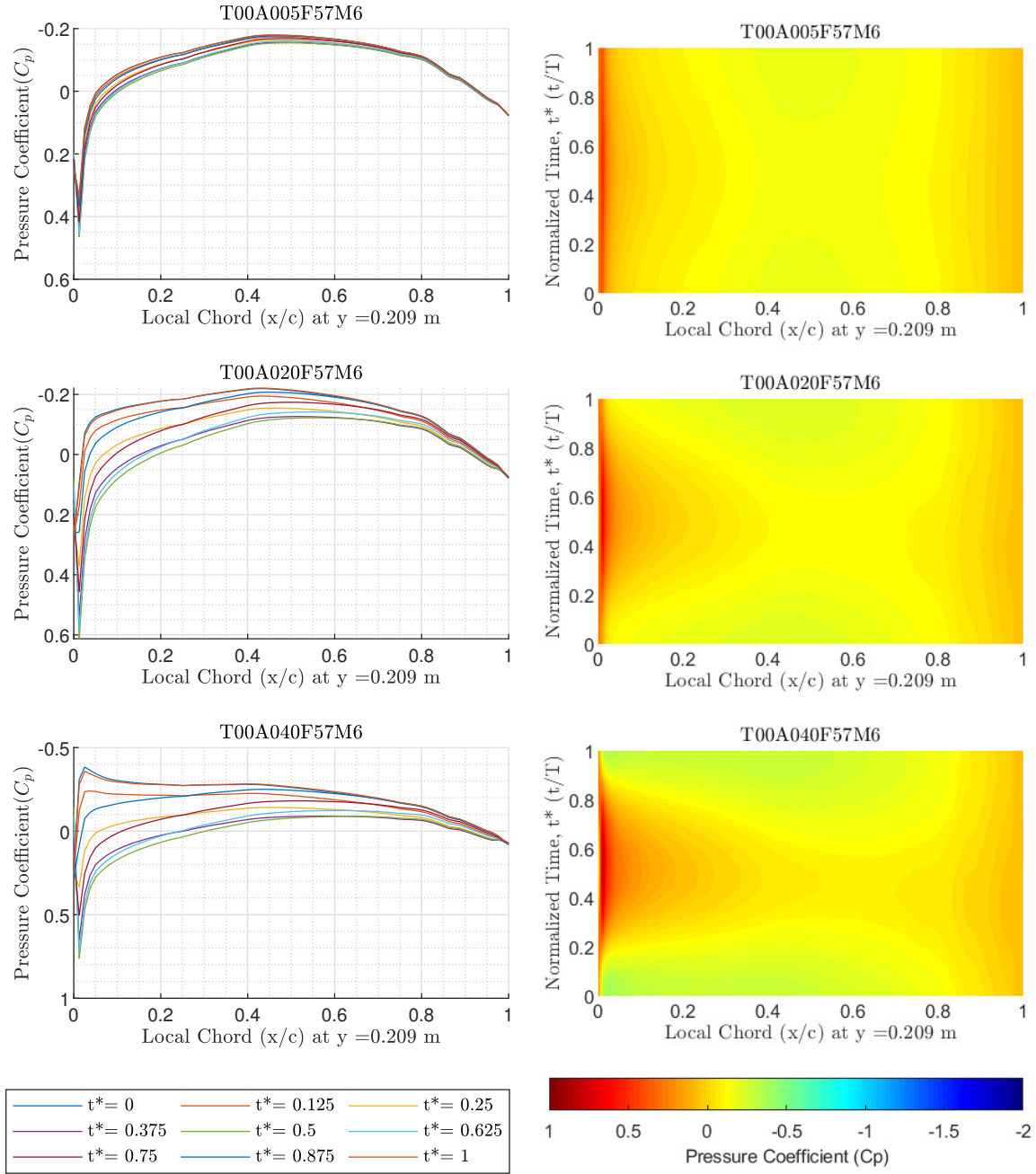


Figure A.5: Pressure distributions at Mach number 0.6. Frequency = 5.7 Hz, trim = 0°, amplitude = 0.5°, 2°, & 4°

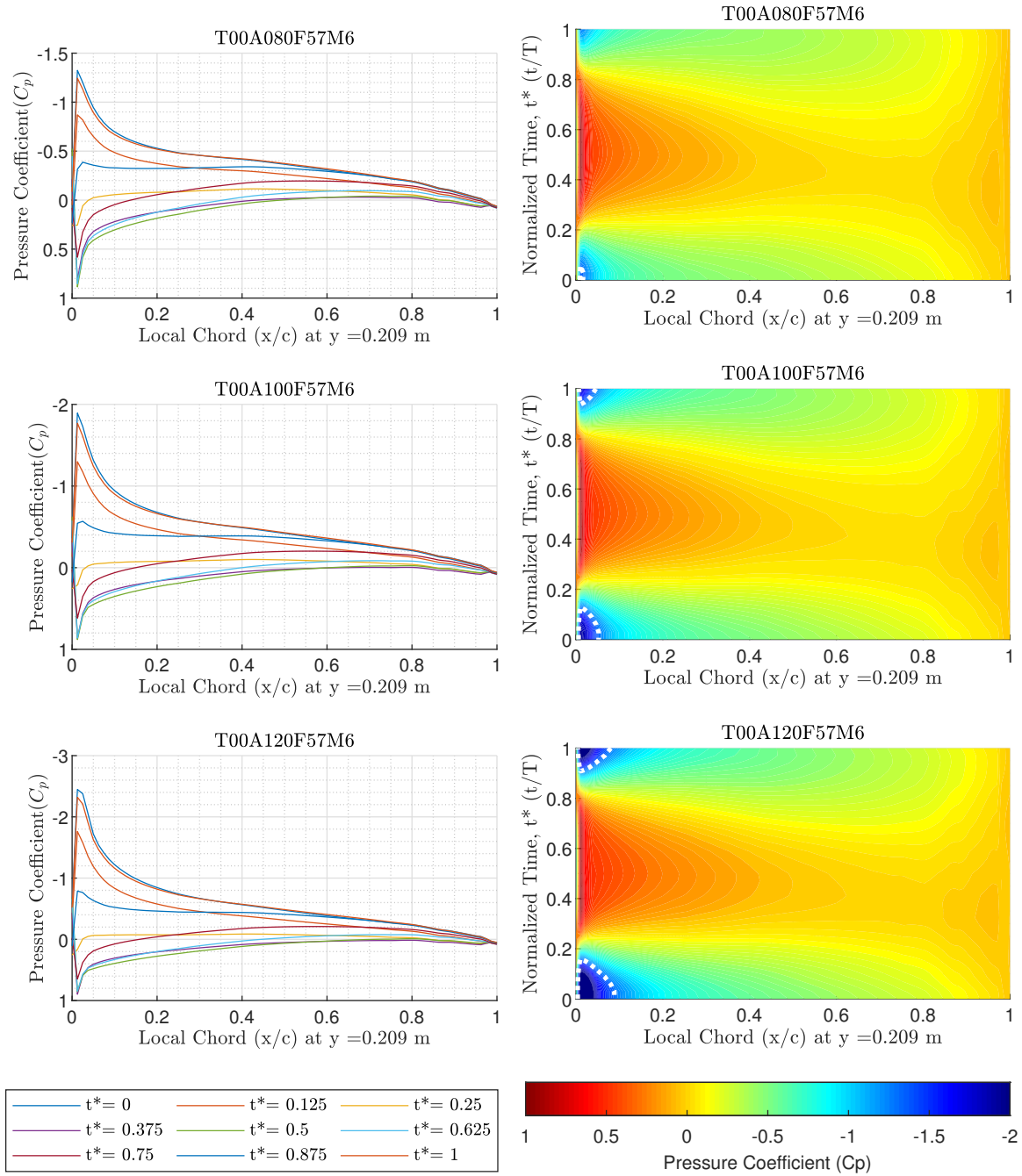


Figure A.6: Pressure distributions at Mach number 0.6. Frequency = 5.7 Hz, trim = 0°, amplitude = 8°, 10°, & 12°

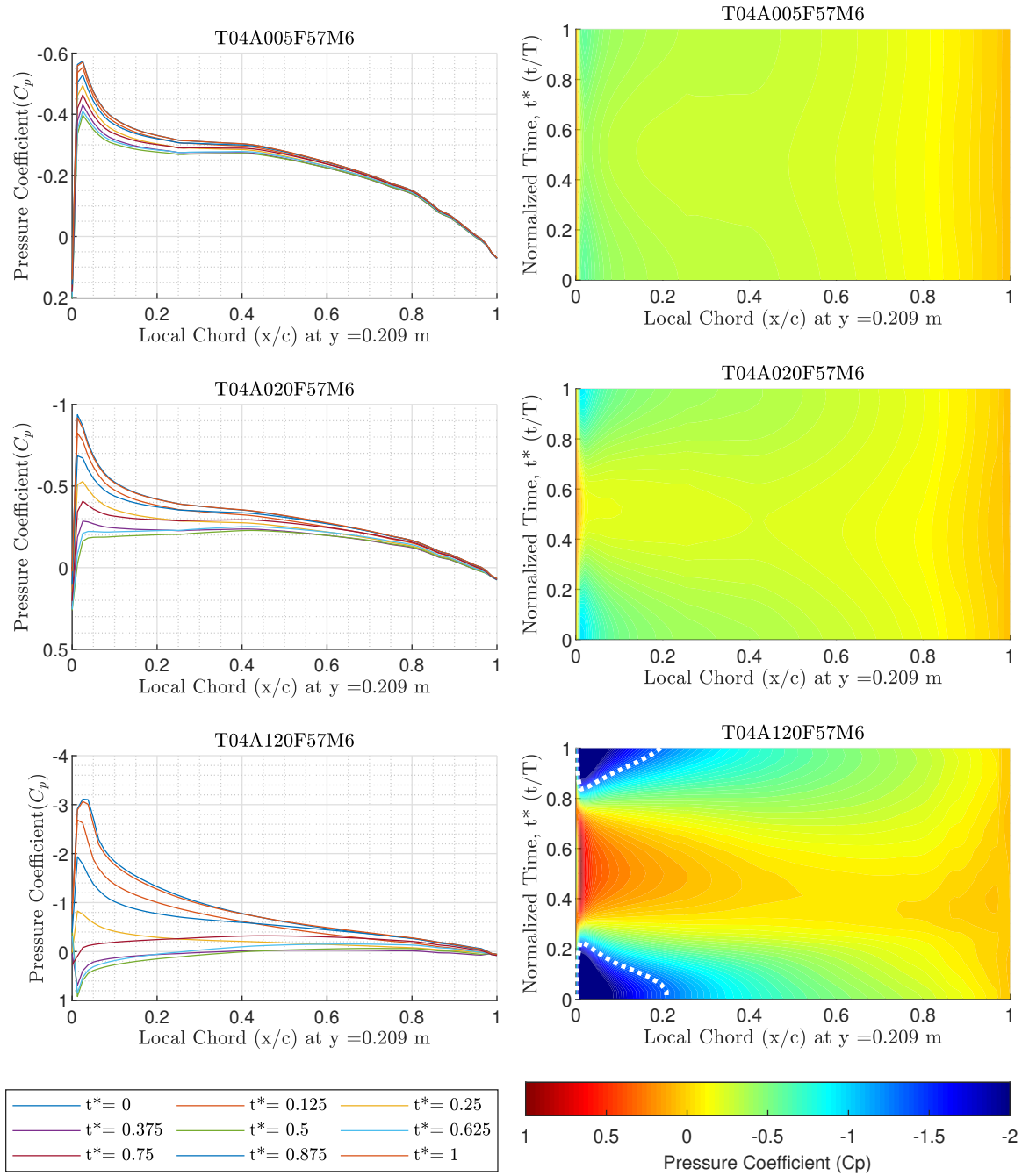


Figure A.7: Pressure distributions at Mach number 0.6. Frequency = 5.7 Hz, trim = 4°, amplitude = 0.5°, 2°, & 12°

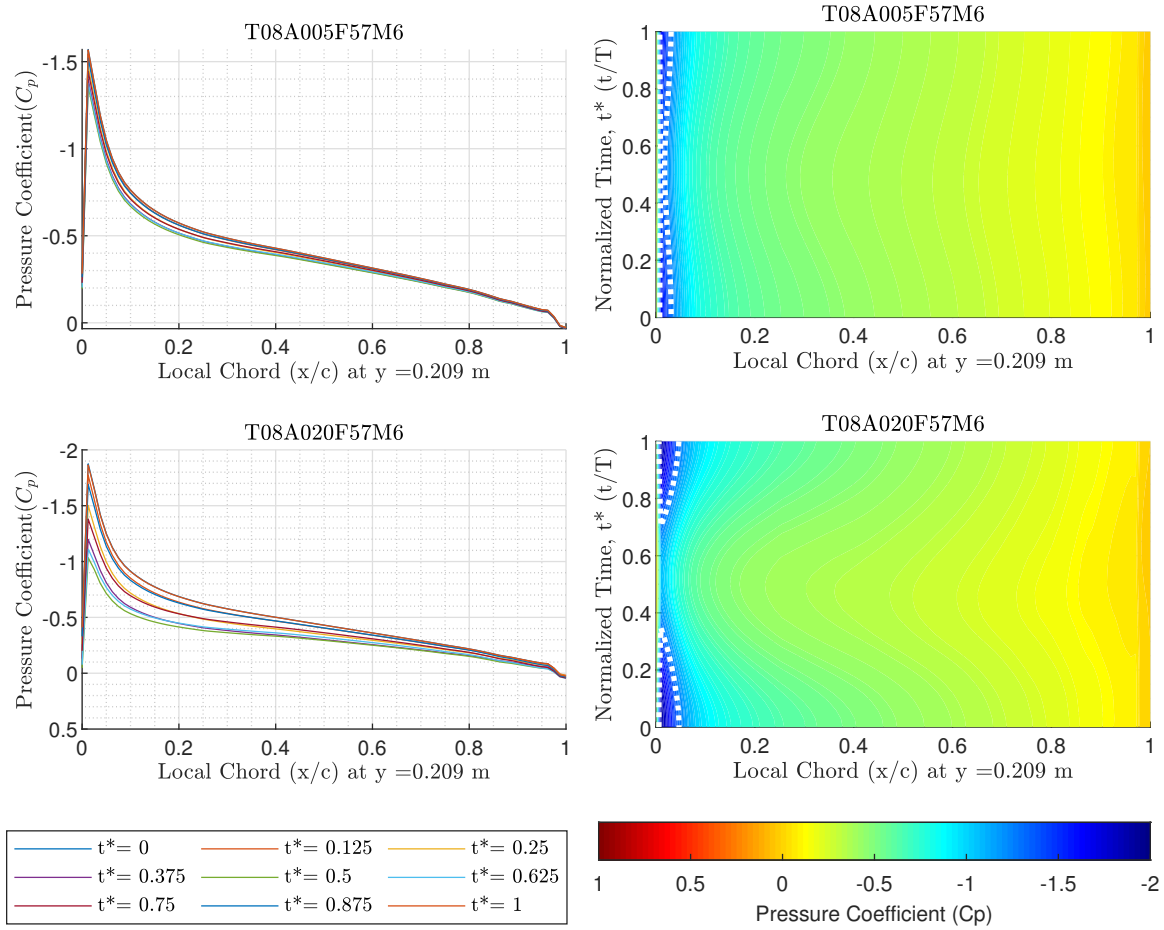


Figure A.8: Pressure distributions at Mach number 0.6. Frequency = 5.7 Hz, trim = 8°, amplitude = 0.5° & 2°

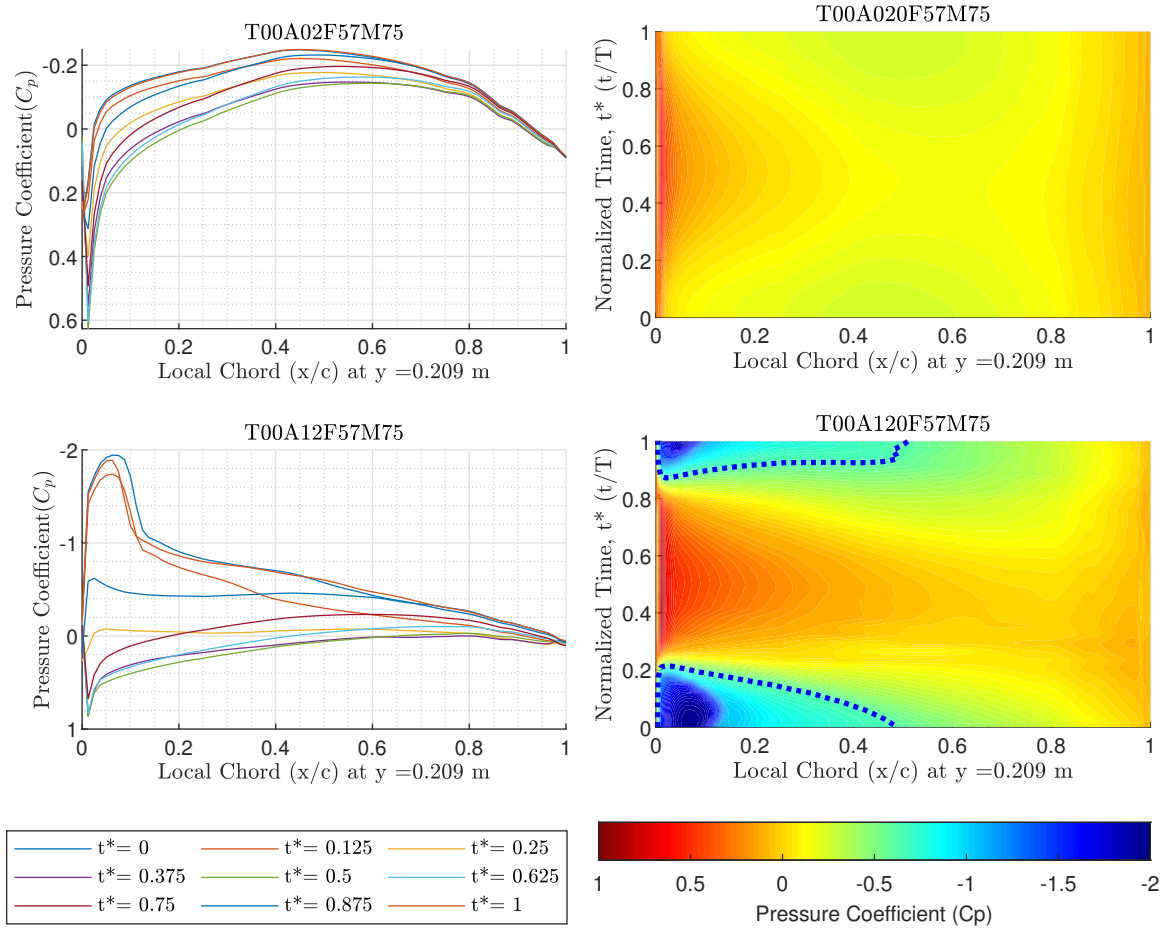


Figure A.9: Pressure distributions at Mach number 0.75. Frequency = 5.7 Hz, trim = 0°, amplitude = 2° & 12°

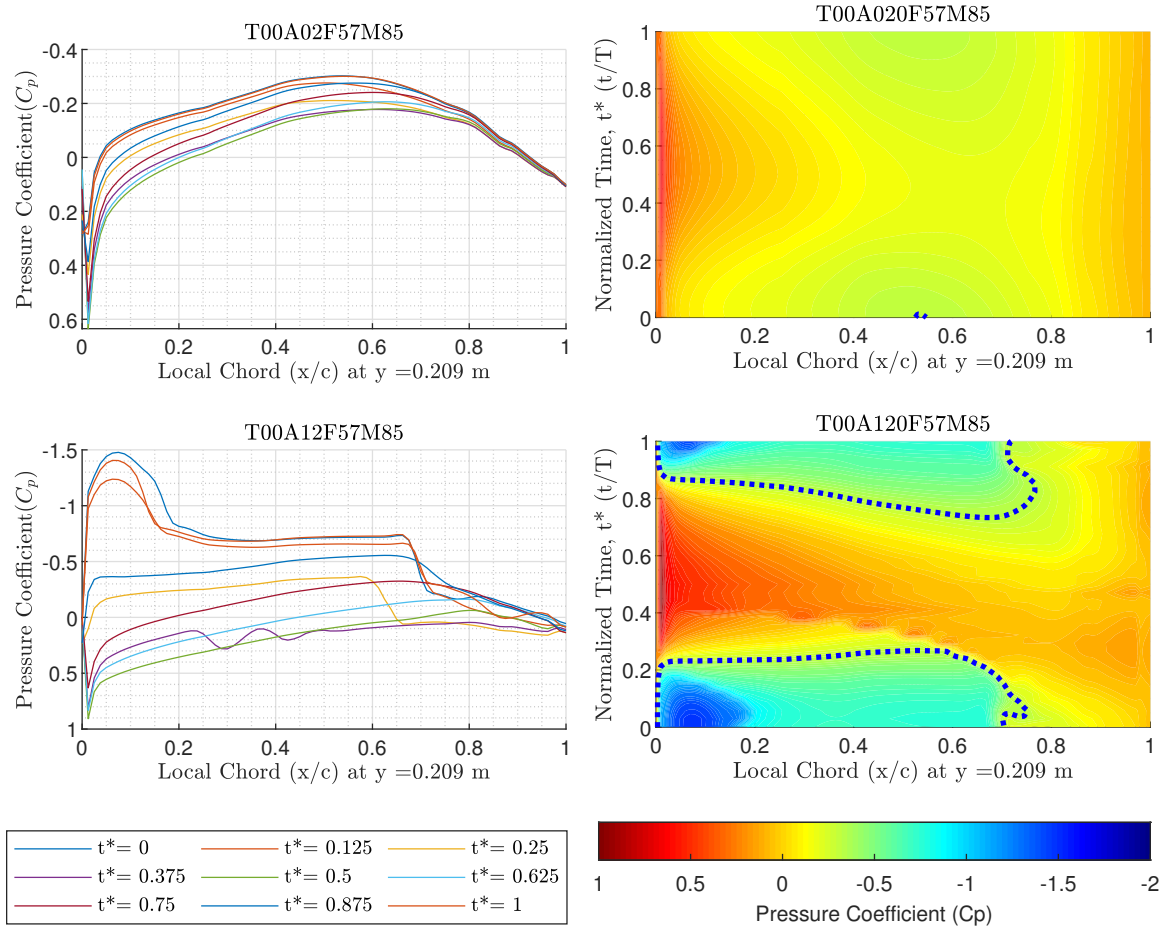


Figure A.10: Pressure distributions at Mach number 0.85. Frequency = 5.7 Hz, trim = 0°, amplitude = 2° & 12°

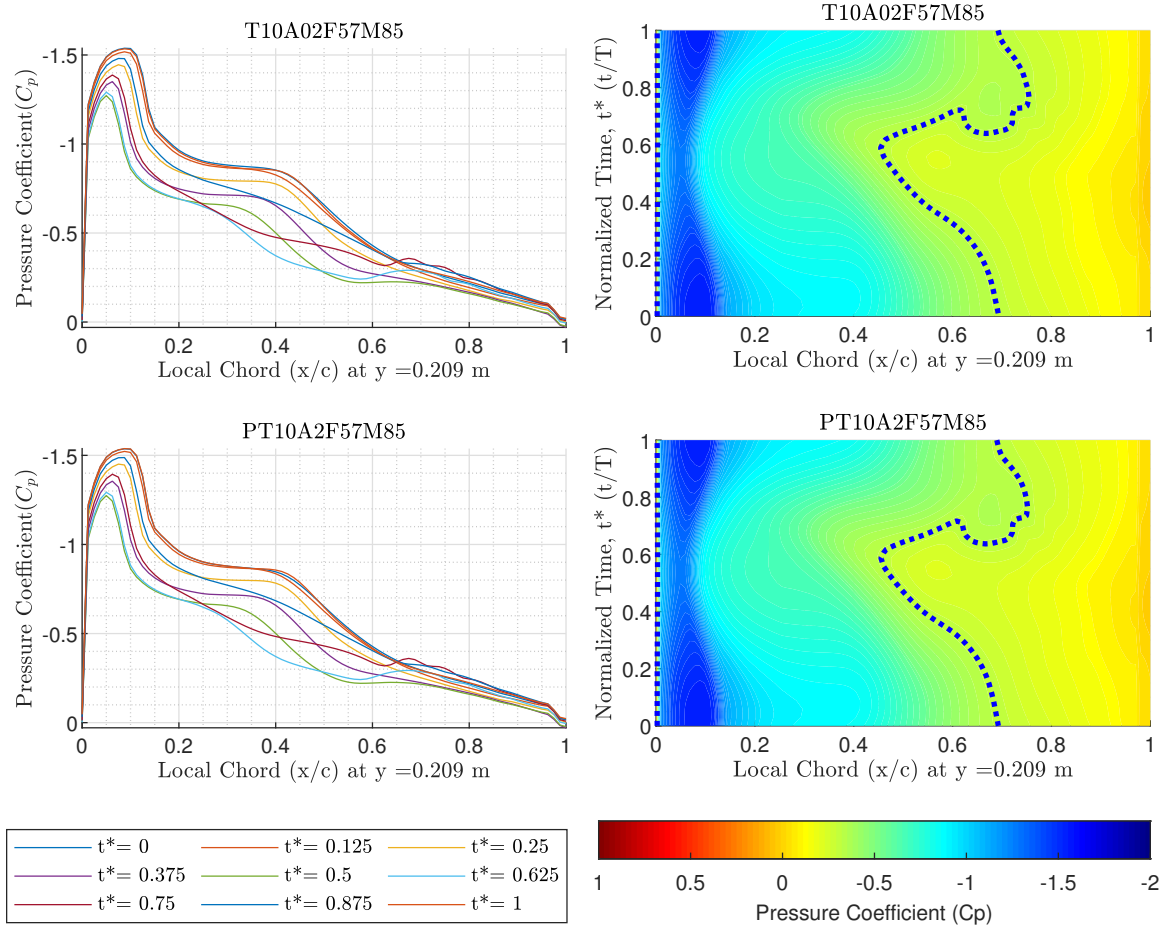


Figure A.11: Pressure distributions at Mach number 0.85. Frequency = 5.7 Hz, trim = 0° , amplitude = 2° . Top used $-\cosine$ function, and bottom used $+\cosine$ function.

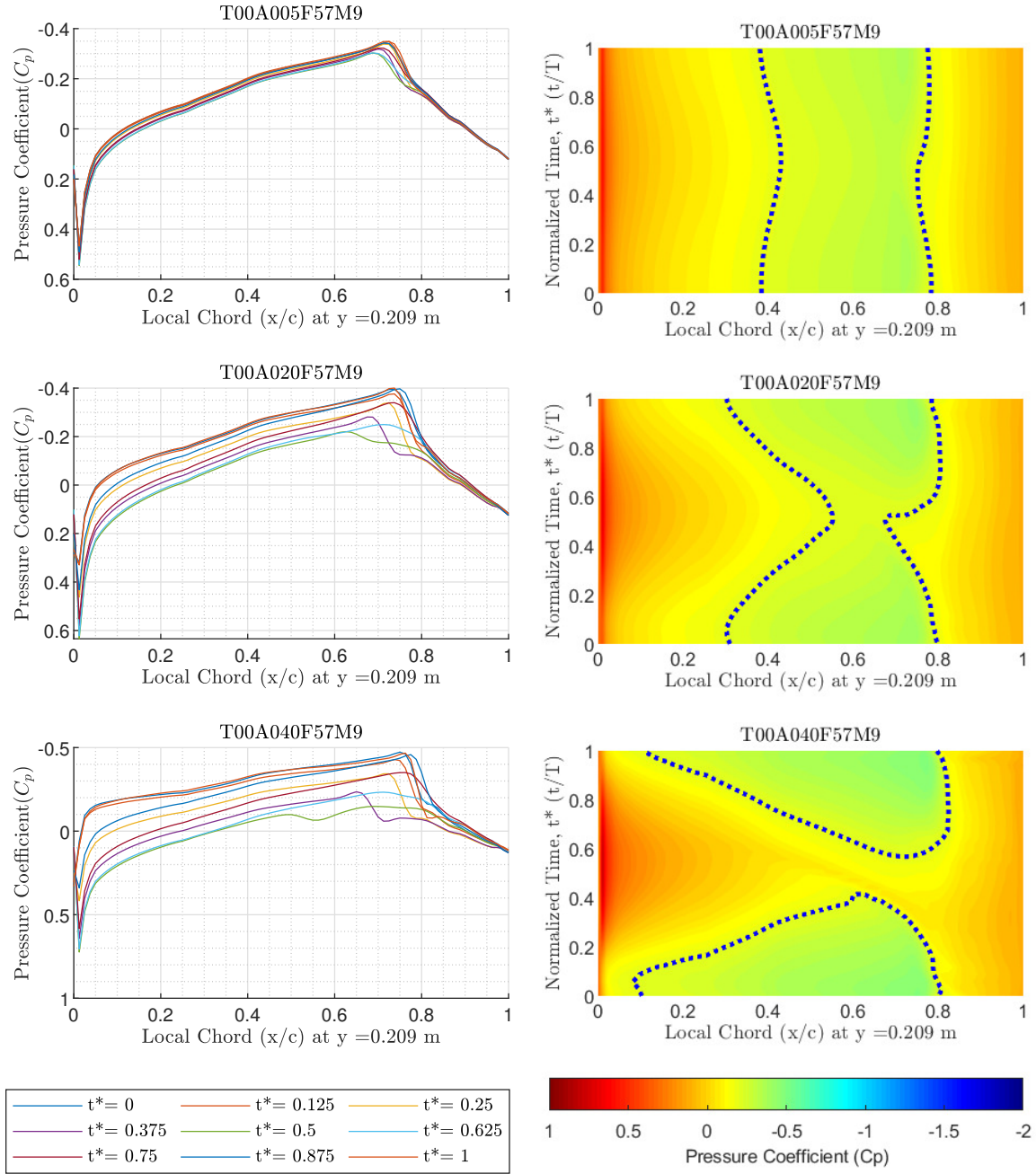


Figure A.12: Pressure distributions at Mach number 0.9. Frequency = 5.7 Hz, trim = 0°, amplitude = 0.5°, 2°, & 4°

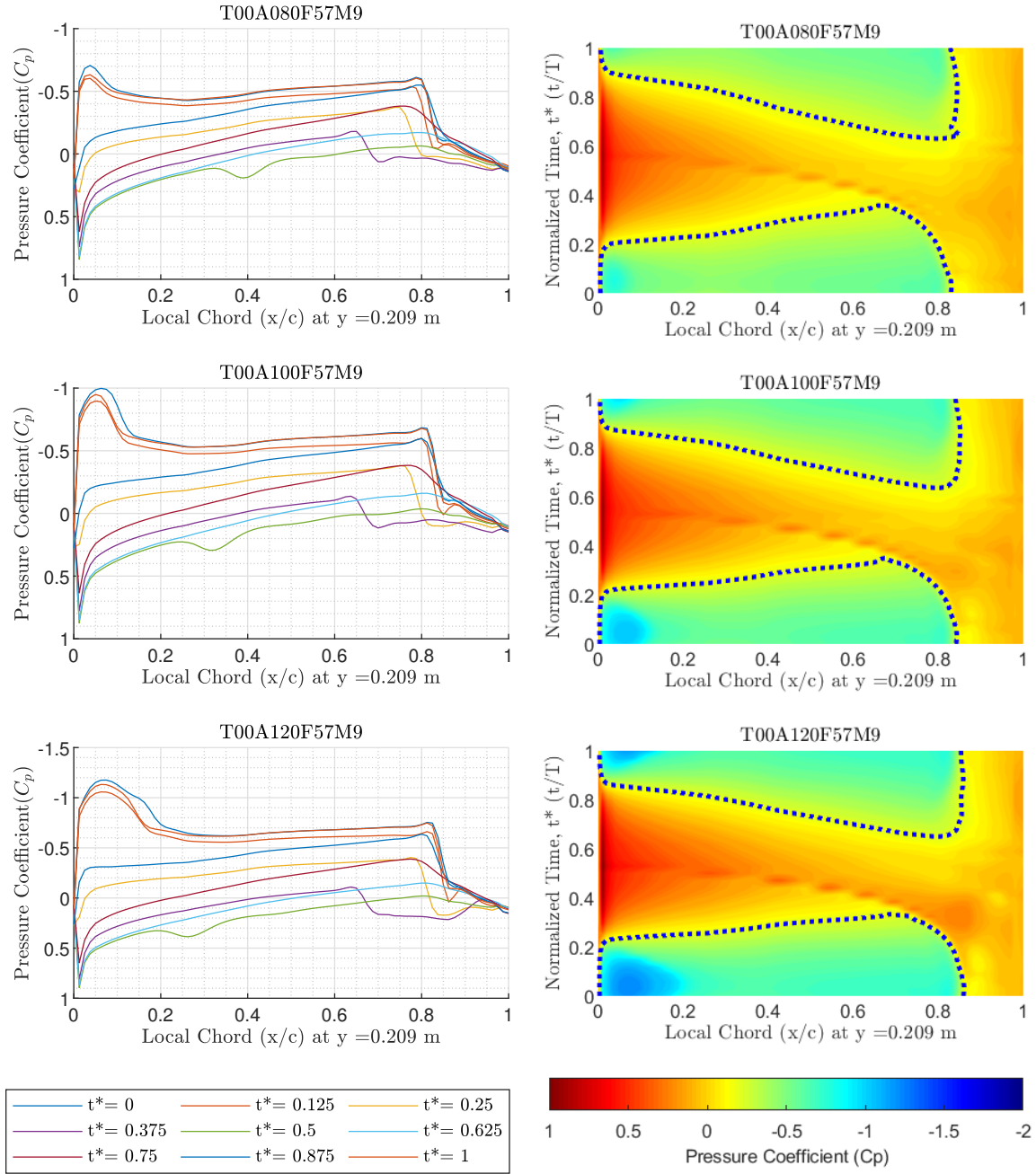


Figure A.13: Pressure distributions at Mach number 0.9. Frequency = 5.7 Hz, trim = 0°, amplitude = 8°, 10°, & 12°

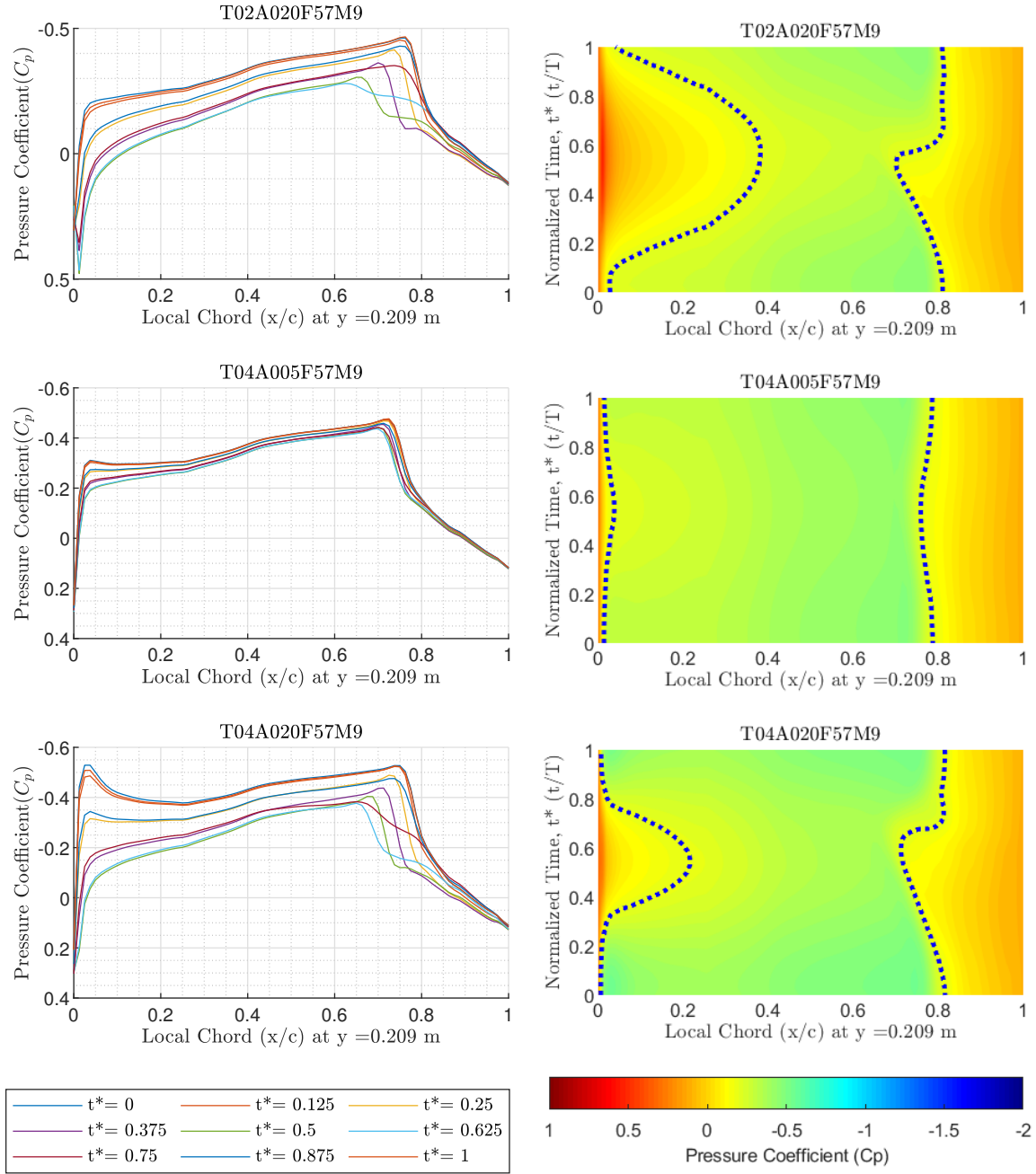


Figure A.14: Pressure distributions at Mach number 0.9. Frequency = 5.7 Hz, (Top) trim = 2° & amplitude = 2° , (middle & bottom) trim = 4° , amplitude = 0.5° & 2°

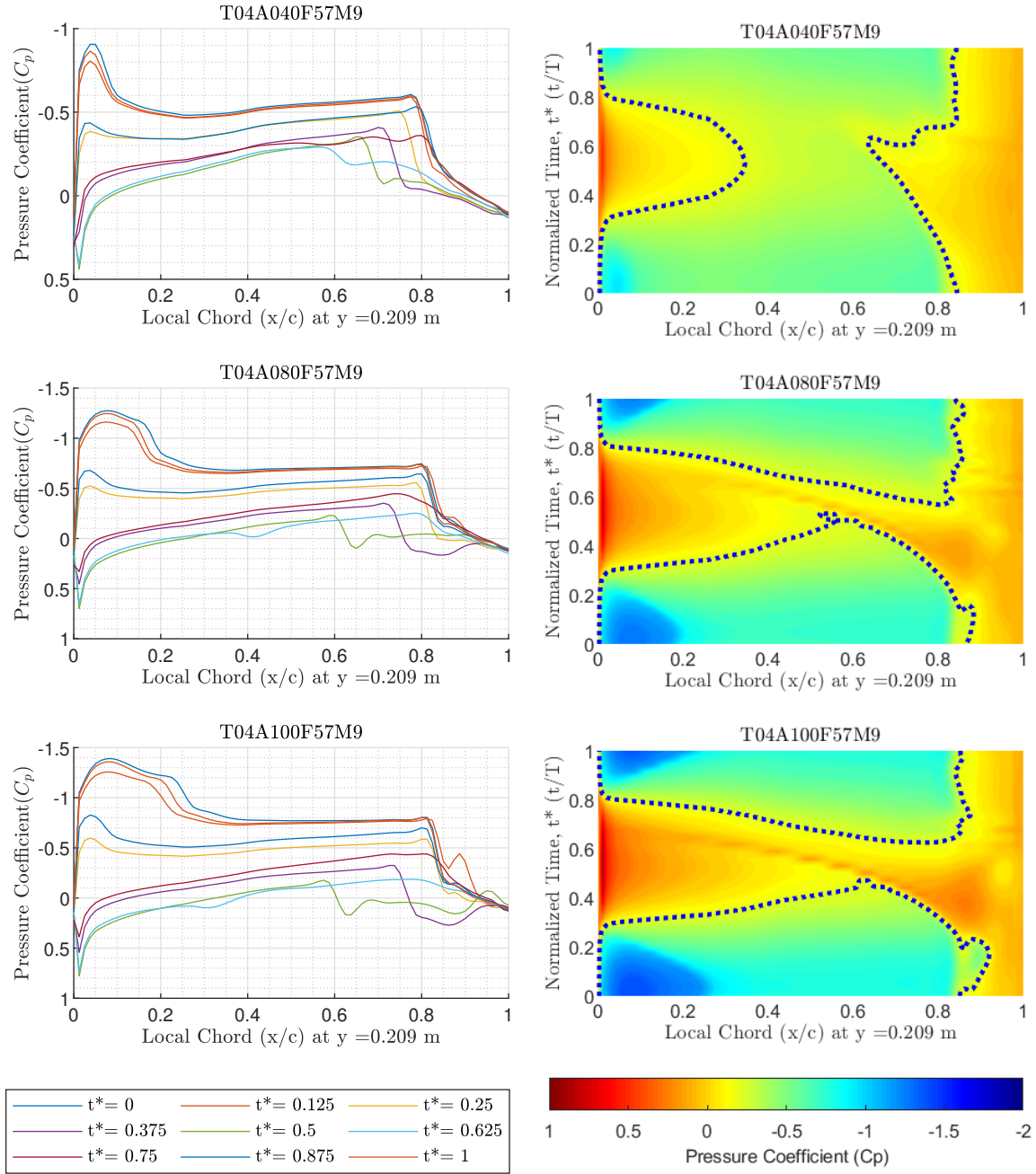


Figure A.15: Pressure distributions at Mach number 0.9. Frequency = 5.7 Hz, trim = 4°, amplitude = 4°, & 10°

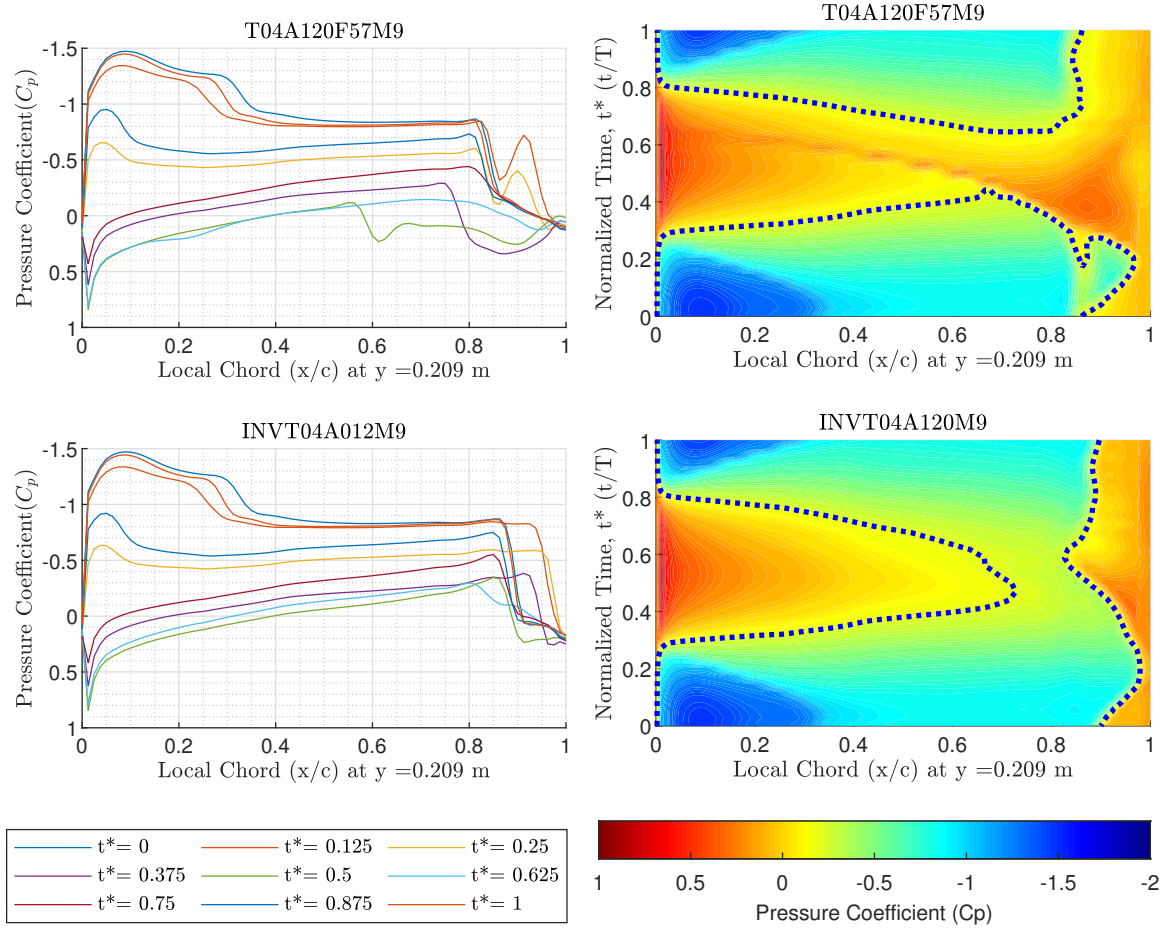


Figure A.16: Pressure distributions at Mach number 0.9. Frequency = 5.7 Hz, trim = 4°, amplitude = 12°. Top used BLC solver, and bottom used fully inviscid solver.

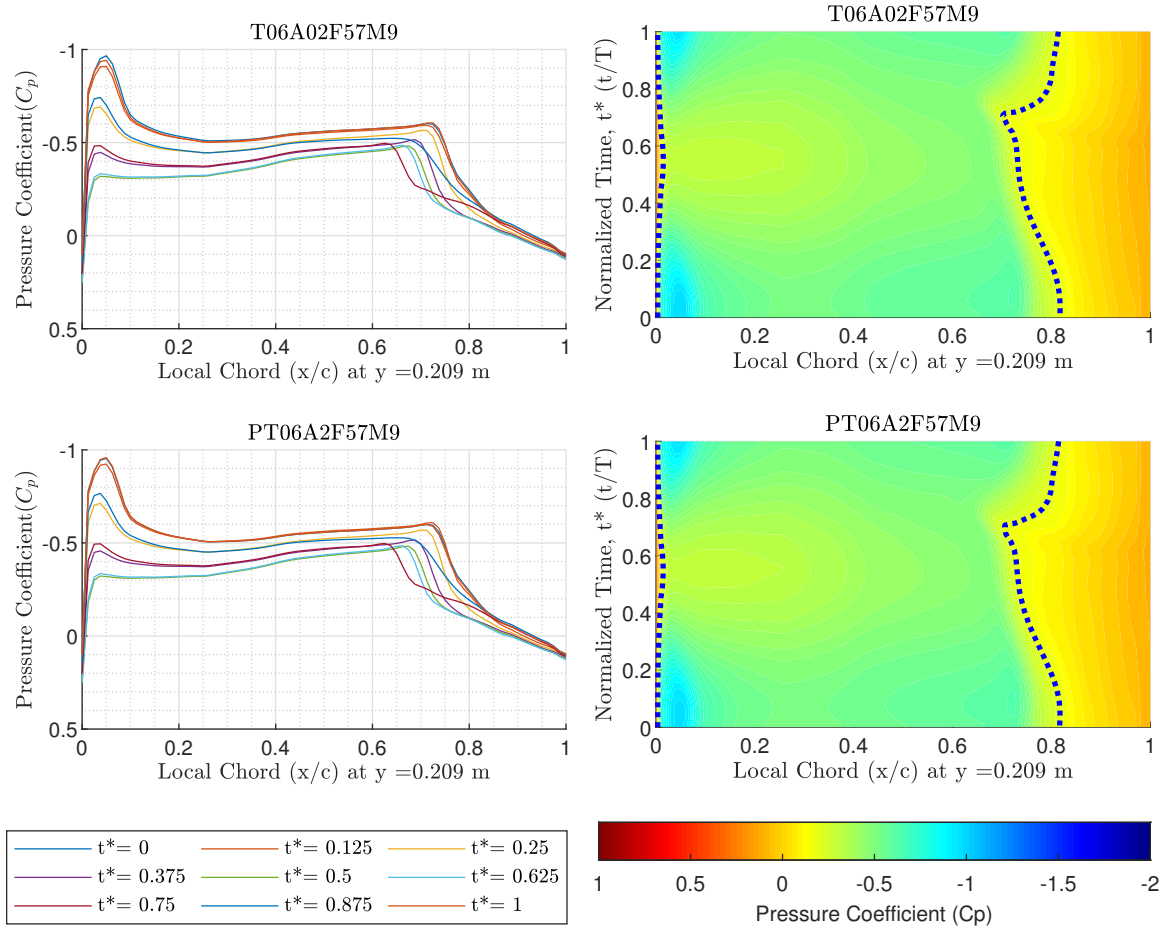


Figure A.17: Pressure distributions at Mach number 0.9. Frequency = 5.7 Hz, trim = 6°, amplitude = 2°. The Bottom plot used a +cosine function.

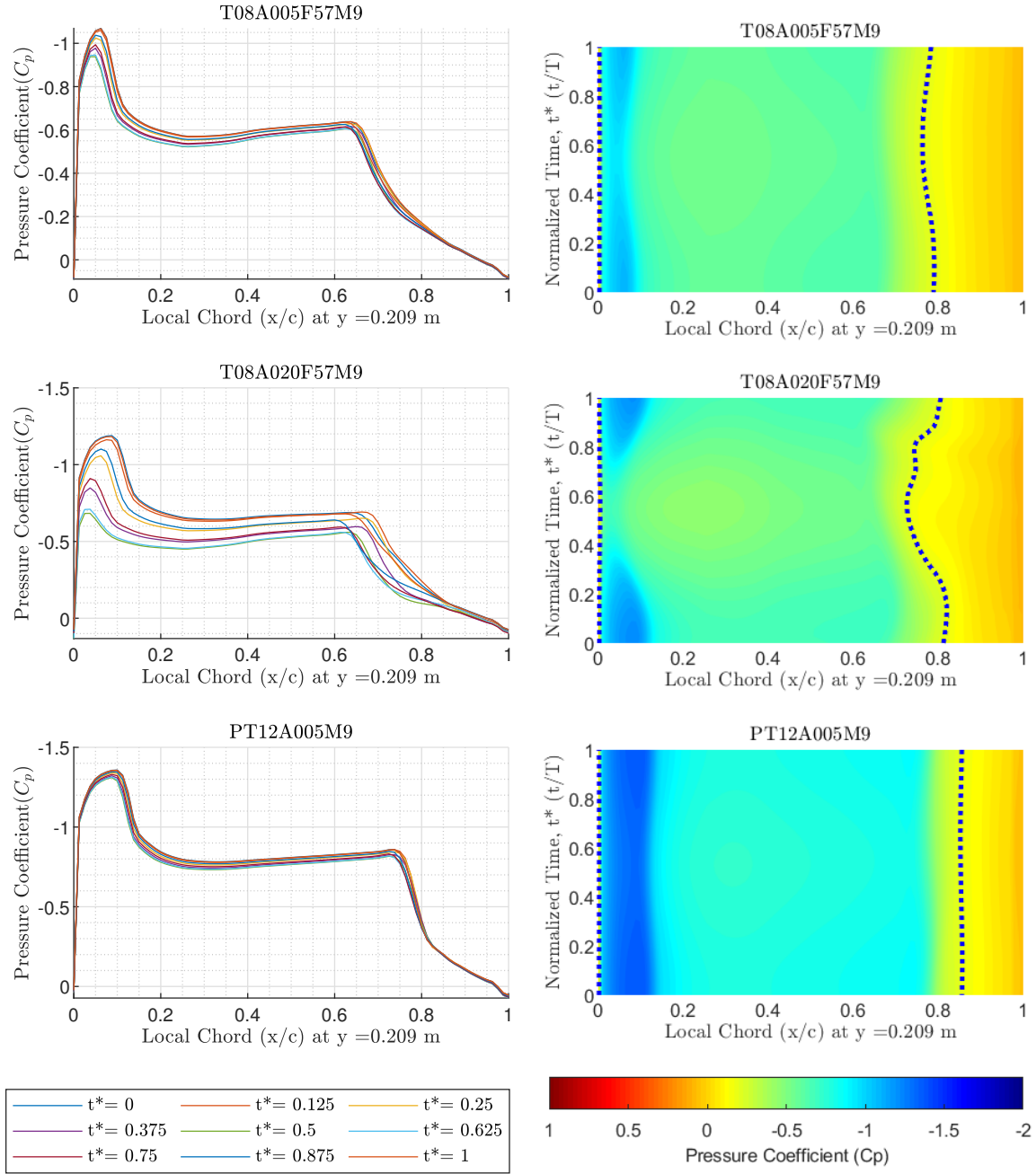


Figure A.18: Pressure distributions at Mach number 0.9. Frequency = 5.7 Hz, Top and middle plots had trim = 8° , amplitude = 0.5° & 2° . Bottom plots had trim = 12° , amplitude = 0.5° , & used a +cosine function.

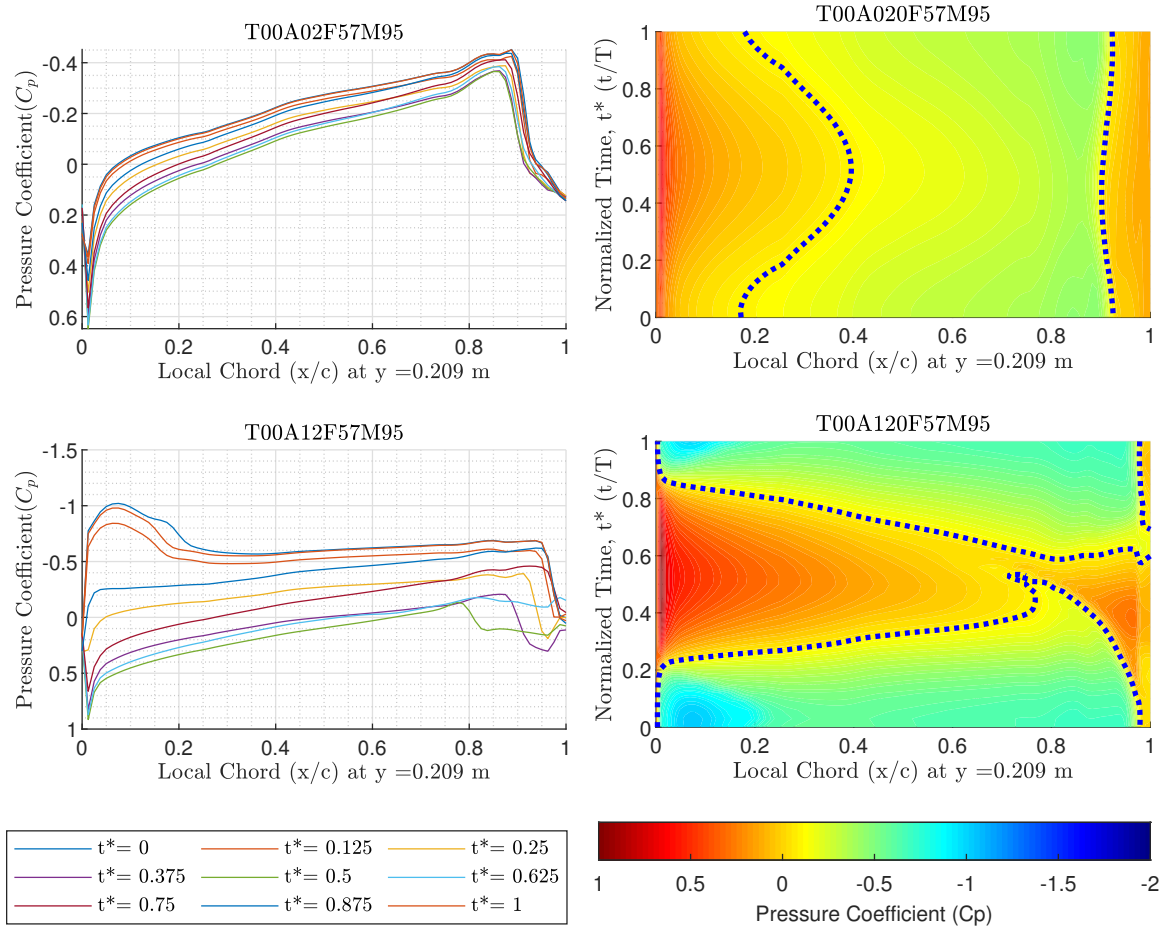


Figure A.19: Pressure distributions at Mach number 0.95. Frequency = 5.7 Hz, trim = 0°, amplitude = 2° & 12°

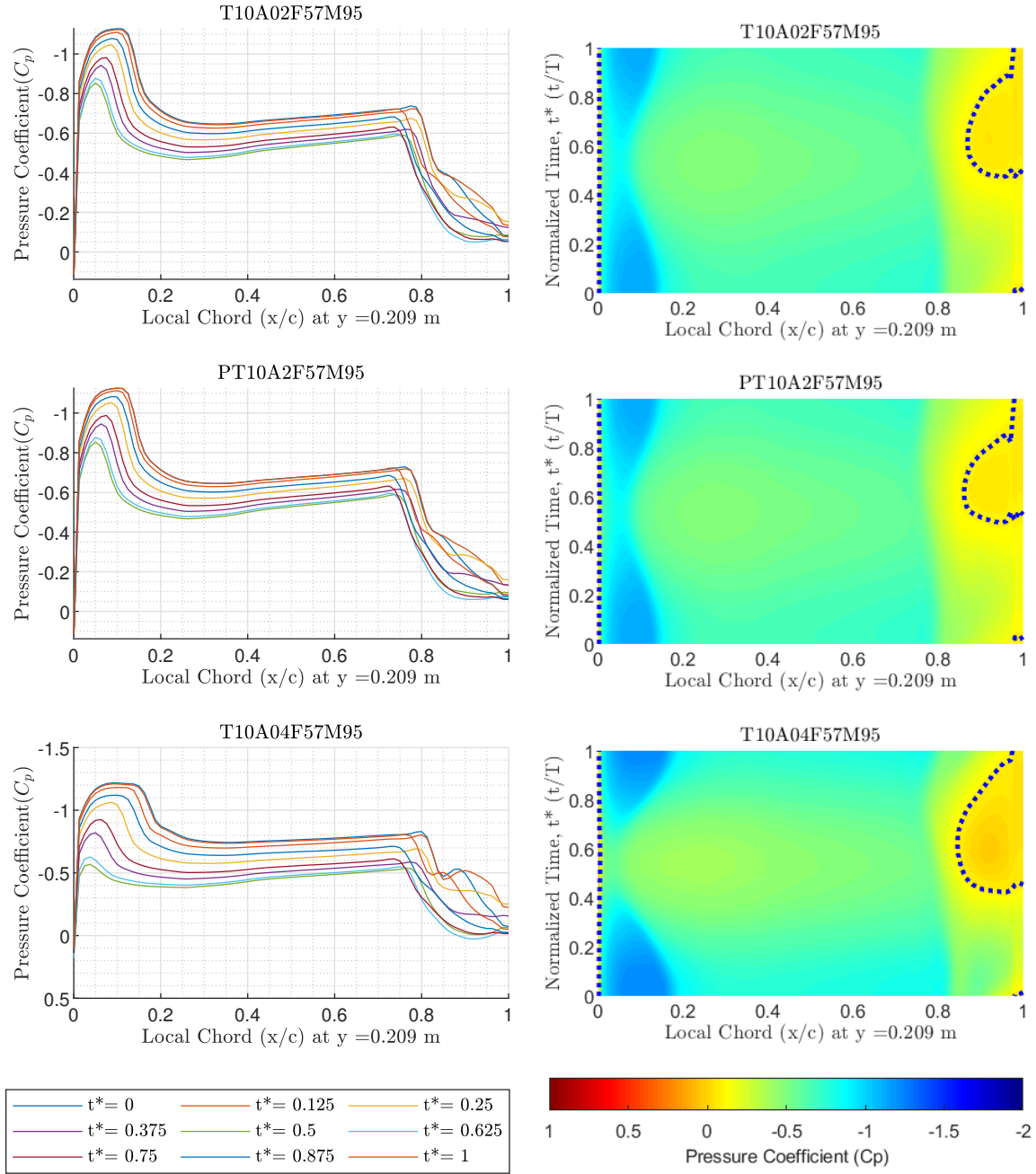


Figure A.20: Pressure distributions at Mach number 0.95. Frequency = 5.7 Hz, trim = 10°, amplitude = 2°, 2°, & 4°. Middle plots used a +cosine function.

Appendix B. C_p Data for Wing Station 2

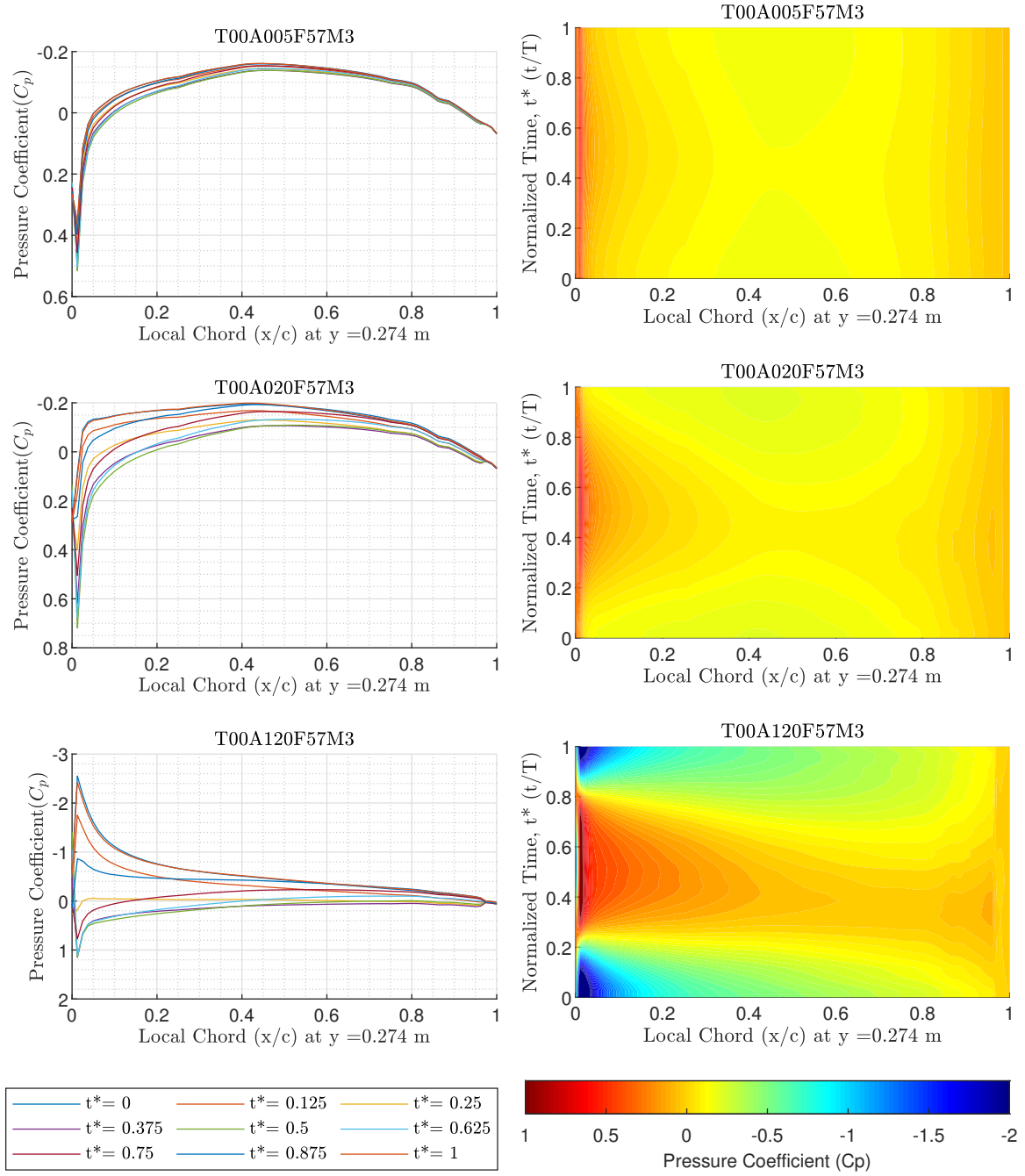


Figure B.1: Pressure distributions at Mach number 0.3. Frequency = 5.7 Hz, trim = 0° , amplitude = 0.5° , 2° , & 12°

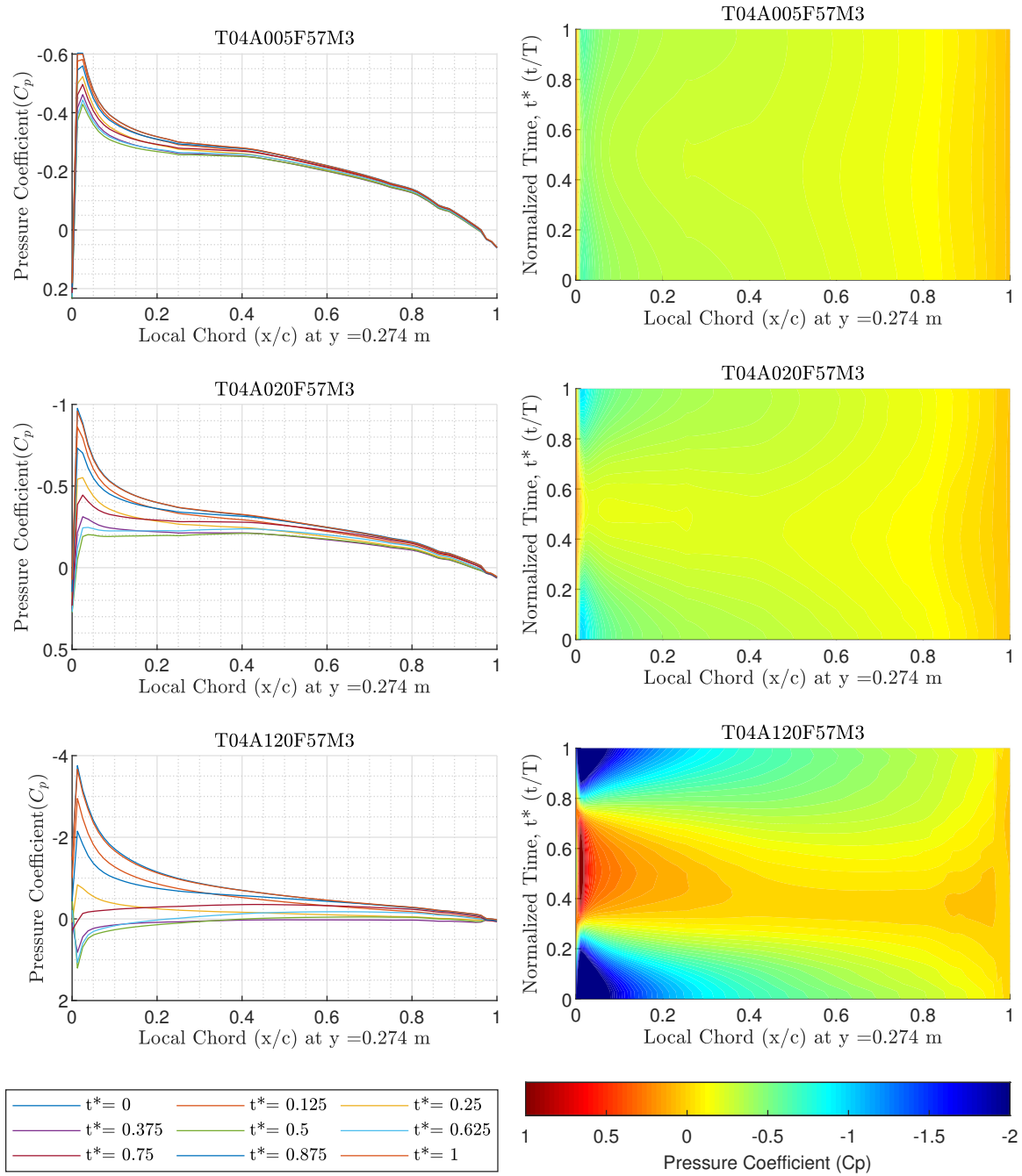


Figure B.2: Pressure distributions at Mach number 0.3. Frequency = 5.7 Hz, trim = 4°, amplitude = 0.5°, 2°, & 12°

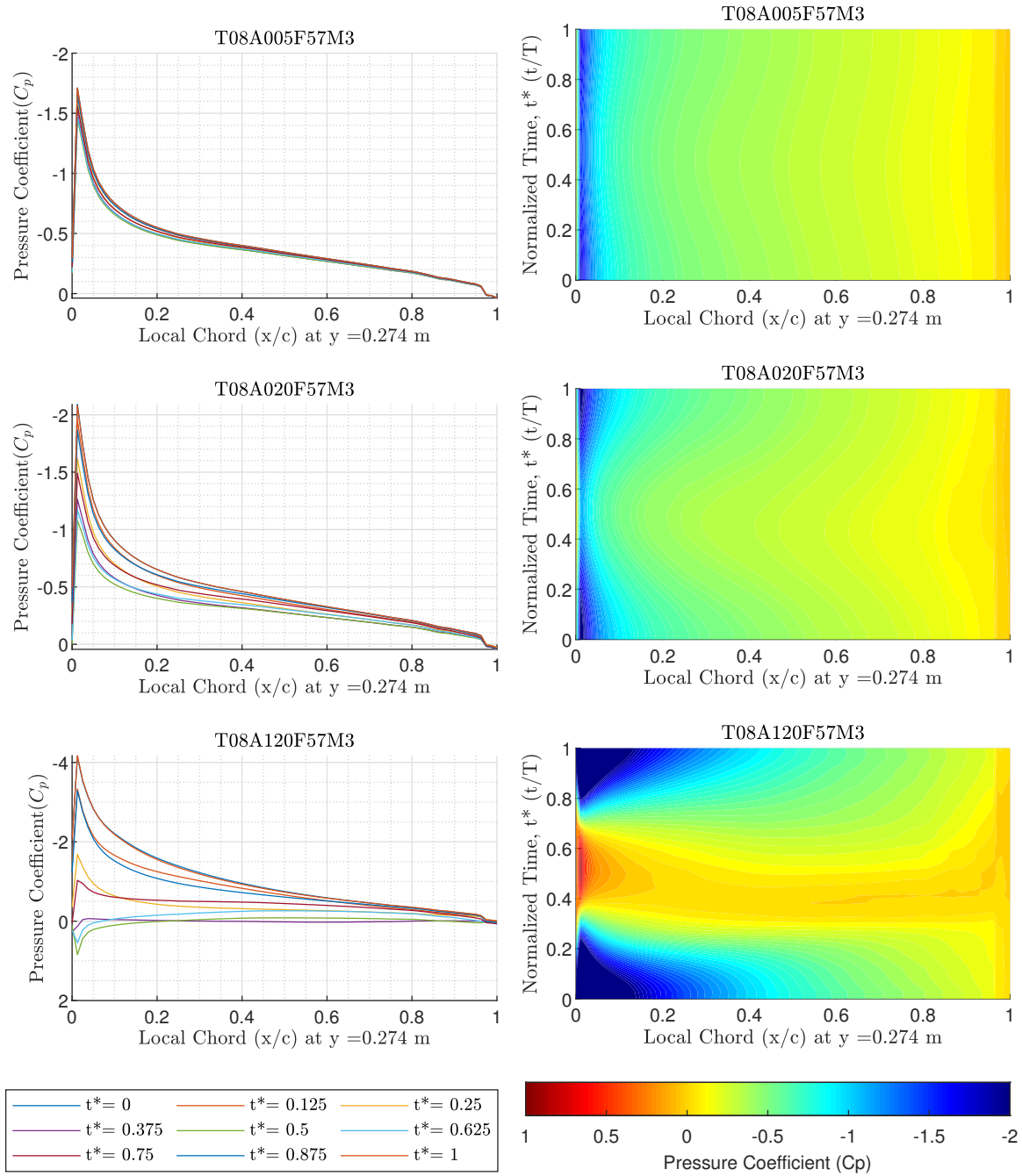


Figure B.3: Pressure distributions at Mach number 0.3. Frequency = 5.7 Hz, trim = 8° , amplitude = 0.5° , 2° , & 12°

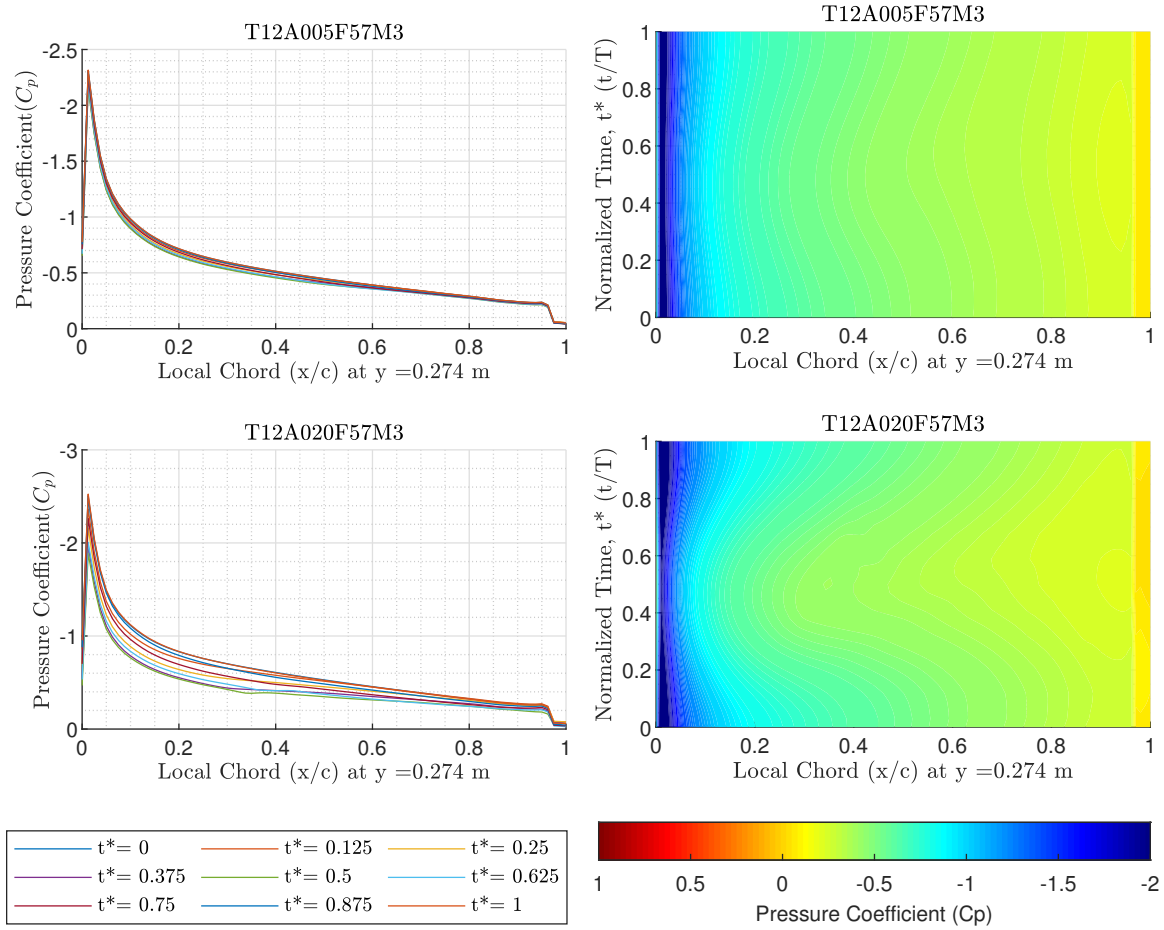


Figure B.4: Pressure distributions at Mach number 0.3. Frequency = 5.7 Hz, trim = 12°, amplitude = 0.5° & 2°

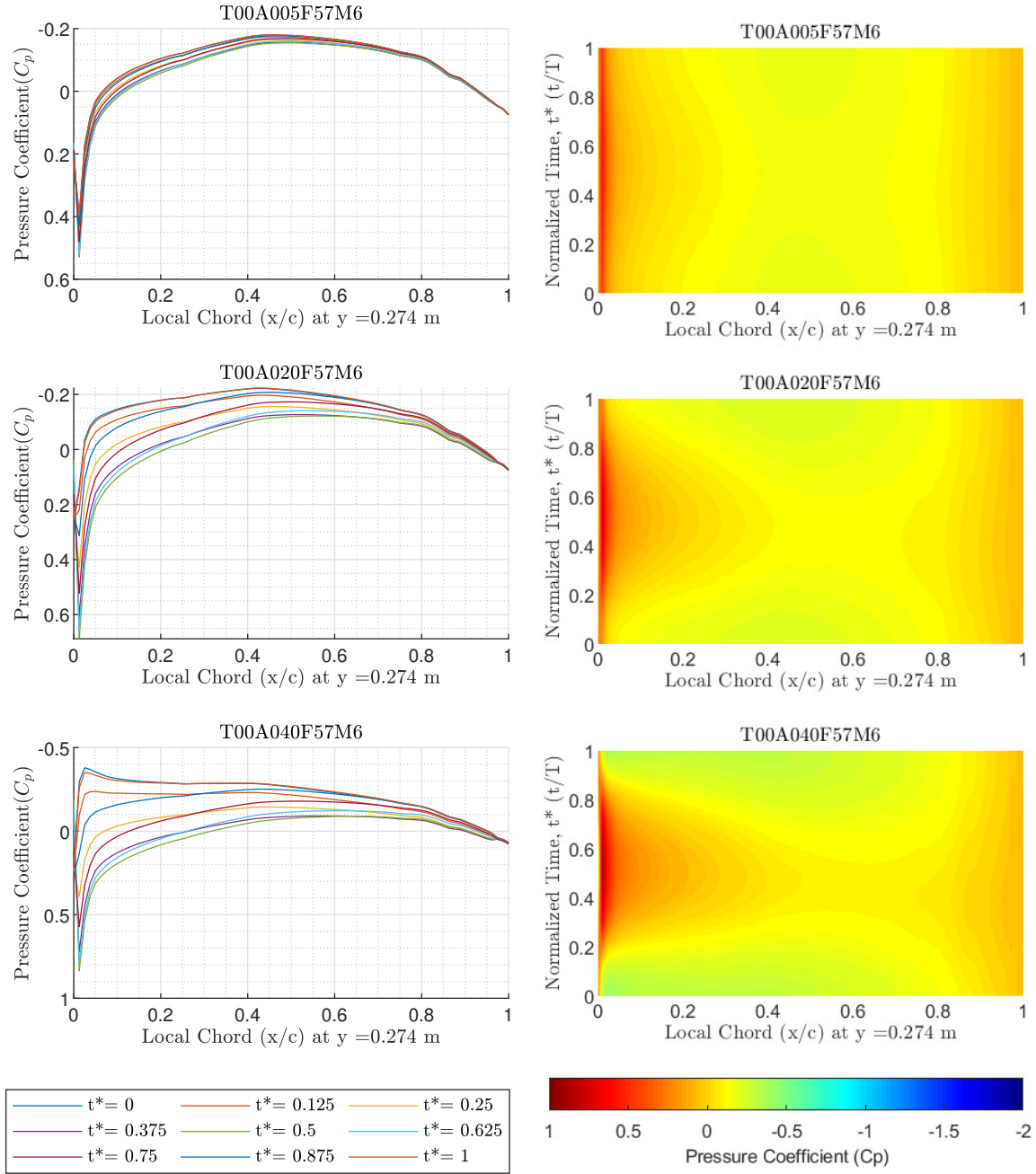


Figure B.5: Pressure distributions at Mach number 0.6. Frequency = 5.7 Hz, trim = 0°, amplitude = 0.5°, 2°, & 4°

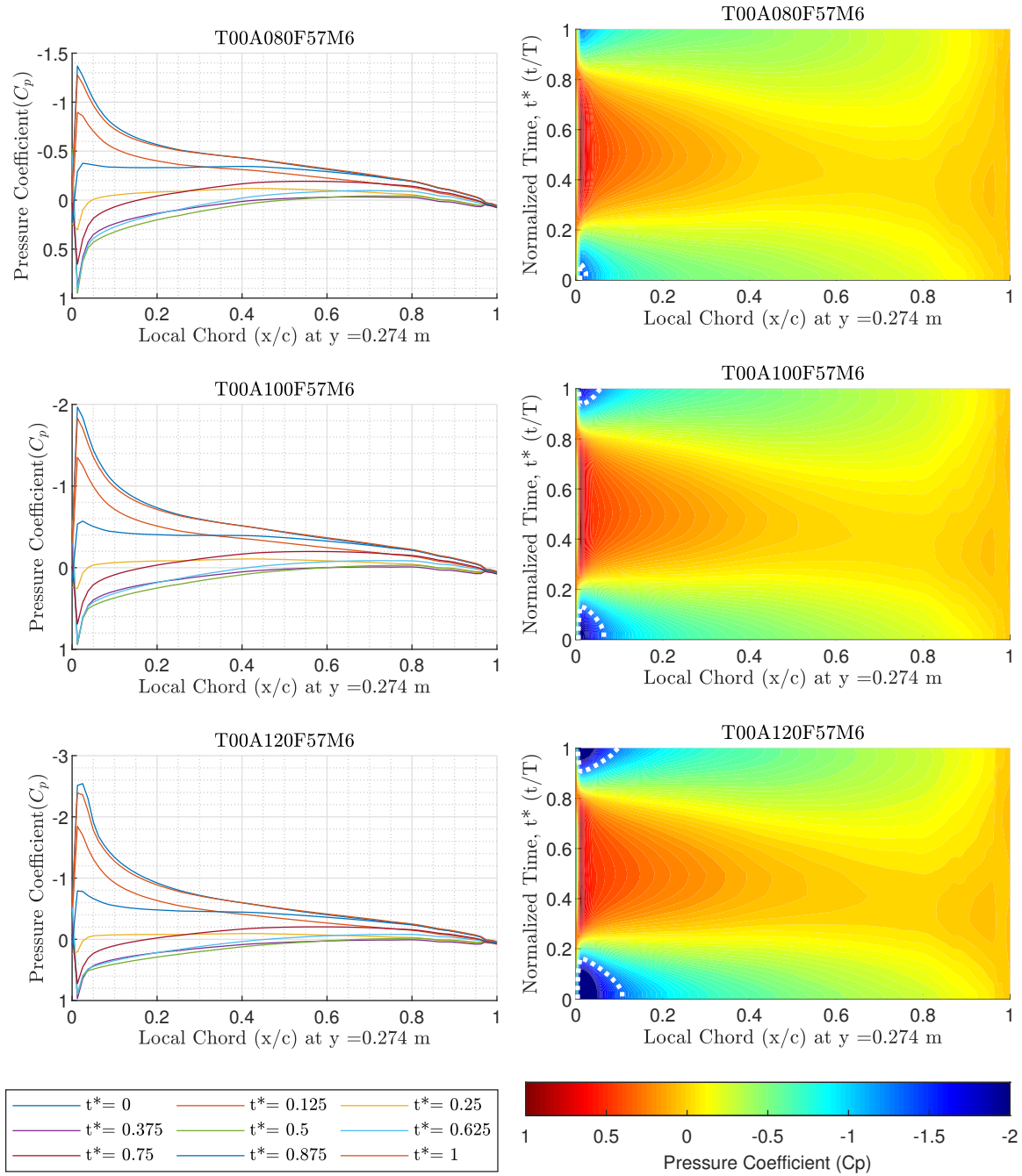


Figure B.6: Pressure distributions at Mach number 0.6. Frequency = 5.7 Hz, trim = 0°, amplitude = 8°, 10°, & 12°

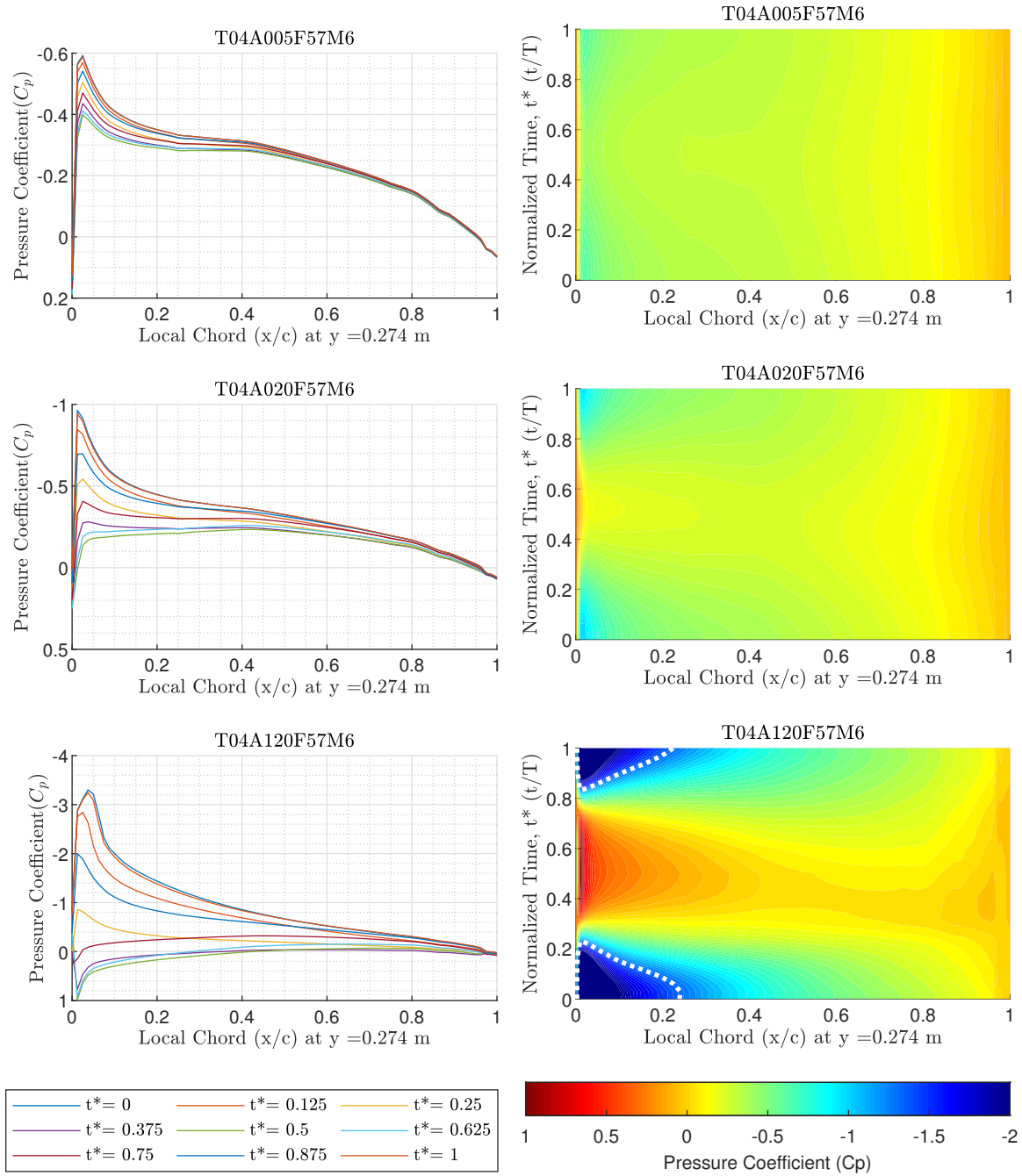


Figure B.7: Pressure distributions at Mach number 0.6. Frequency = 5.7 Hz, trim = 4°, amplitude = 0.5°, 2°, & 12°

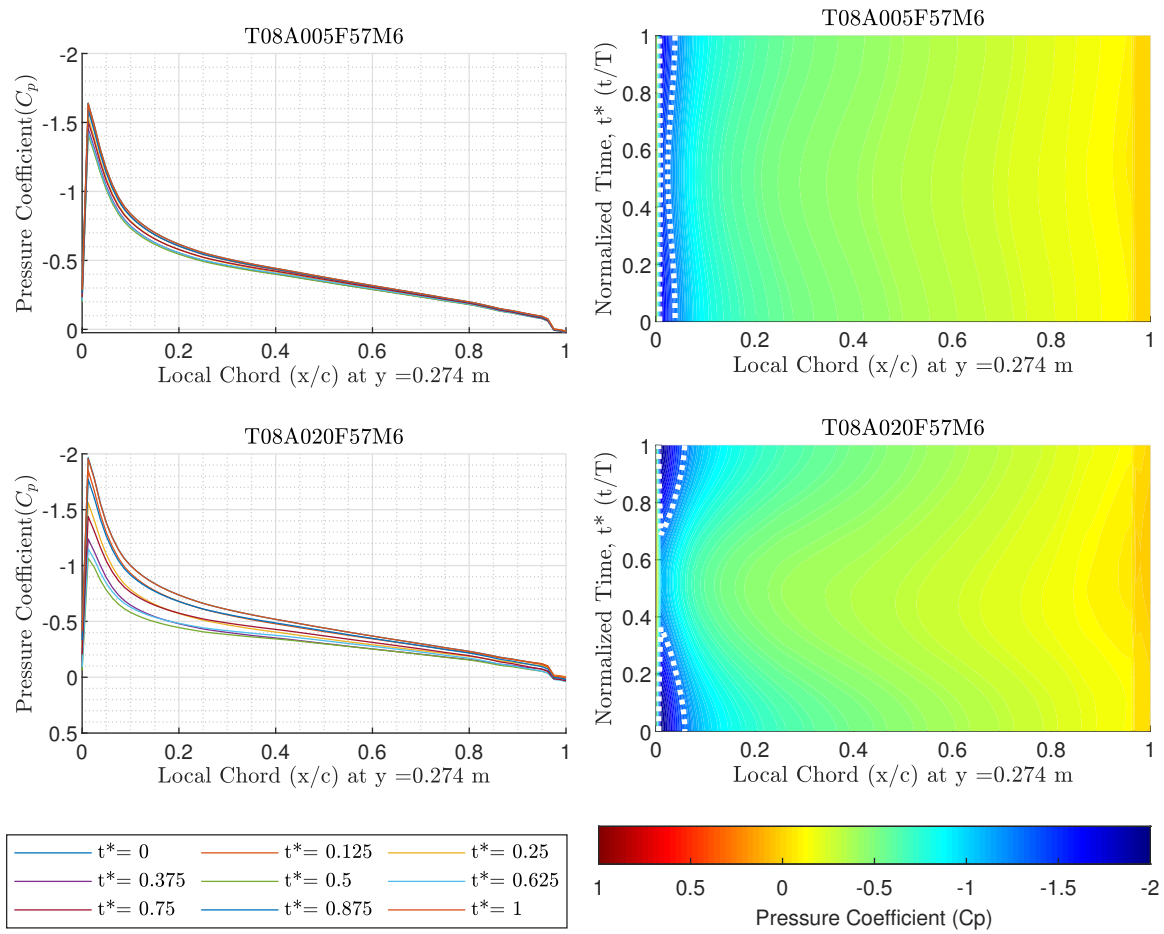


Figure B.8: Pressure distributions at Mach number 0.6. Frequency = 5.7 Hz, trim = 8°, amplitude = 0.5° & 2°

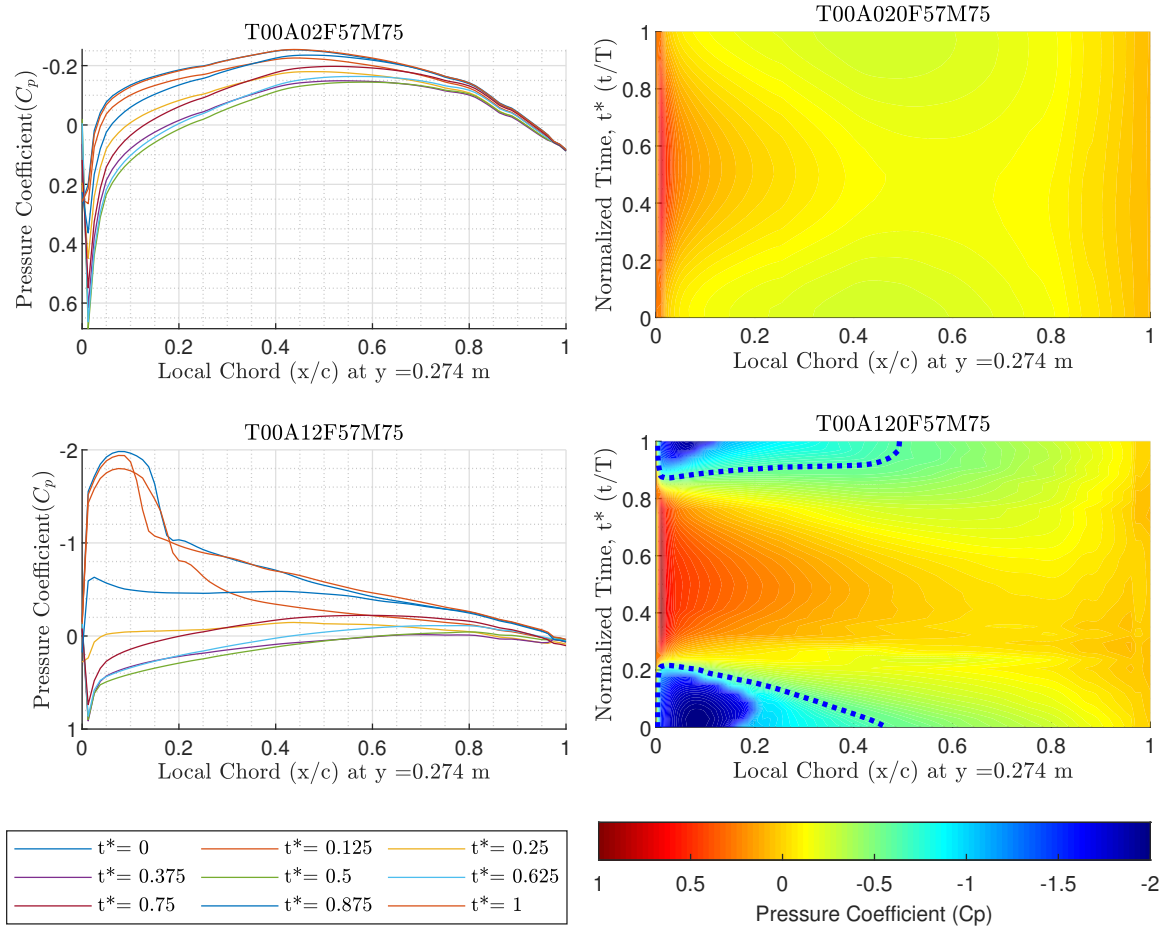


Figure B.9: Pressure distributions at Mach number 0.75. Frequency = 5.7 Hz, trim = 0°, amplitude = 2° & 12°

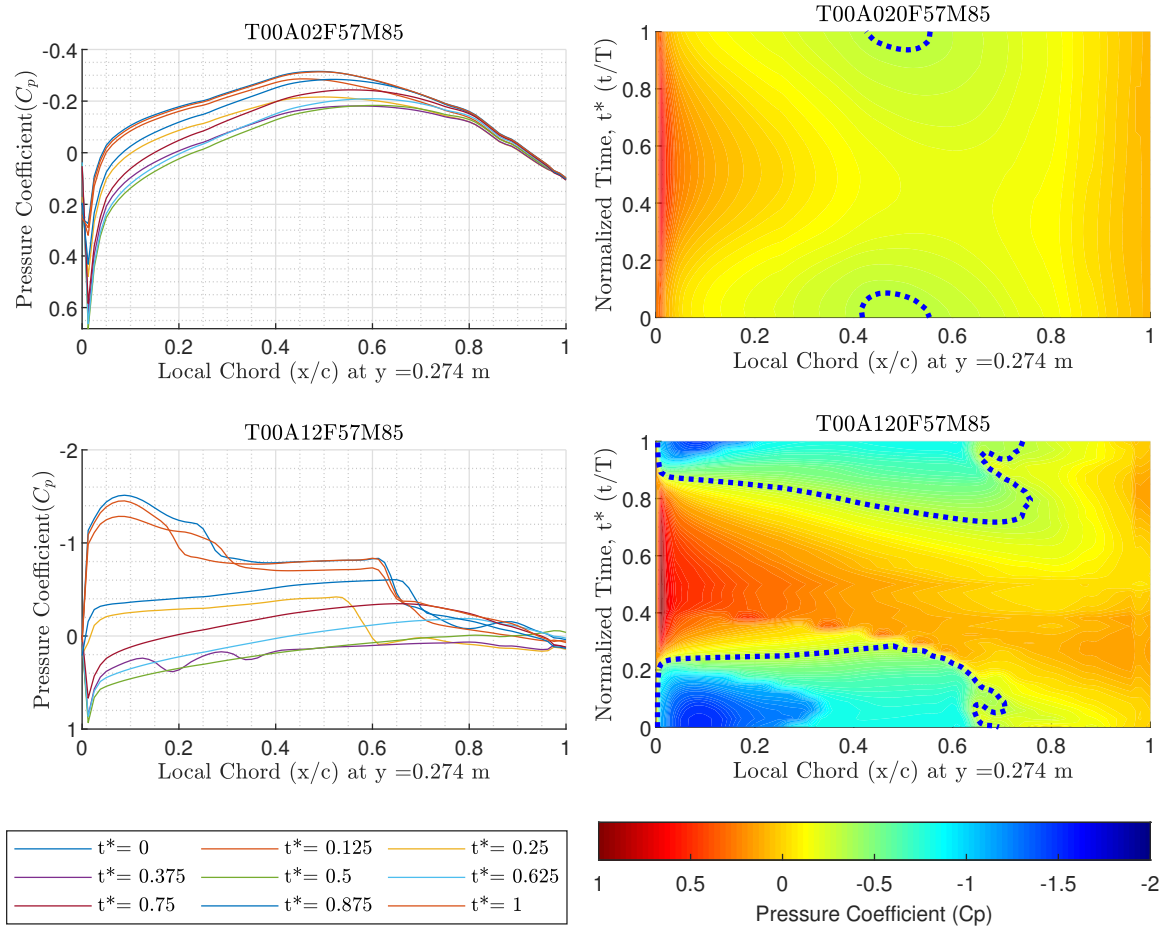


Figure B.10: Pressure distributions at Mach number 0.85. Frequency = 5.7 Hz, trim = 0°, amplitude = 2° & 12°

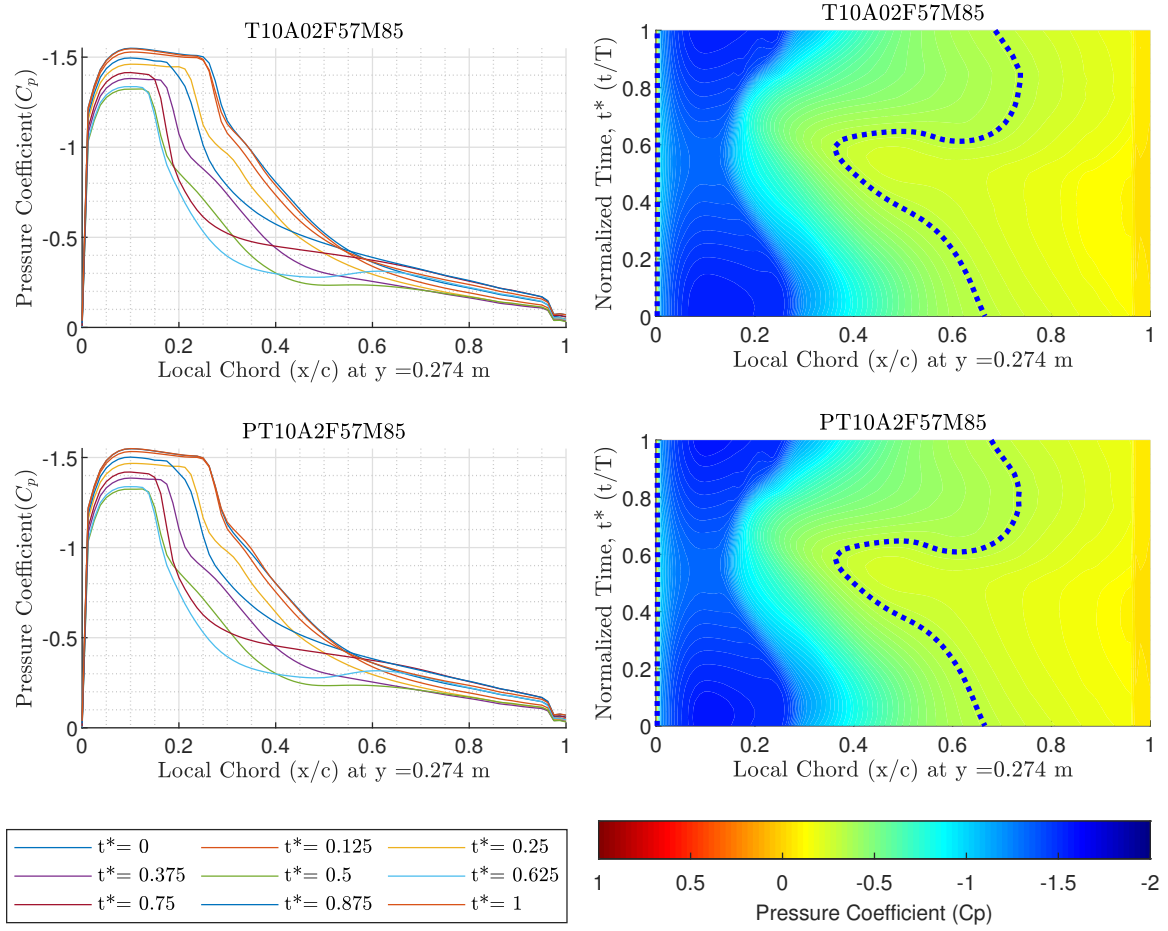
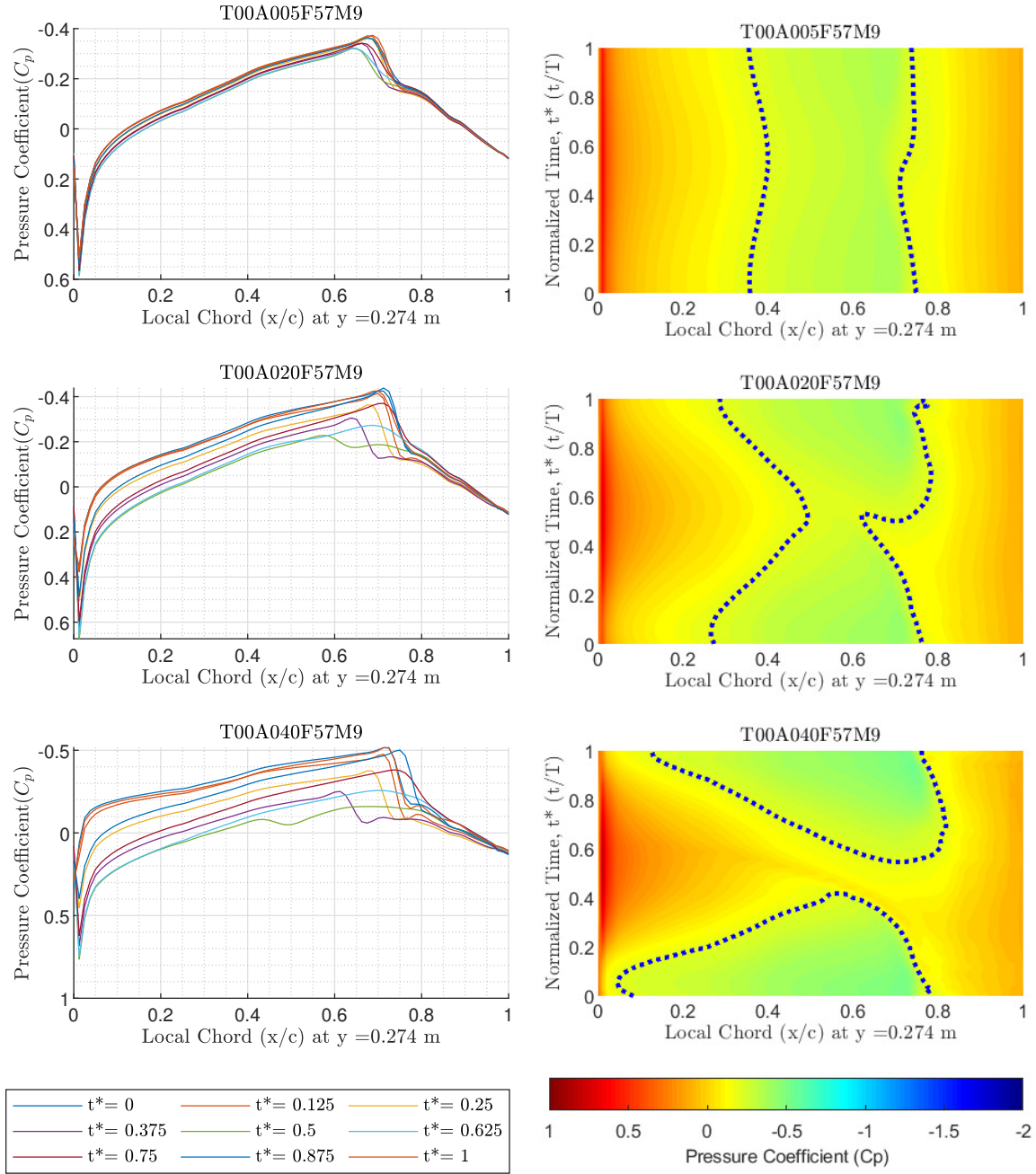


Figure B.11: Pressure distributions at Mach number 0.85. Frequency = 5.7 Hz, trim = 0°, amplitude = 2°. Top used -cosine function, and bottom used +cosine function.



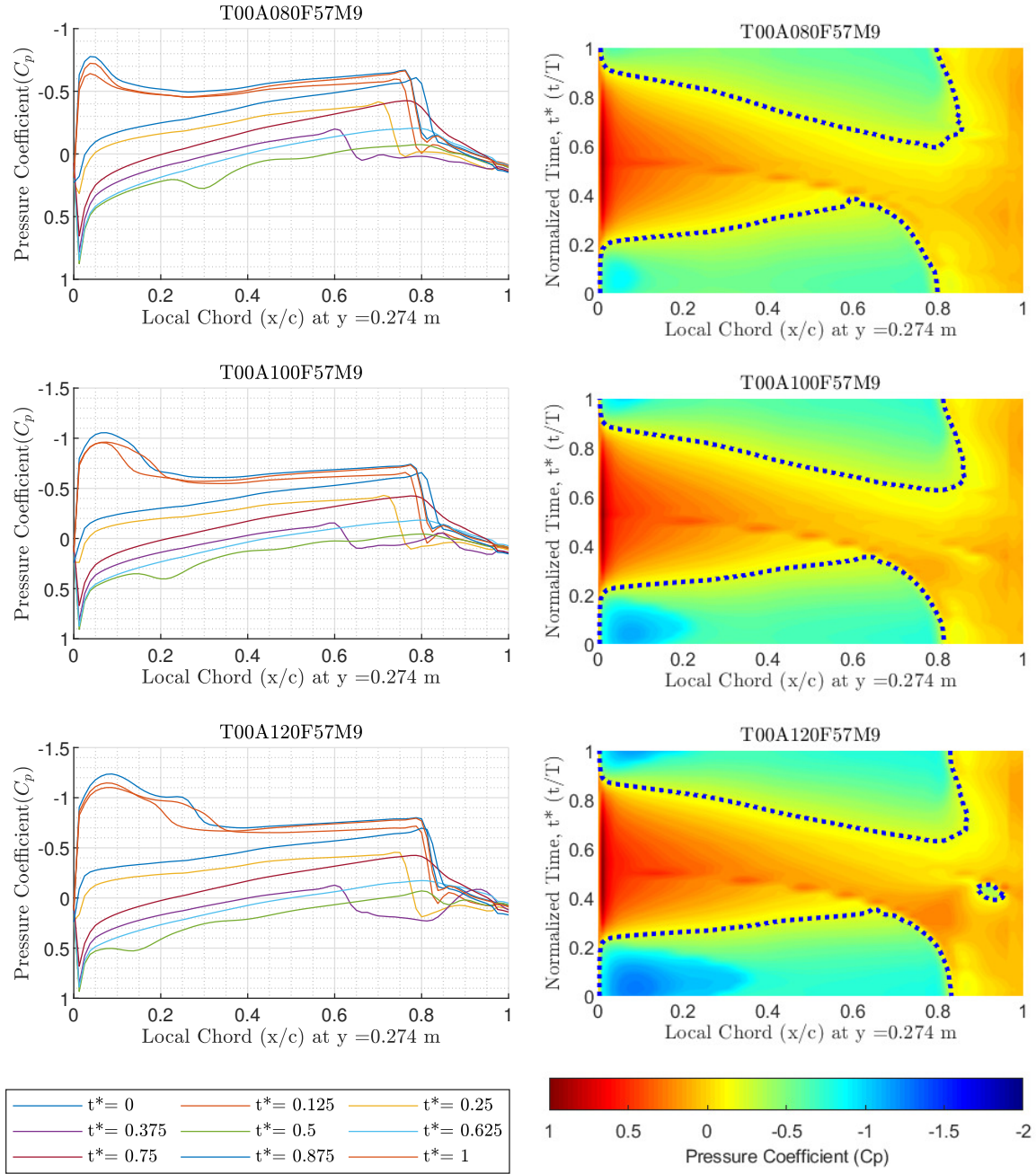


Figure B.13: Pressure distributions at Mach number 0.9. Frequency = 5.7 Hz, trim = 0°, amplitude = 8°, 10°, & 12°

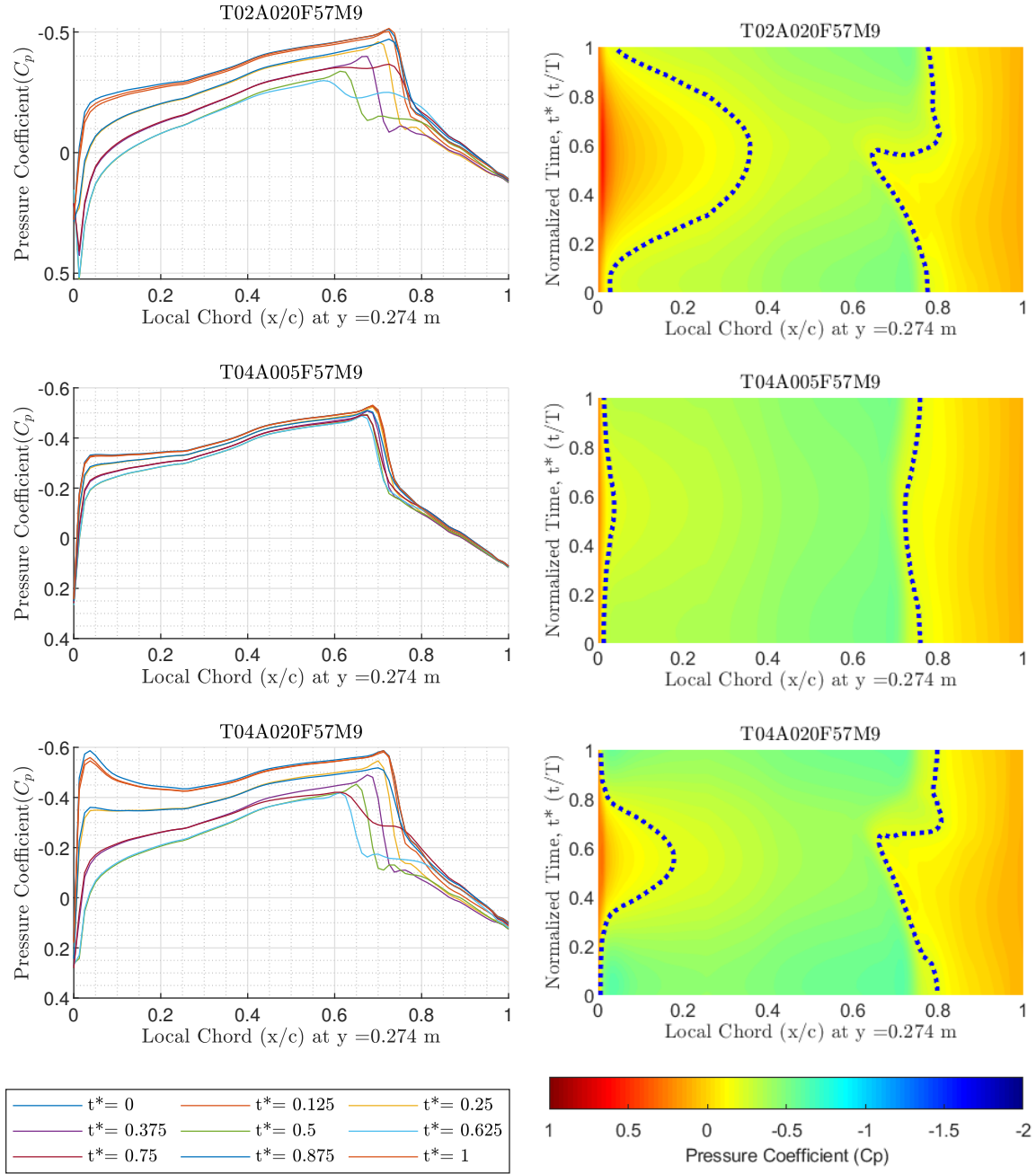


Figure B.14: Pressure distributions at Mach number 0.9. Frequency = 5.7 Hz, (Top) trim = 2° & amplitude = 2° , (middle & bottom) trim = 4° , amplitude = 0.5° & 2°

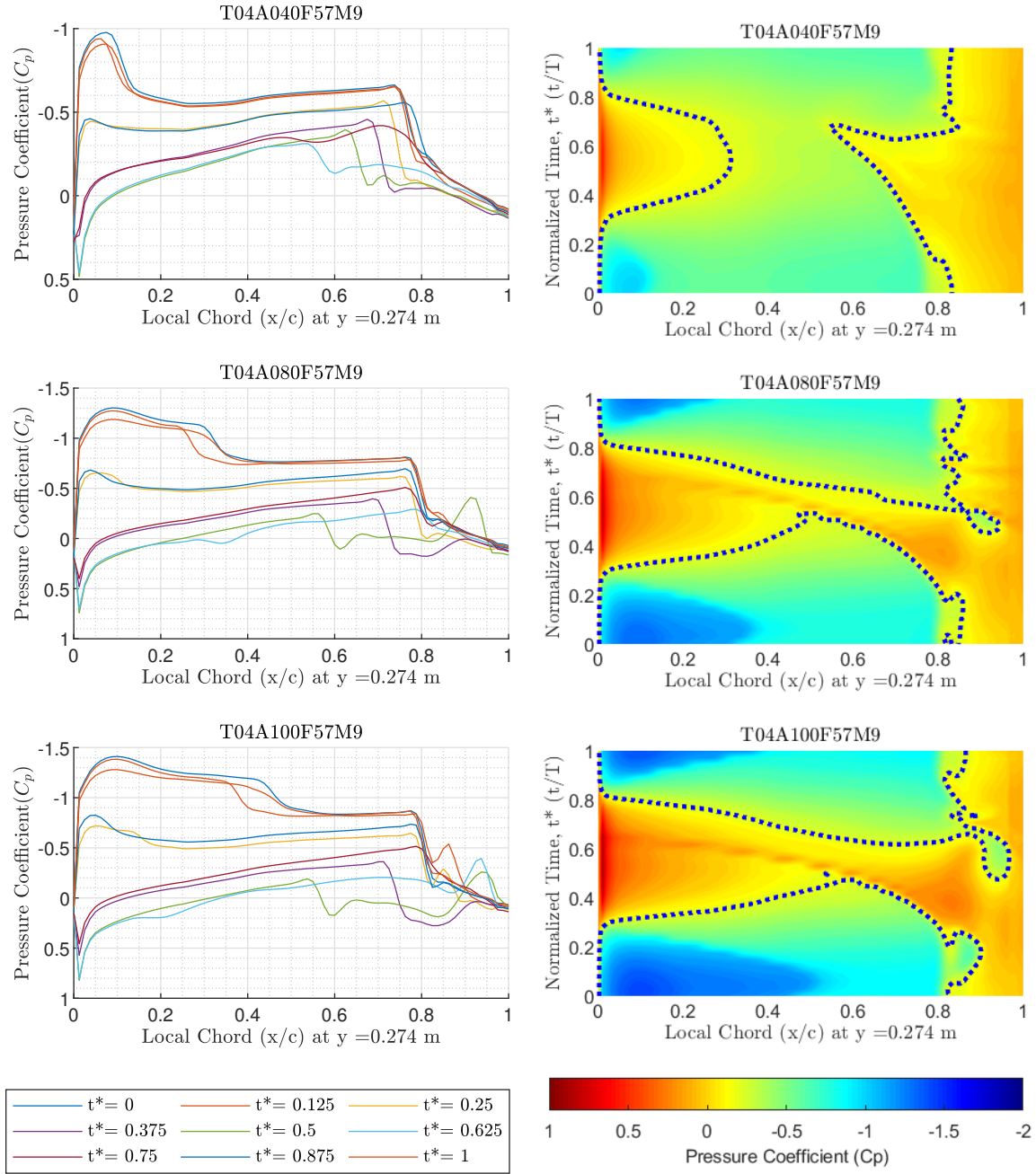


Figure B.15: Pressure distributions at Mach number 0.9. Frequency = 5.7 Hz, trim = 4°, amplitude = 4°, & 10°

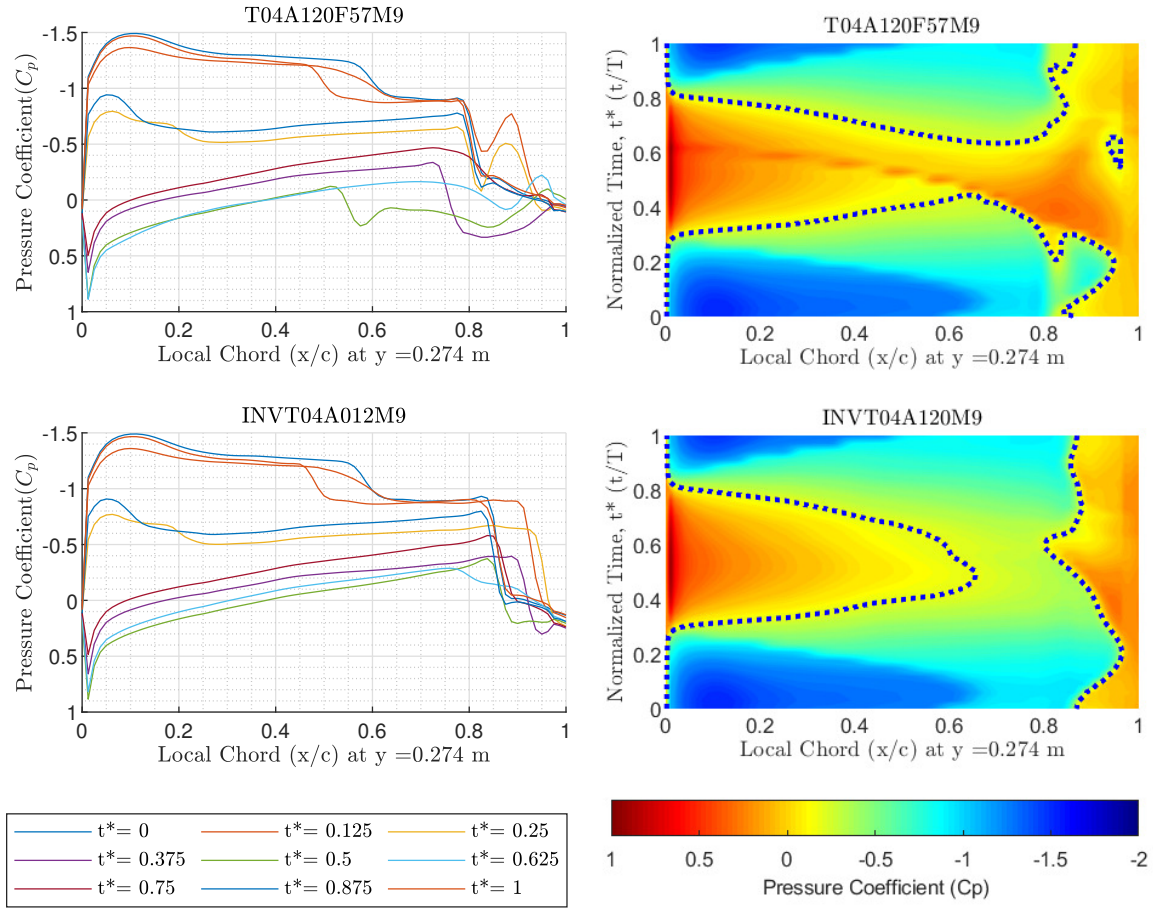


Figure B.16: Pressure distributions at Mach number 0.9. Frequency = 5.7 Hz, trim = 4°, amplitude = 12°. Top used BLC solver, and bottom used fully inviscid solver.

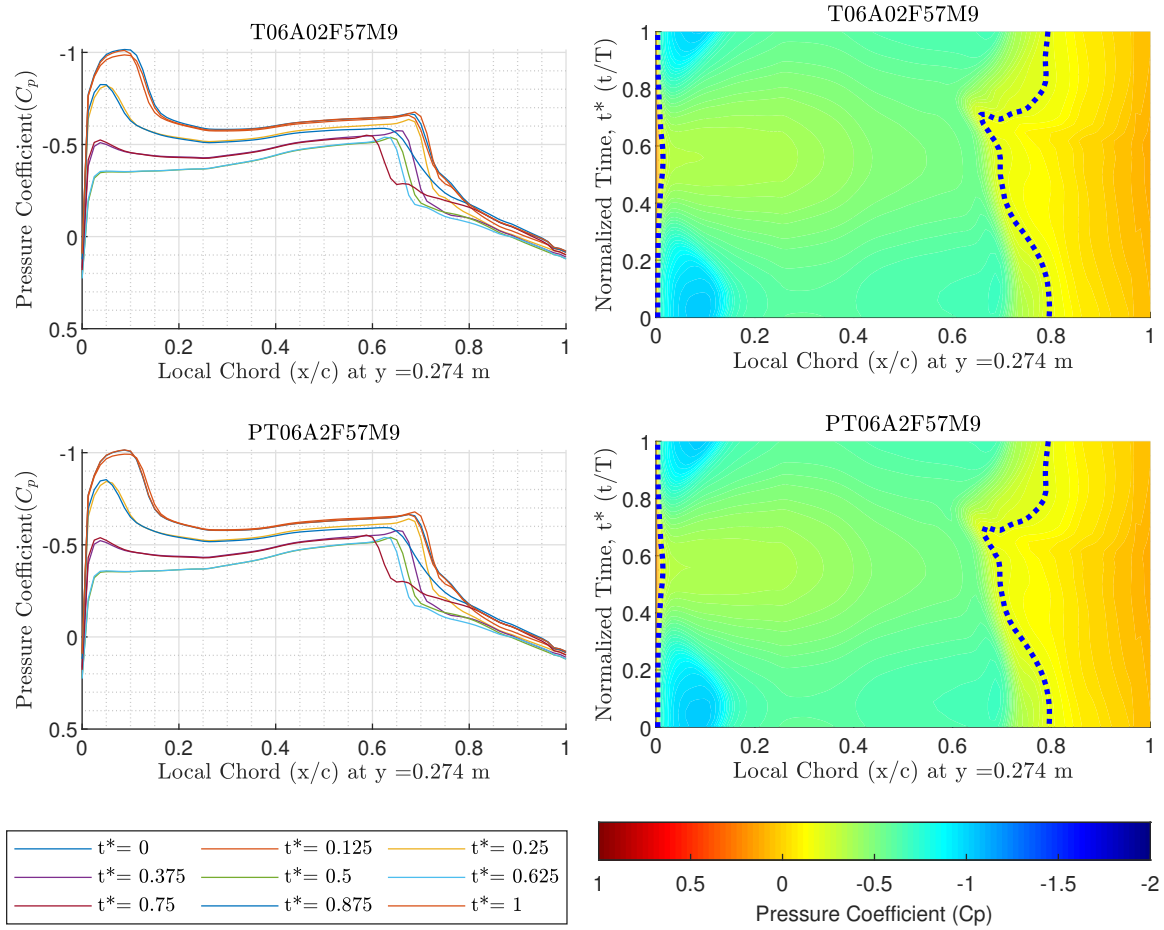


Figure B.17: Pressure distributions at Mach number 0.9. Frequency = 5.7 Hz, trim = 6°, amplitude = 2°. The Bottom plot used a +cosine function.

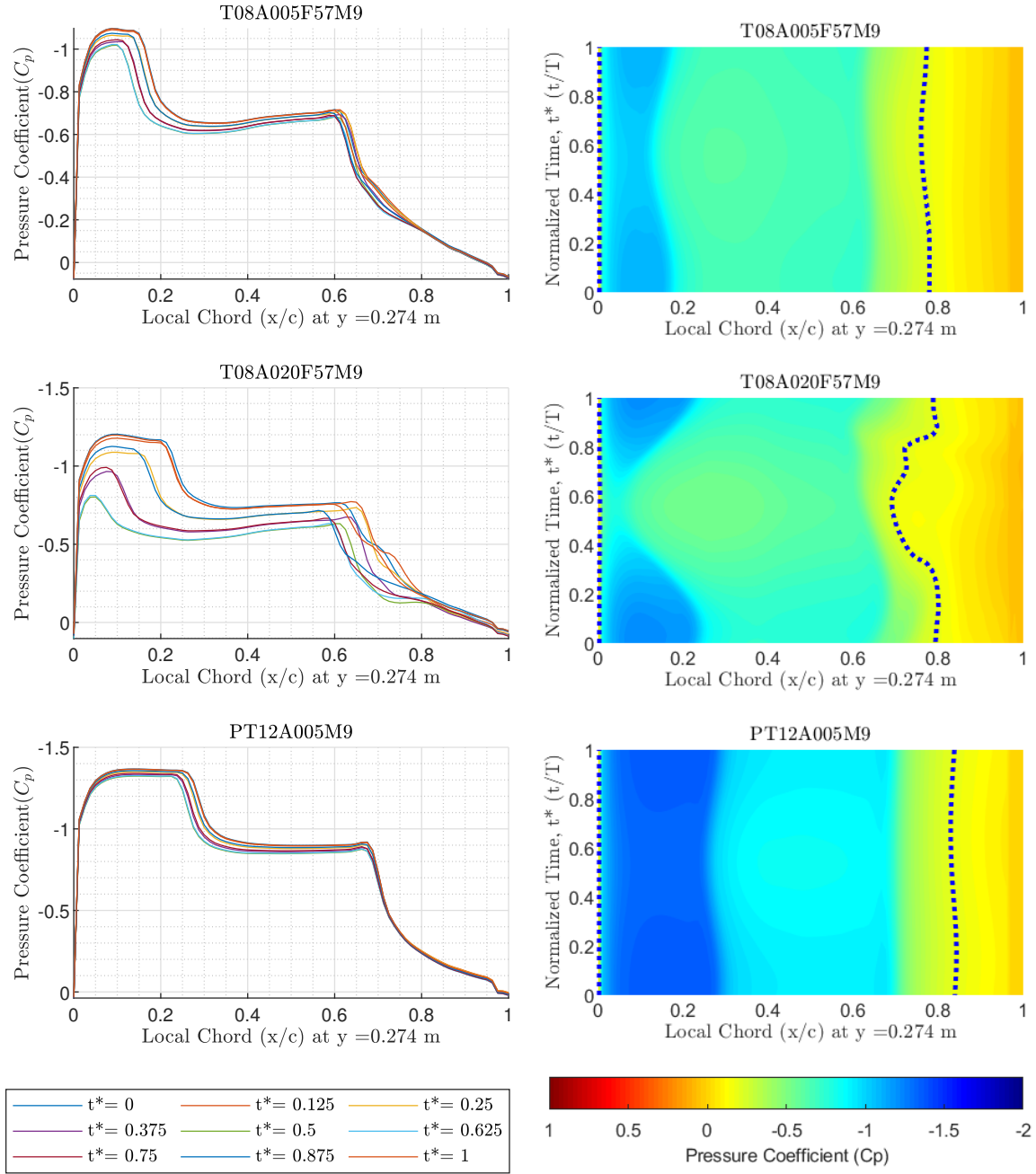


Figure B.18: Pressure distributions at Mach number 0.9. Frequency = 5.7 Hz, Top and middle plots had trim = 8° , amplitude = 0.5° & 2° . Bottom plots had trim = 12° , amplitude = 0.5° , & used a +cosine function.

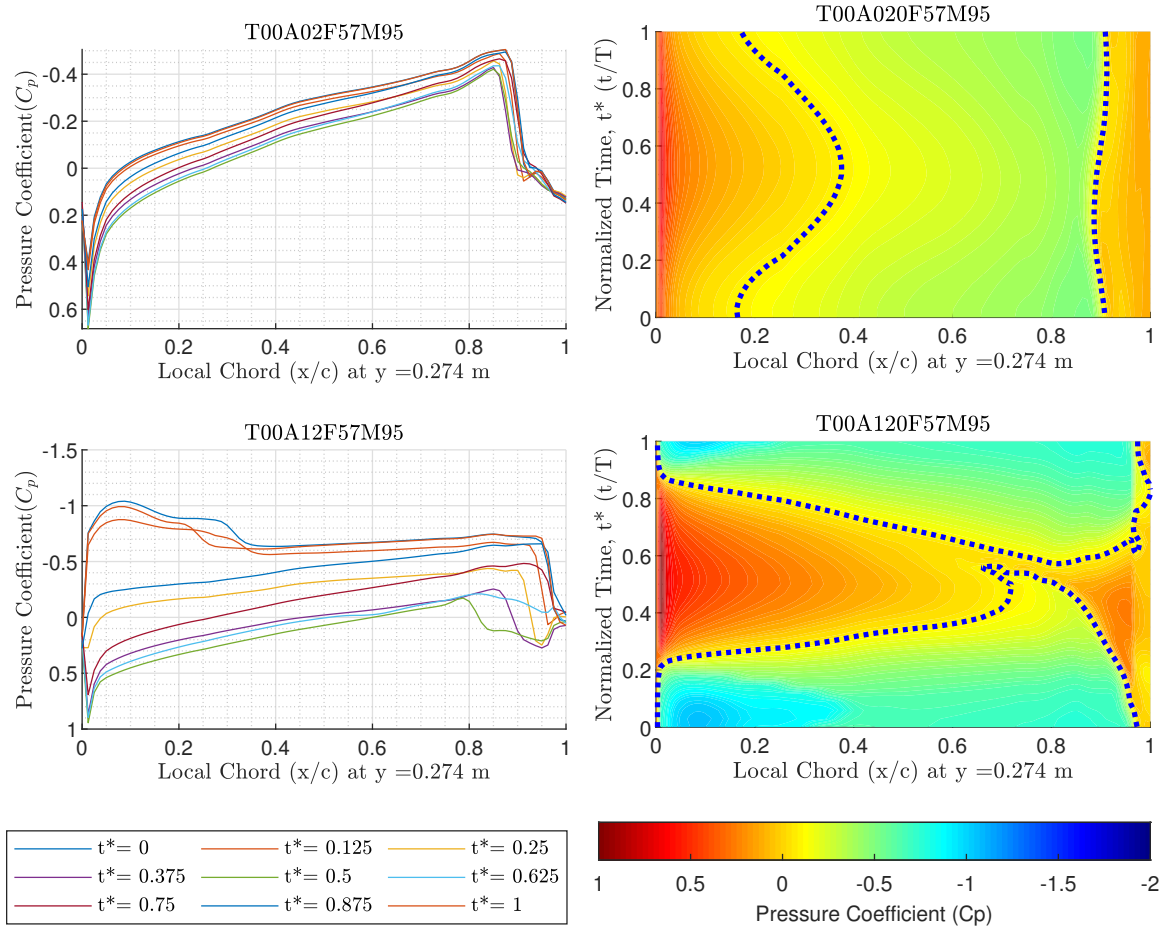


Figure B.19: Pressure distributions at Mach number 0.95. Frequency = 5.7 Hz, trim = 0°, amplitude = 2° & 12°

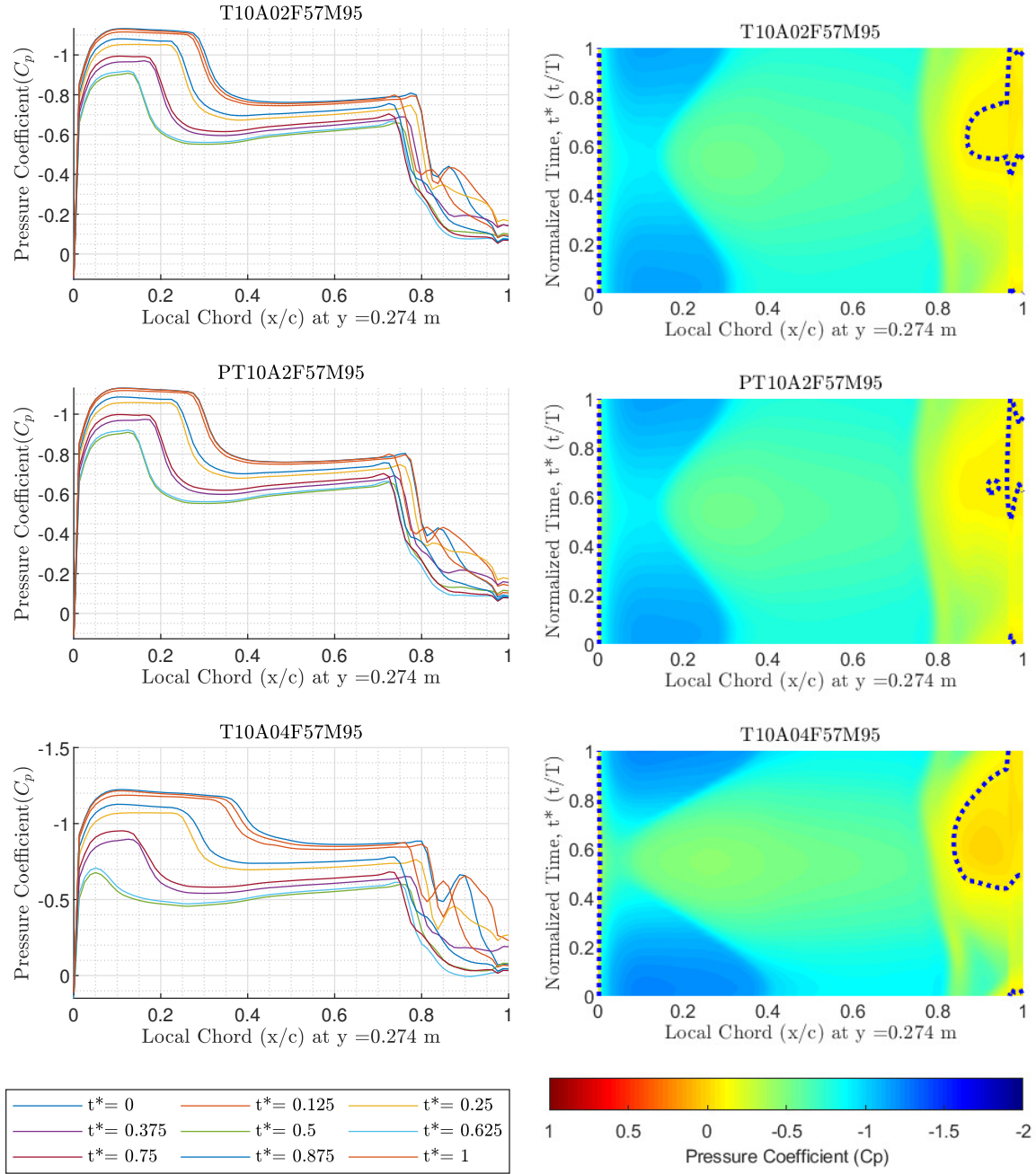


Figure B.20: Pressure distributions at Mach number 0.95. Frequency = 5.7 Hz, trim = 10° , amplitude = 2° , 2° , & 4° . Middle plots used a +cosine function.

Appendix C. C_p Data for Wing Station 3

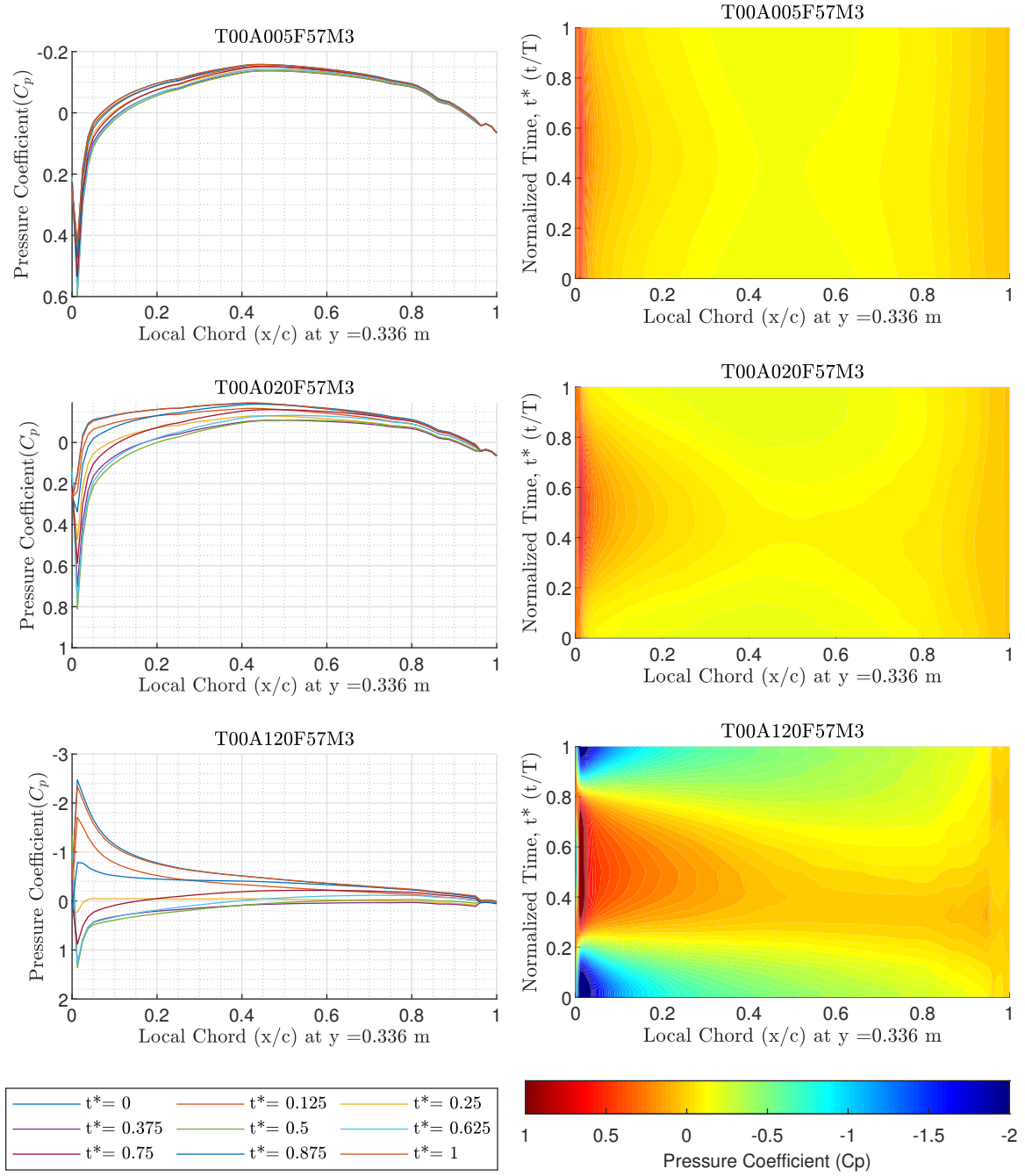


Figure C.1: Pressure distributions at Mach number 0.3. Frequency = 5.7 Hz, trim = 0°, amplitude = 0.5°, 2°, & 12°

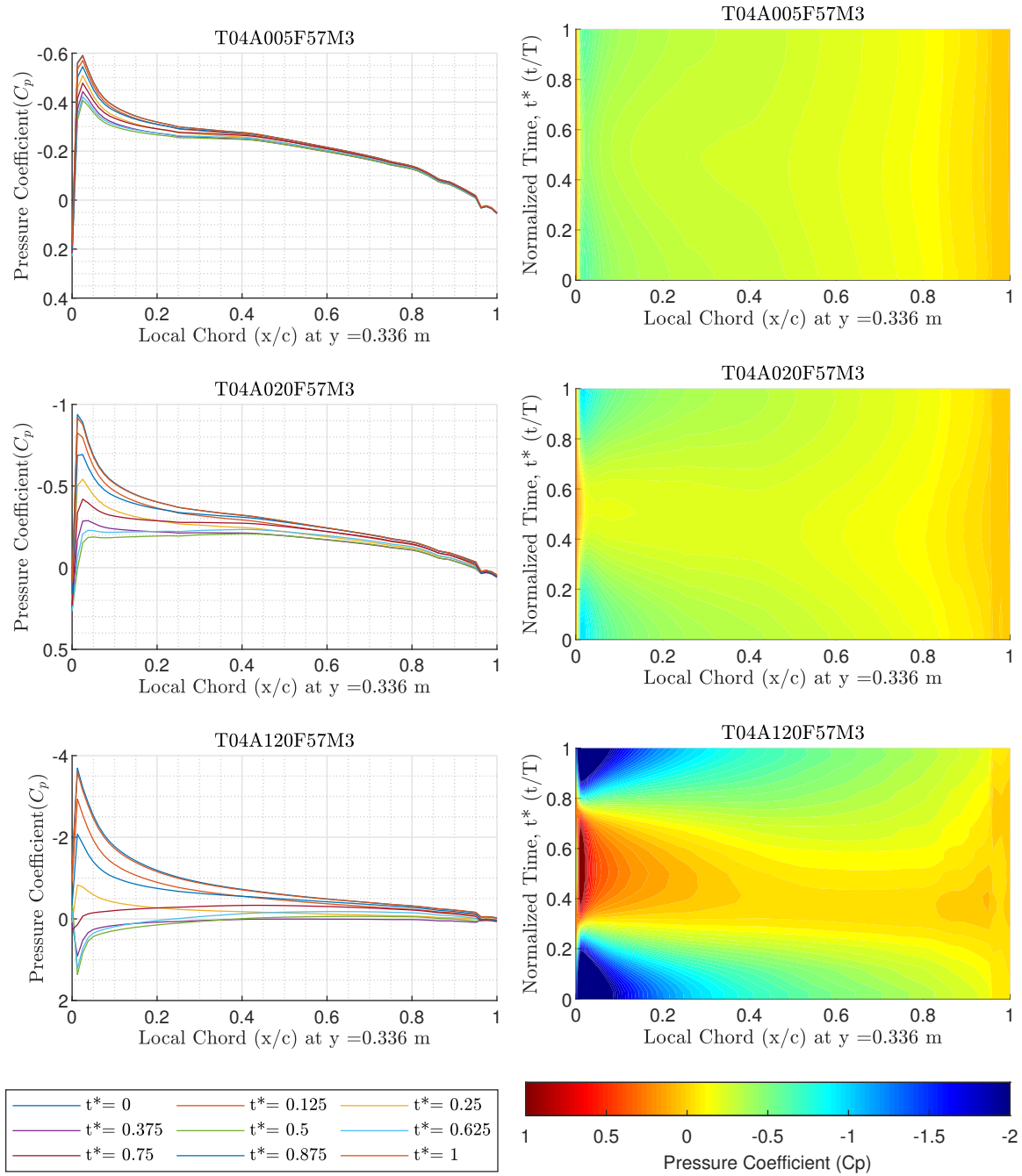


Figure C.2: Pressure distributions at Mach number 0.3. Frequency = 5.7 Hz, trim = 4°, amplitude = 0.5°, 2°, & 12°

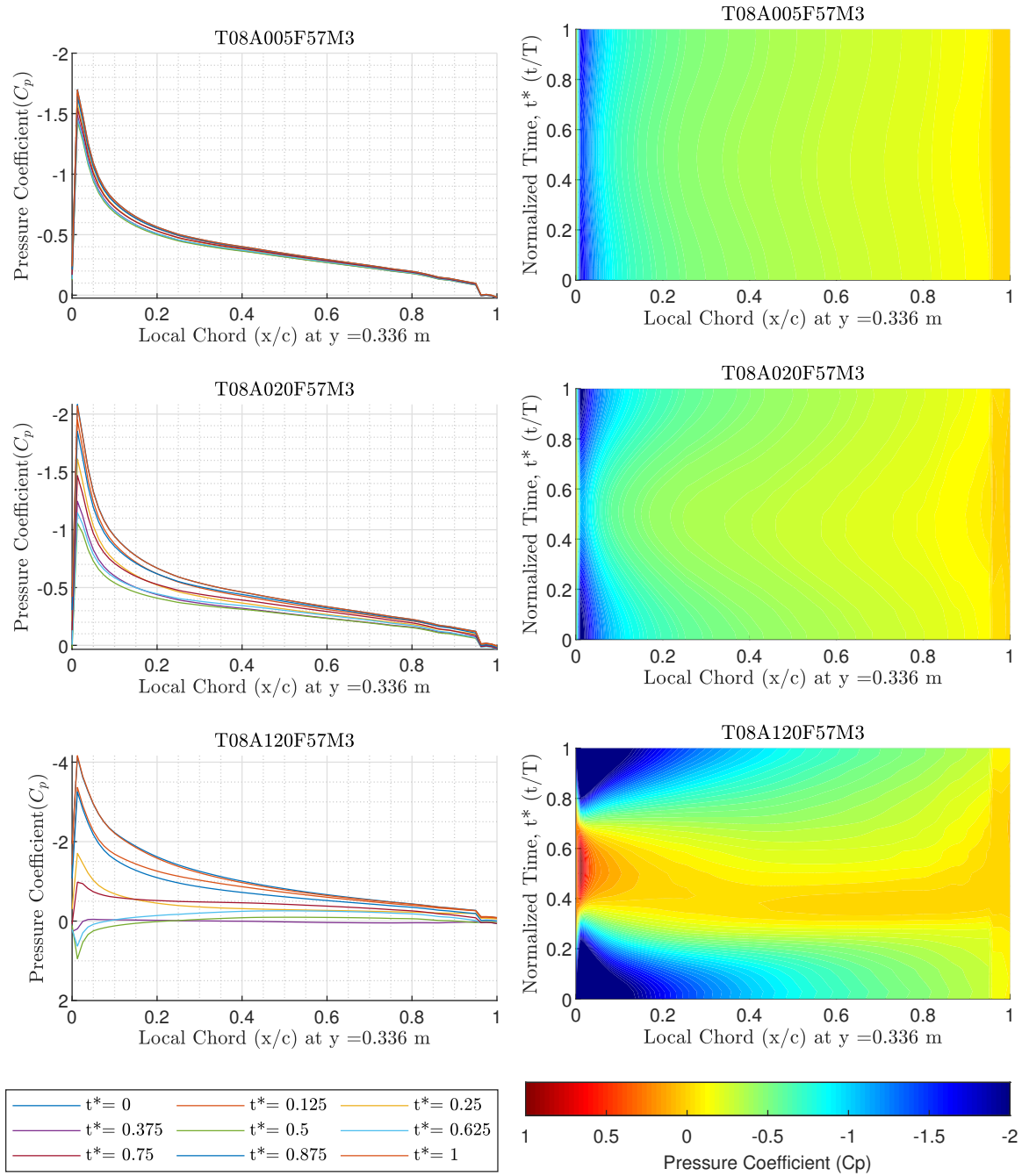


Figure C.3: Pressure distributions at Mach number 0.3. Frequency = 5.7 Hz, trim = 8°, amplitude = 0.5°, 2°, & 12°

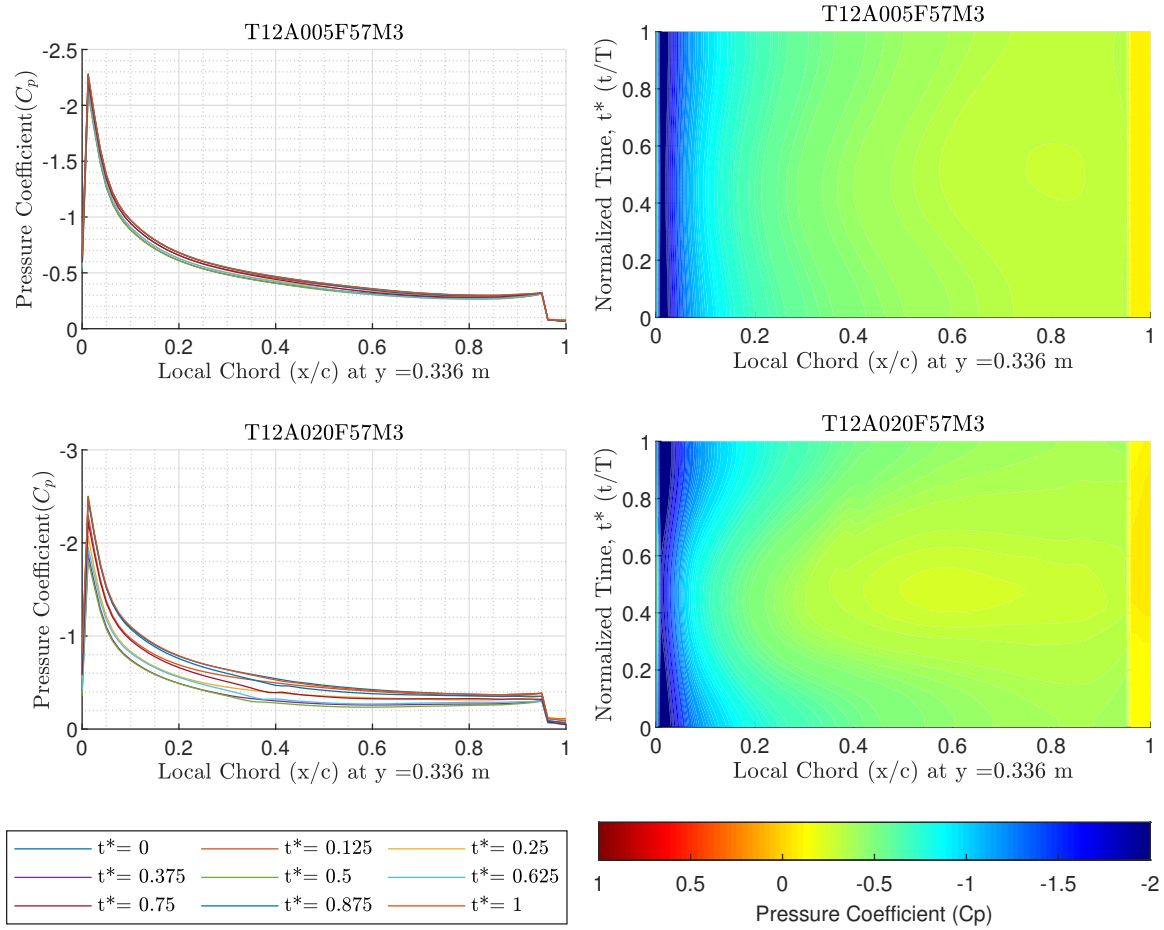


Figure C.4: Pressure distributions at Mach number 0.3. Frequency = 5.7 Hz, trim = 12°, amplitude = 0.5° & 2°

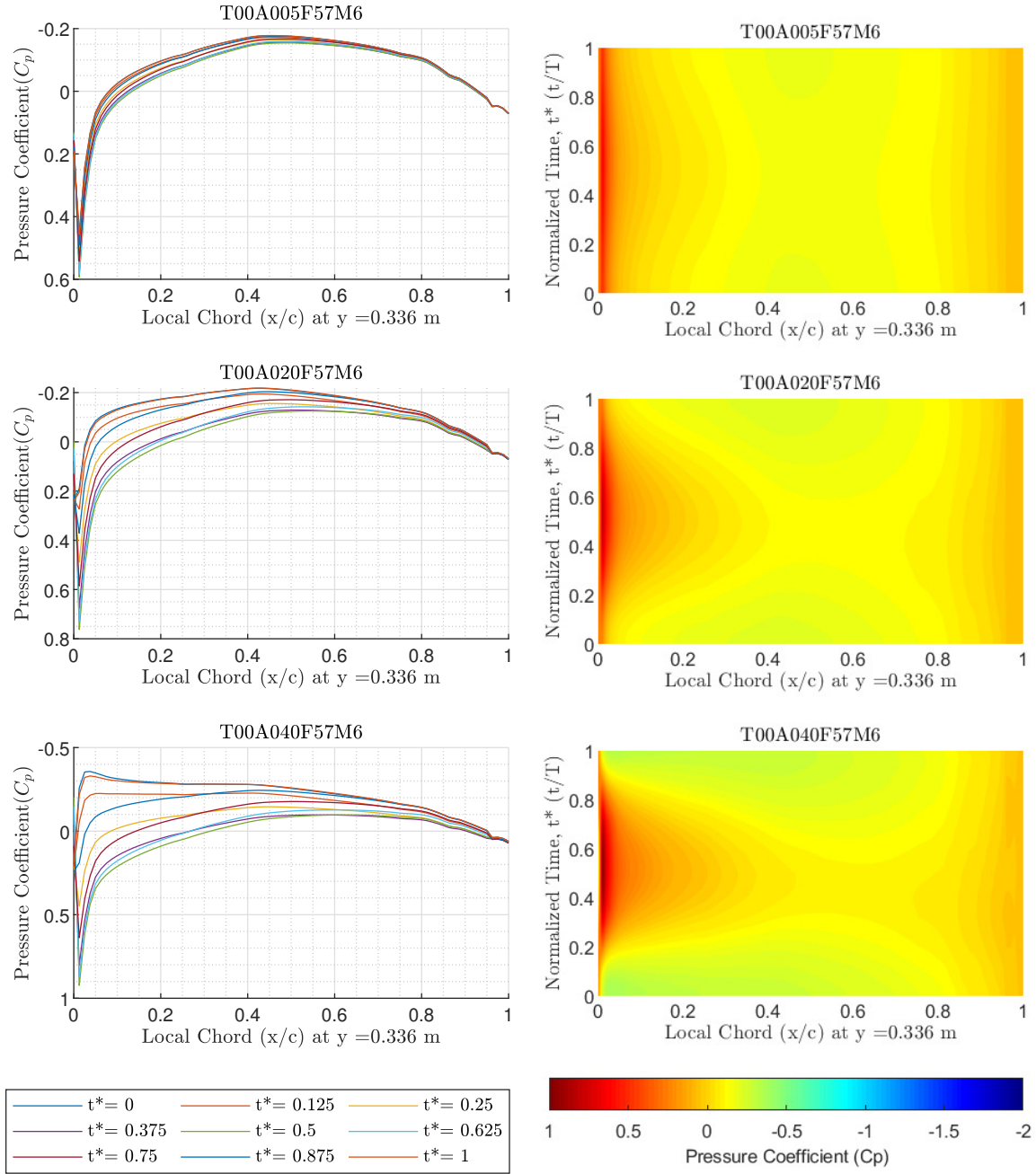


Figure C.5: Pressure distributions at Mach number 0.6. Frequency = 5.7 Hz, trim = 0° , amplitude = 0.5° , 2° , & 4°

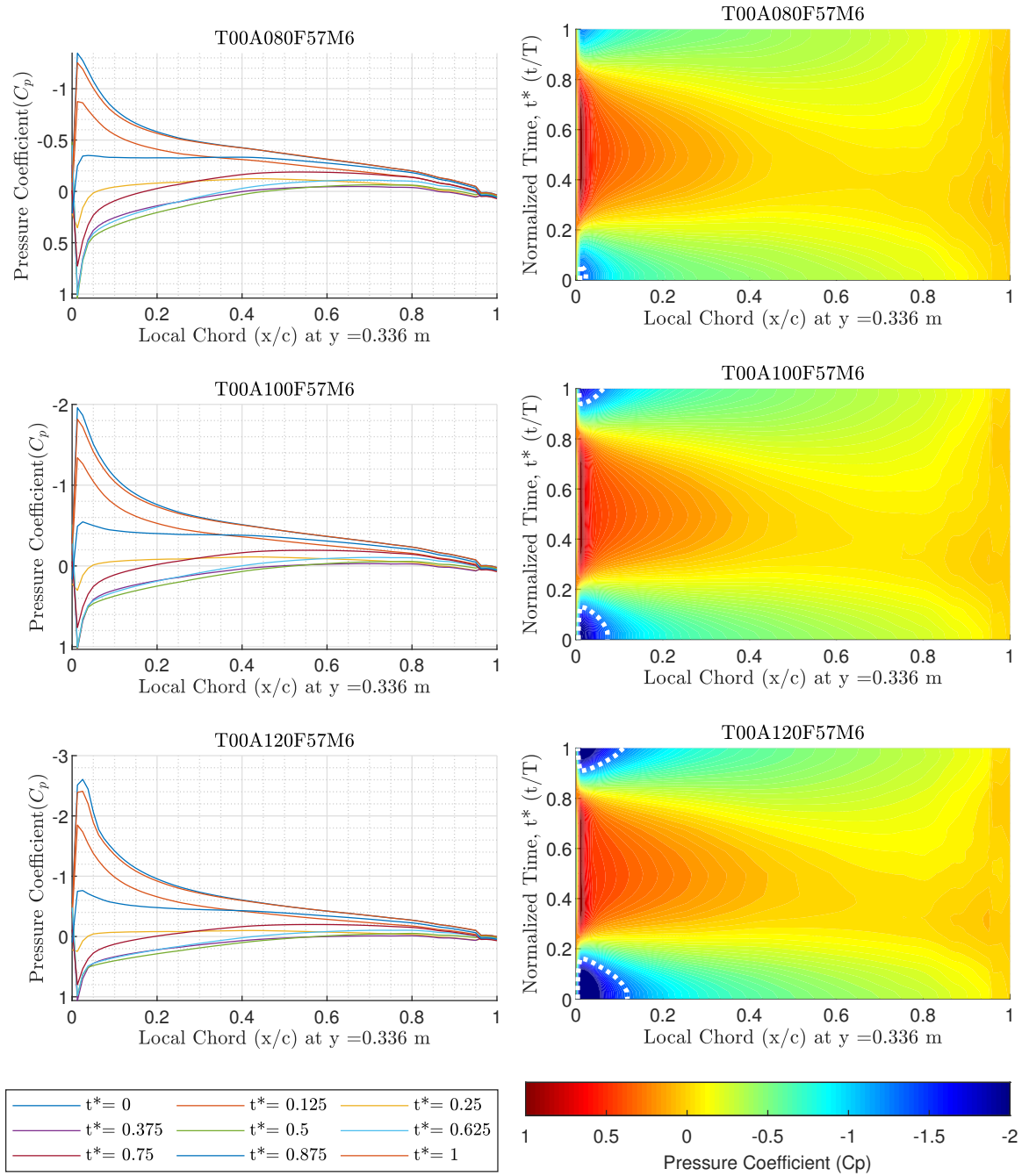


Figure C.6: Pressure distributions at Mach number 0.6. Frequency = 5.7 Hz, trim = 0°, amplitude = 8°, 10°, & 12°

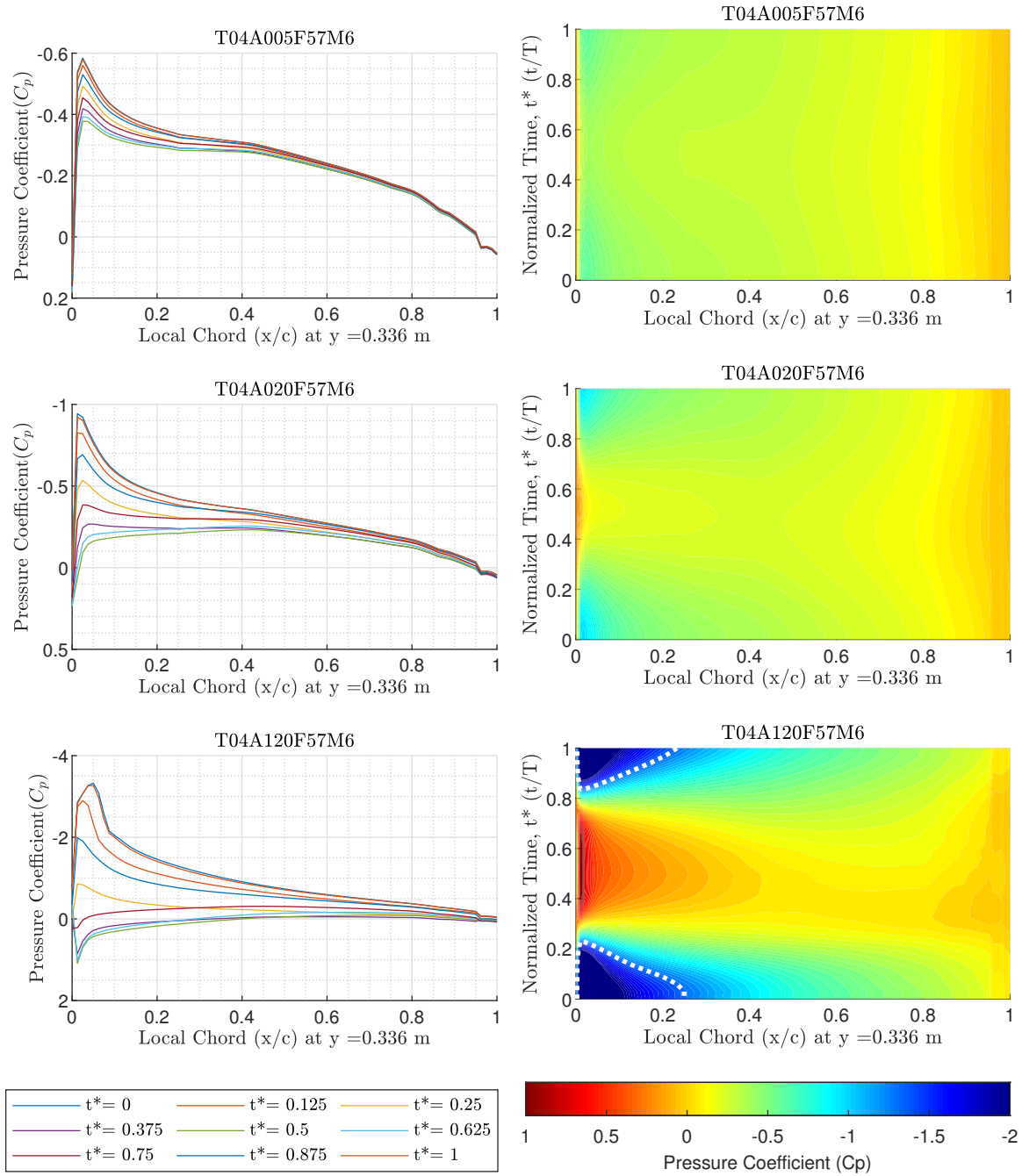


Figure C.7: Pressure distributions at Mach number 0.6. Frequency = 5.7 Hz, trim = 4°, amplitude = 0.5°, 2°, & 12°

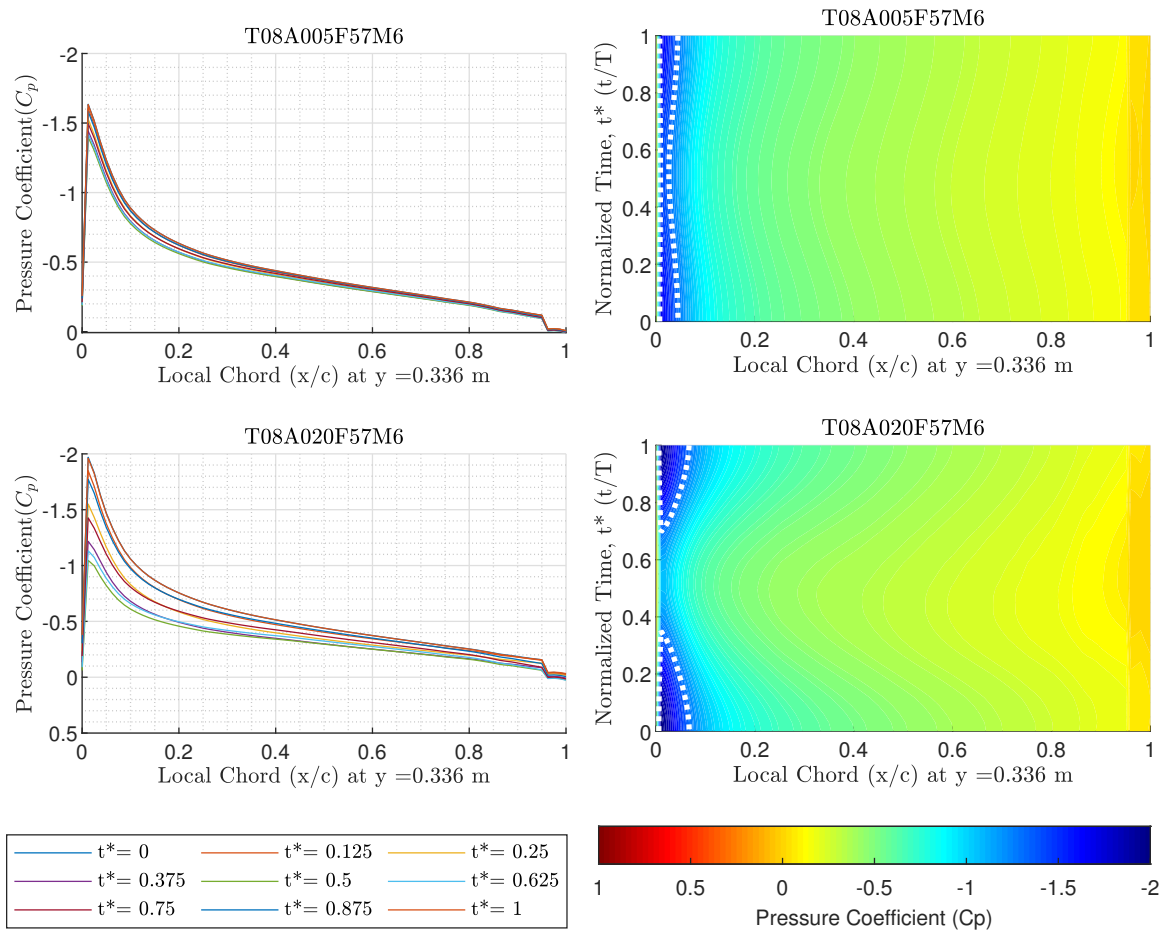


Figure C.8: Pressure distributions at Mach number 0.6. Frequency = 5.7 Hz, trim = 8° , amplitude = 0.5° & 2°

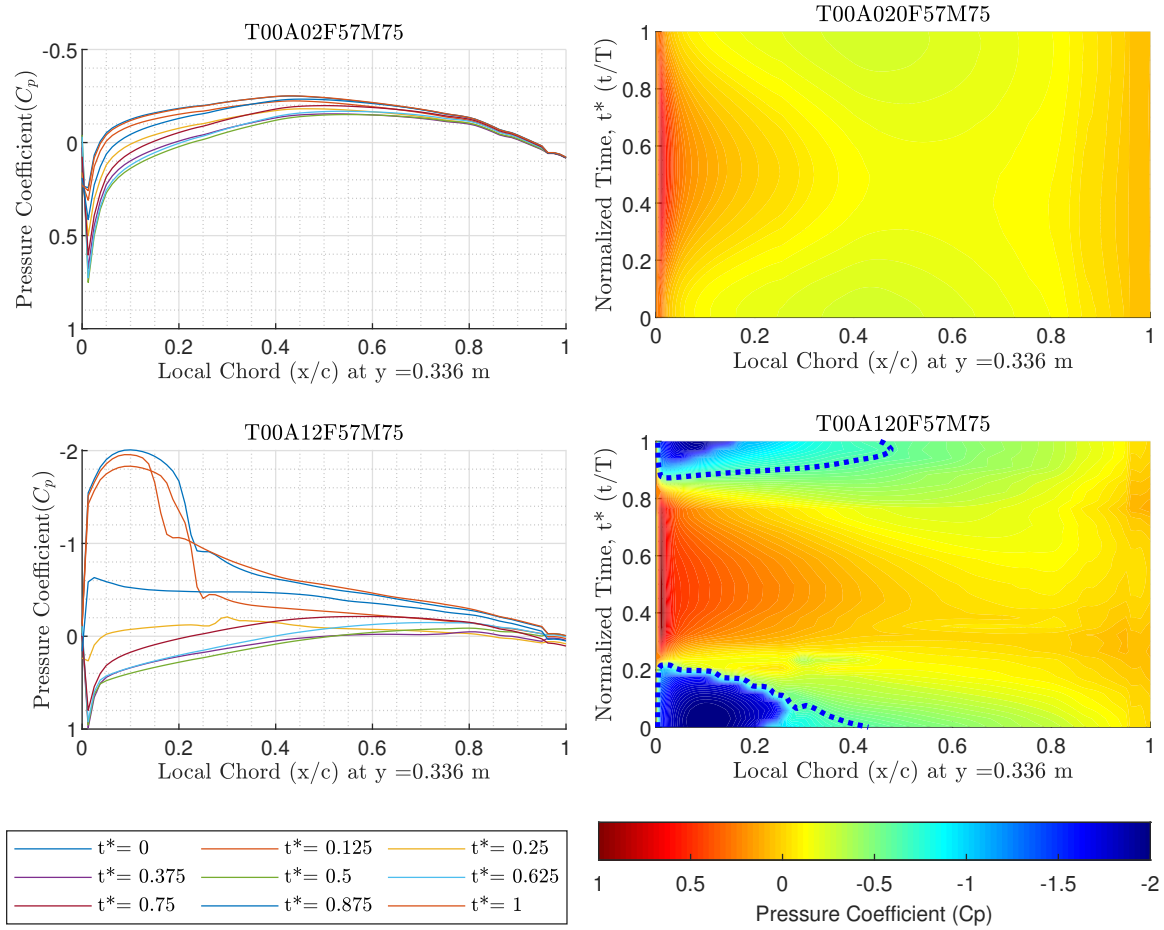


Figure C.9: Pressure distributions at Mach number 0.75. Frequency = 5.7 Hz, trim = 0°, amplitude = 2° & 12°

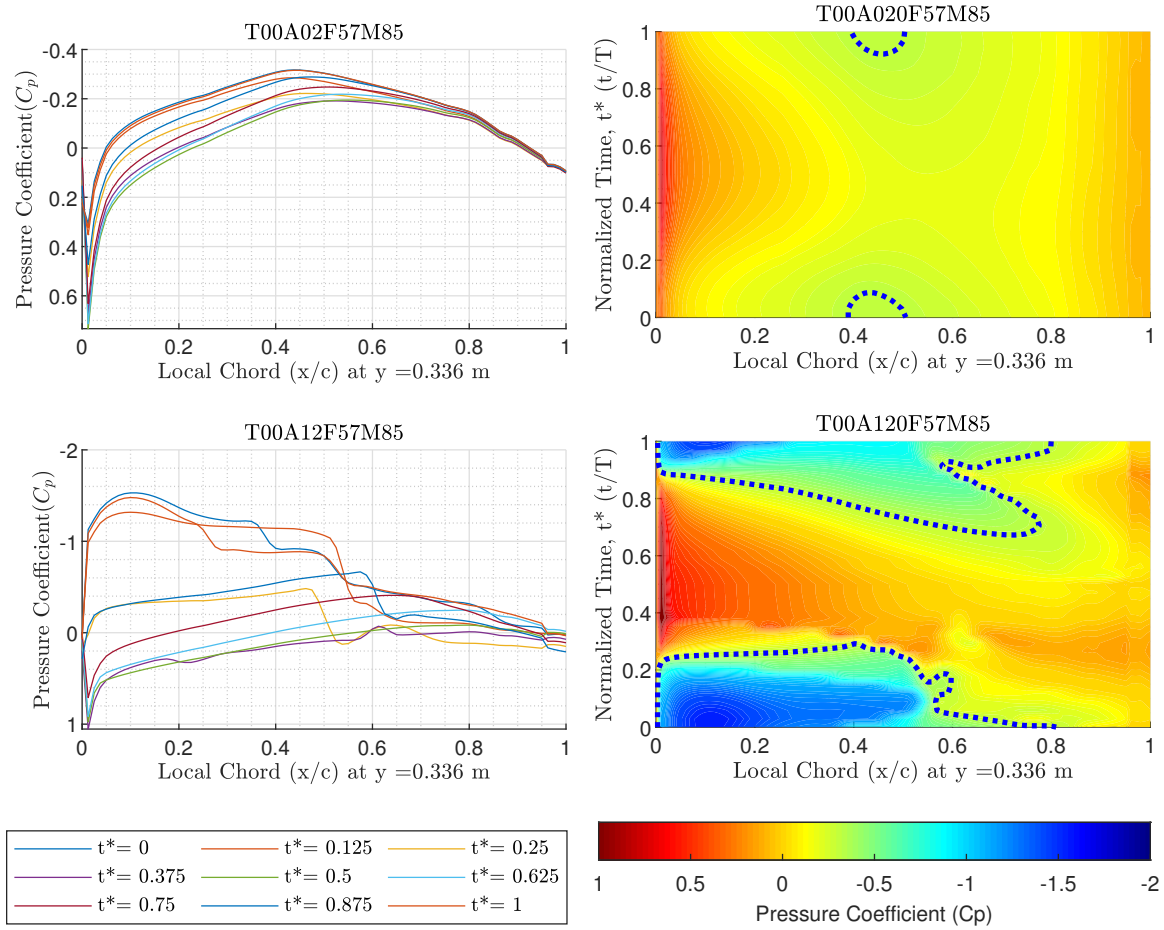


Figure C.10: Pressure distributions at Mach number 0.85. Frequency = 5.7 Hz, trim = 0°, amplitude = 2° & 12°

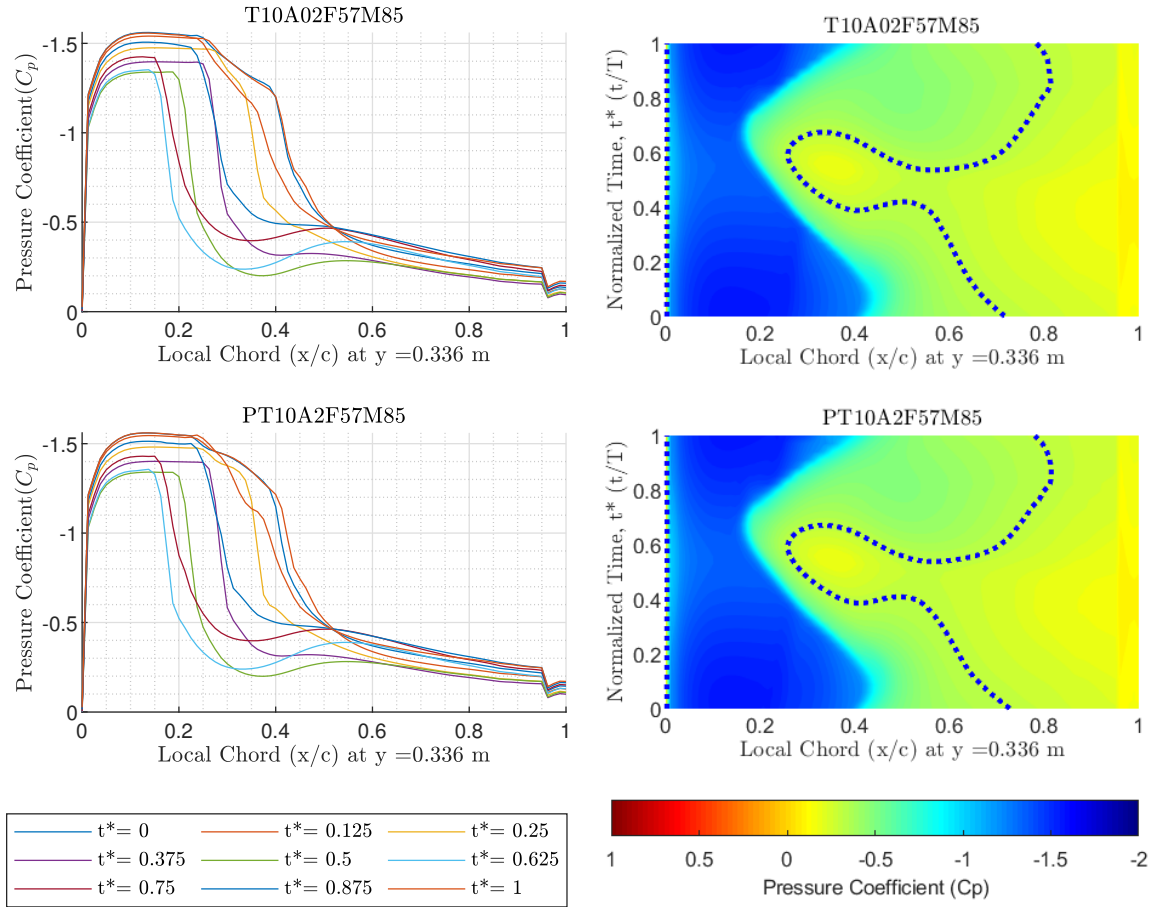


Figure C.11: Pressure distributions at Mach number 0.85. Frequency = 5.7 Hz, trim = 0° , amplitude = 2° . Top used -cosine function, and bottom used +cosine function.

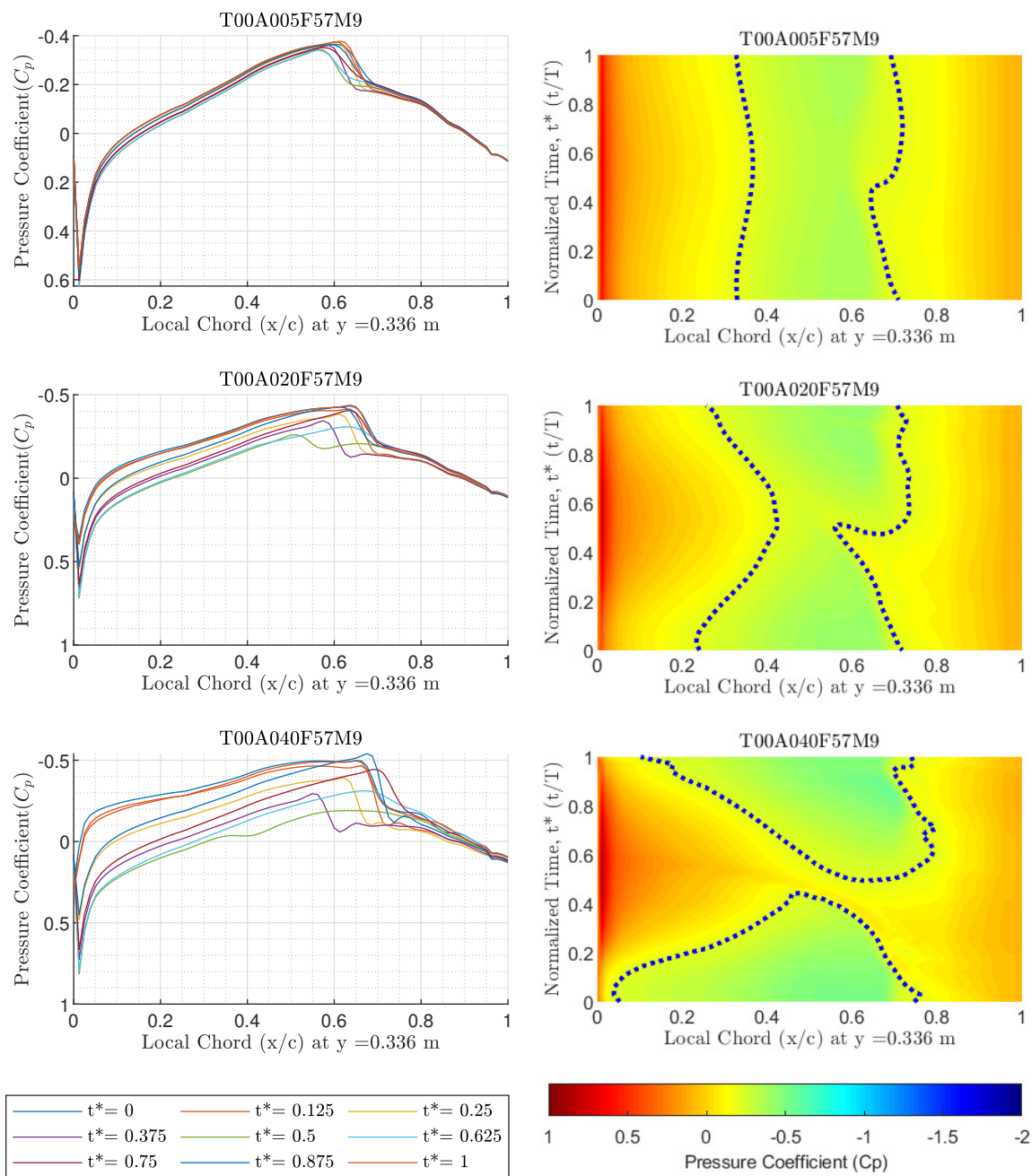


Figure C.12: Pressure distributions at Mach number 0.9. Frequency = 5.7 Hz, trim = 0°, amplitude = 0.5°, 2°, & 4°

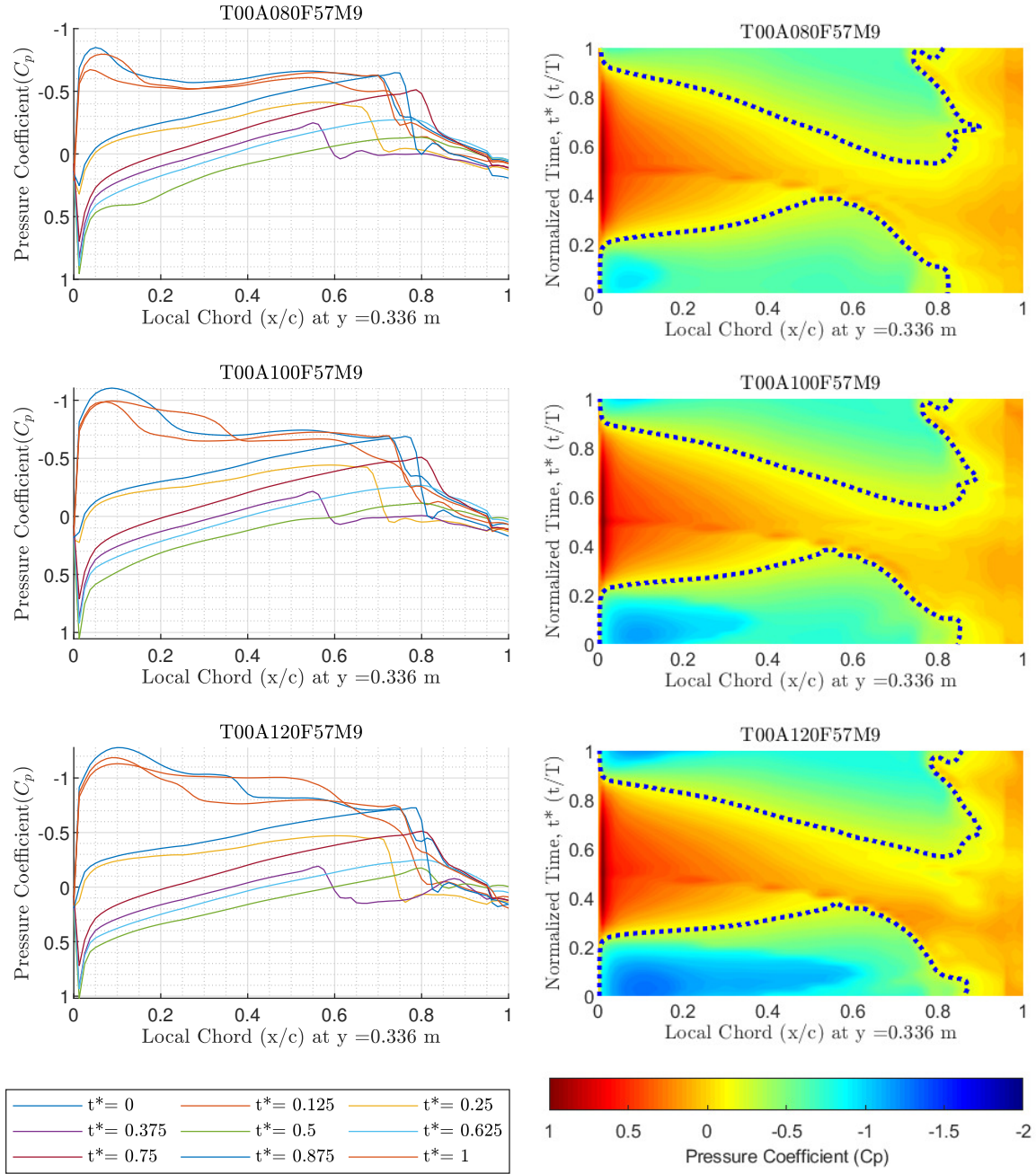


Figure C.13: Pressure distributions at Mach number 0.9. Frequency = 5.7 Hz, trim = 0° , amplitude = 8° , 10° , & 12°

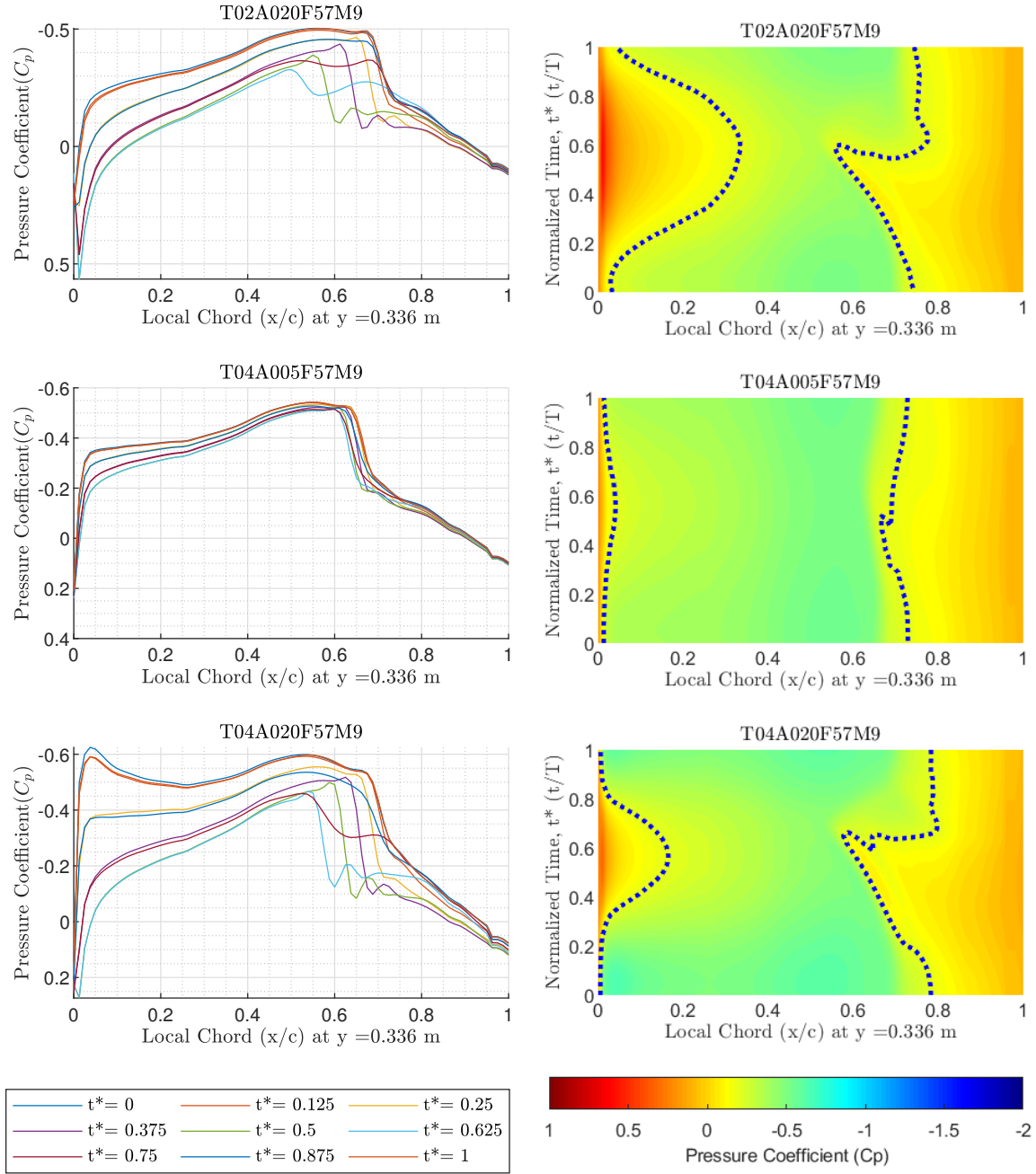


Figure C.14: Pressure distributions at Mach number 0.9. Frequency = 5.7 Hz, (Top) trim = 2° & amplitude = 2° , (middle & bottom) trim = 4° , amplitude = 0.5° & 2°

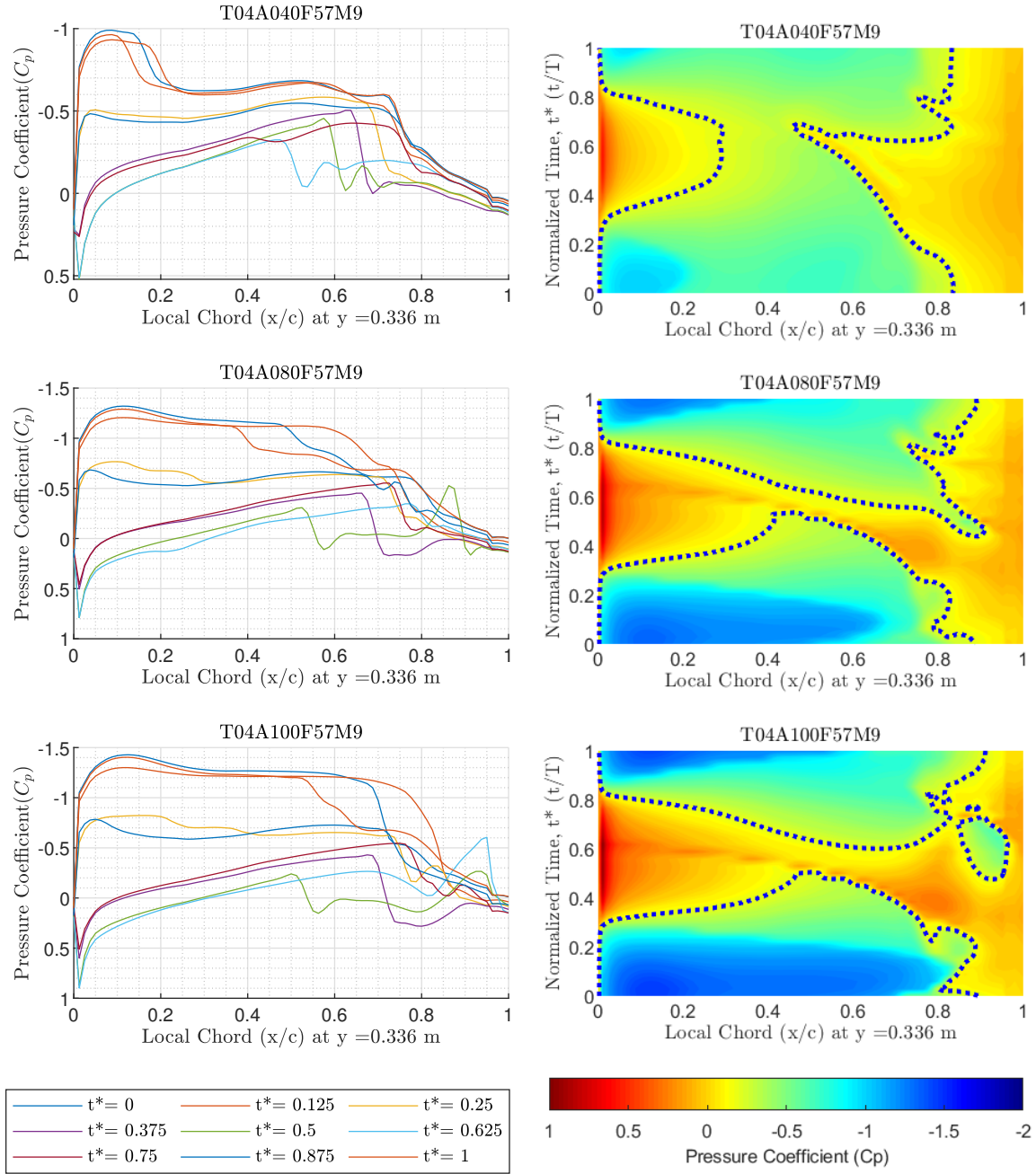


Figure C.15: Pressure distributions at Mach number 0.9. Frequency = 5.7 Hz, trim = 4°, amplitude = 4°, & 10°

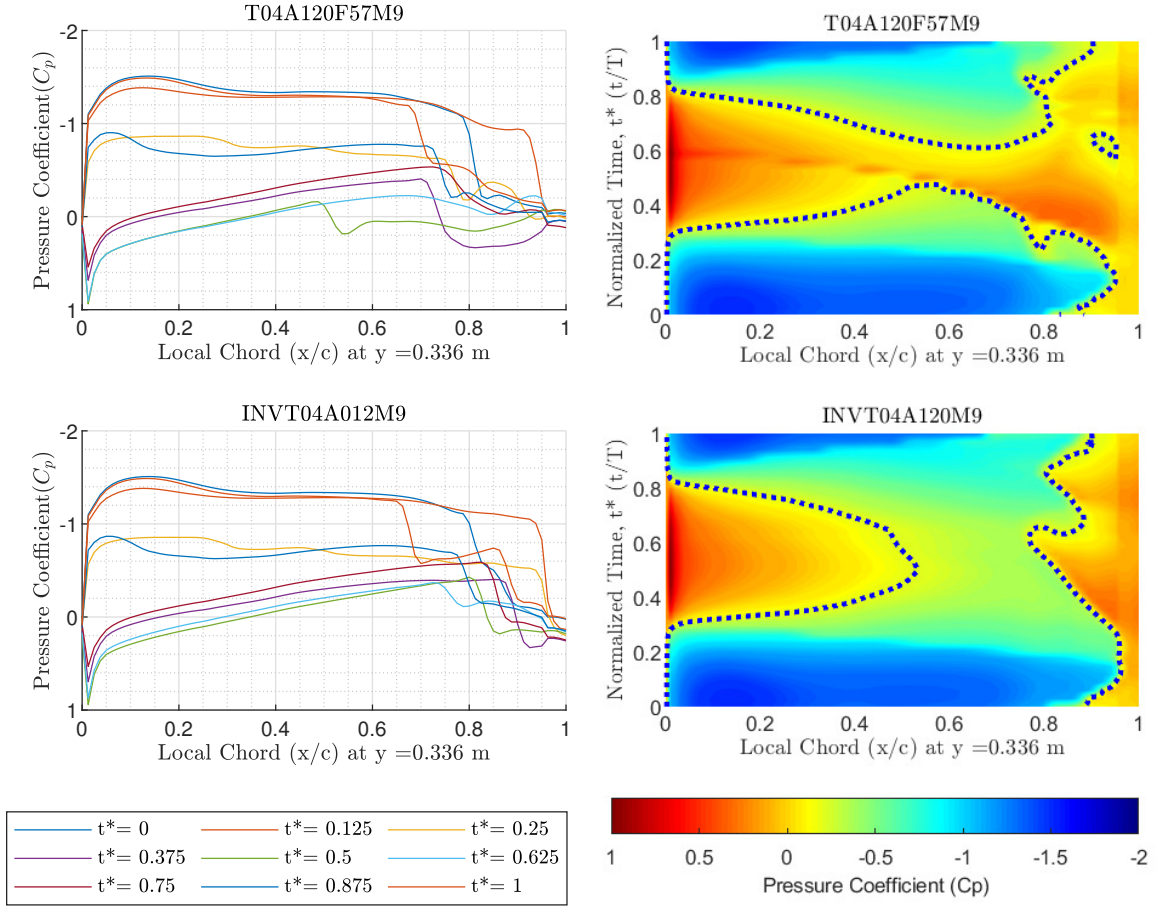


Figure C.16: Pressure distributions at Mach number 0.9. Frequency = 5.7 Hz, trim = 4°, amplitude = 12°. Top used BLC solver, and bottom used fully inviscid solver.

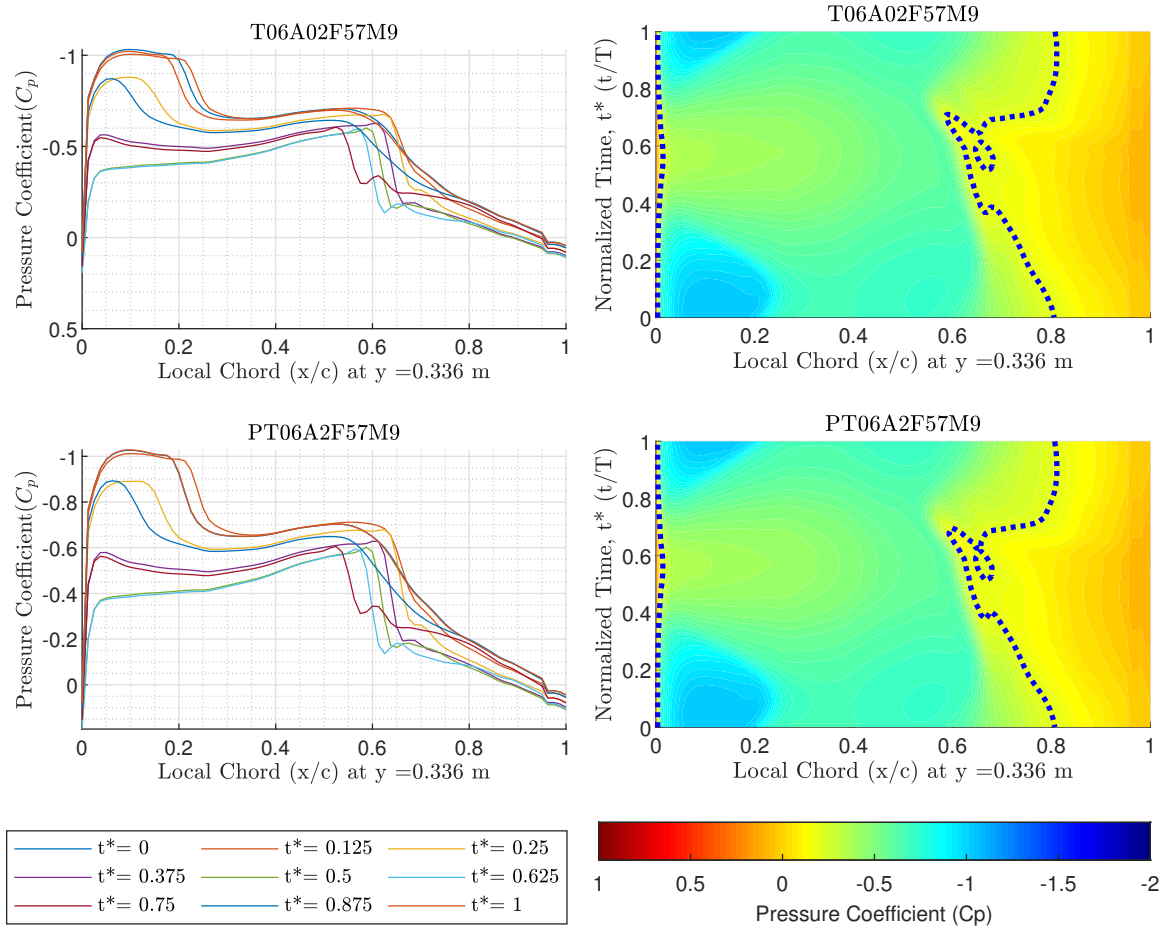


Figure C.17: Pressure distributions at Mach number 0.9. Frequency = 5.7 Hz, trim = 6°, amplitude = 2°. The Bottom plot used a +cosine function.

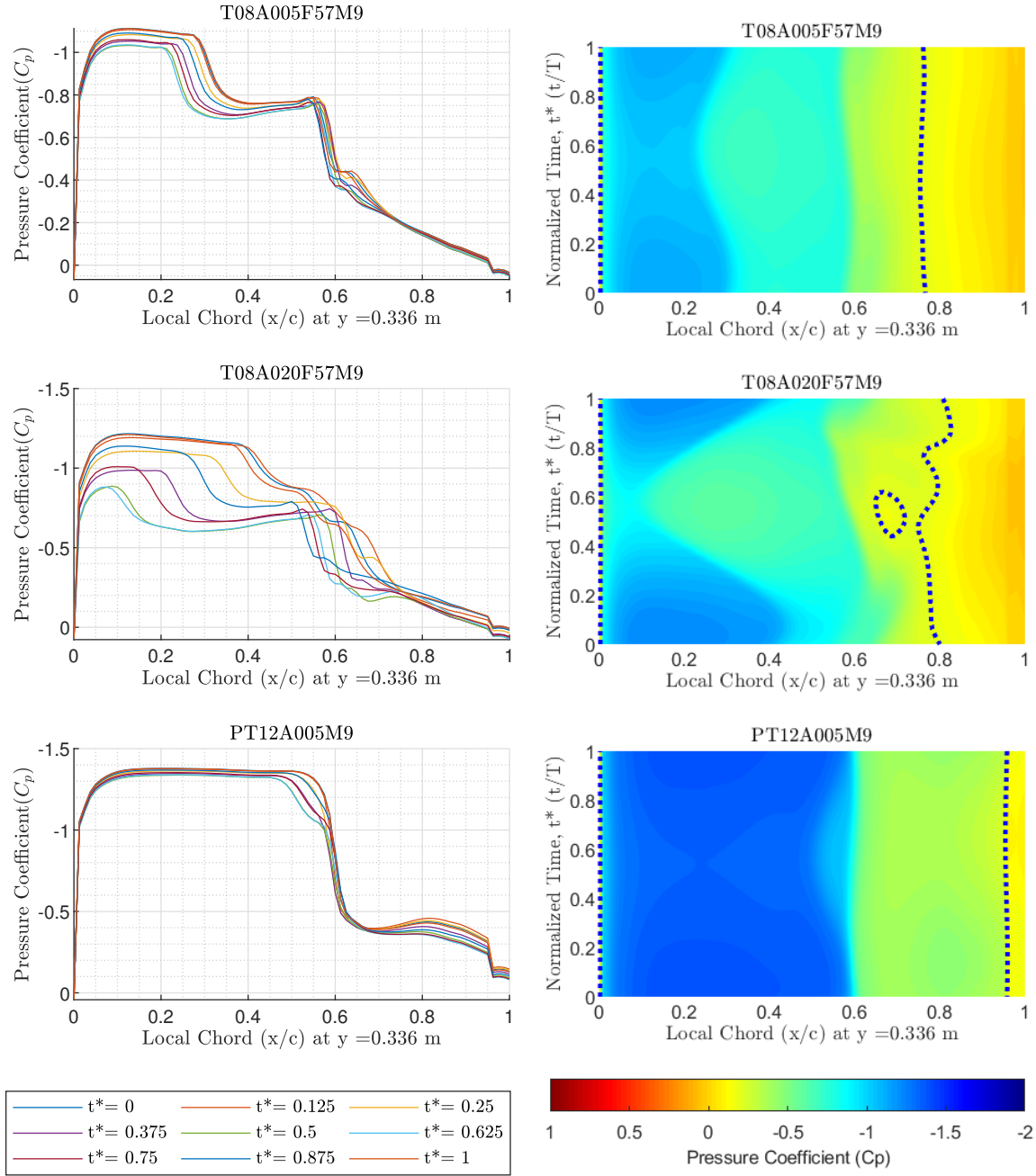


Figure C.18: Pressure distributions at Mach number 0.9. Frequency = 5.7 Hz, Top and middle plots had trim = 8° , amplitude = 0.5° & 2° . Bottom plots had trim = 12° , amplitude = 0.5° , & used a +cosine function.

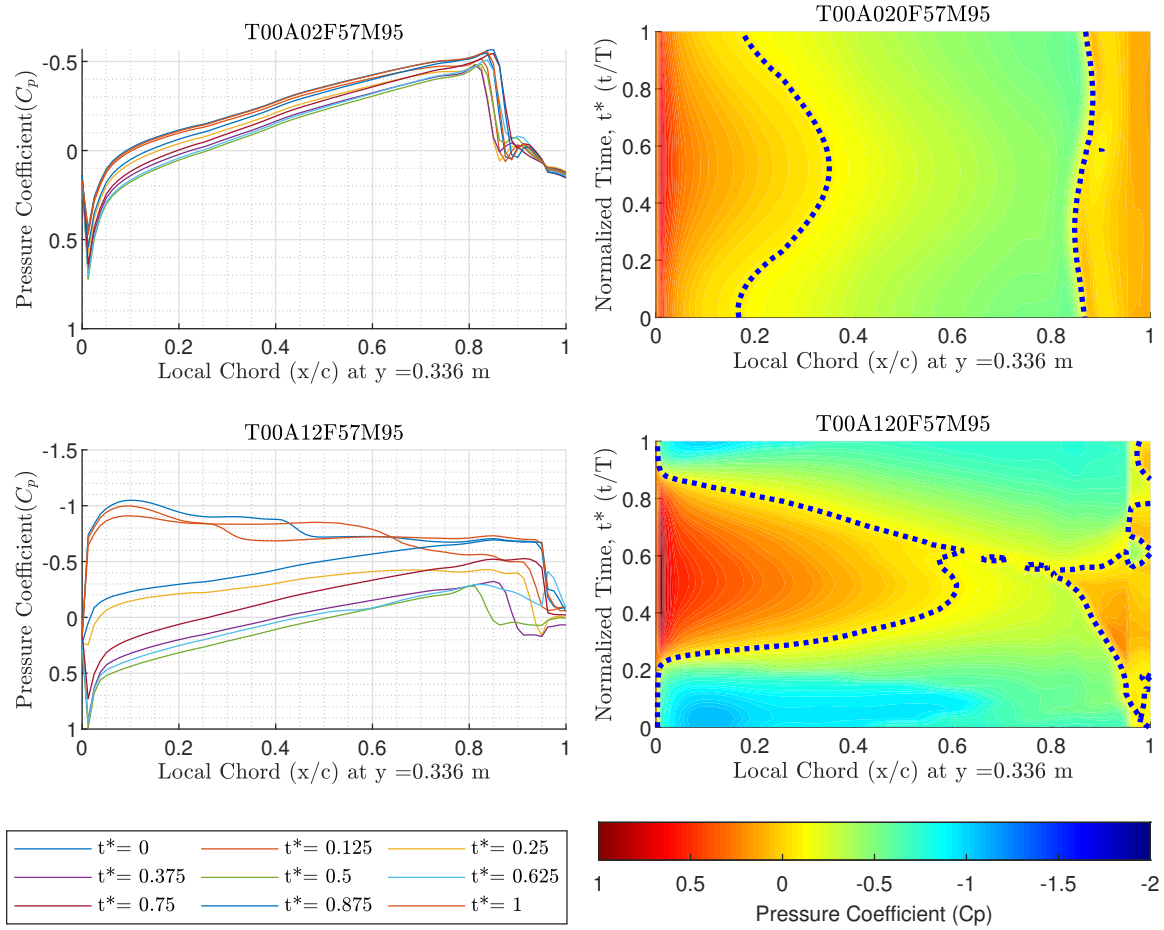


Figure C.19: Pressure distributions at Mach number 0.95. Frequency = 5.7 Hz, trim = 0°, amplitude = 2° & 12°

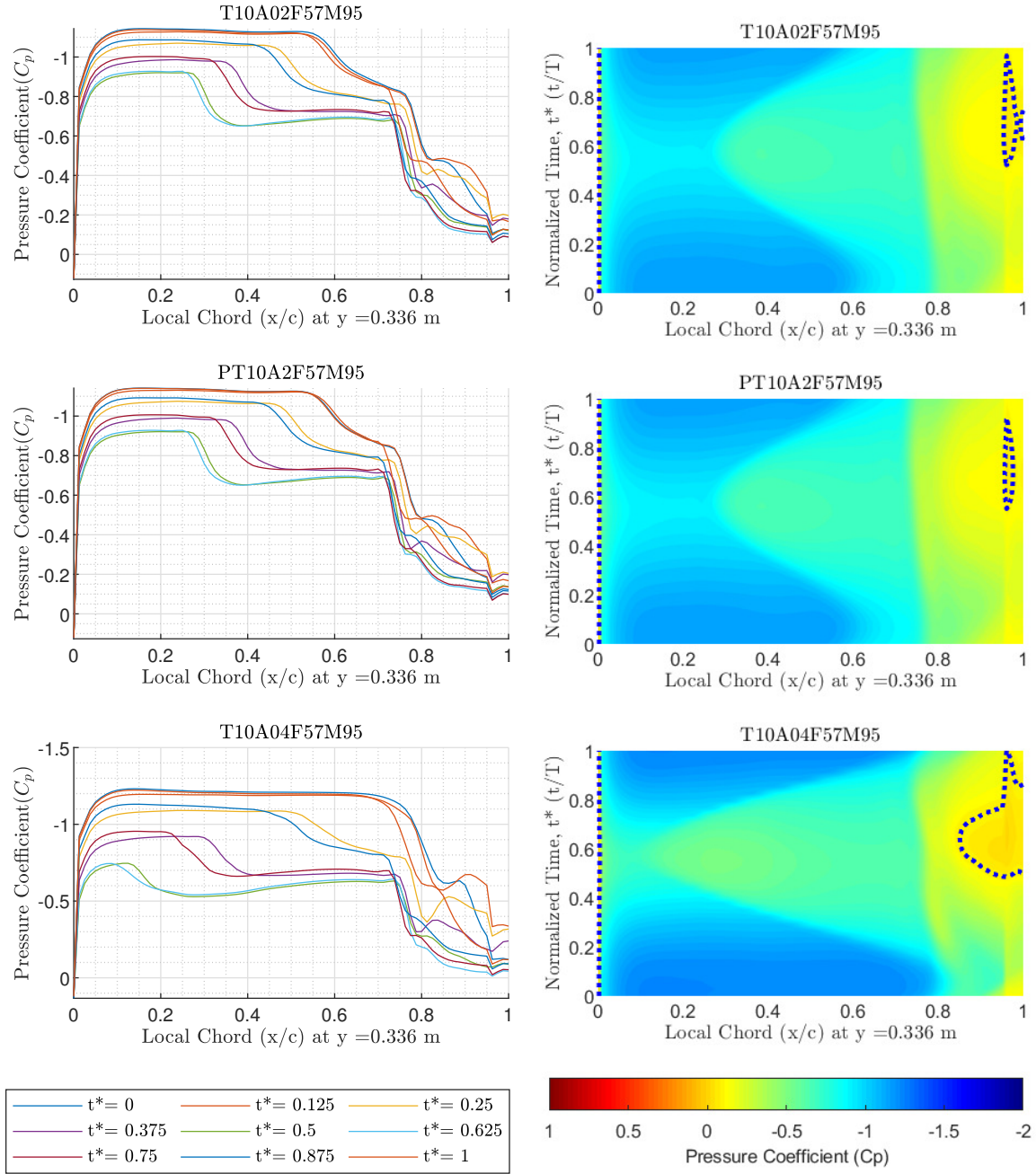


Figure C.20: Pressure distributions at Mach number 0.95. Frequency = 5.7 Hz, trim = 10°, amplitude = 2°, 2°, & 4°. Middle plots used a +cosine function.

Appendix D. C_p Data for Wing Station 4

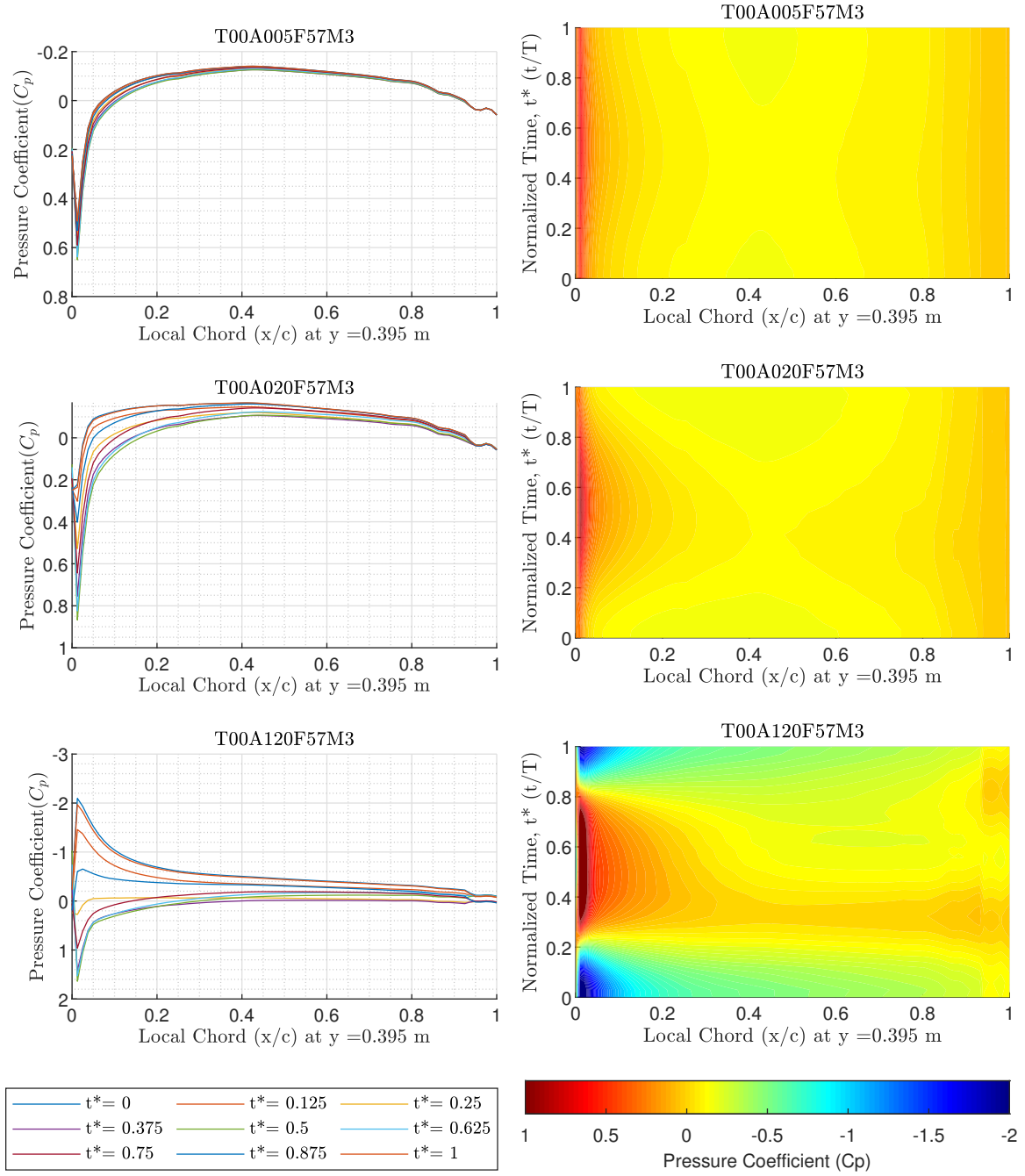


Figure D.1: Pressure distributions at Mach number 0.3. Frequency = 5.7 Hz, trim = 0° , amplitude = 0.5° , 2° , & 12°

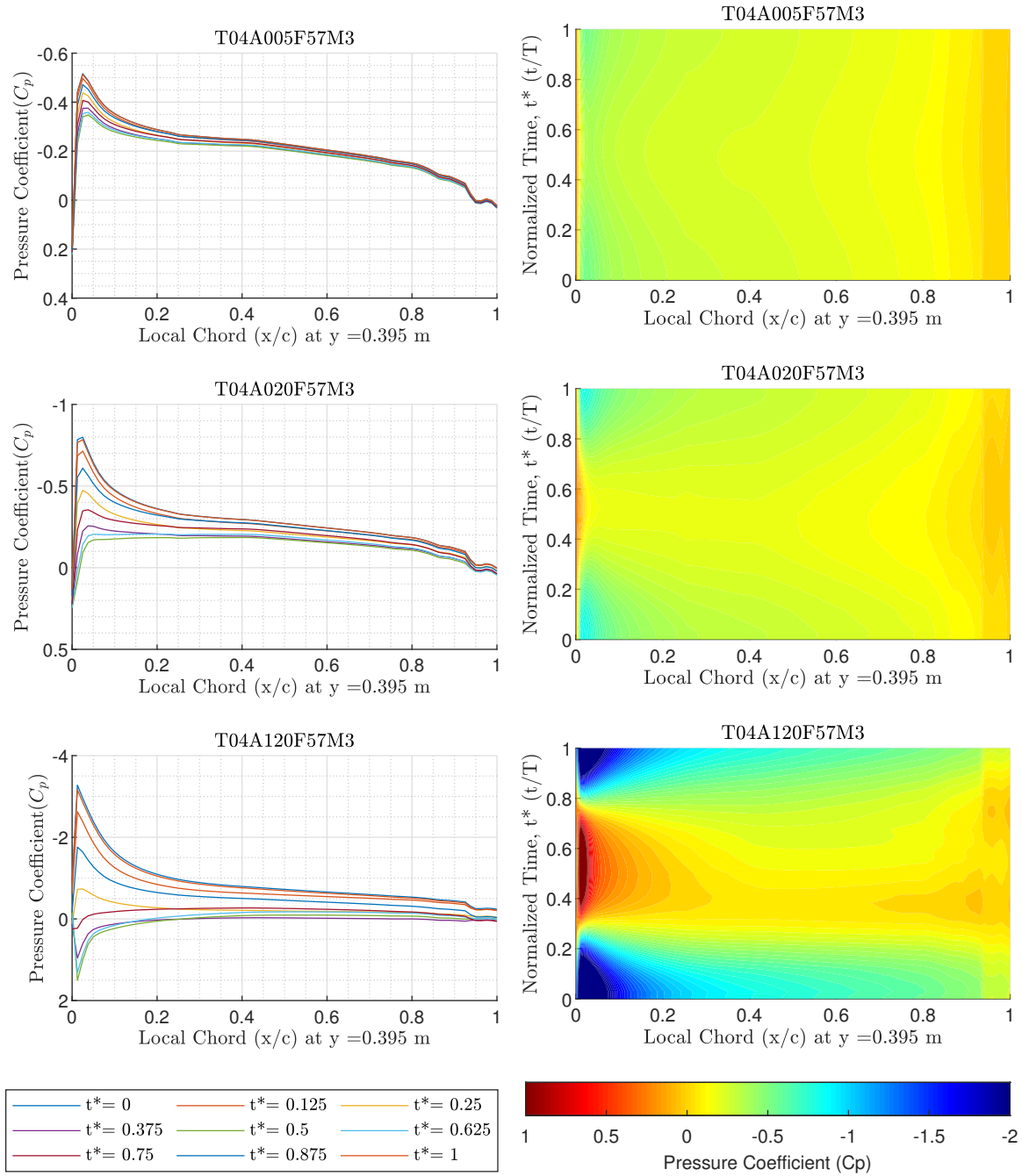


Figure D.2: Pressure distributions at Mach number 0.3. Frequency = 5.7 Hz, trim = 4°, amplitude = 0.5°, 2°, & 12°

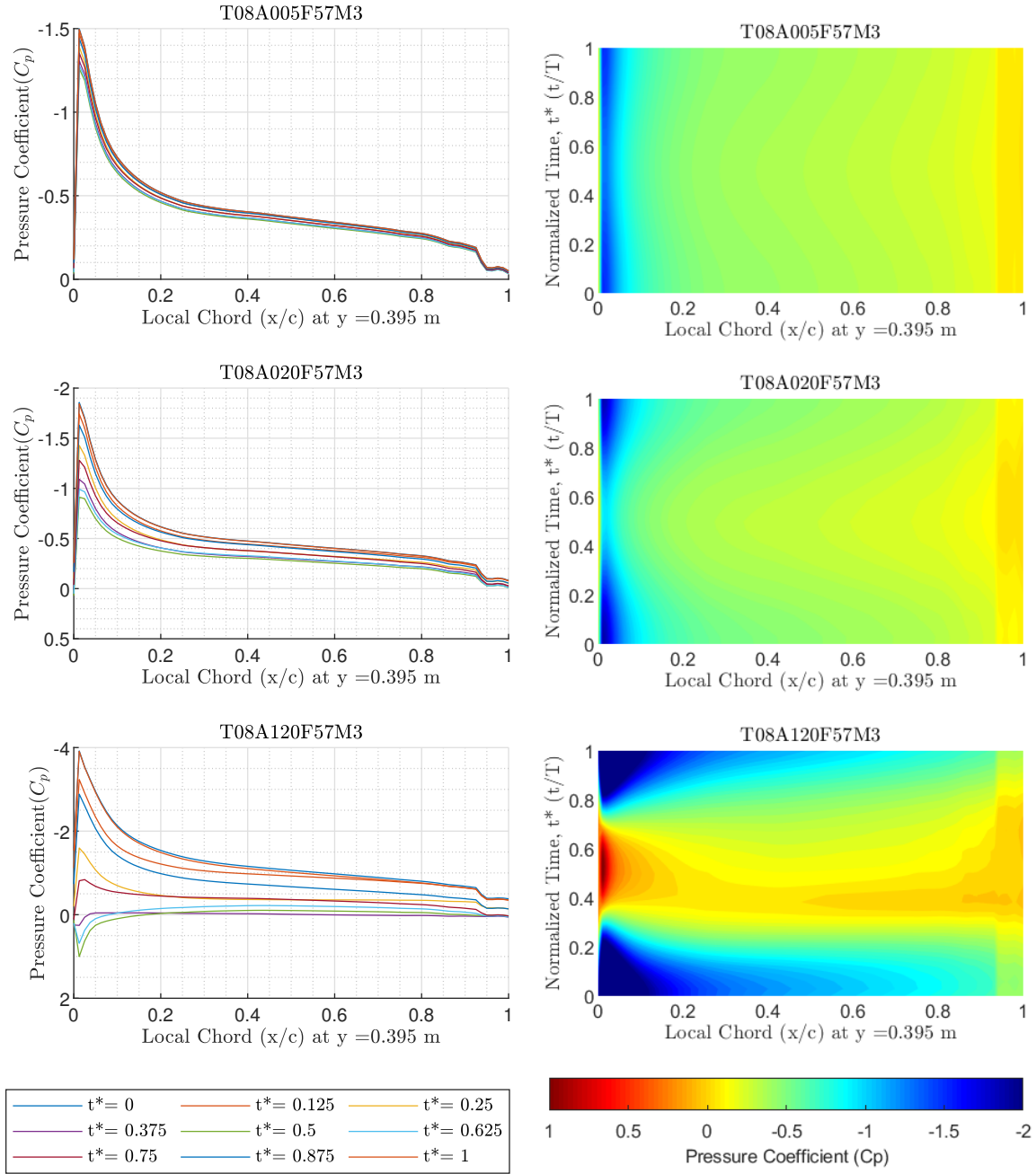


Figure D.3: Pressure distributions at Mach number 0.3. Frequency = 5.7 Hz, trim = 8°, amplitude = 0.5°, 2°, & 12°

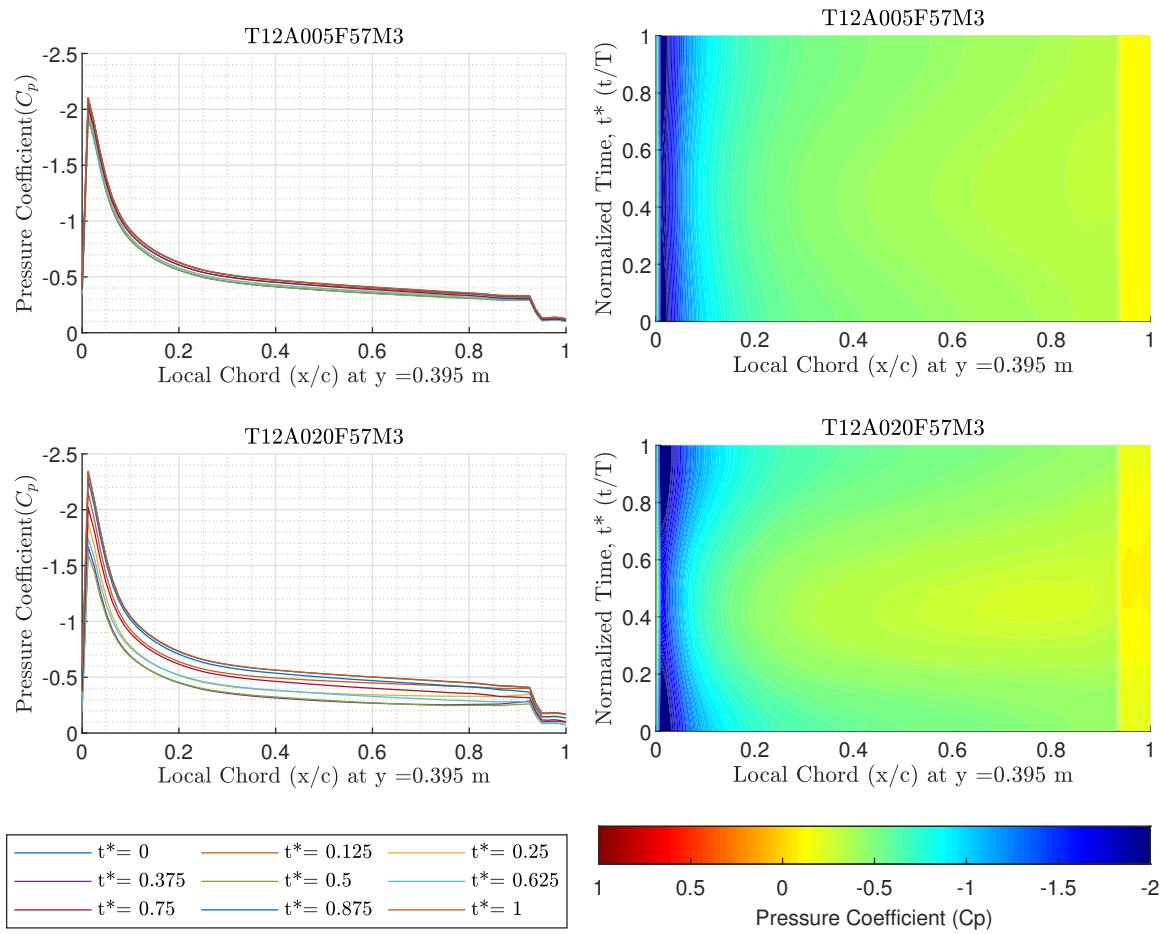


Figure D.4: Pressure distributions at Mach number 0.3. Frequency = 5.7 Hz, trim = 12°, amplitude = 0.5° & 2°

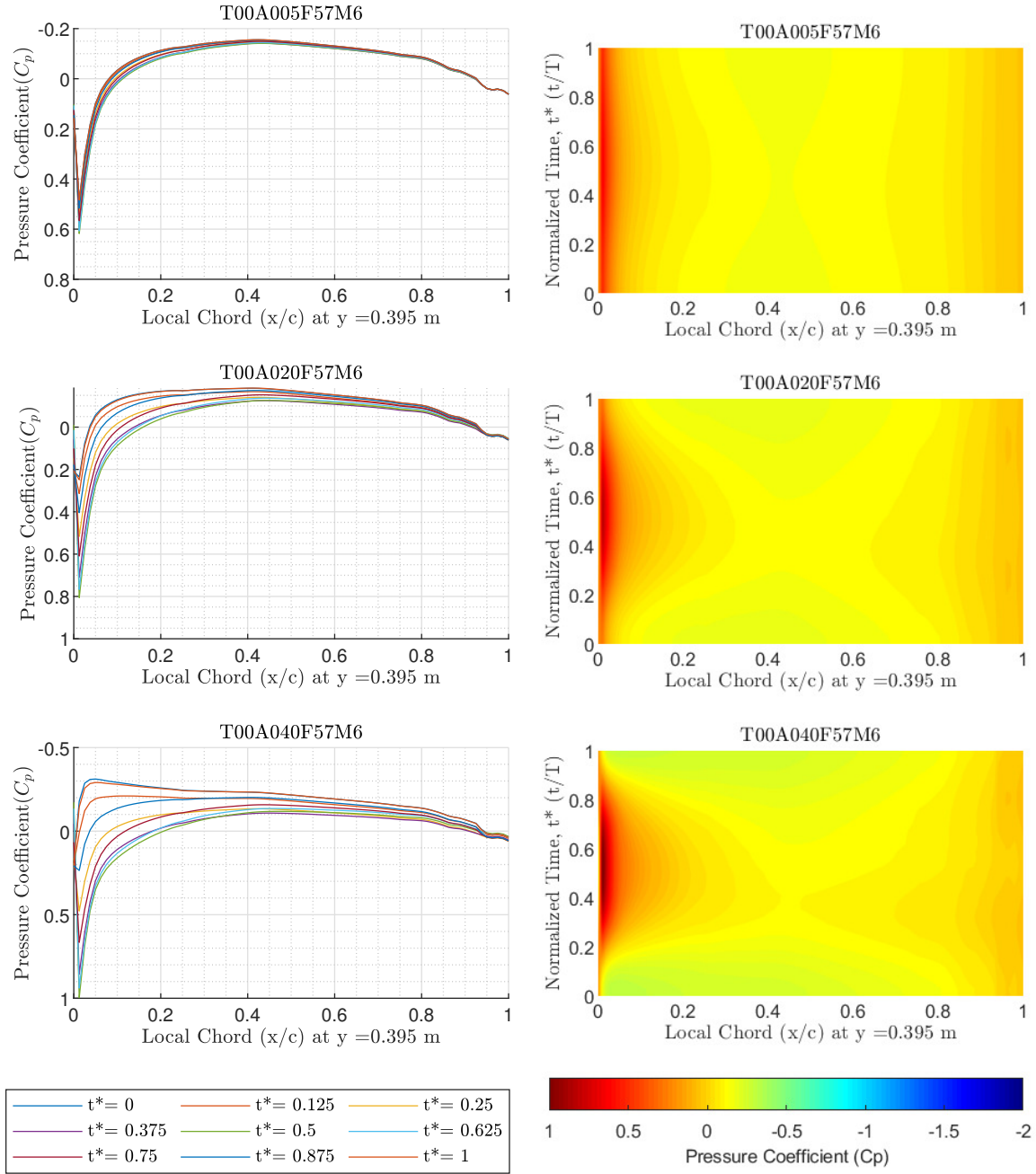


Figure D.5: Pressure distributions at Mach number 0.6. Frequency = 5.7 Hz, trim = 0° , amplitude = 0.5° , 2° , & 4°

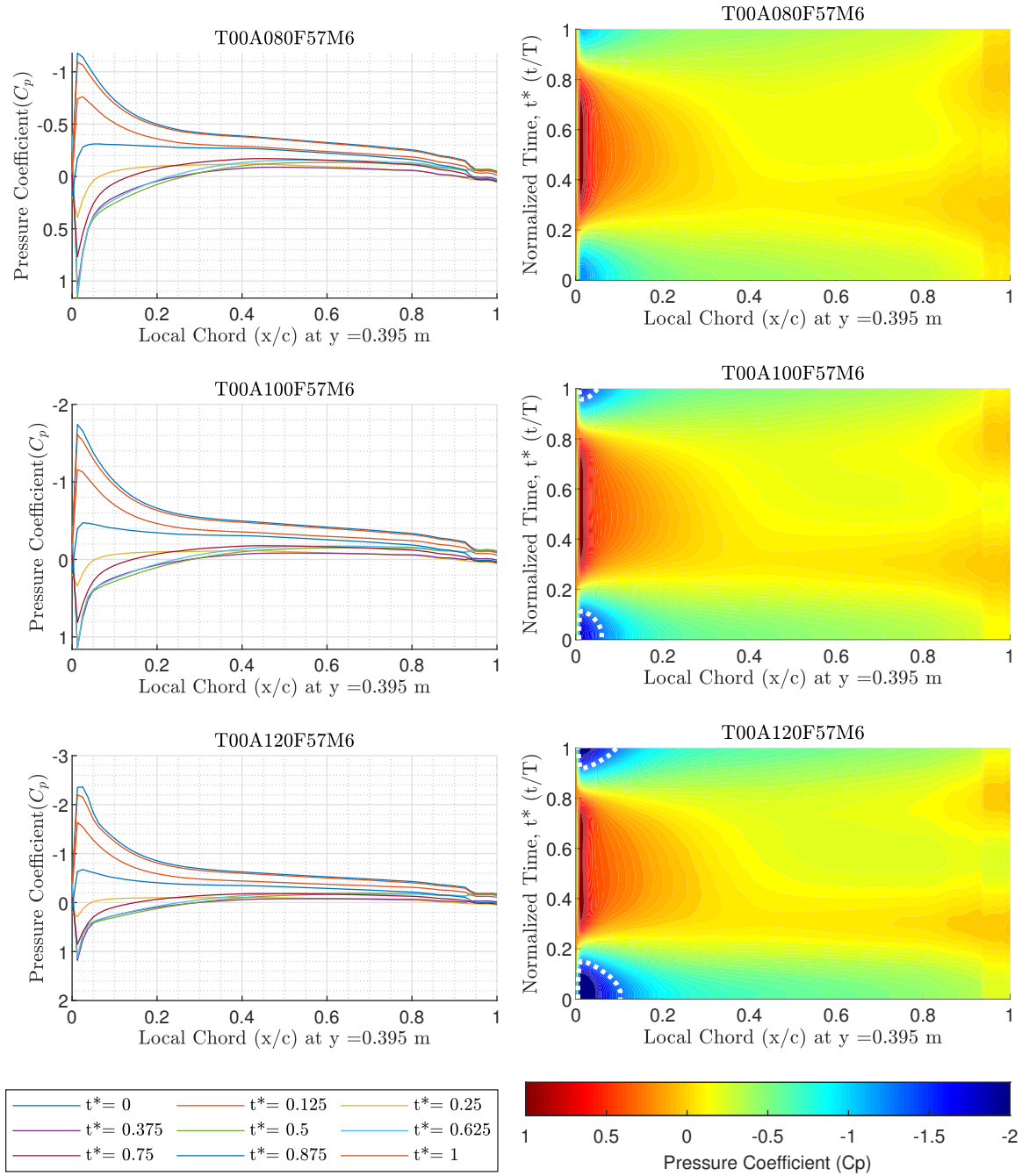


Figure D.6: Pressure distributions at Mach number 0.6. Frequency = 5.7 Hz, trim = 0°, amplitude = 8°, 10°, & 12°

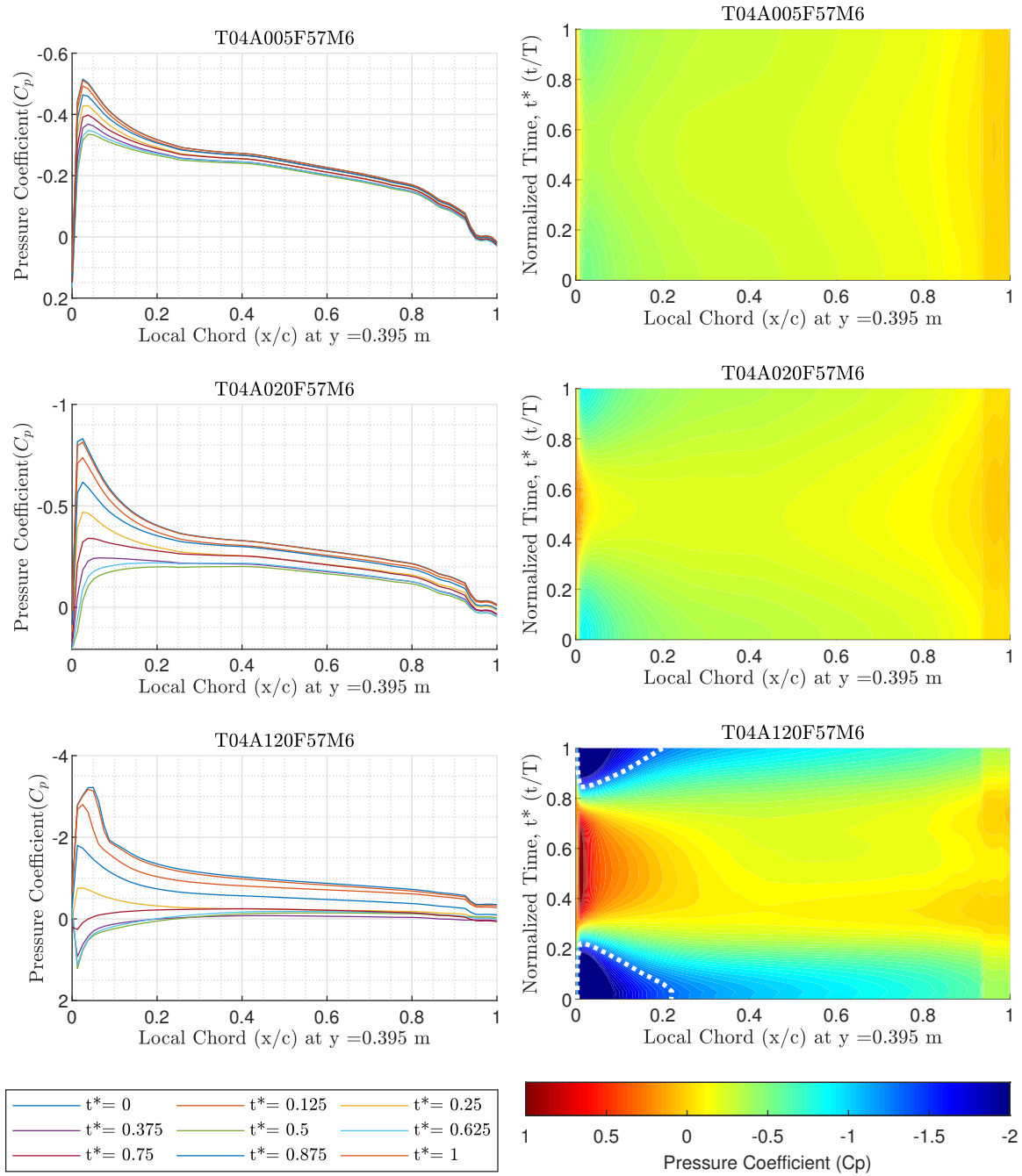


Figure D.7: Pressure distributions at Mach number 0.6. Frequency = 5.7 Hz, trim = 4°, amplitude = 0.5°, 2°, & 12°

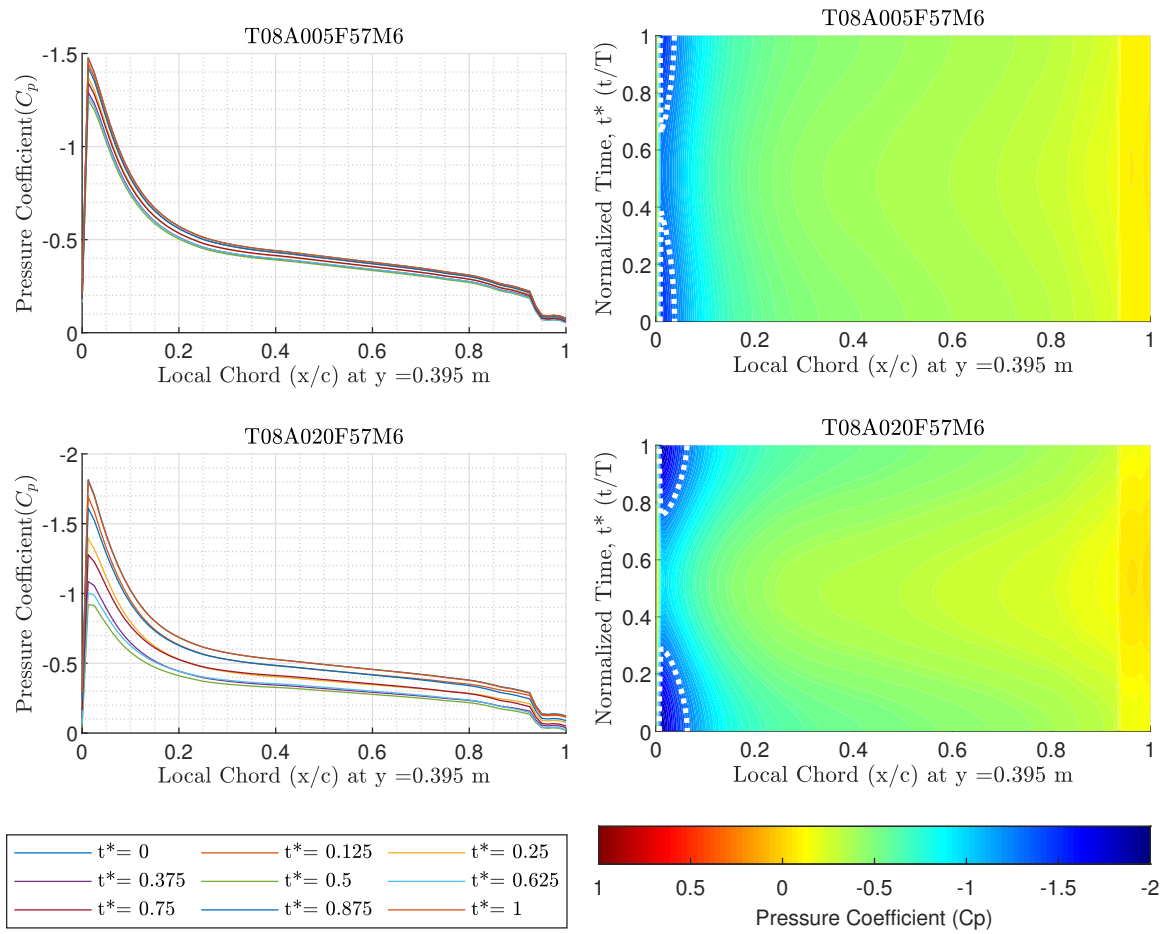


Figure D.8: Pressure distributions at Mach number 0.6. Frequency = 5.7 Hz, trim = 8°, amplitude = 0.5° & 2°

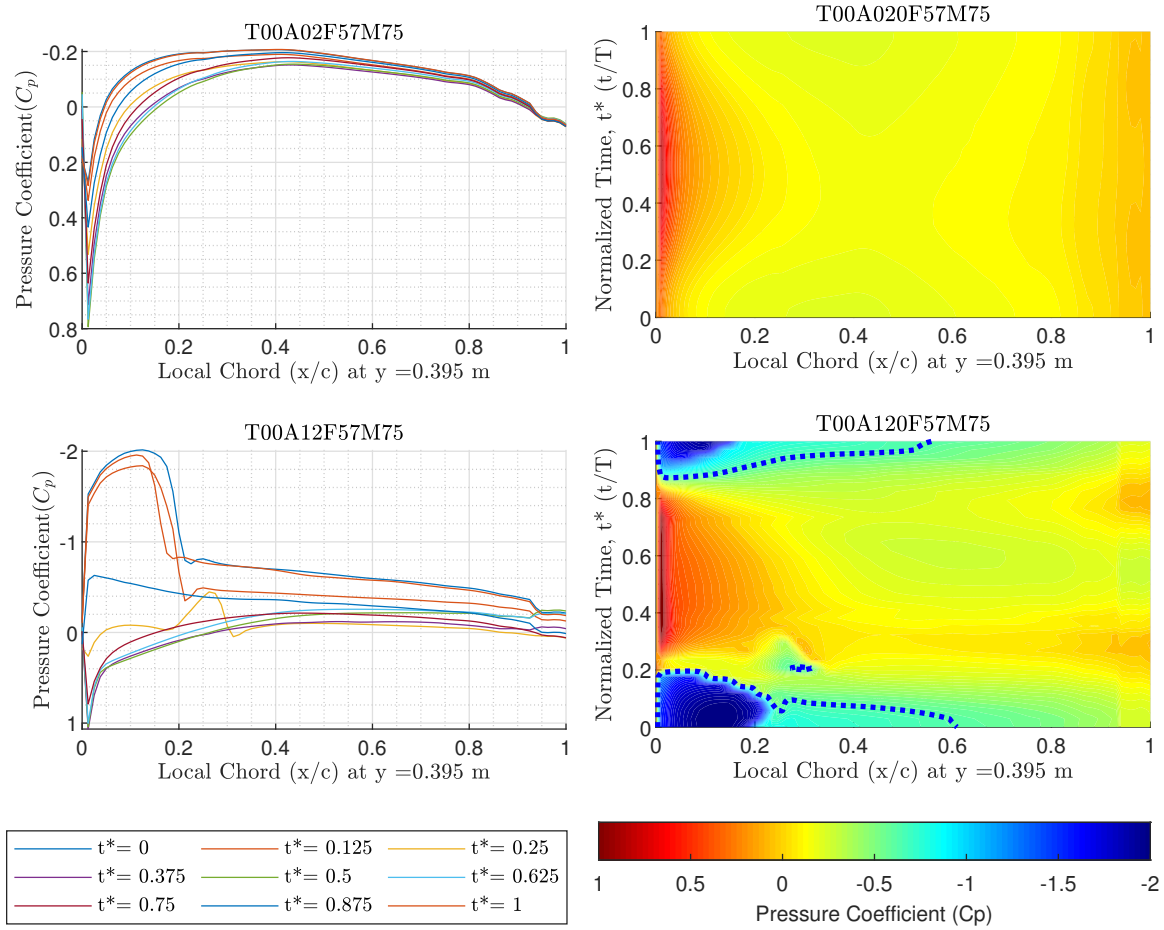


Figure D.9: Pressure distributions at Mach number 0.75. Frequency = 5.7 Hz, trim = 0°, amplitude = 2° & 12°

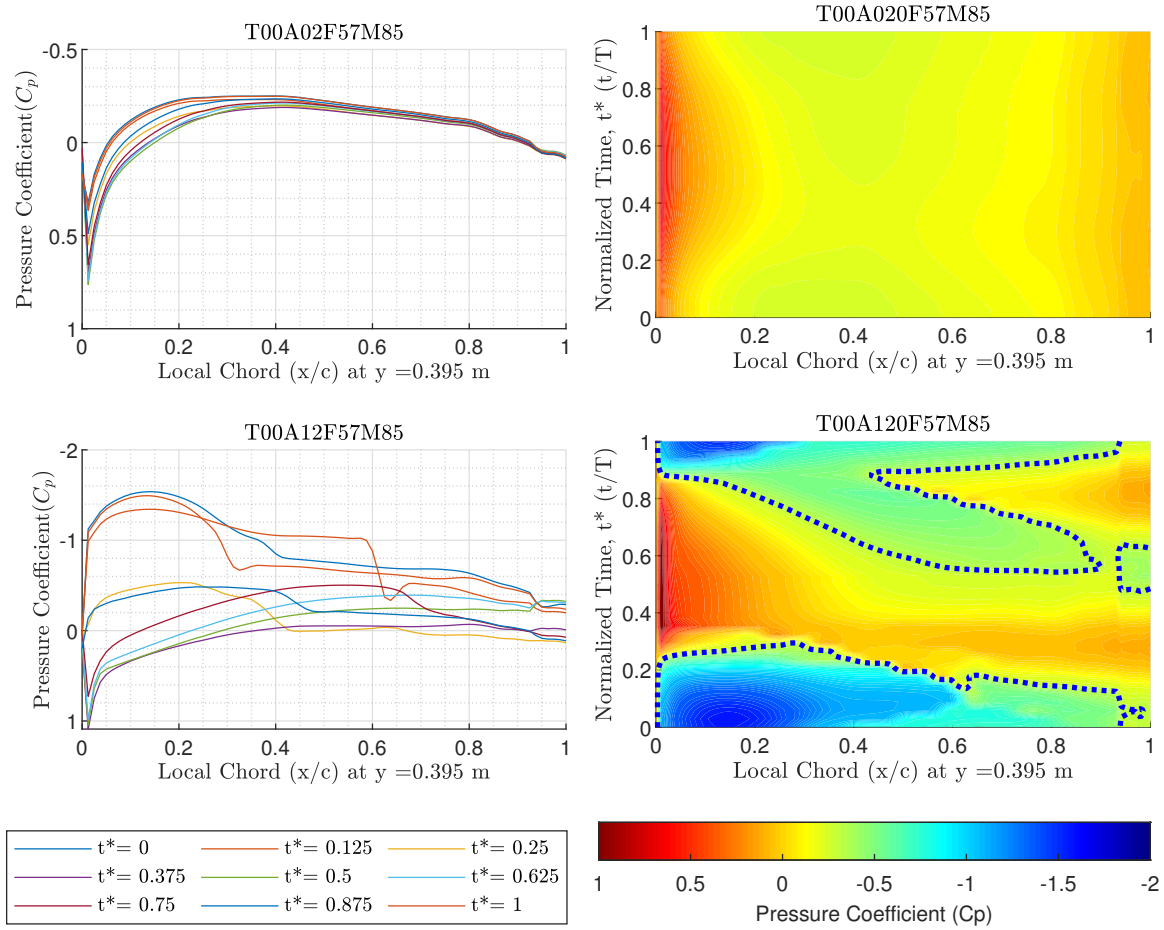


Figure D.10: Pressure distributions at Mach number 0.85. Frequency = 5.7 Hz, trim = 0°, amplitude = 2° & 12°

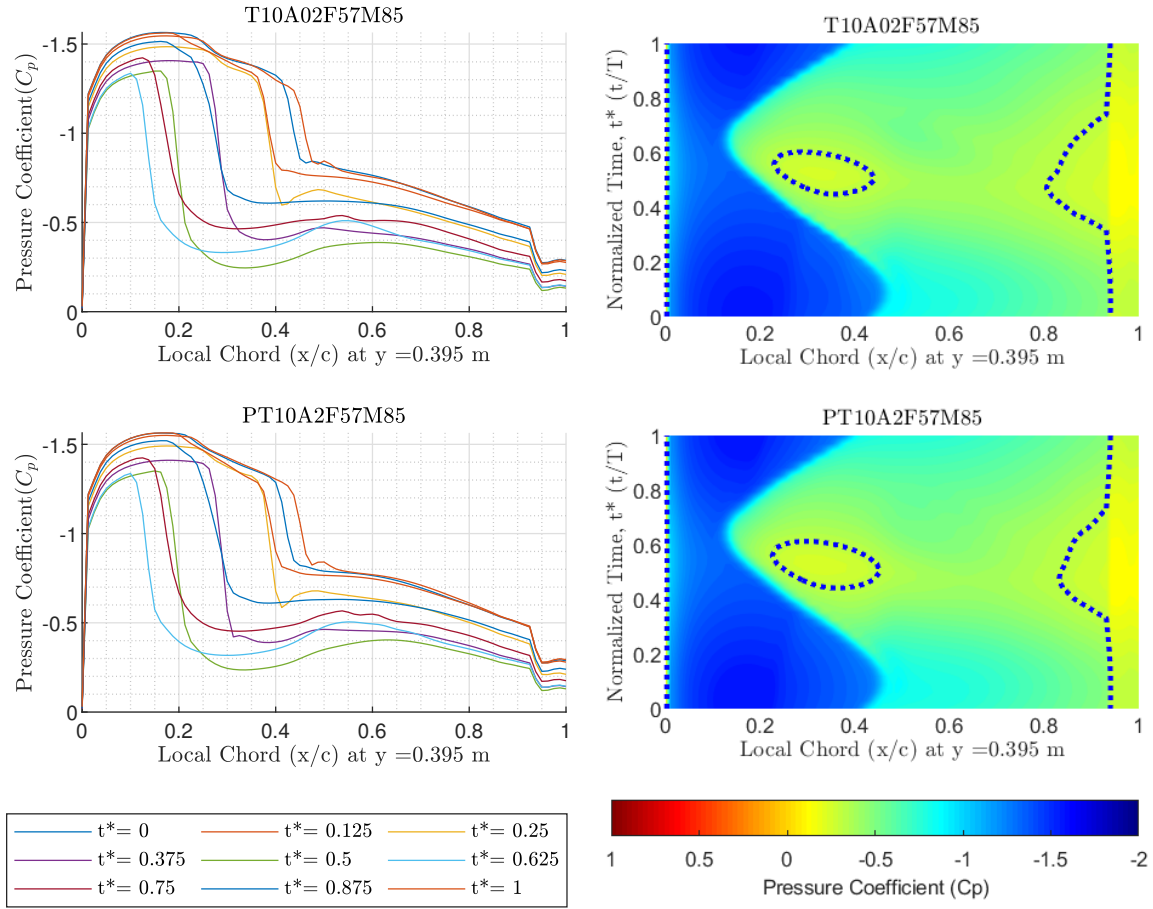


Figure D.11: Pressure distributions at Mach number 0.85. Frequency = 5.7 Hz, trim = 0° , amplitude = 2° . Top used $-\cosine$ function, and bottom used $+\cosine$ function.

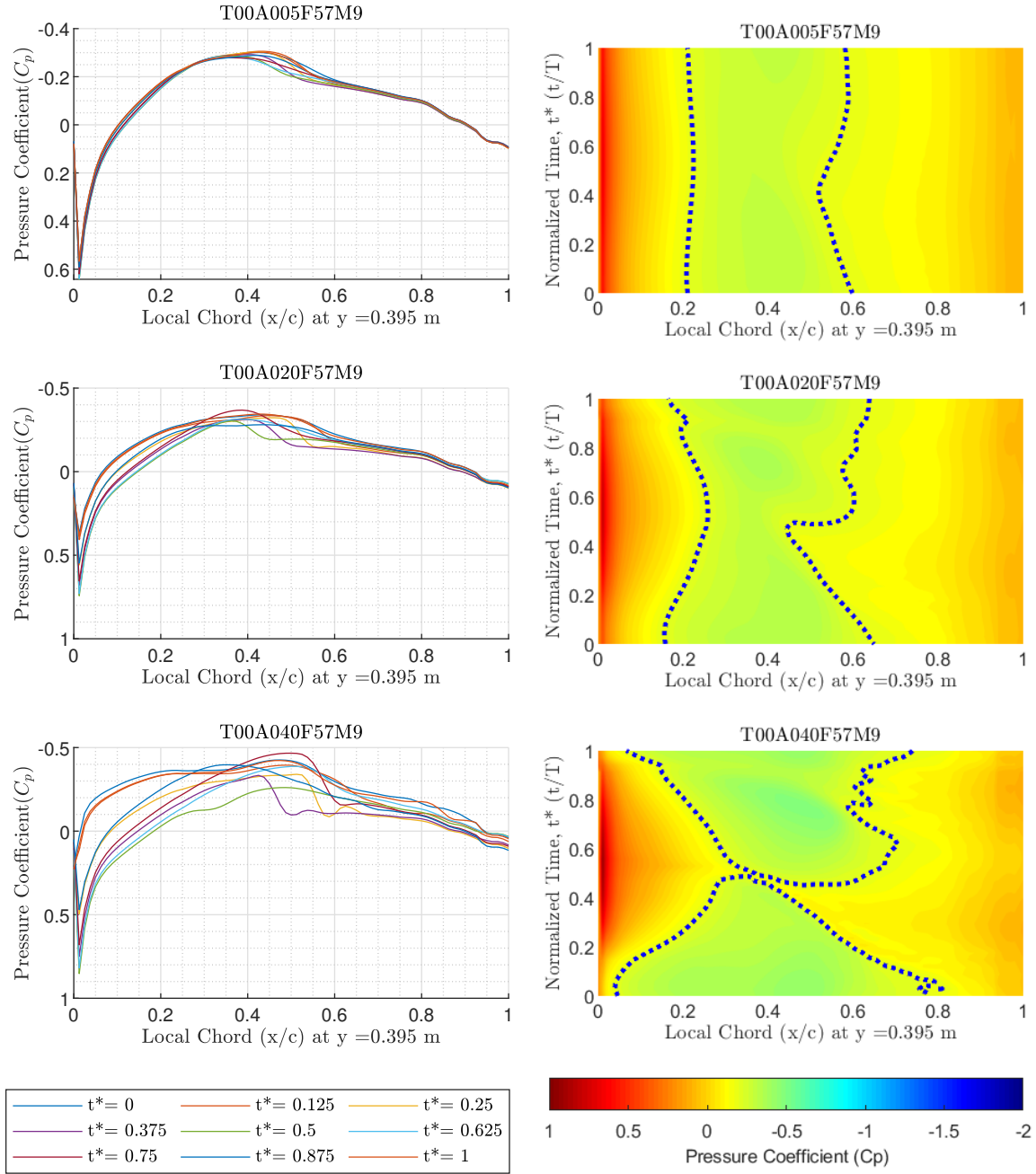


Figure D.12: Pressure distributions at Mach number 0.9. Frequency = 5.7 Hz, trim = 0°, amplitude = 0.5°, 2°, & 4°

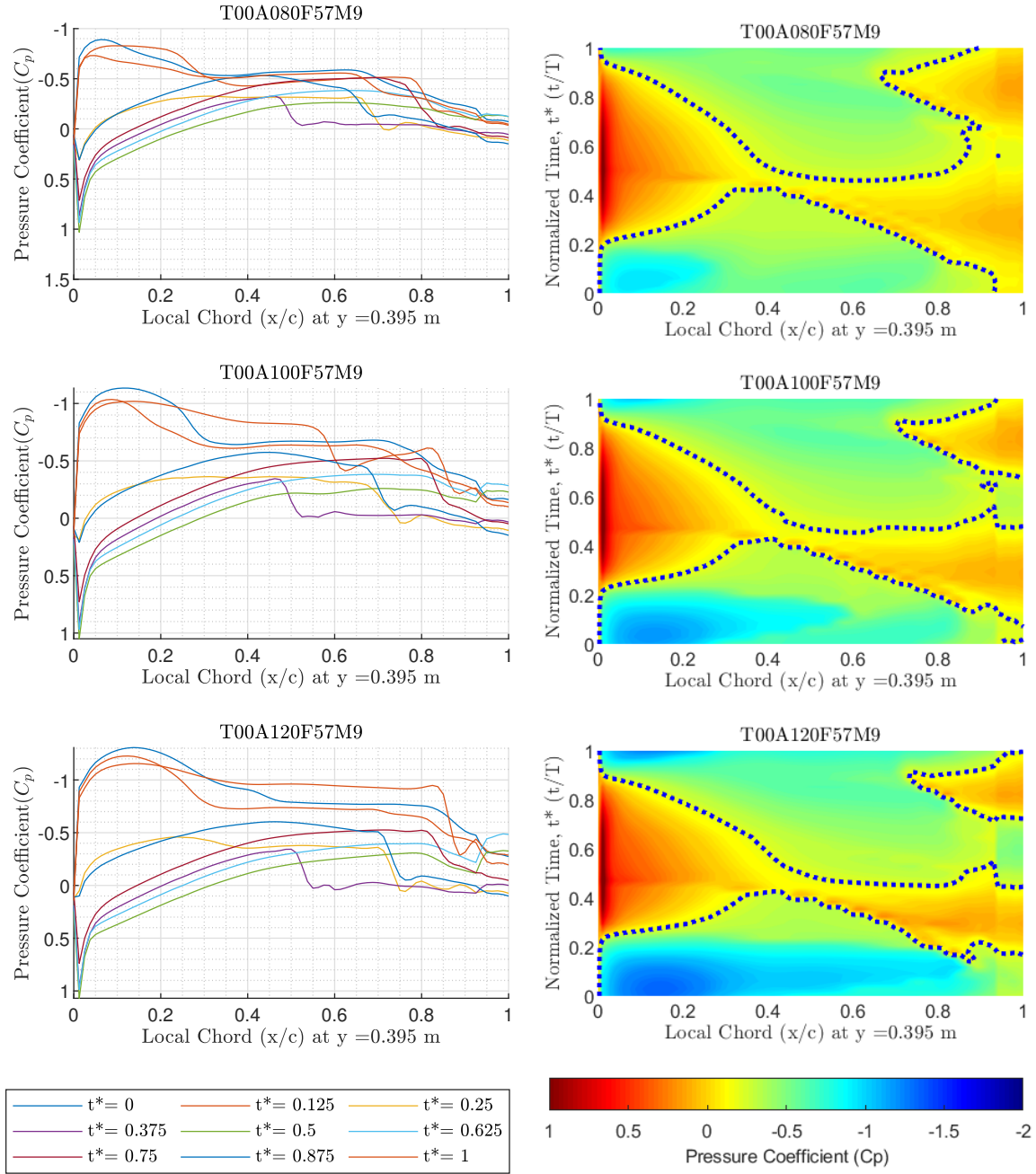


Figure D.13: Pressure distributions at Mach number 0.9. Frequency = 5.7 Hz, trim = 0°, amplitude = 8°, 10°, & 12°

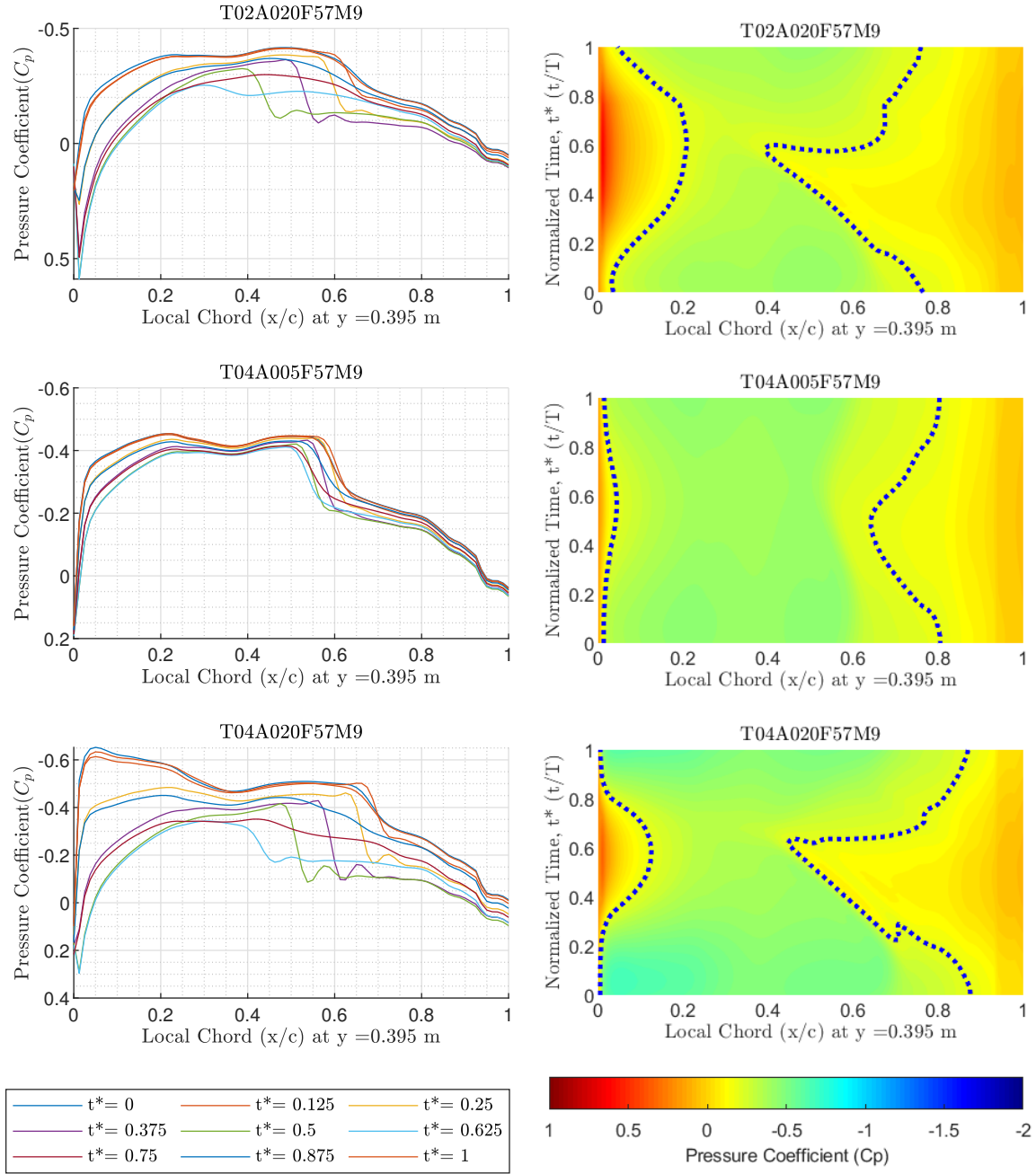


Figure D.14: Pressure distributions at Mach number 0.9. Frequency = 5.7 Hz, (Top) trim = 2° & amplitude = 2° , (middle & bottom) trim = 4° , amplitude = 0.5° & 2°

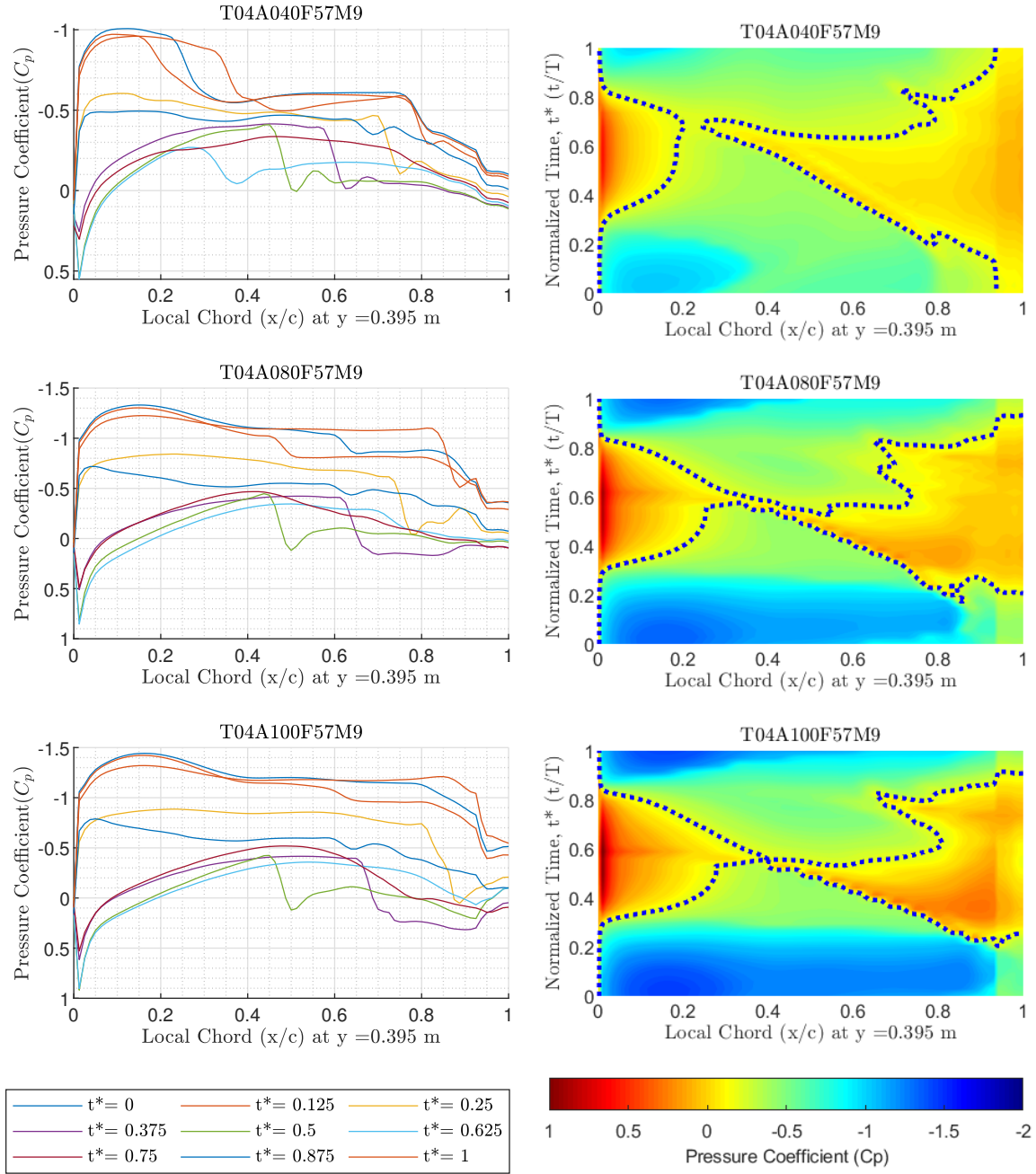


Figure D.15: Pressure distributions at Mach number 0.9. Frequency = 5.7 Hz, trim = 4°, amplitude = 4°, & 10°

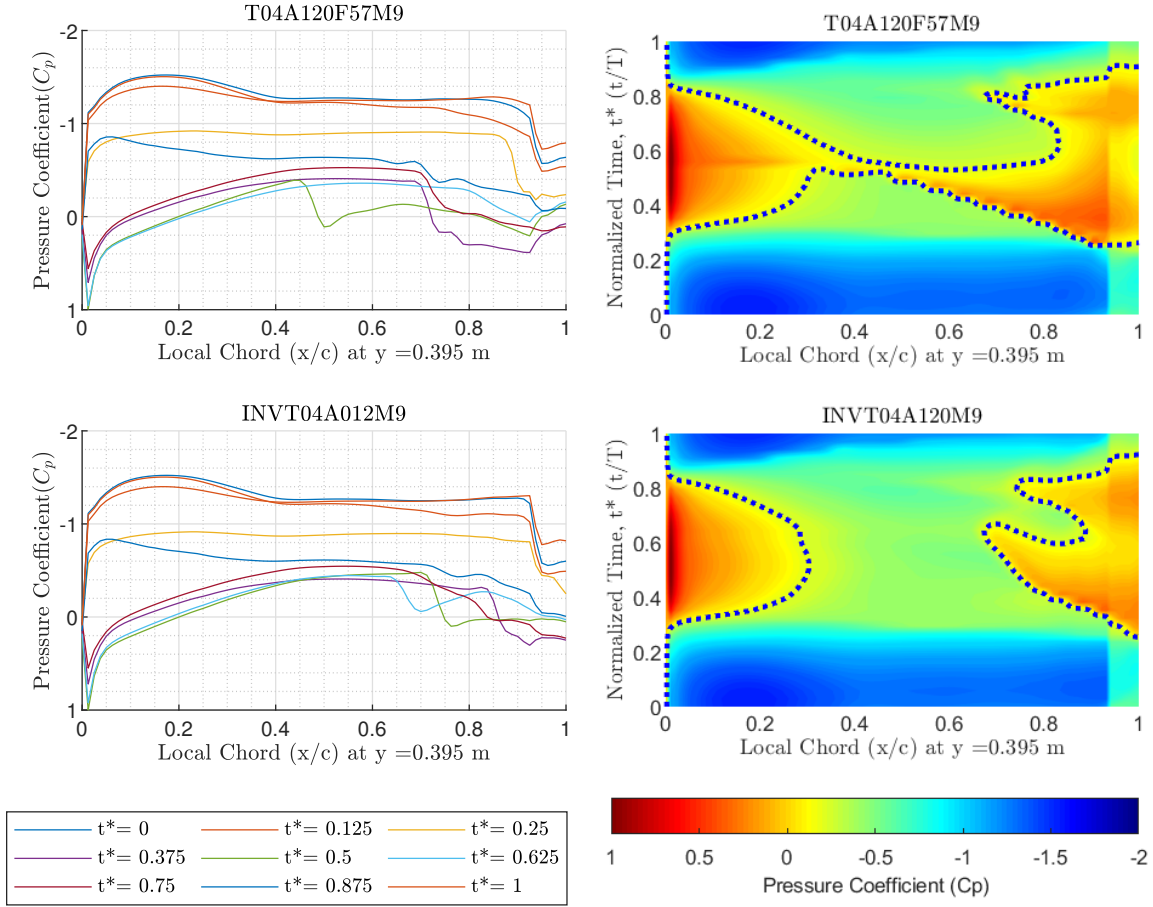


Figure D.16: Pressure distributions at Mach number 0.9. Frequency = 5.7 Hz, trim = 4°, amplitude = 12°. Top used BLC solver, and bottom used fully inviscid solver.

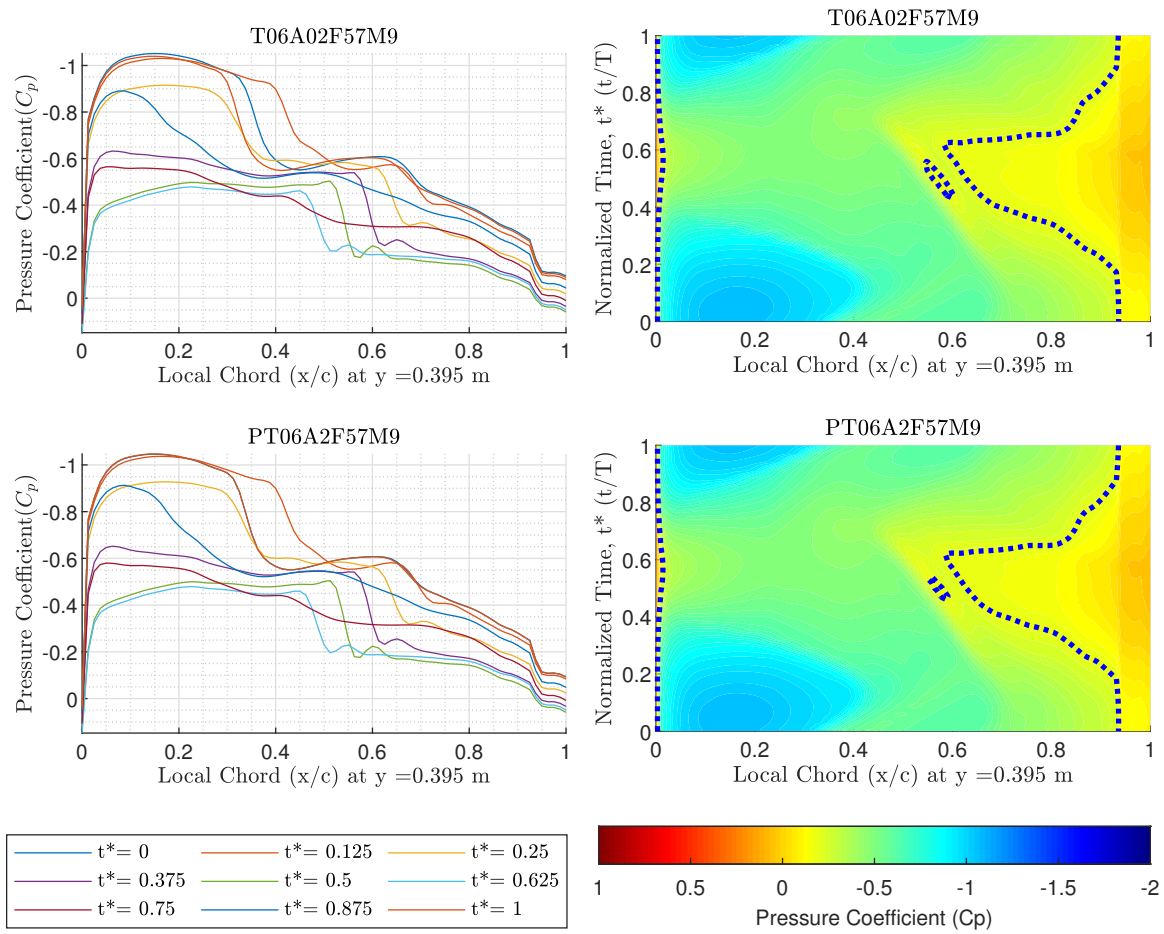


Figure D.17: Pressure distributions at Mach number 0.9. Frequency = 5.7 Hz, trim = 6°, amplitude = 2°. The bottom plot used a +cosine function.

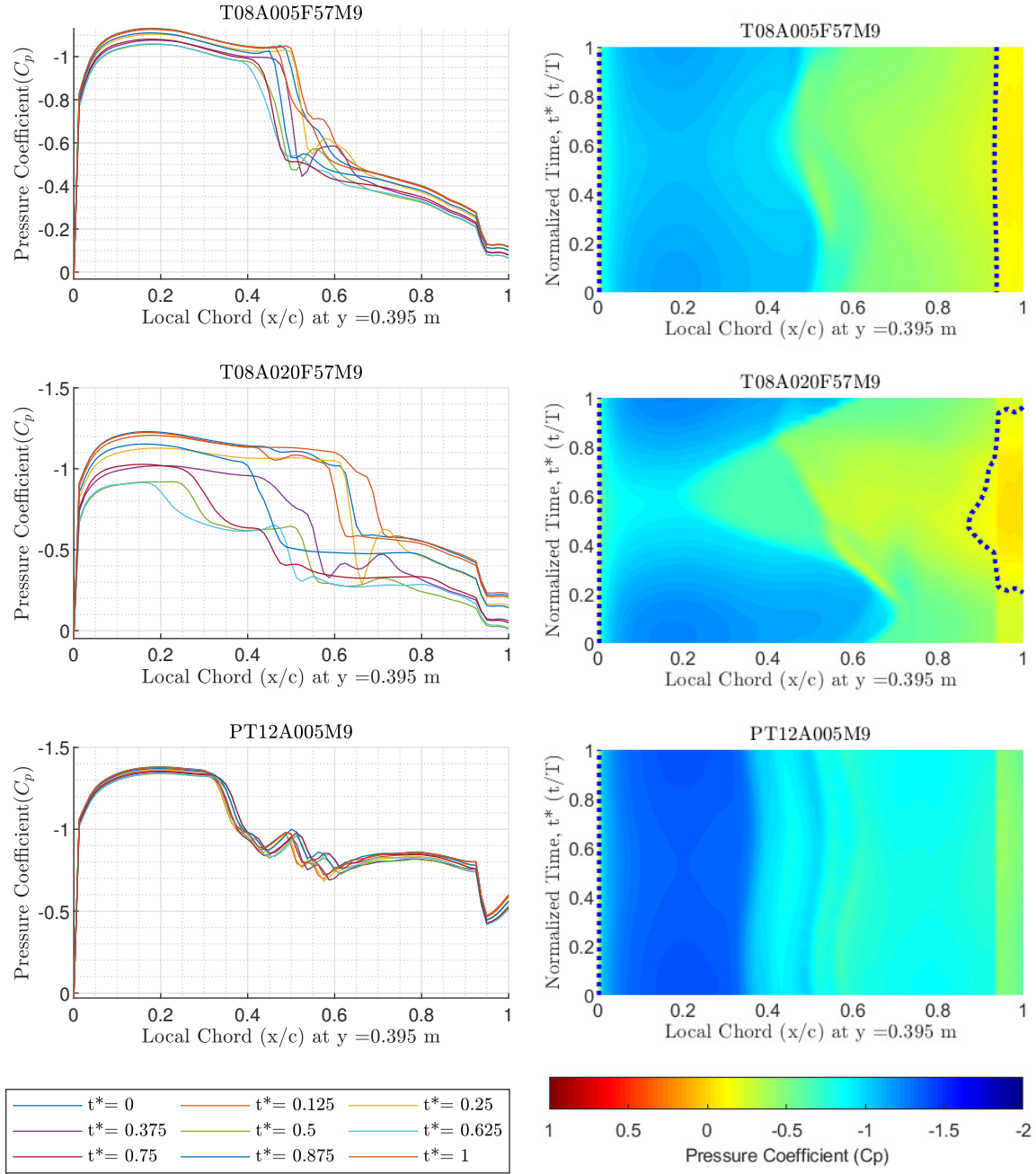


Figure D.18: Pressure distributions at Mach number 0.9. Frequency = 5.7 Hz, Top and middle plots had trim = 8° , amplitude = 0.5° & 2° . Bottom plots had trim = 12° , amplitude = 0.5° , & used a +cosine function.

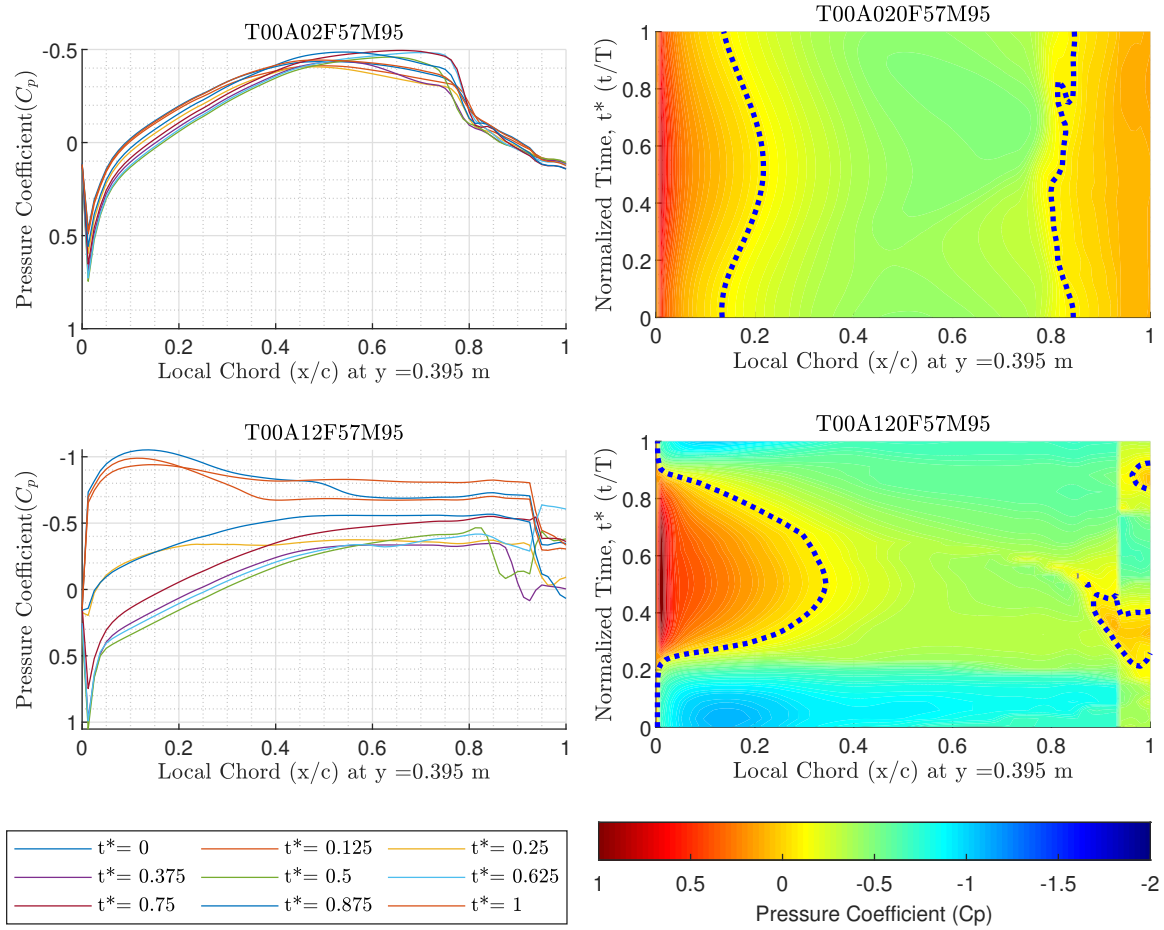


Figure D.19: Pressure distributions at Mach number 0.95. Frequency = 5.7 Hz, trim = 0°, amplitude = 2° & 12°

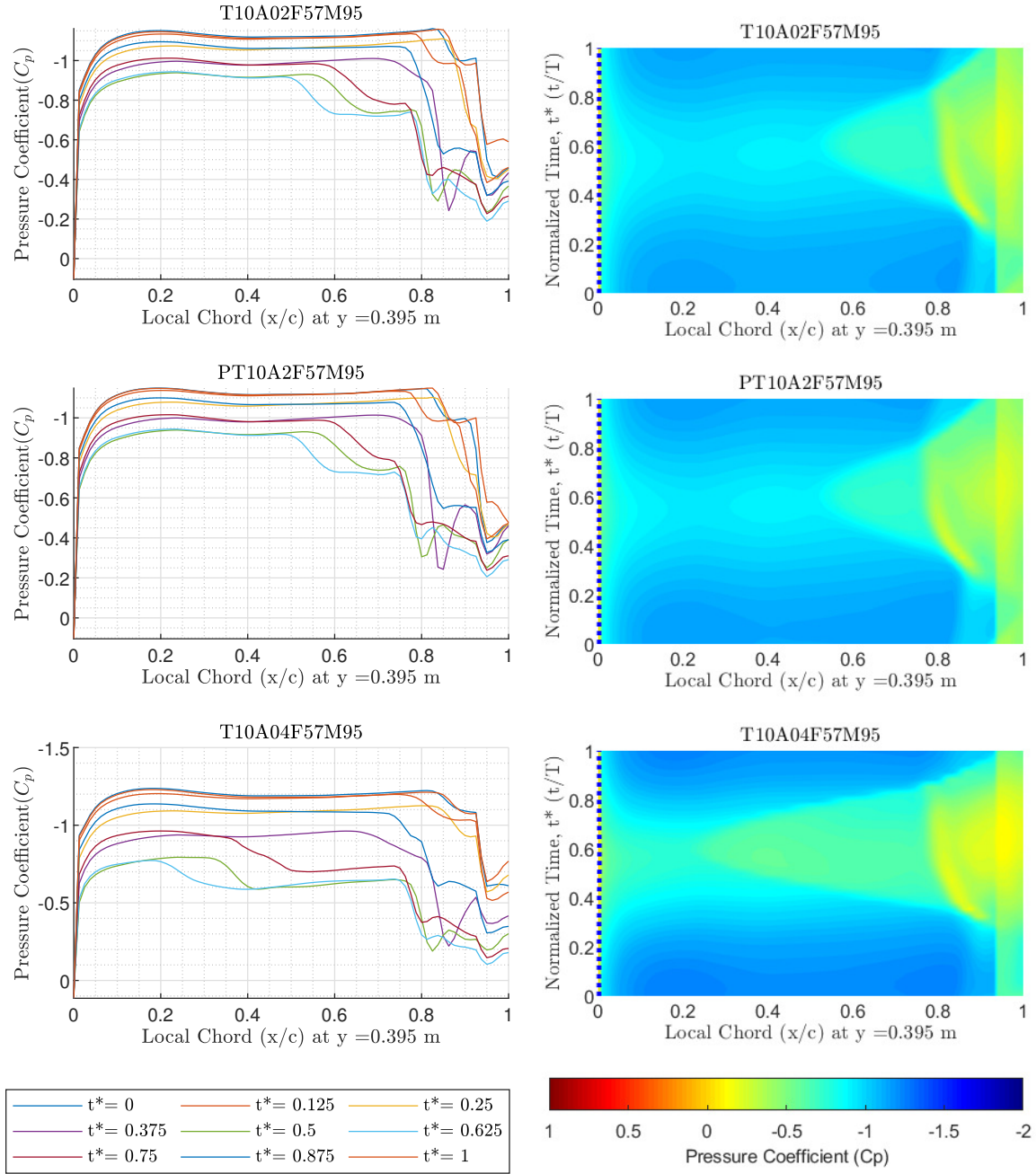


Figure D.20: Pressure distributions at Mach number 0.95. Frequency = 5.7 Hz, trim = 10° , amplitude = 2° , 2° , & 4° . Middle plots used a +cosine function.

Appendix E. C_m Data for Wing Station 1-4

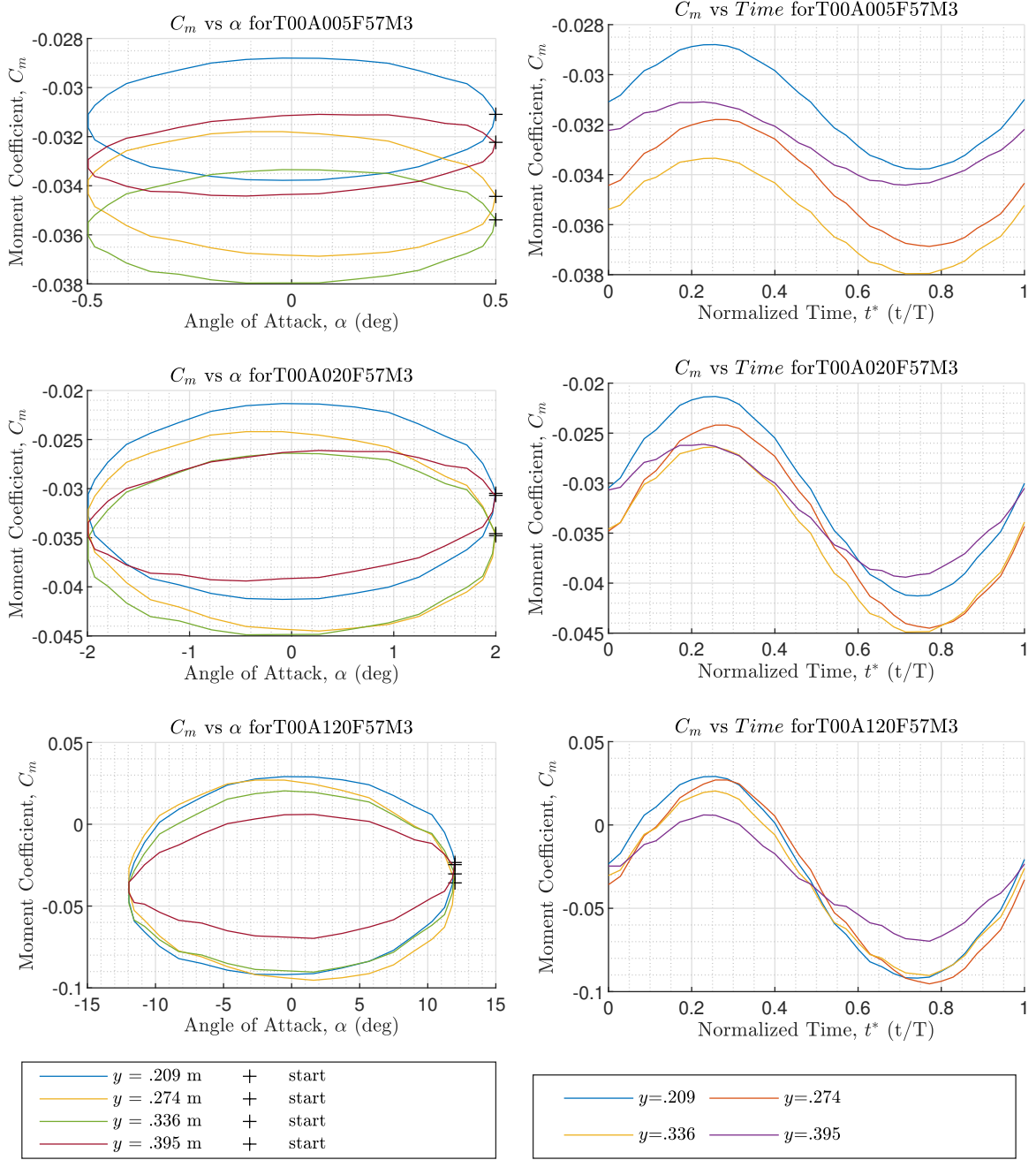


Figure E.1: Moment time histories at Mach number 0.3. Frequency = 5.7 Hz, trim = 0° , amplitude = 0.5° , 2° , & 12°

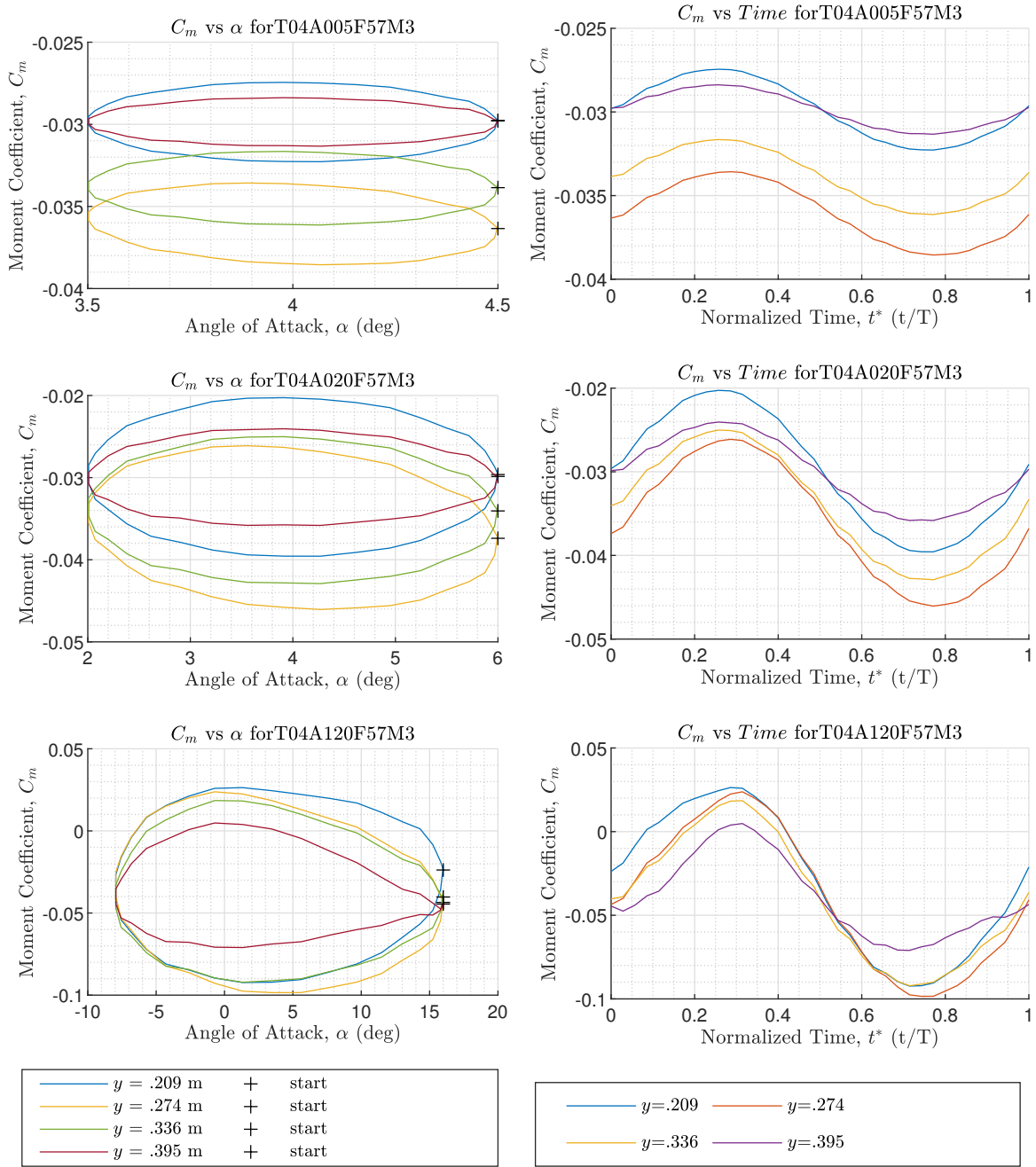


Figure E.2: Moment time histories at Mach number 0.3. Frequency = 5.7 Hz, trim = 4°, amplitude = 0.5°, 2°, & 12°

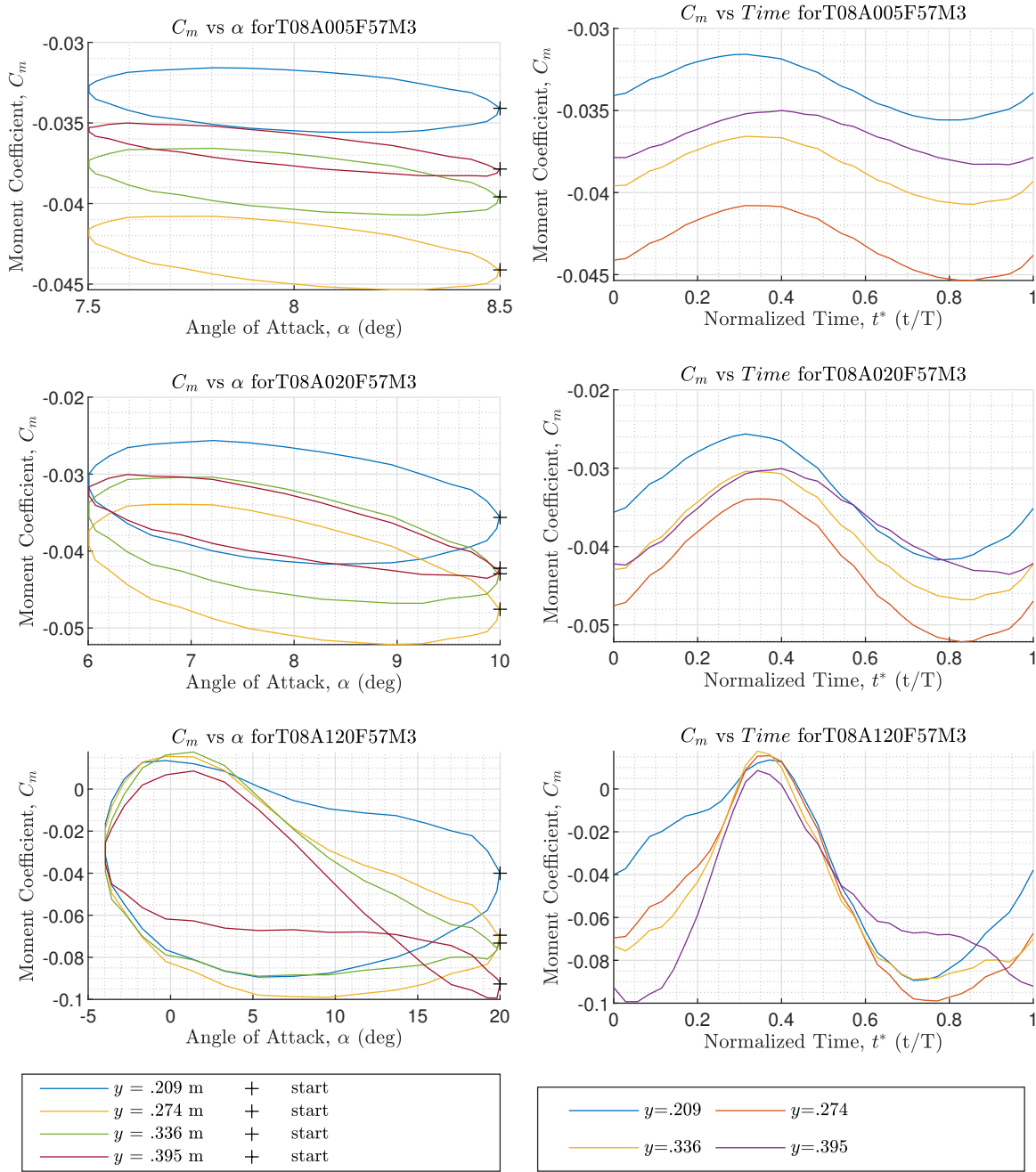


Figure E.3: Moment time histories at Mach number 0.3. Frequency = 5.7 Hz, trim = 8° , amplitude = 0.5° , 2° , & 12°

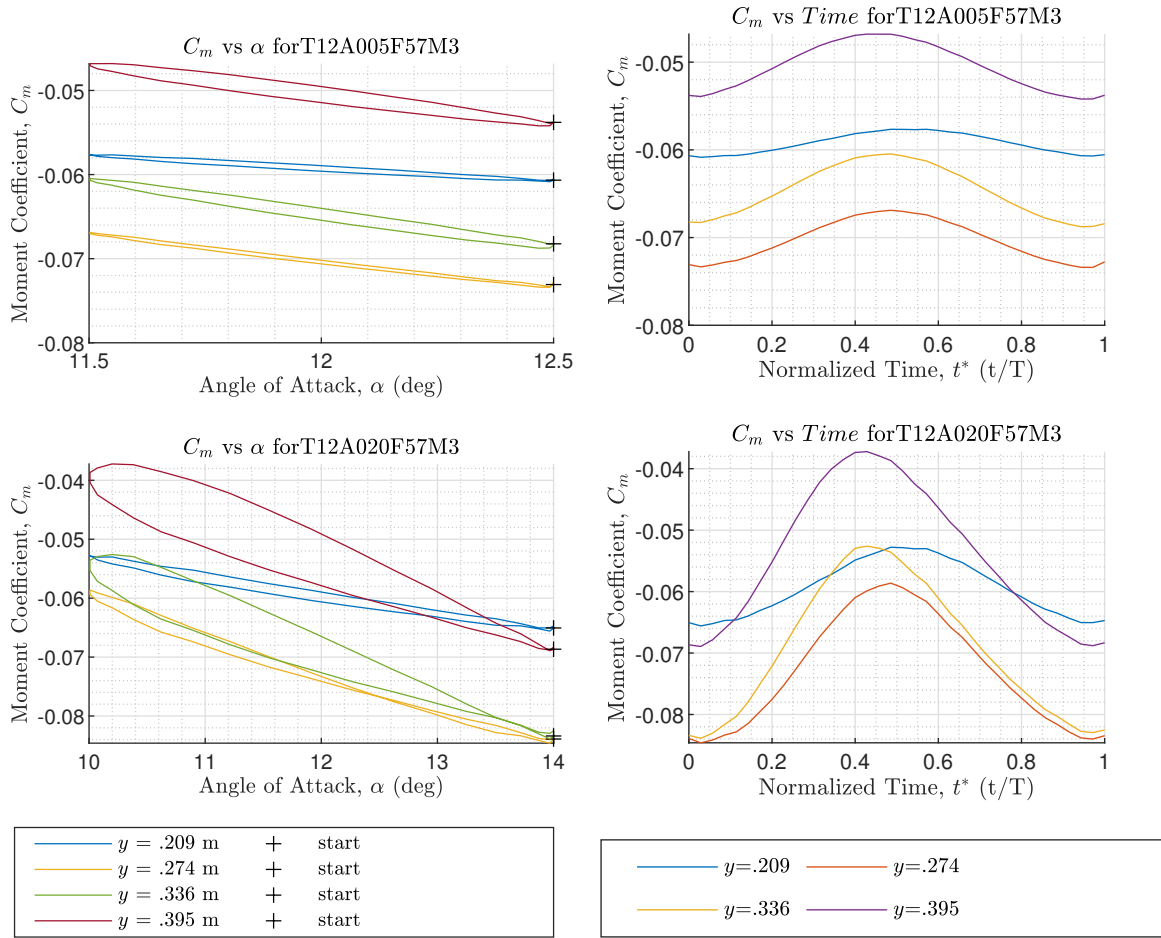


Figure E.4: Moment time histories at Mach number 0.3. Frequency = 5.7 Hz, trim = 12°, amplitude = 0.5° & 2°

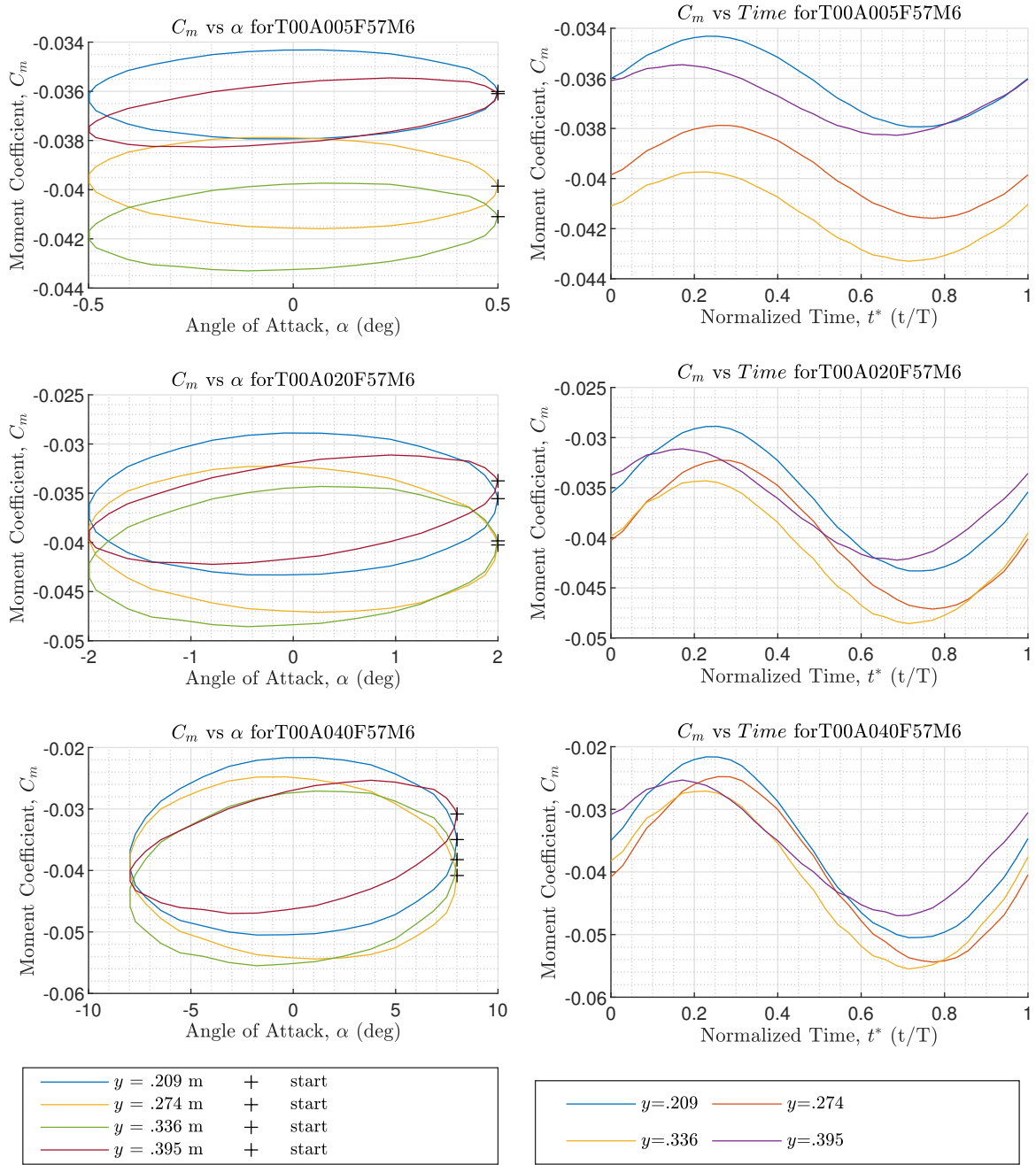


Figure E.5: Moment time histories at Mach number 0.6. Frequency = 5.7 Hz, trim = 0° , amplitude = 0.5° , 2° , & 4°

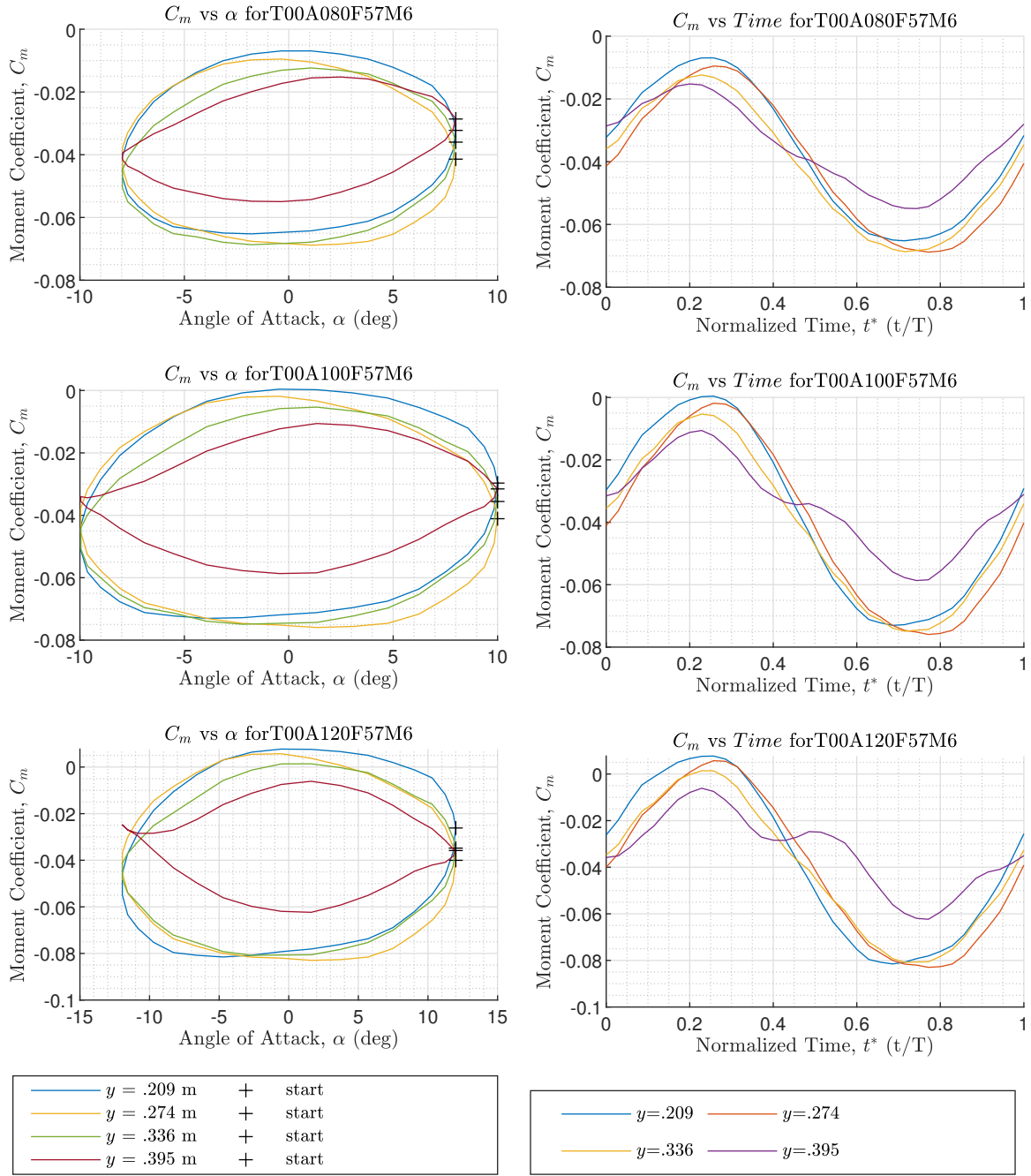


Figure E.6: Moment time histories at Mach number 0.6. Frequency = 5.7 Hz, trim = 0° , amplitude = 8° , 10° , & 12°

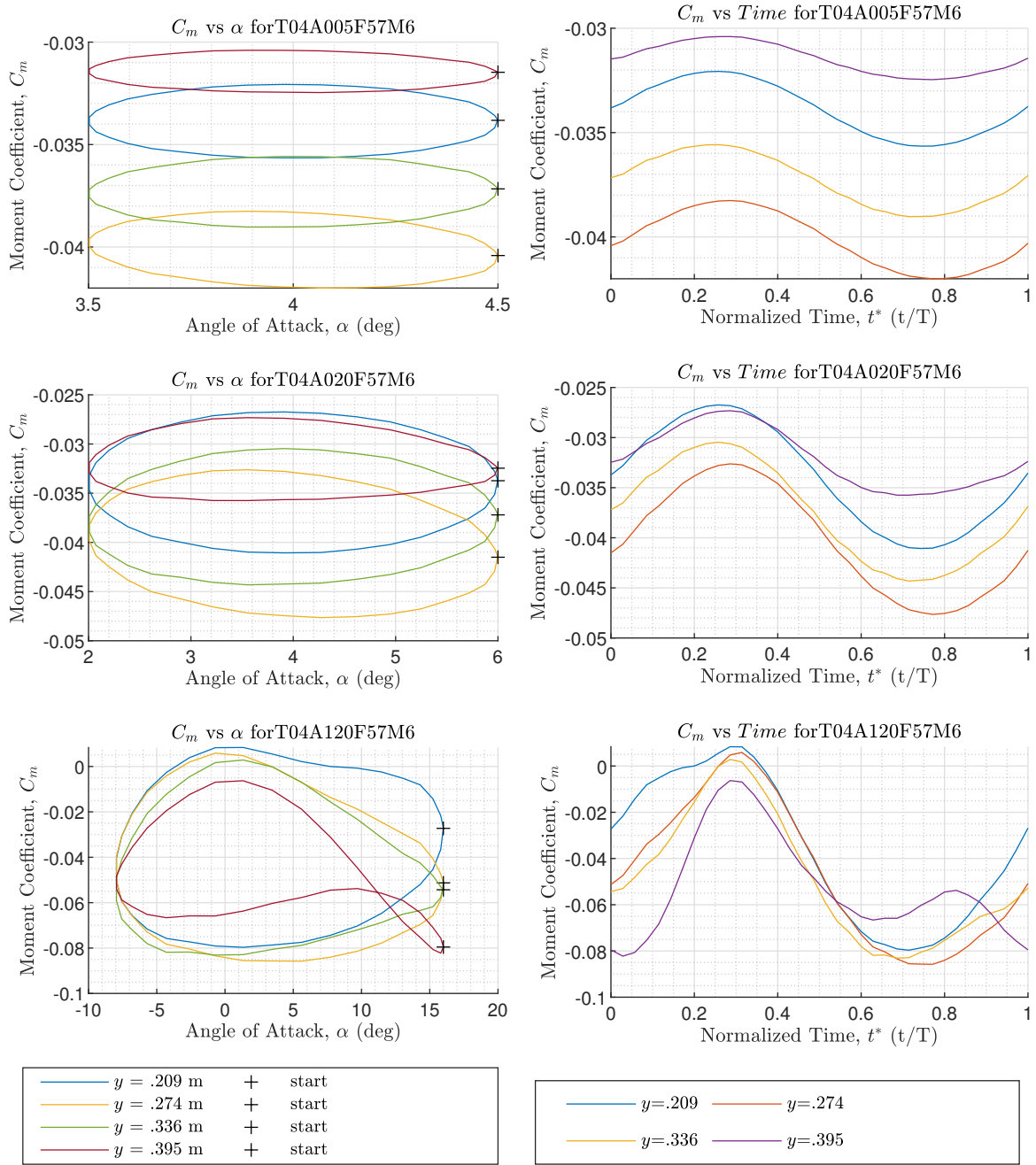


Figure E.7: Moment time histories at Mach number 0.6. Frequency = 5.7 Hz, trim = 4°, amplitude = 0.5°, 2°, & 12°

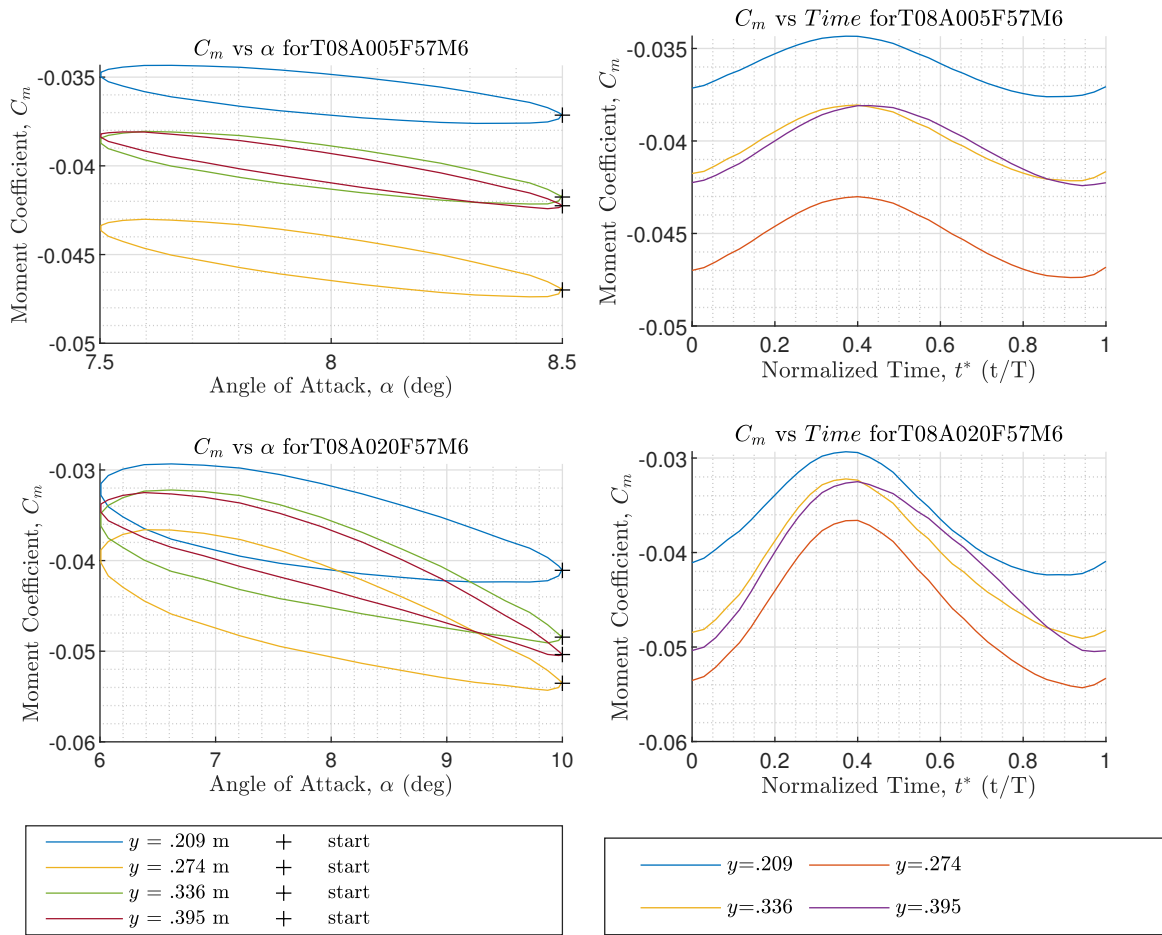


Figure E.8: Moment time histories at Mach number 0.6. Frequency = 5.7 Hz, trim = 8° , amplitude = 0.5° & 2°

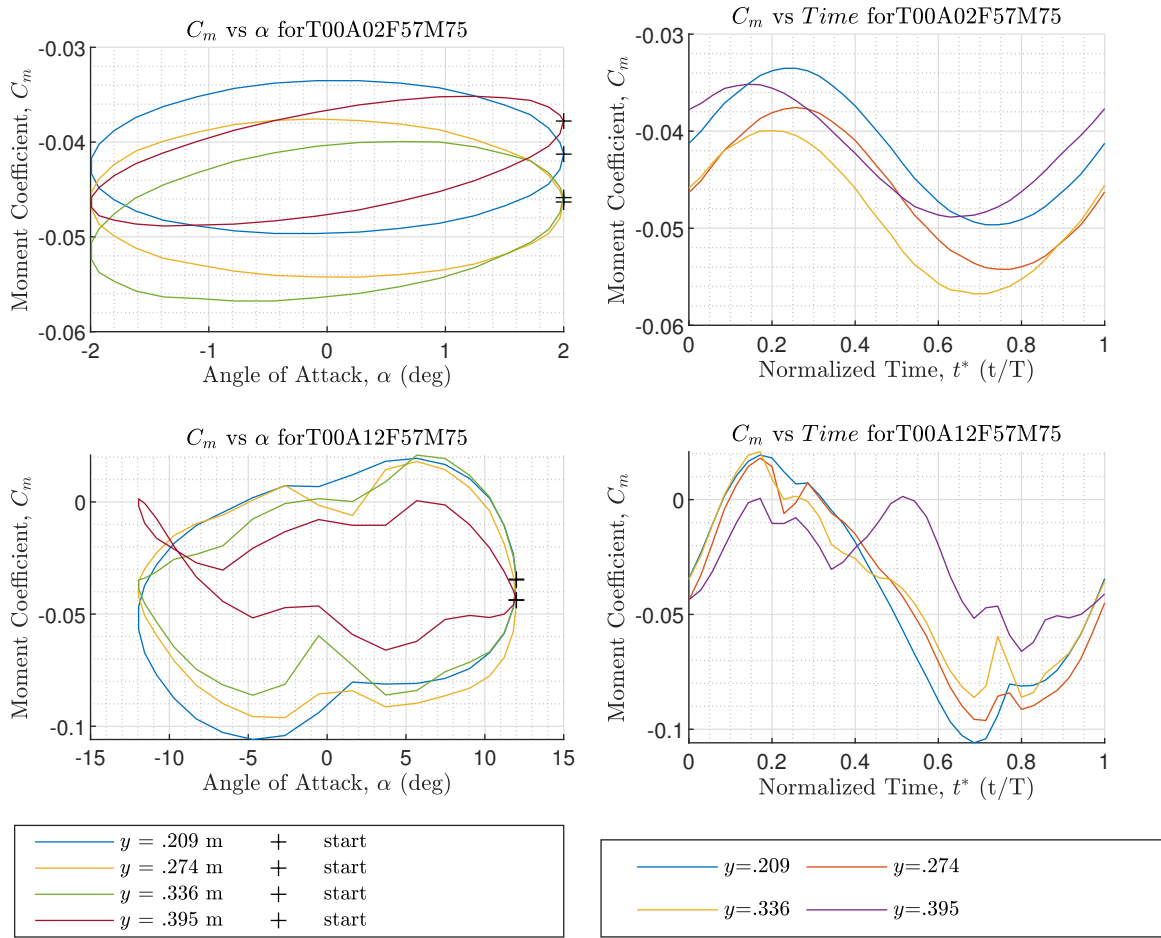


Figure E.9: Moment time histories at Mach number 0.75. Frequency = 5.7 Hz, trim = 0° , amplitude = 2° & 12°

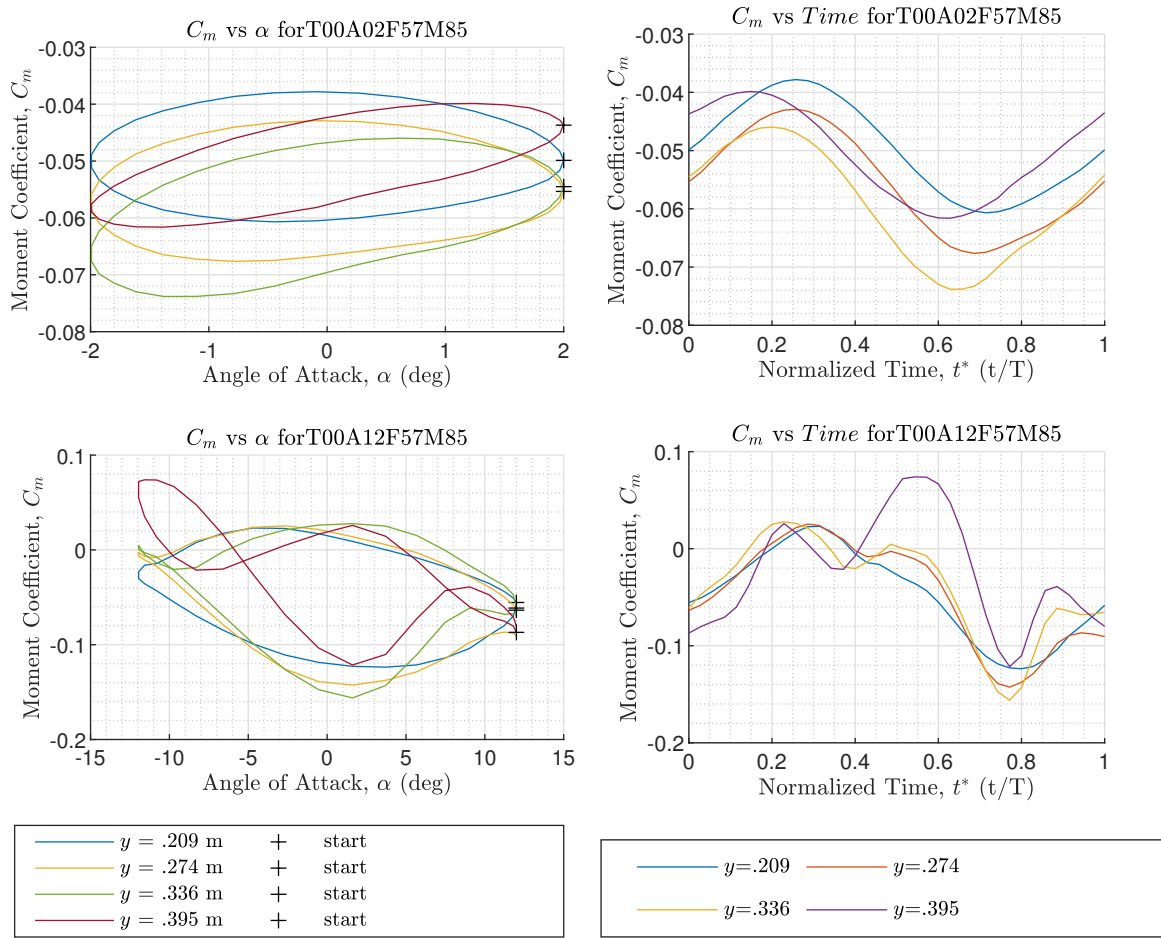


Figure E.10: Moment time histories at Mach number 0.85. Frequency = 5.7 Hz, trim = 0° , amplitude = 2° & 12°

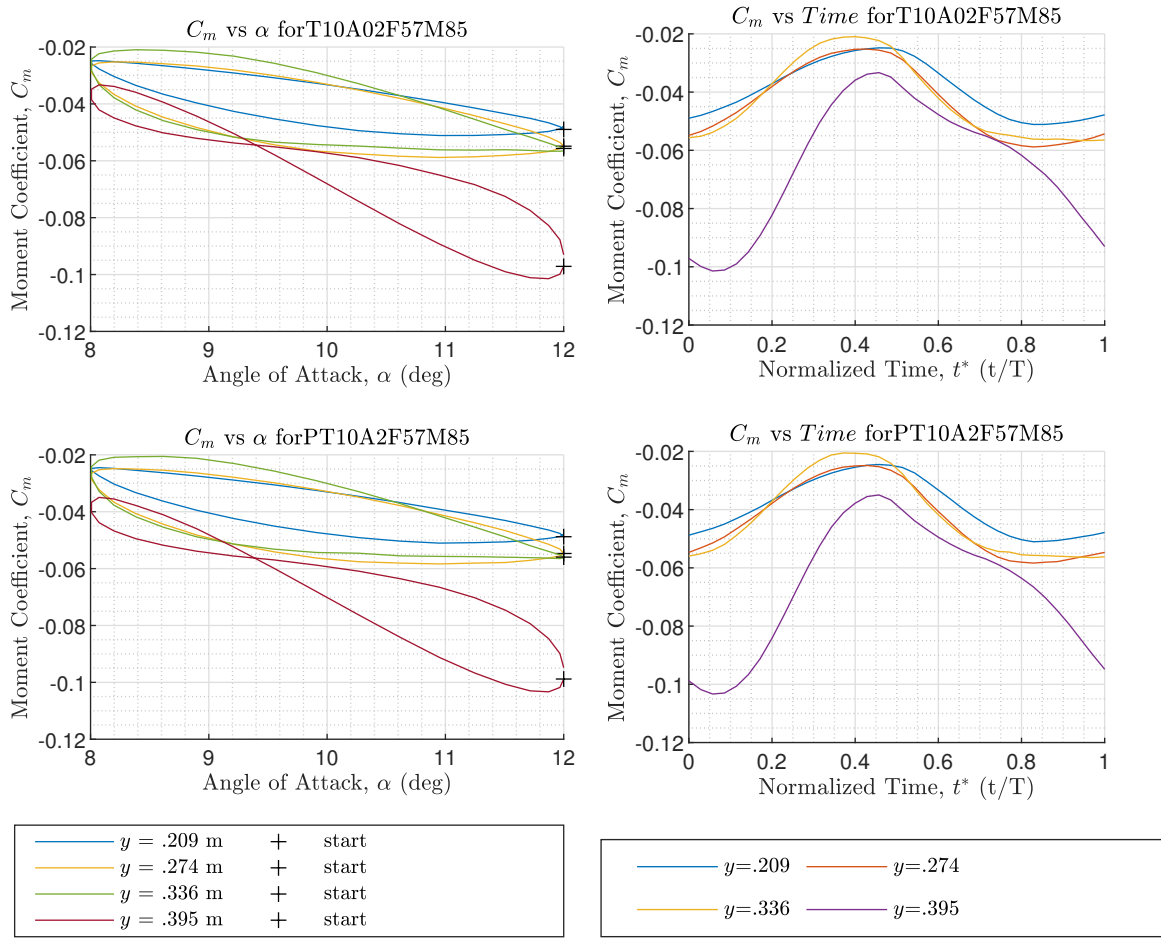


Figure E.11: Moment time histories at Mach number 0.85. Frequency = 5.7 Hz, trim = 0° , amplitude = 2° . Top used -cosine function, and bottom used +cosine function.

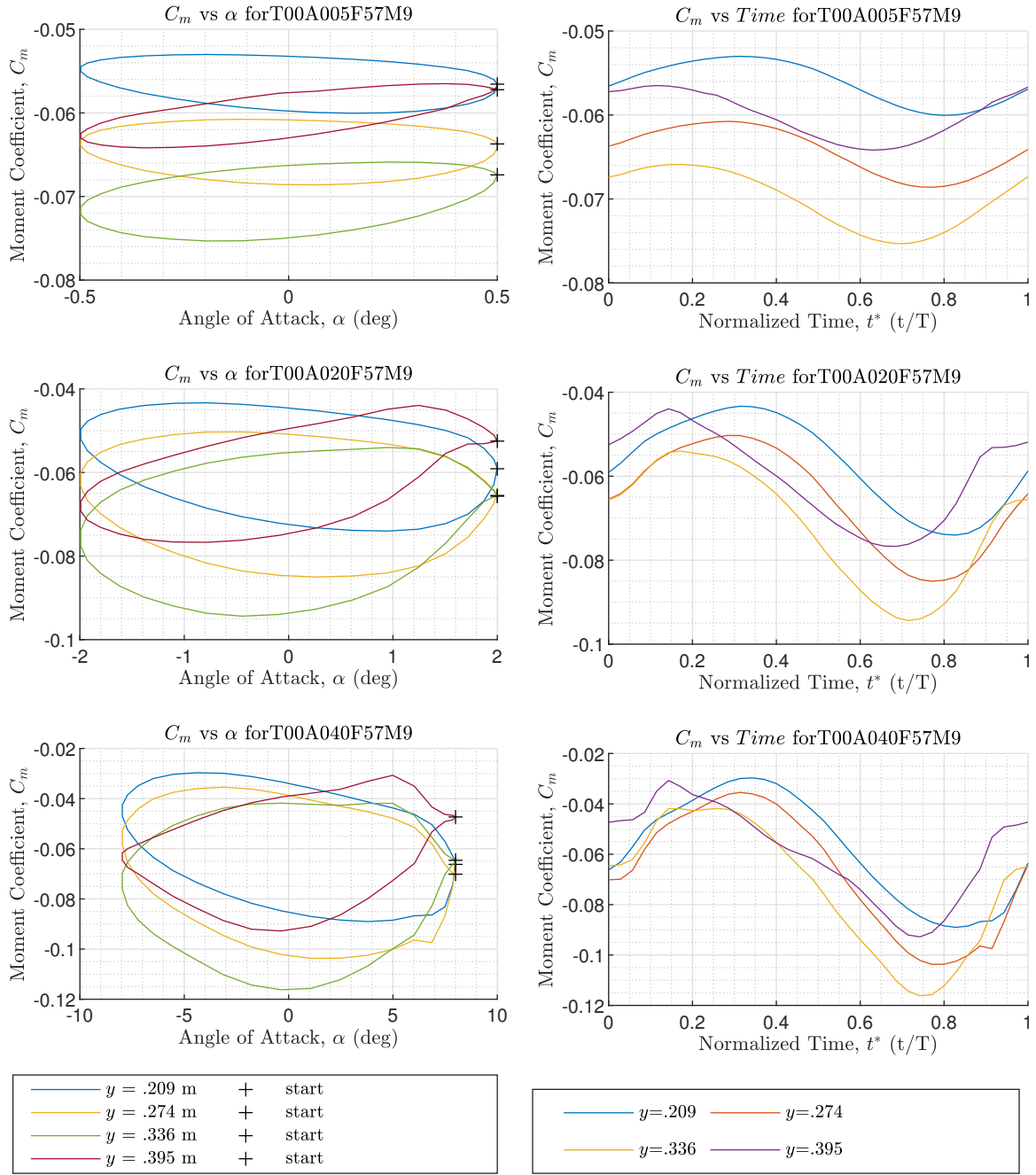


Figure E.12: Moment time histories at Mach number 0.9. Frequency = 5.7 Hz, trim = 0° , amplitude = 0.5° , 2° , & 4°

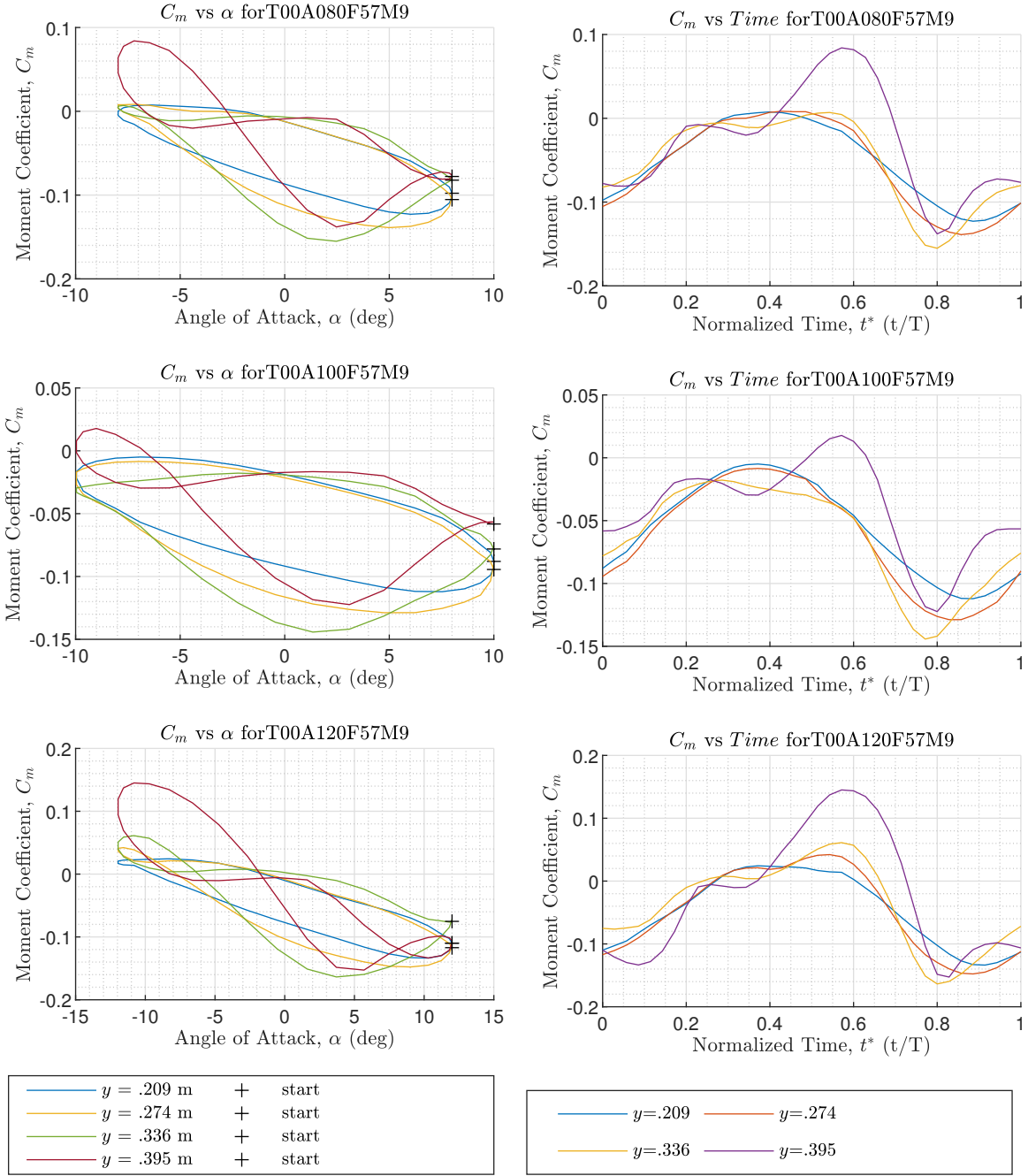


Figure E.13: Moment time histories at Mach number 0.9. Frequency = 5.7 Hz, trim = 0° , amplitude = 8° , 10° , & 12°

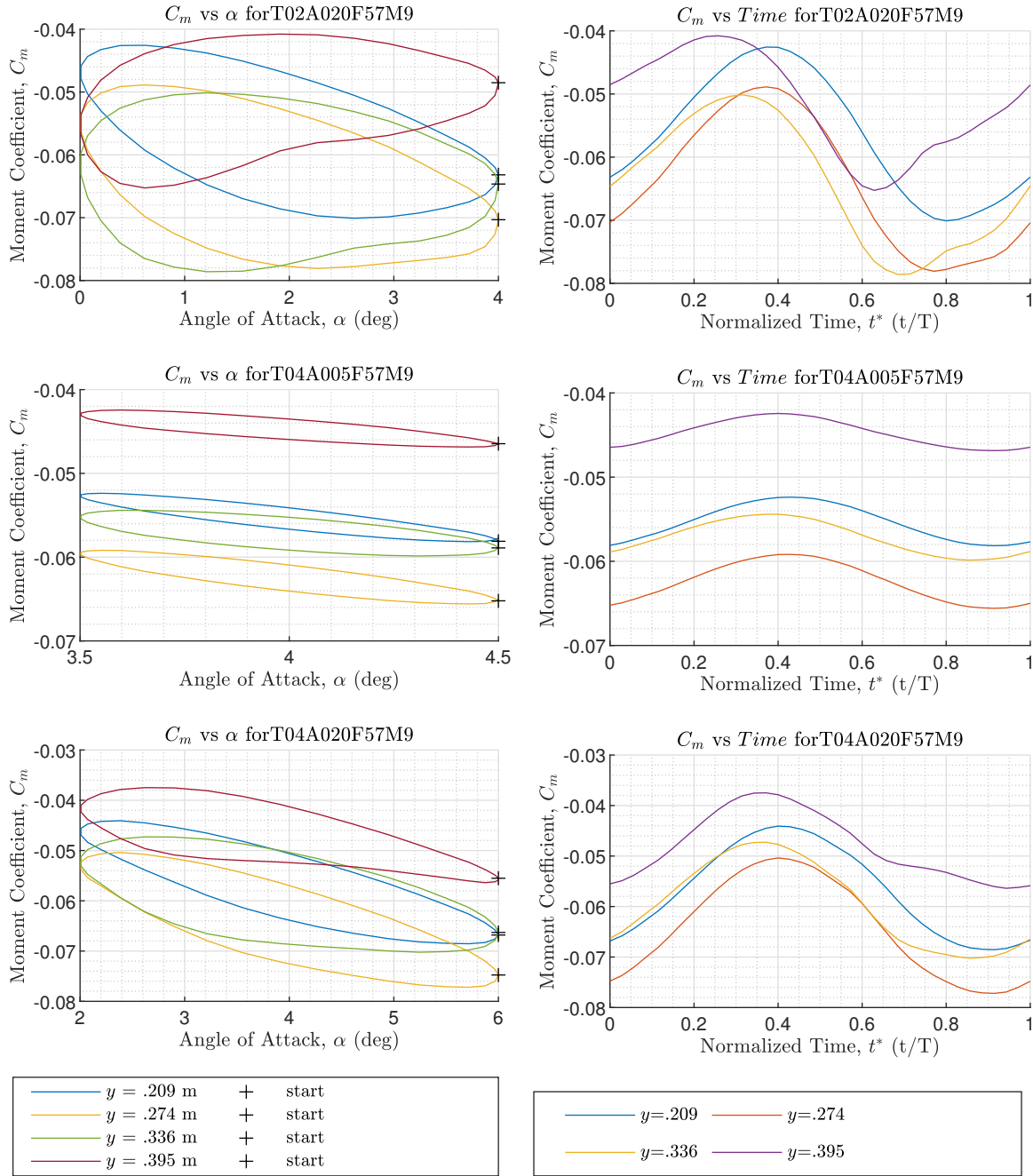


Figure E.14: Moment time histories at Mach number 0.9. Frequency = 5.7 Hz, (Top) trim = 2° & amplitude = 2°, (middle & bottom) trim = 4°, amplitude = 0.5° & 2°

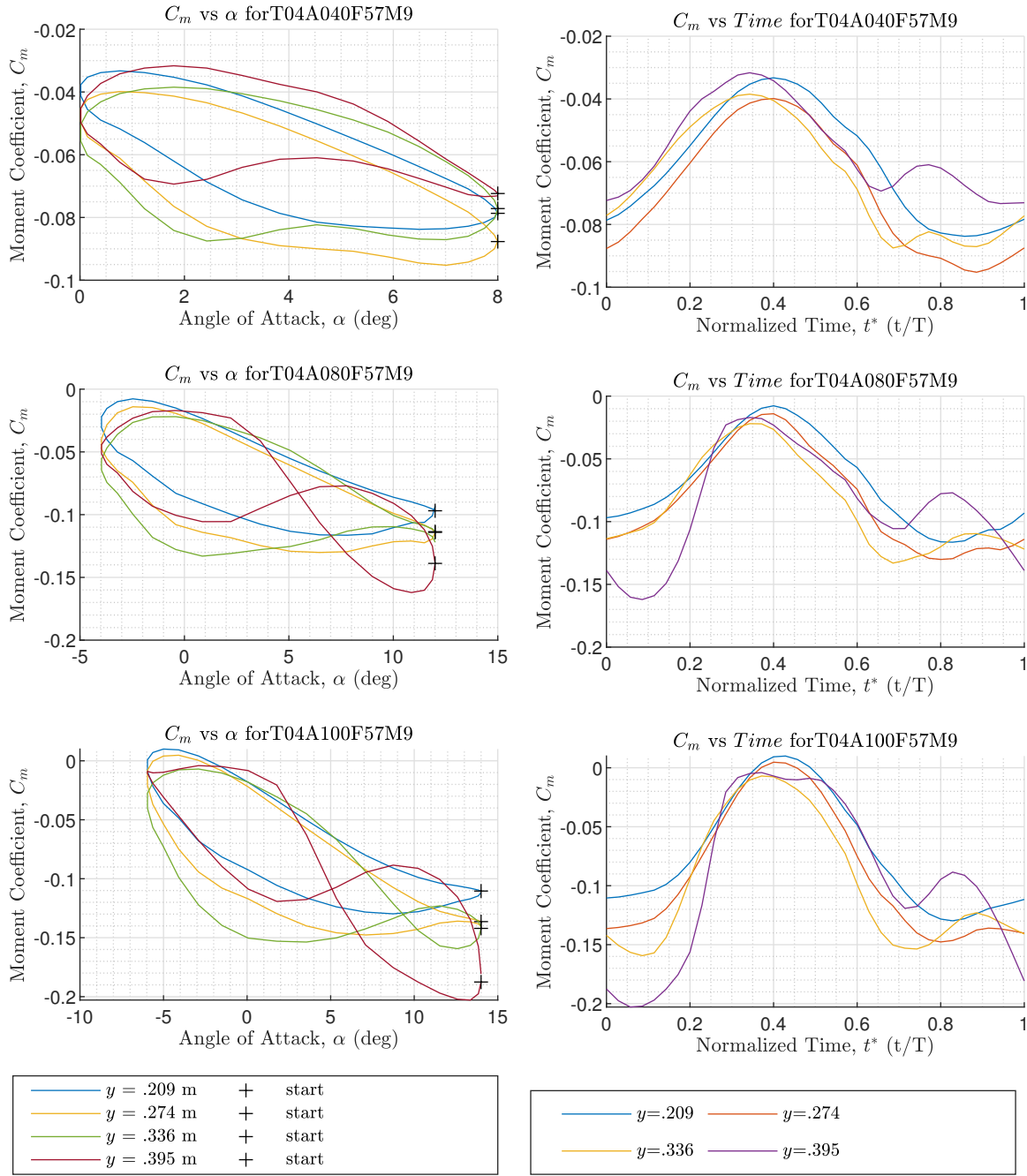


Figure E.15: Moment time histories at Mach number 0.9. Frequency = 5.7 Hz, trim = 4°, amplitude = 4°, 8°, & 10°

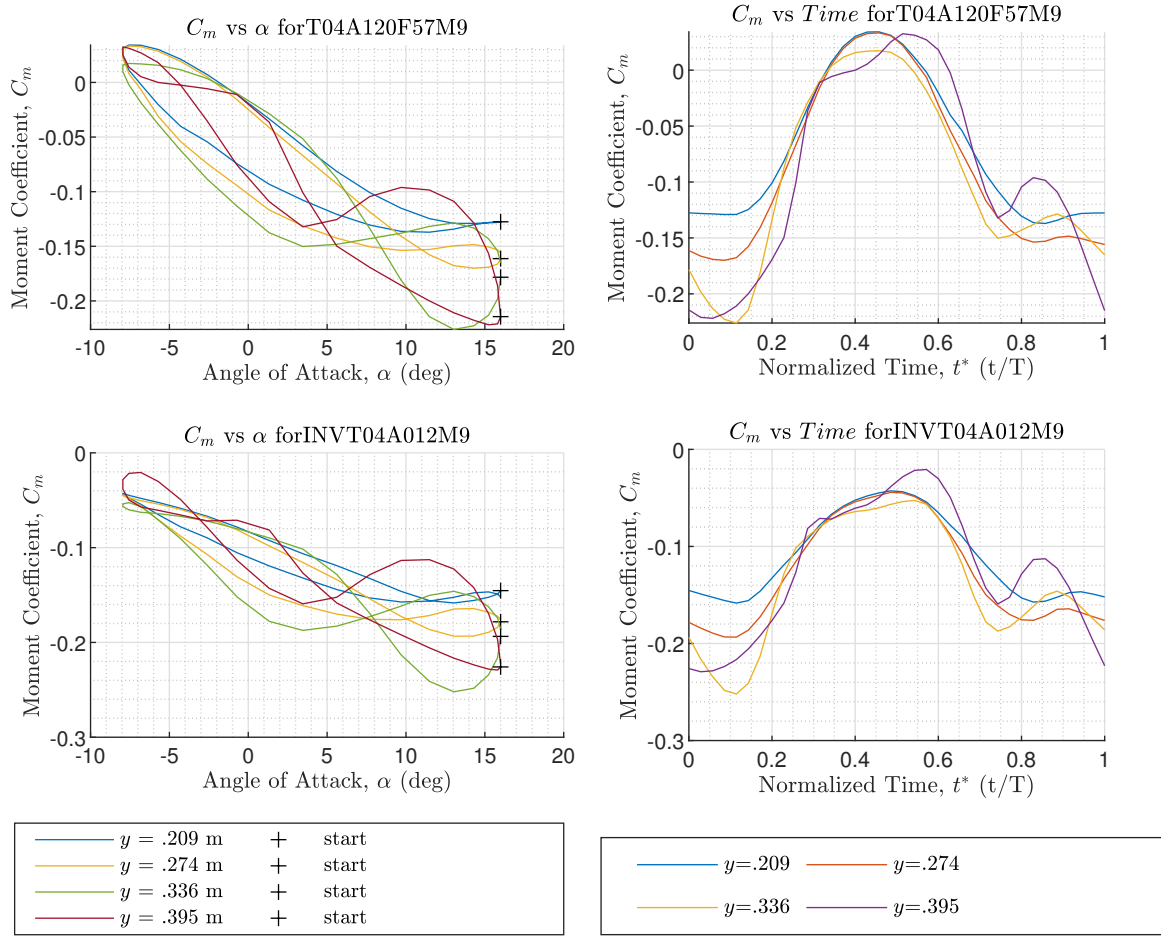


Figure E.16: Moment time histories at Mach number 0.9. Frequency = 5.7 Hz, trim = 4°, amplitude = 12°. Top used BLC solver, and bottom used fully inviscid solver.

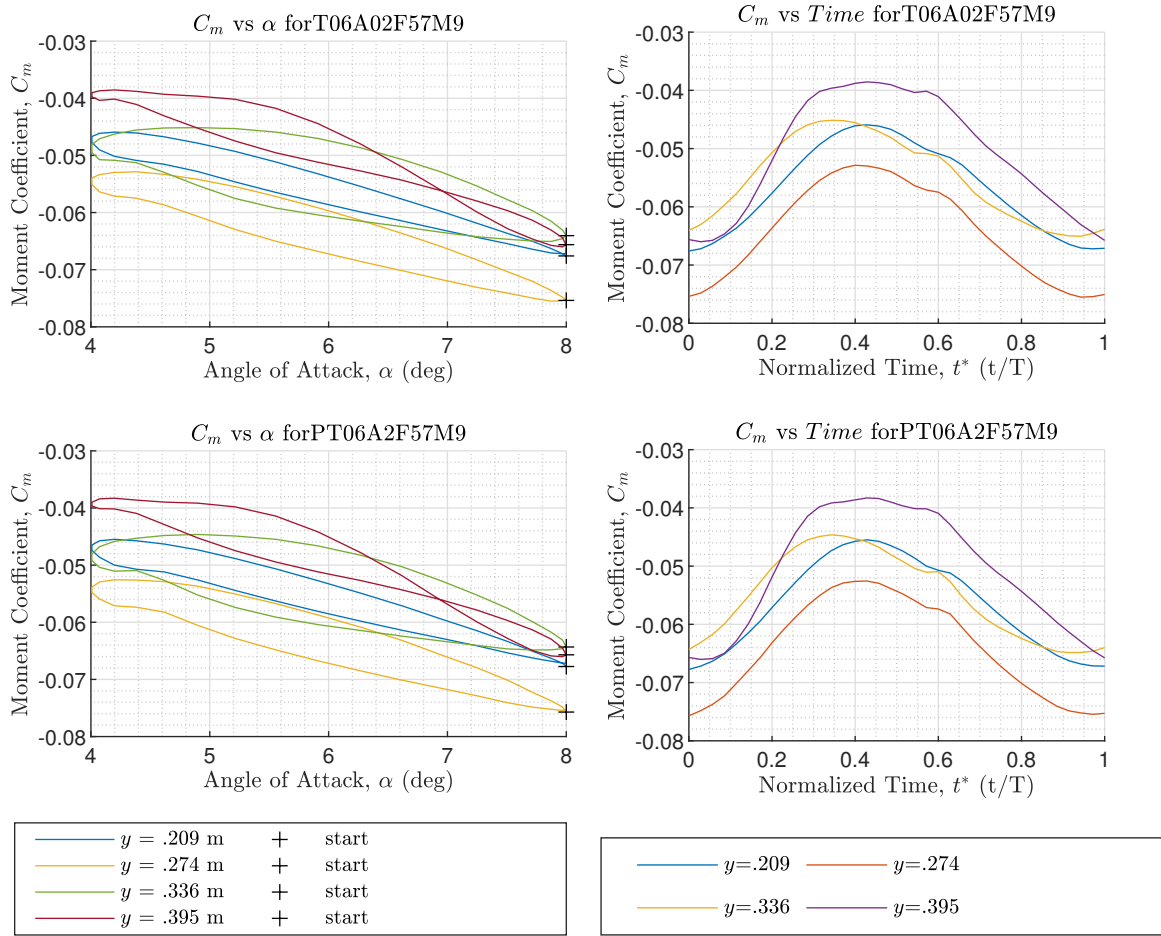


Figure E.17: Moment time histories at Mach number 0.9. Frequency = 5.7 Hz, trim = 6°, amplitude = 2°. The bottom plot used a +cosine function.

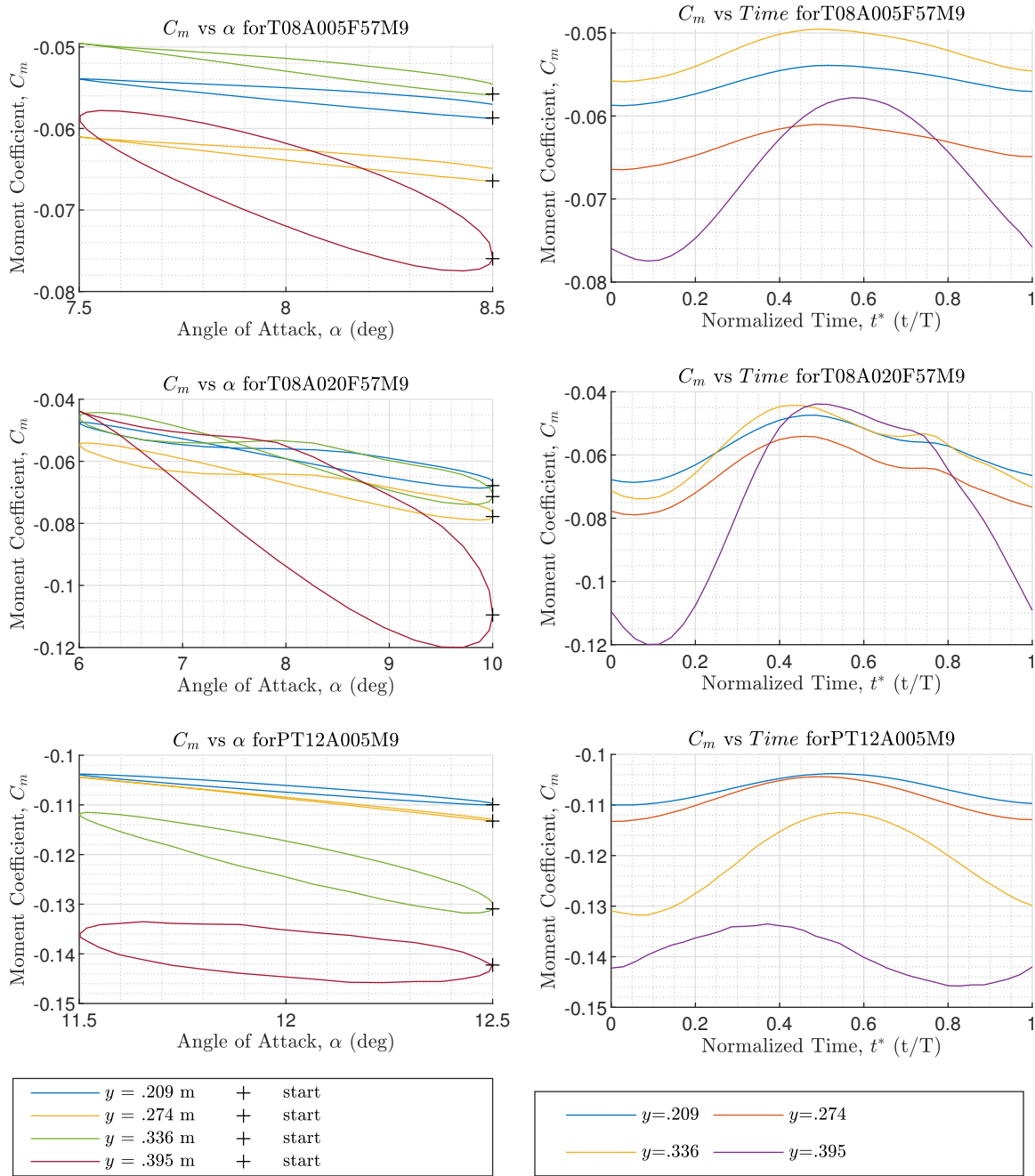


Figure E.18: Moment time histories at Mach number 0.9. Frequency = 5.7 Hz, Top and middle plots had trim = 8° , amplitude = 0.5° & 2° . Bottom plots had trim = 12° , amplitude = 0.5° , & used a +cosine function.

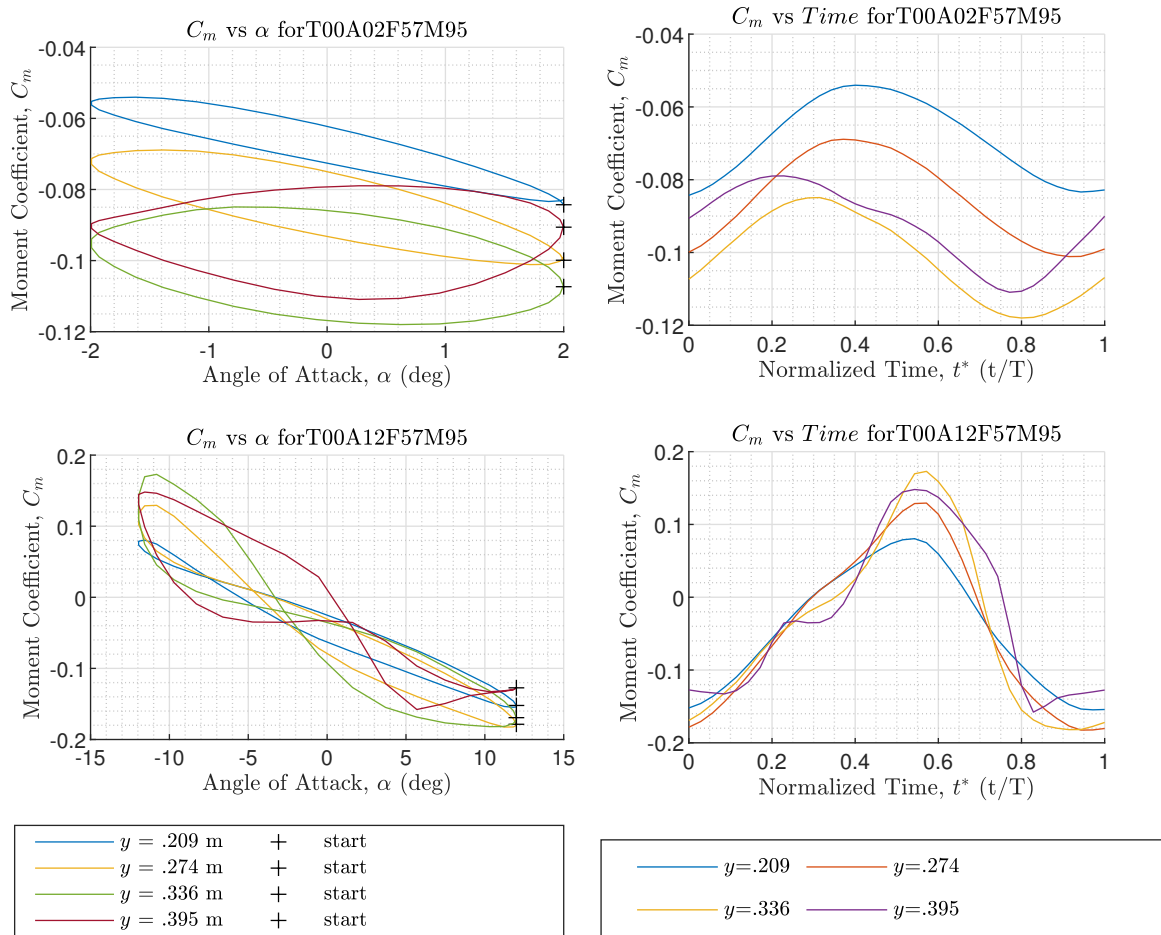


Figure E.19: Moment time histories at Mach number 0.95. Frequency = 5.7 Hz, trim = 0° , amplitude = 2° & 12°

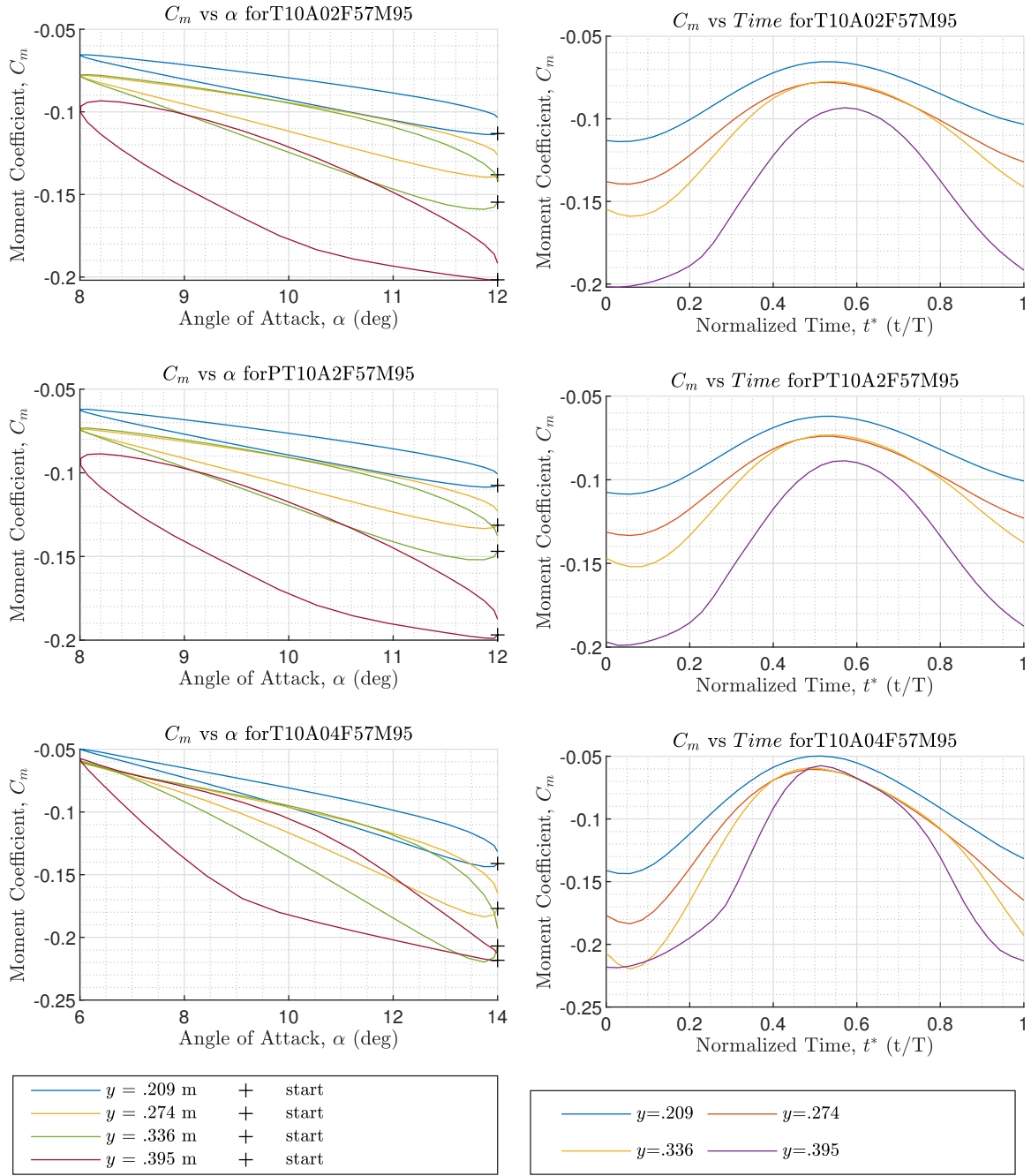


Figure E.20: Moment time histories at Mach number 0.95. Frequency = 5.7 Hz, trim = 10°, amplitude = 2°, 2°, & 4°. Middle plots used a +cosine function.

Appendix F. C_l Data for Wing Station 1-4

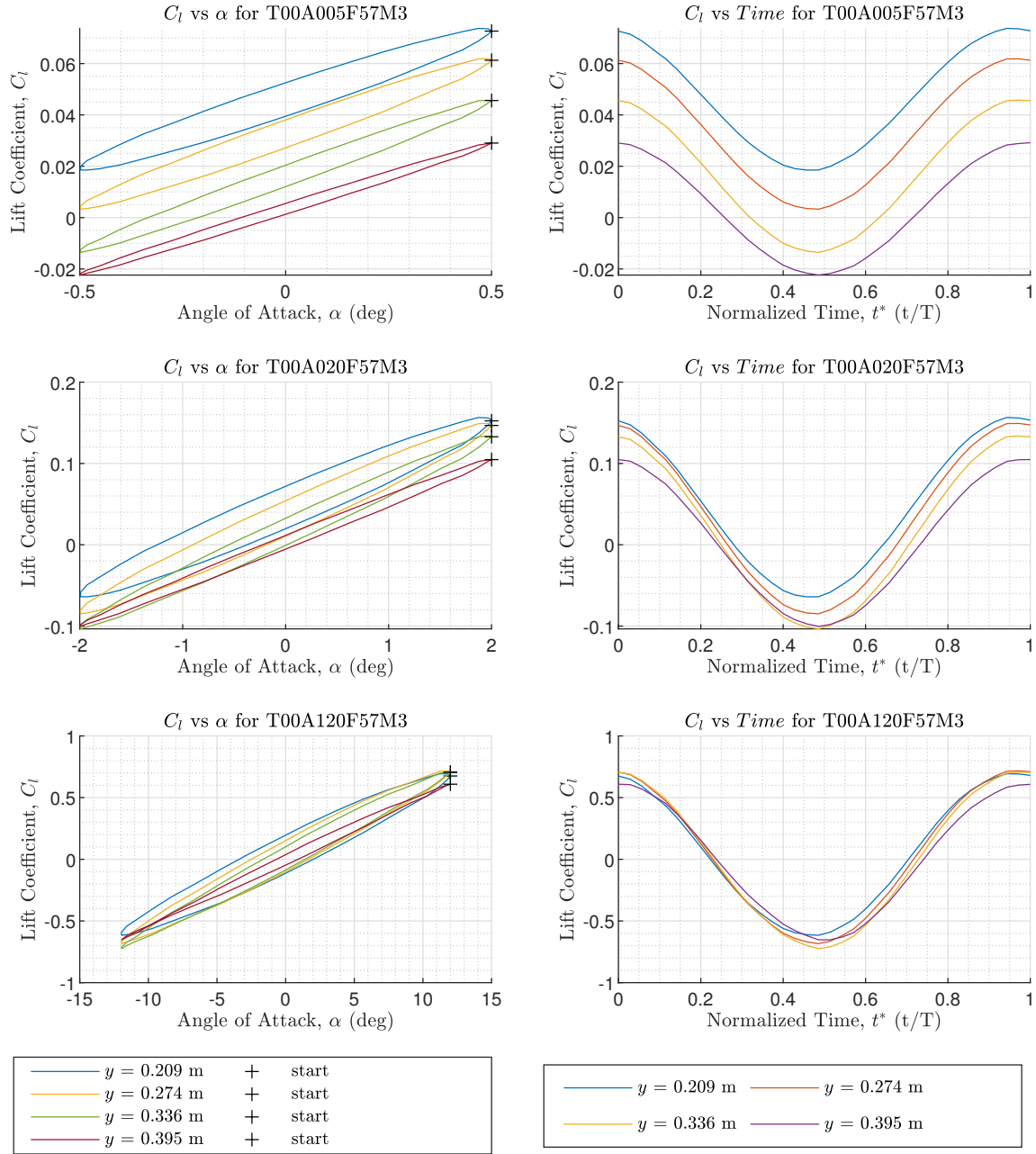


Figure F.1: Lift time histories at Mach number 0.3. Frequency = 5.7 Hz, trim = 0° , amplitude = 0.5° , 2° , & 12°

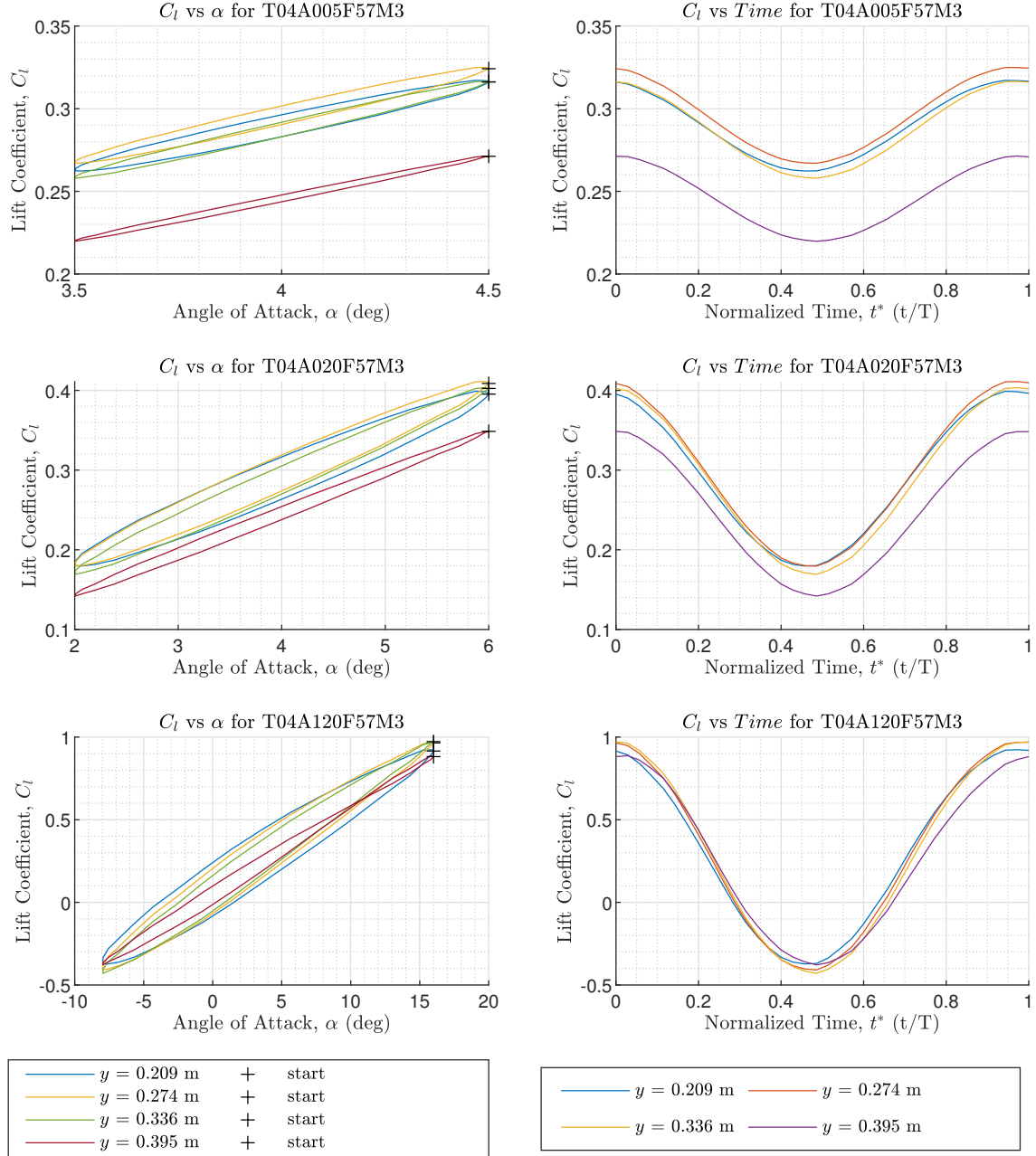


Figure F.2: Lift time histories at Mach number 0.3. Frequency = 5.7 Hz, trim = 4°, amplitude = 0.5°, 2°, & 12°

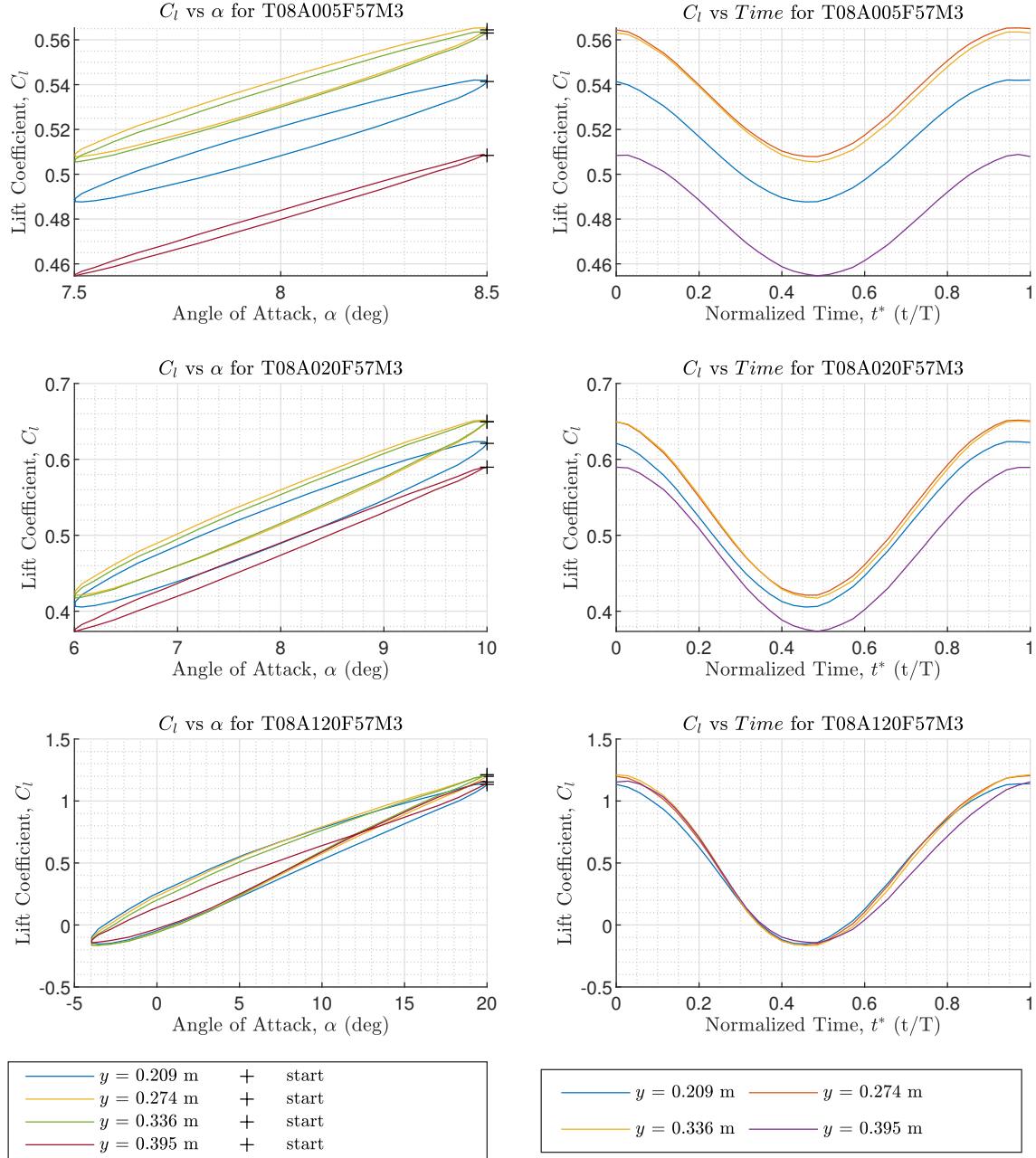


Figure F.3: Lift time histories at Mach number 0.3. Frequency = 5.7 Hz, trim = 8°, amplitude = 0.5°, 2°, & 12°

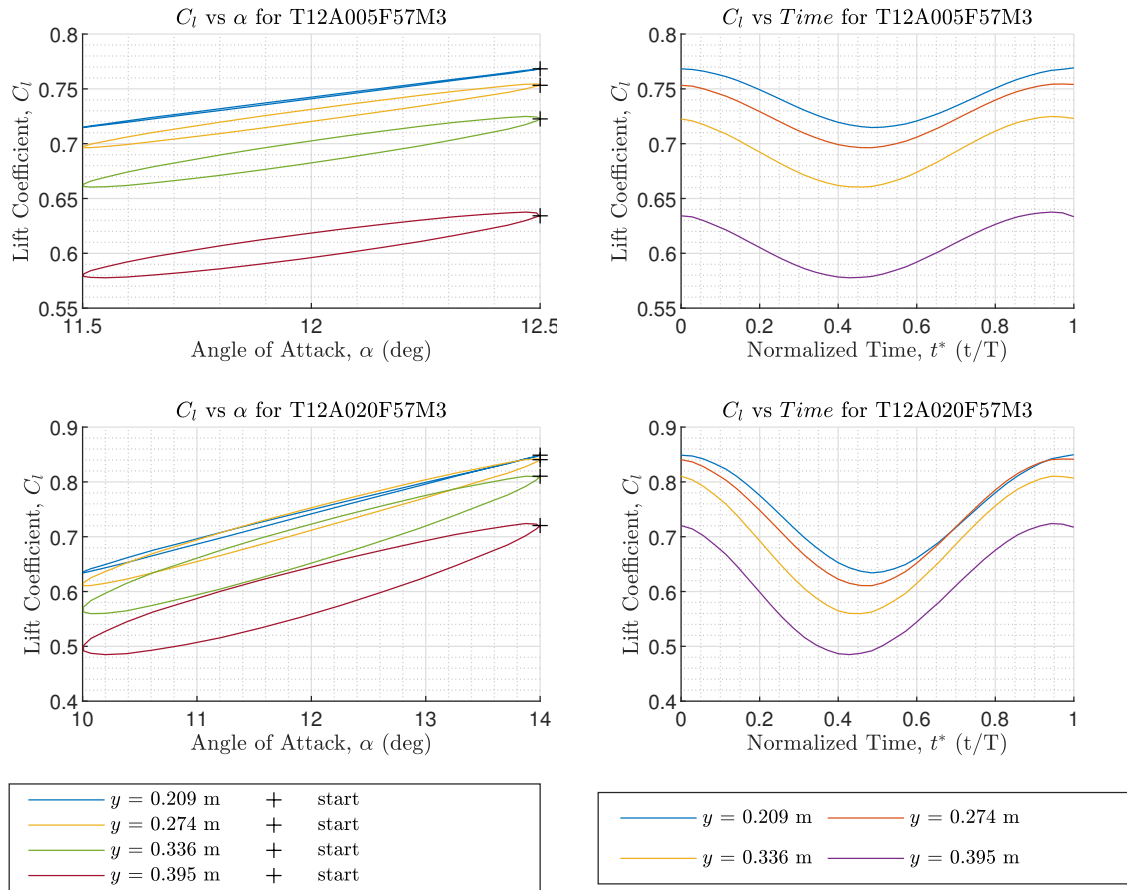


Figure F.4: Lift time histories at Mach number 0.3. Frequency = 5.7 Hz, trim = 12° , amplitude = 0.5° & 2°

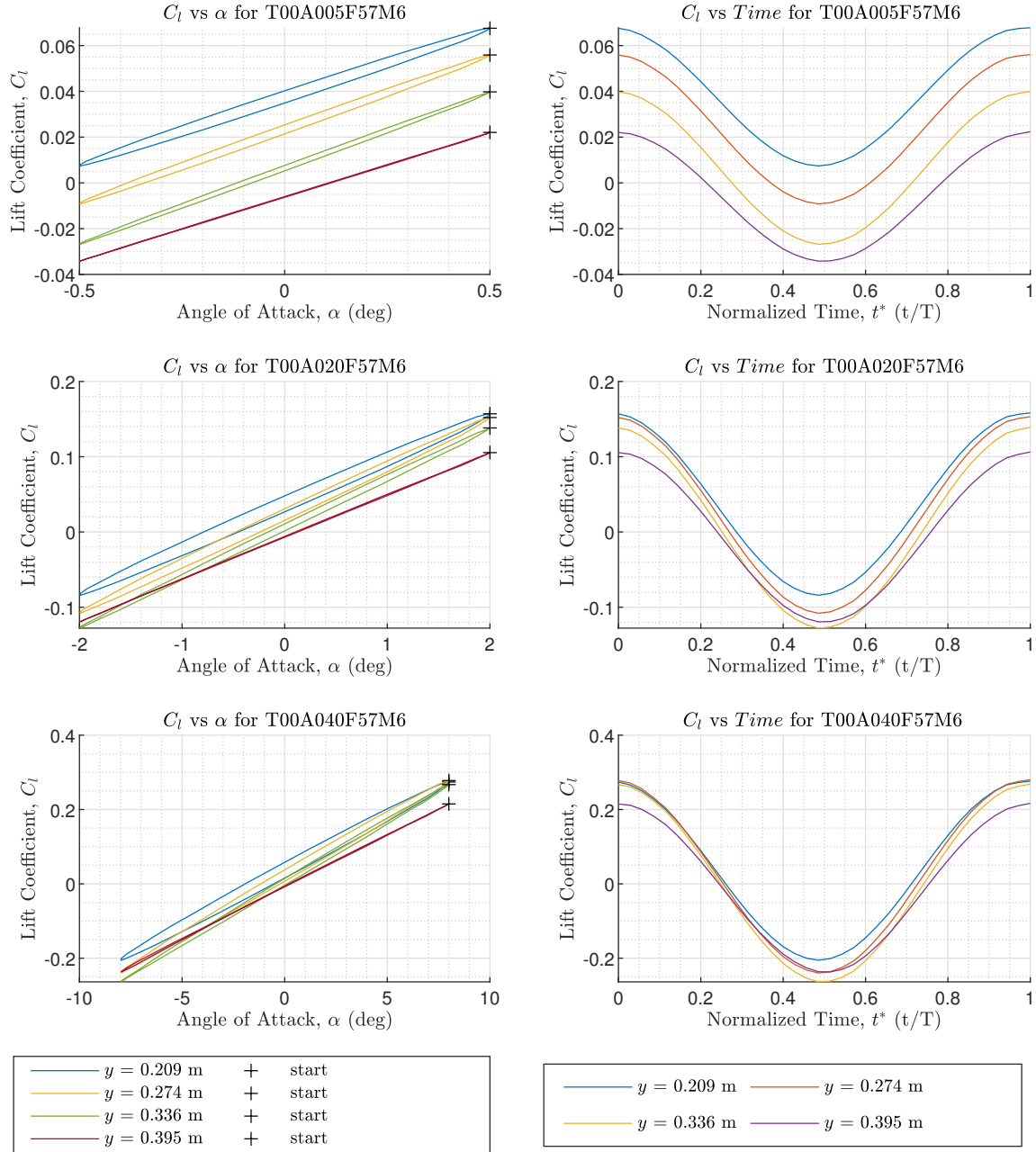


Figure F.5: Lift time histories at Mach number 0.6. Frequency = 5.7 Hz, trim = 0°, amplitude = 0.5°, 2°, & 4°

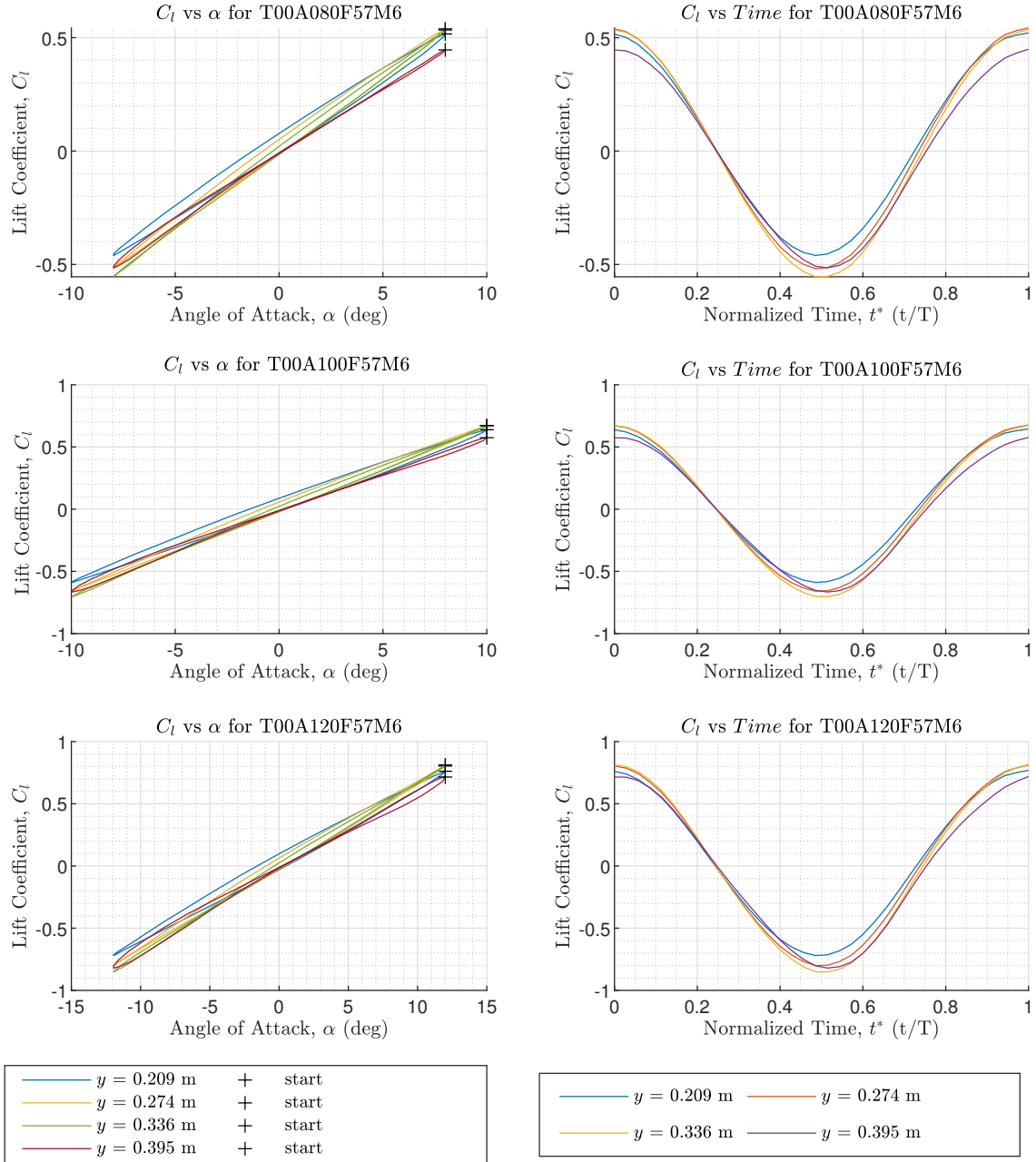


Figure F.6: Lift time histories at Mach number 0.6. Frequency = 5.7 Hz, trim = 0°, amplitude = 8°, 10°, & 12°

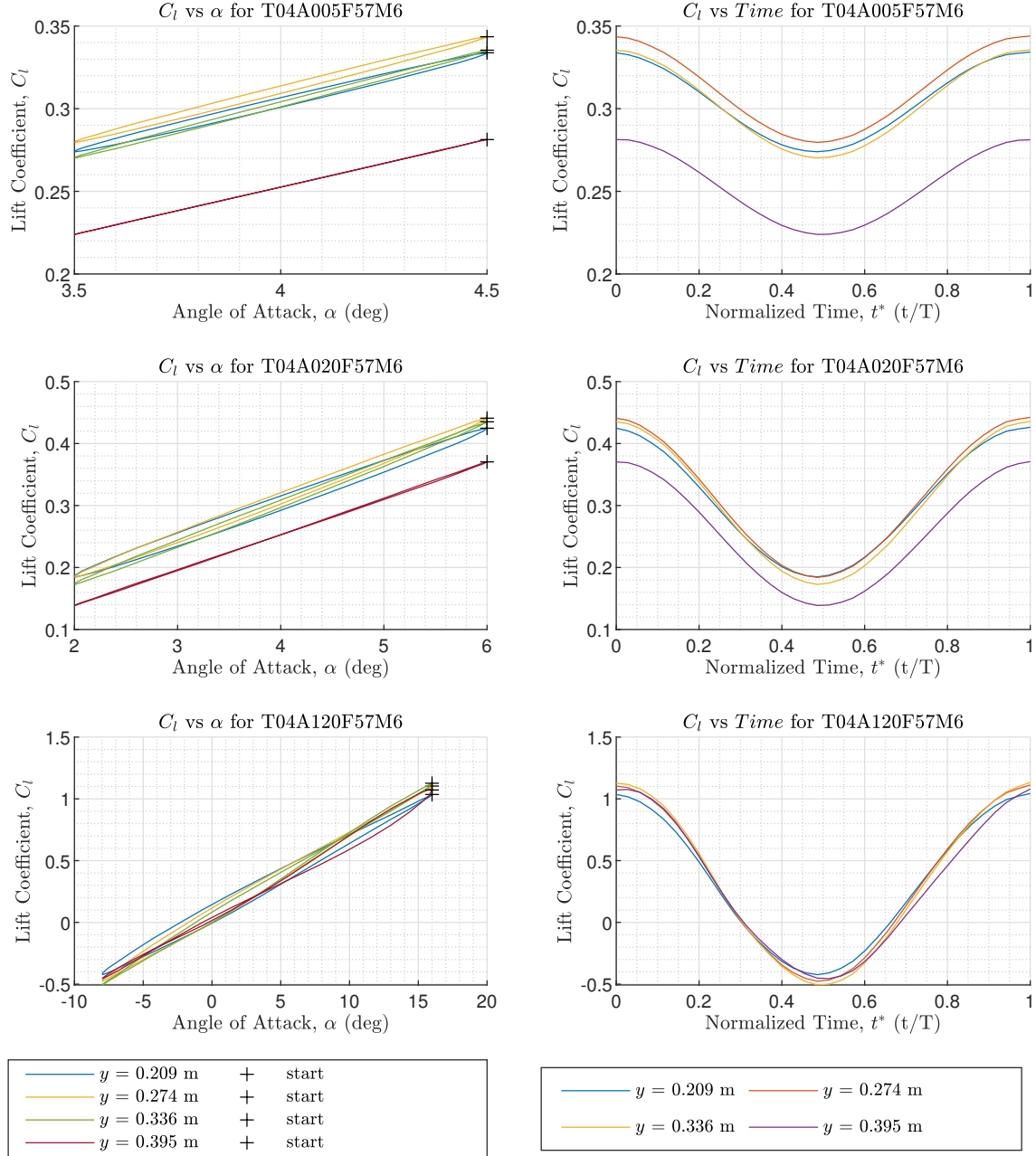


Figure F.7: Lift time histories at Mach number 0.6. Frequency = 5.7 Hz, trim = 4°, amplitude = 0.5°, 2°, & 12°

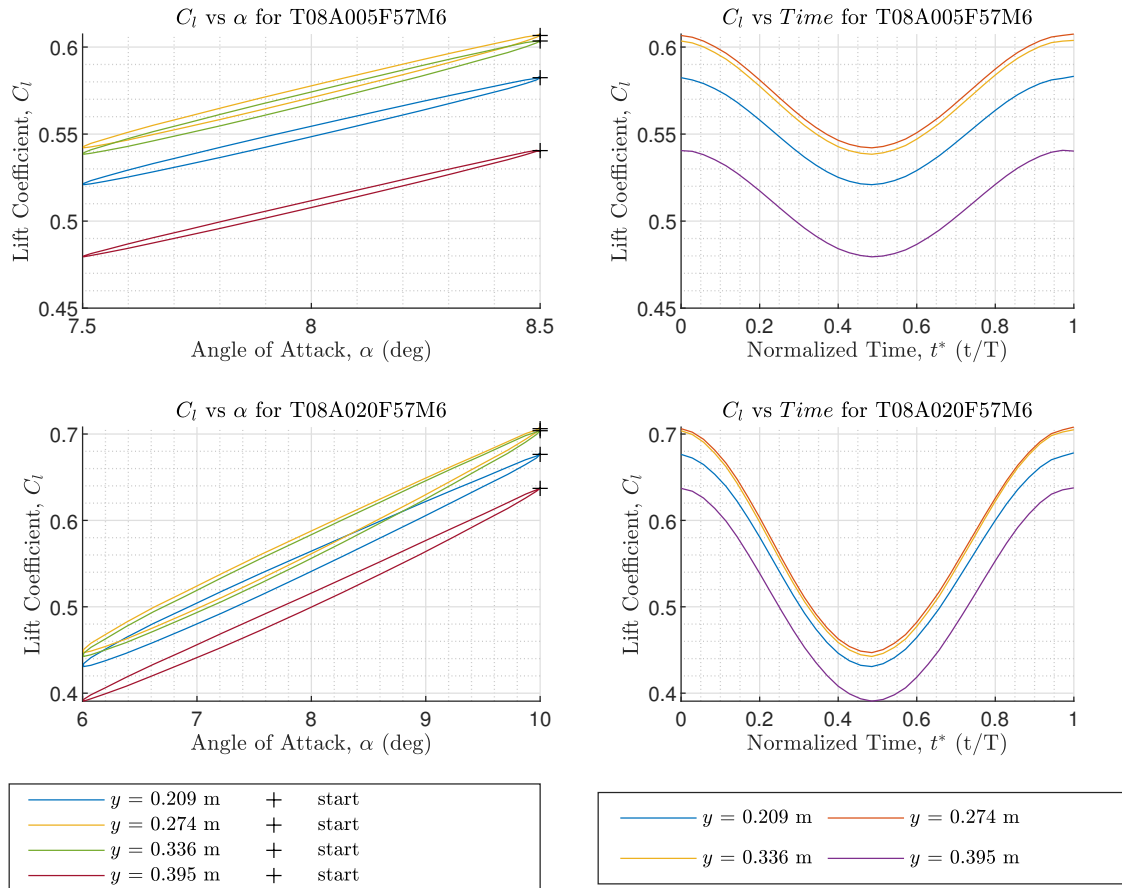


Figure F.8: Lift time histories at Mach number 0.6. Frequency = 5.7 Hz, trim = 8° , amplitude = 0.5° & 2°

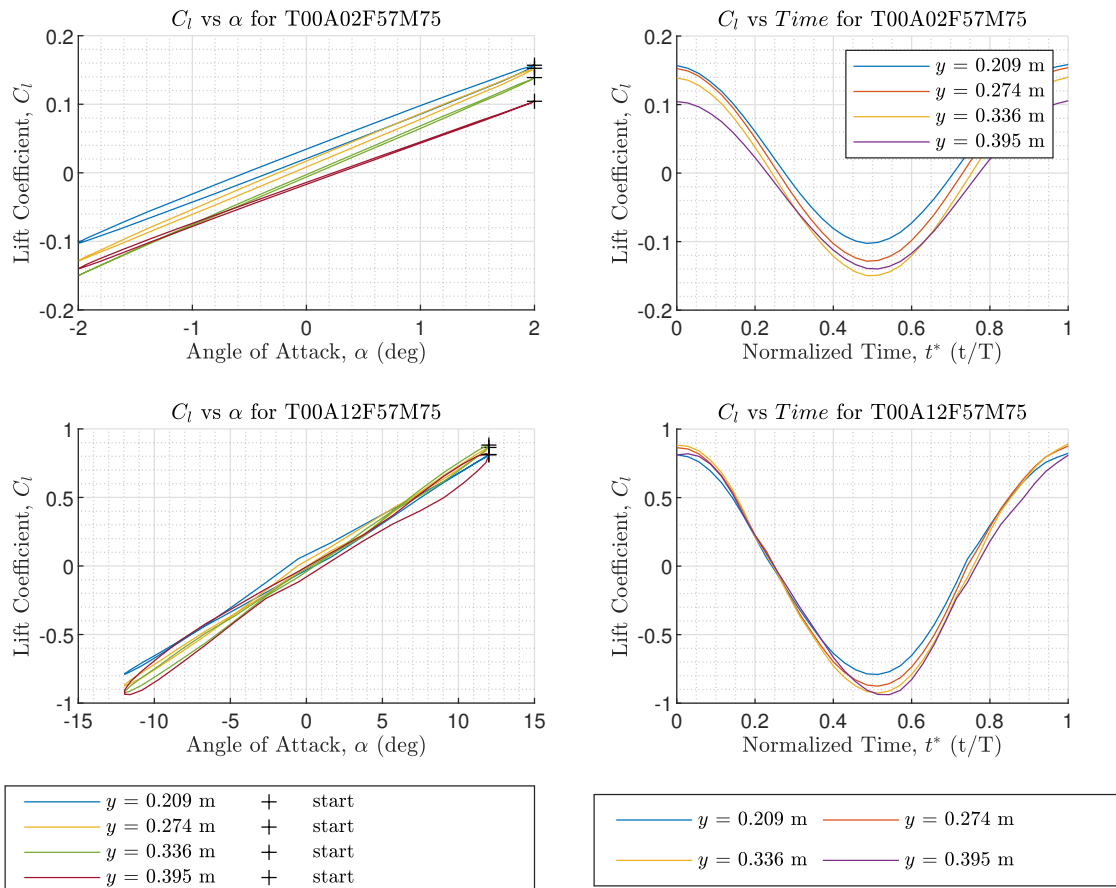


Figure F.9: Lift time histories at Mach number 0.75. Frequency = 5.7 Hz, trim = 0° , amplitude = 2° & 12°

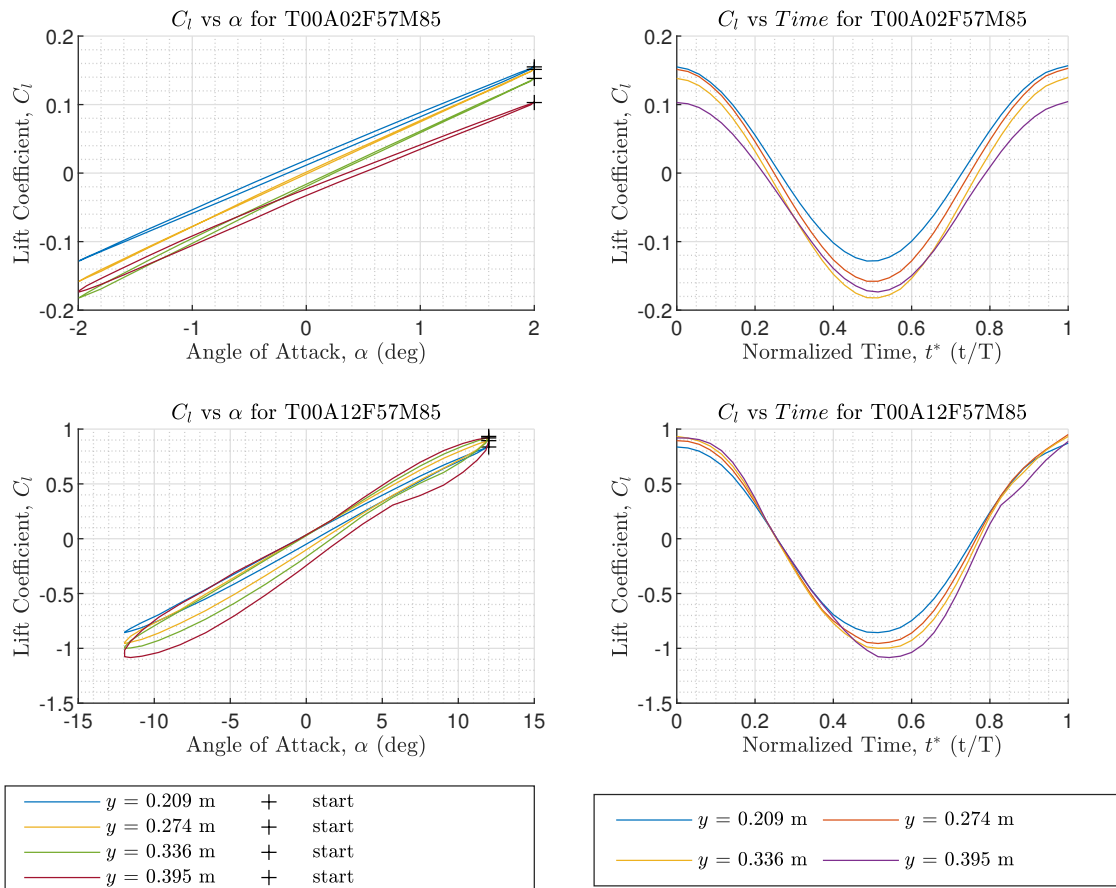


Figure F.10: Lift time histories at Mach number 0.85. Frequency = 5.7 Hz, trim = 0° , amplitude = 2° & 12°

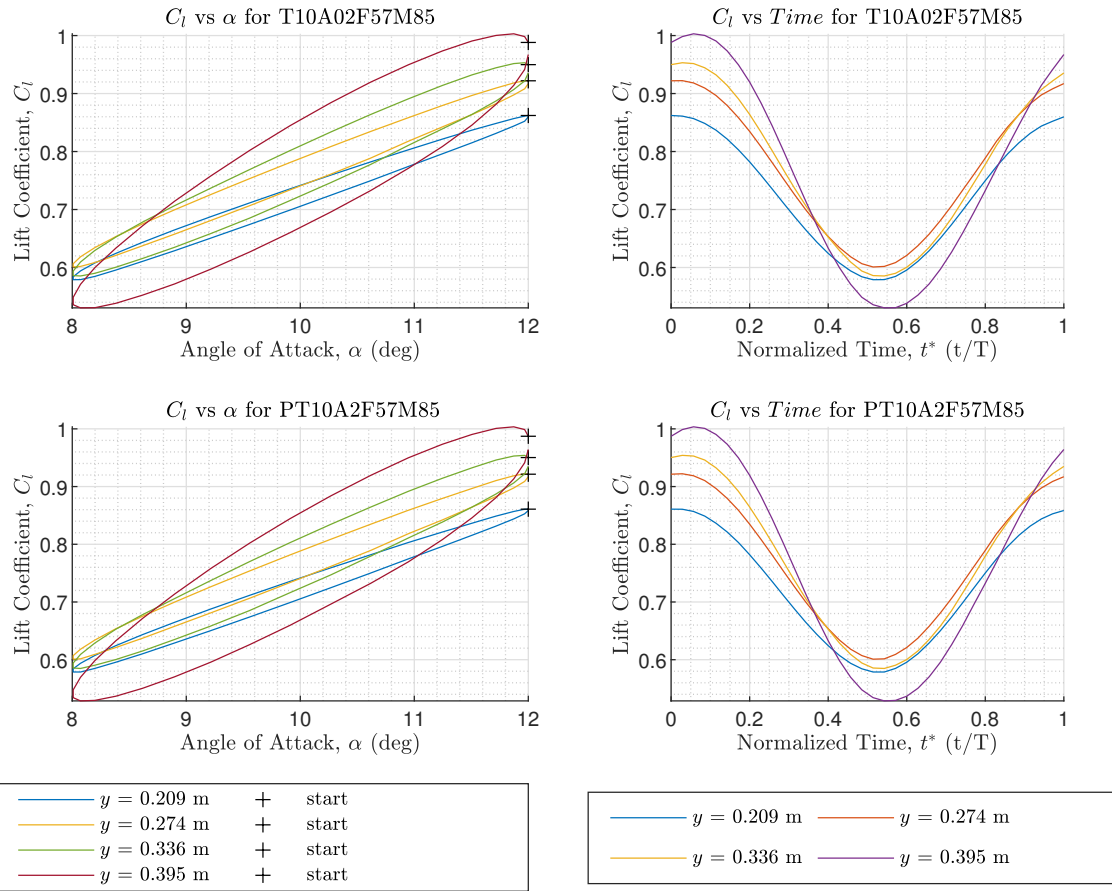


Figure F.11: Lift time histories at Mach number 0.85. Frequency = 5.7 Hz, trim = 0° , amplitude = 2° . Top used -cosine function, and bottom used +cosine function.

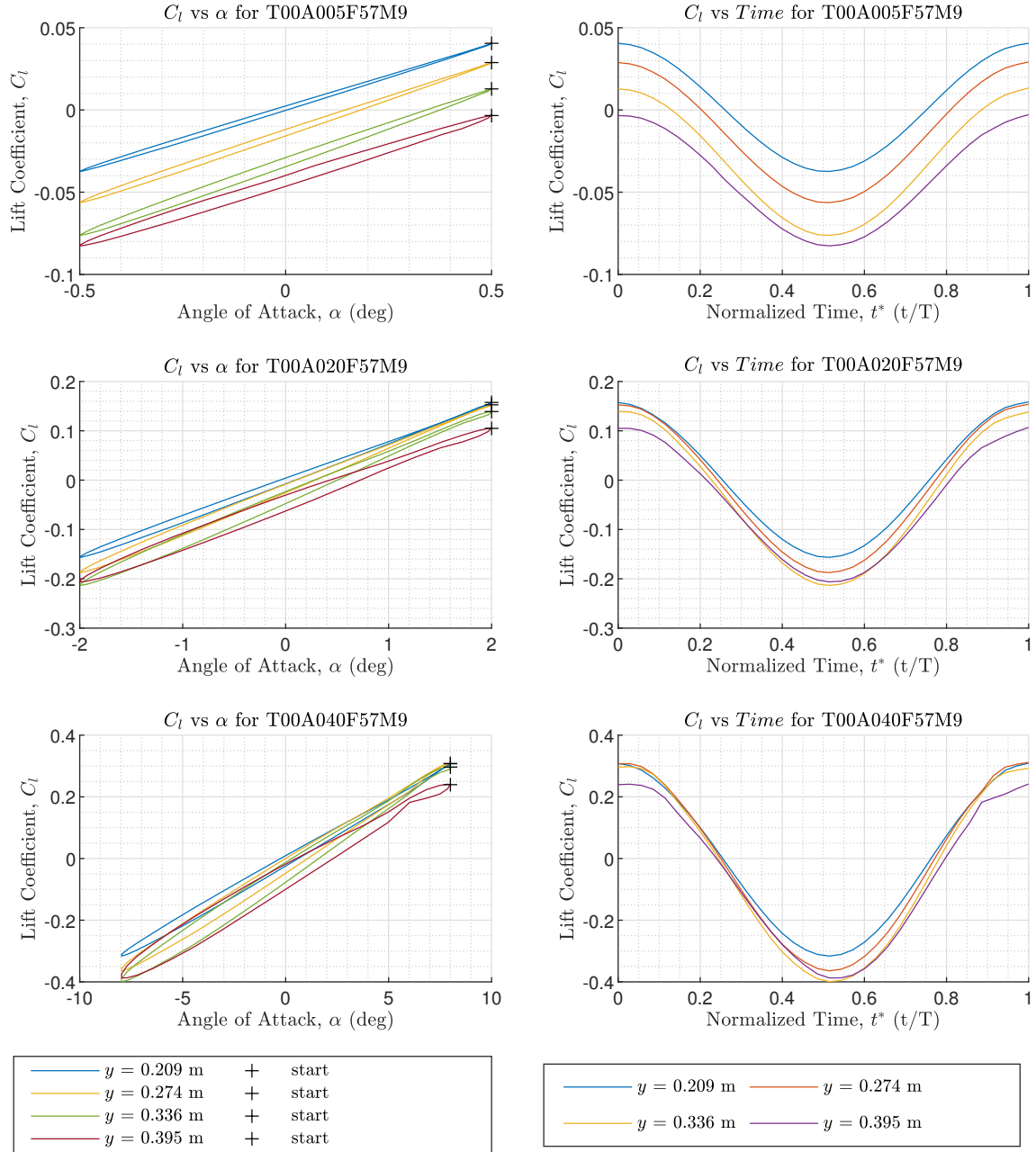


Figure F.12: Lift time histories at Mach number 0.9. Frequency = 5.7 Hz, trim = 0°, amplitude = 0.5°, 2°, & 4°

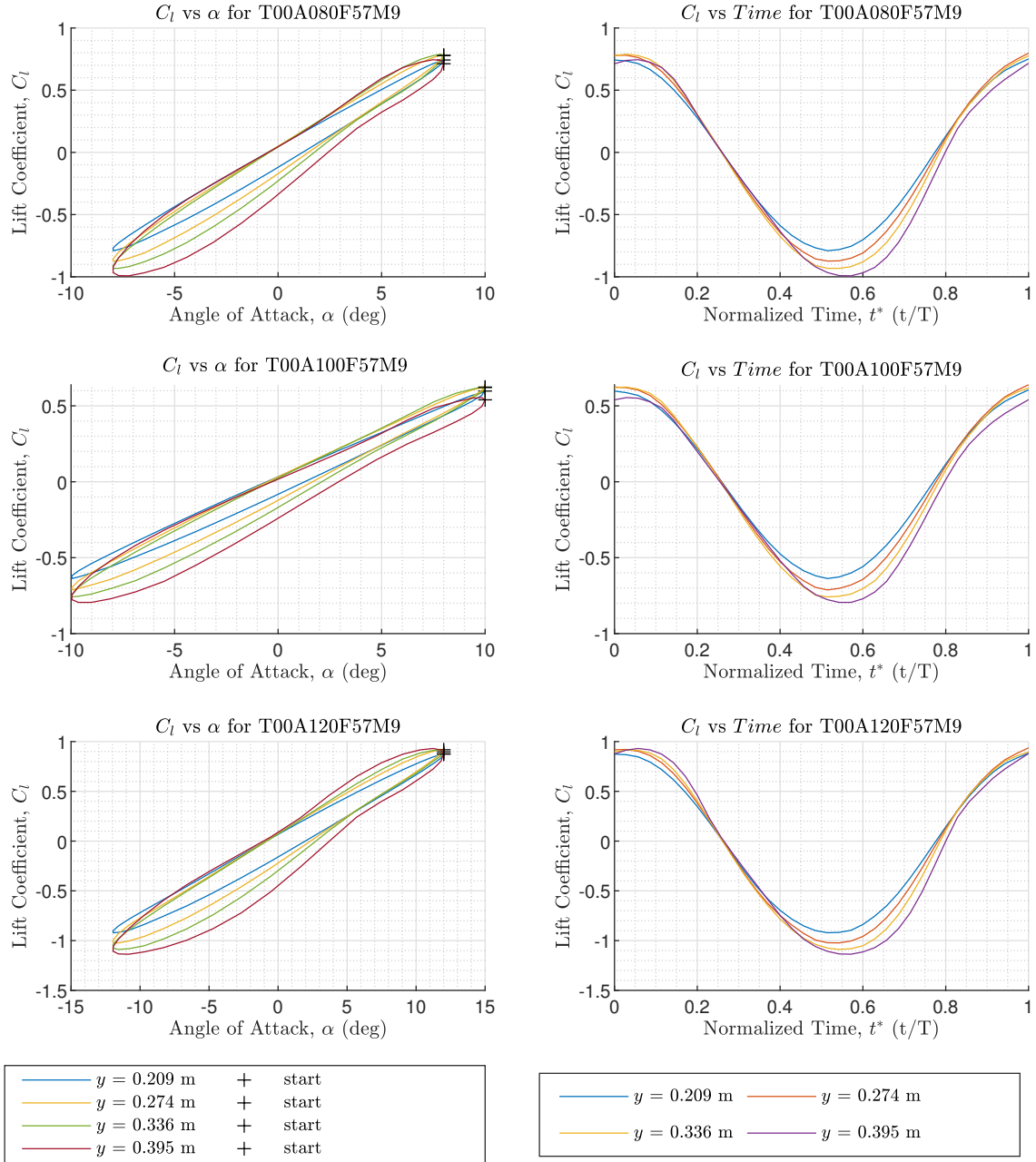


Figure F.13: Lift time histories at Mach number 0.9. Frequency = 5.7 Hz, trim = 0°, amplitude = 8°, 10°, & 12°

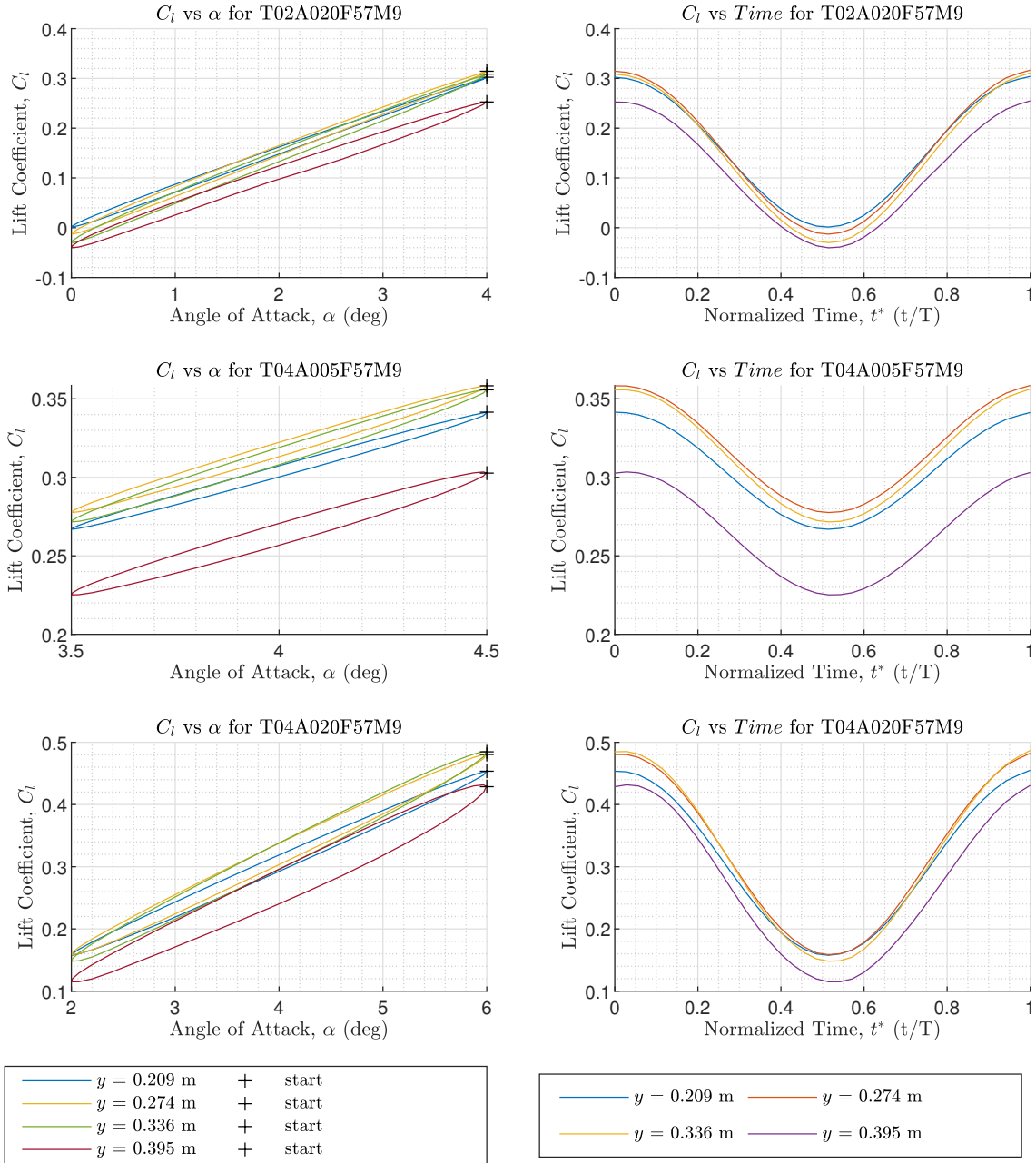


Figure F.14: Lift time histories at Mach number 0.9. Frequency = 5.7 Hz, (Top) trim = 2° & amplitude = 2° , (middle & bottom) trim = 4° , amplitude = 0.5° & 2°

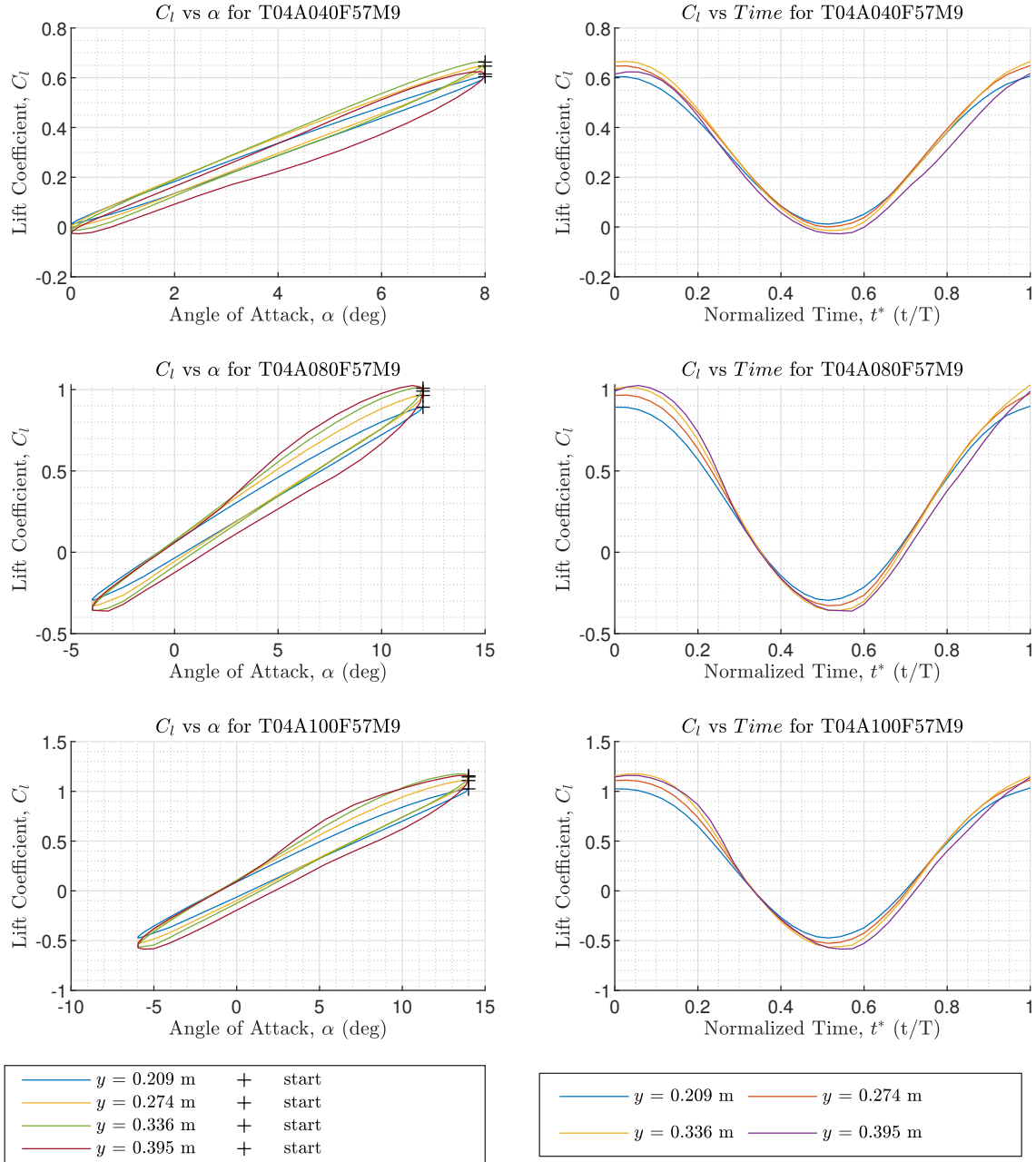


Figure F.15: Lift time histories at Mach number 0.9. Frequency = 5.7 Hz, trim = 4°, amplitude = 4°, 8°, & 10°

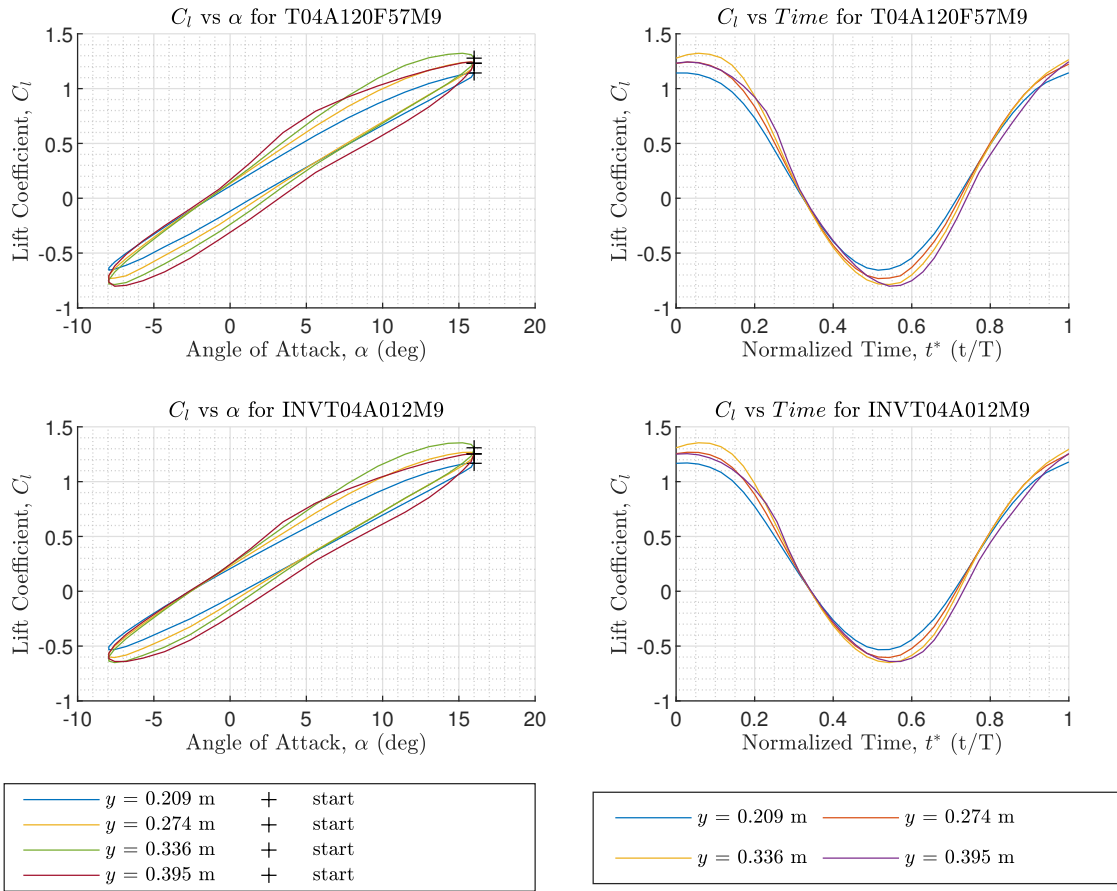


Figure F.16: Lift time histories at Mach number 0.9. Frequency = 5.7 Hz, trim = 4°, amplitude = 12°. Top used BLC solver, and bottom used fully inviscid solver.

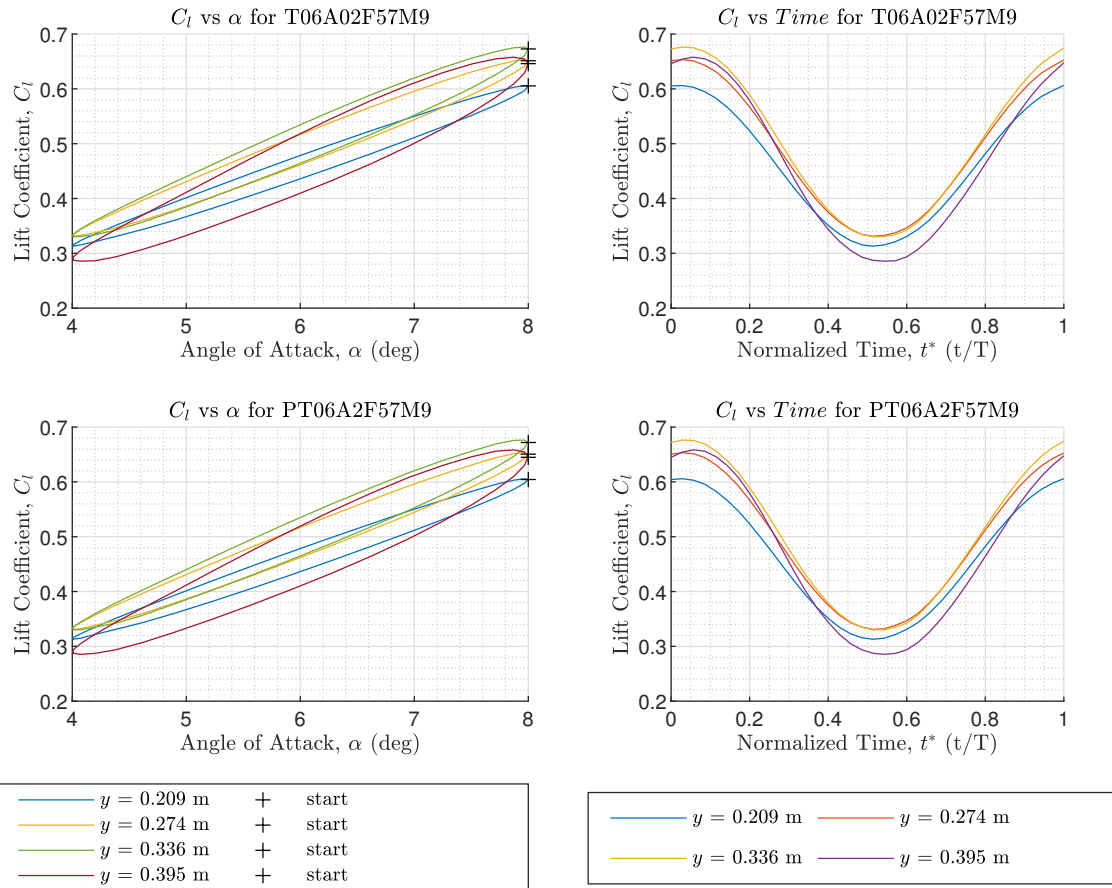


Figure F.17: Lift time histories at Mach number 0.9. Frequency = 5.7 Hz, trim = 6°, amplitude = 2°. The bottom plot used a +cosine function.

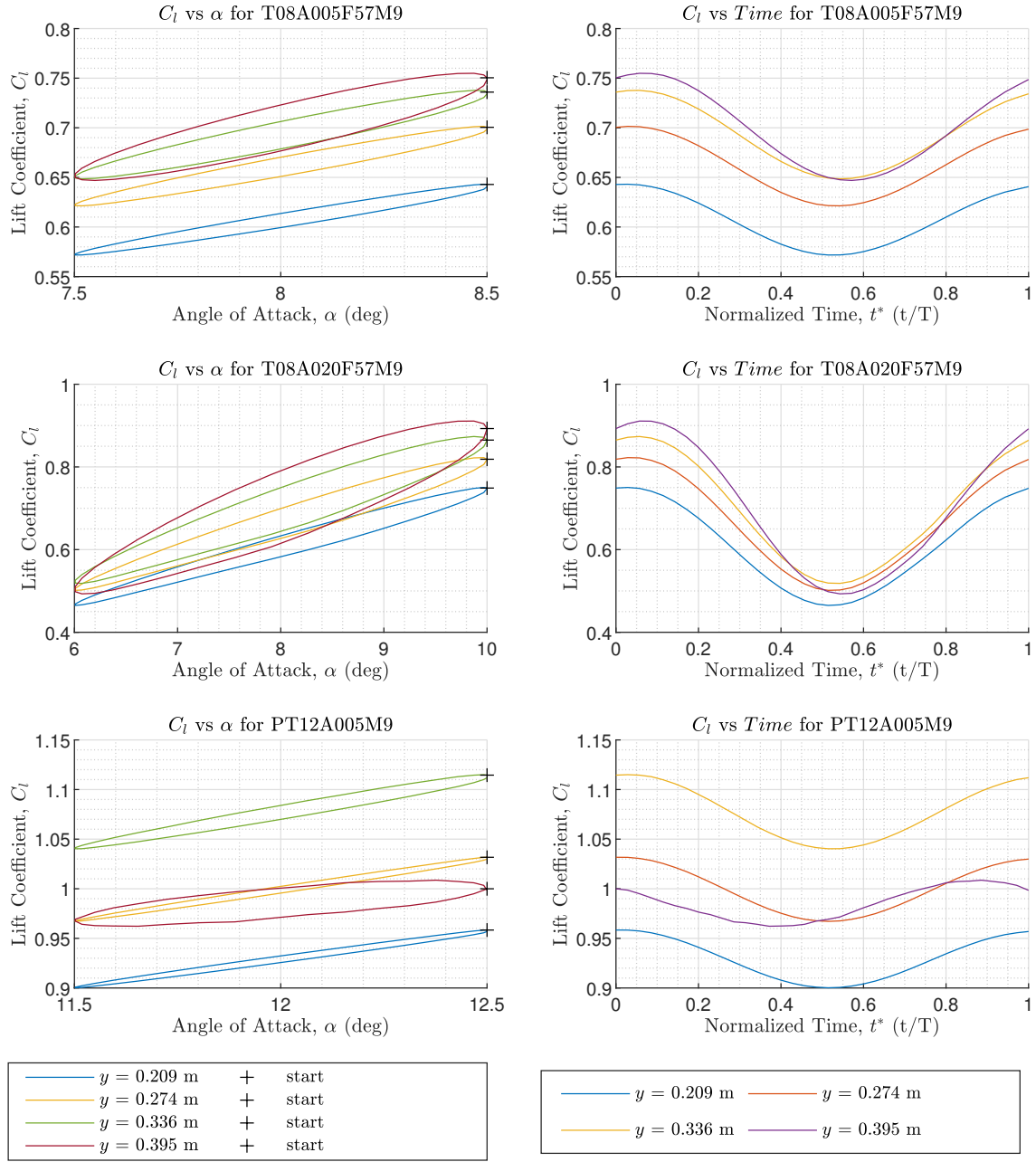


Figure F.18: Lift time histories at Mach number 0.9. Frequency = 5.7 Hz, Top and middle plots had trim = 8°, amplitude = 0.5° & 2°. Bottom plots had trim = 12°, amplitude = 0.5°, & used a +cosine function.

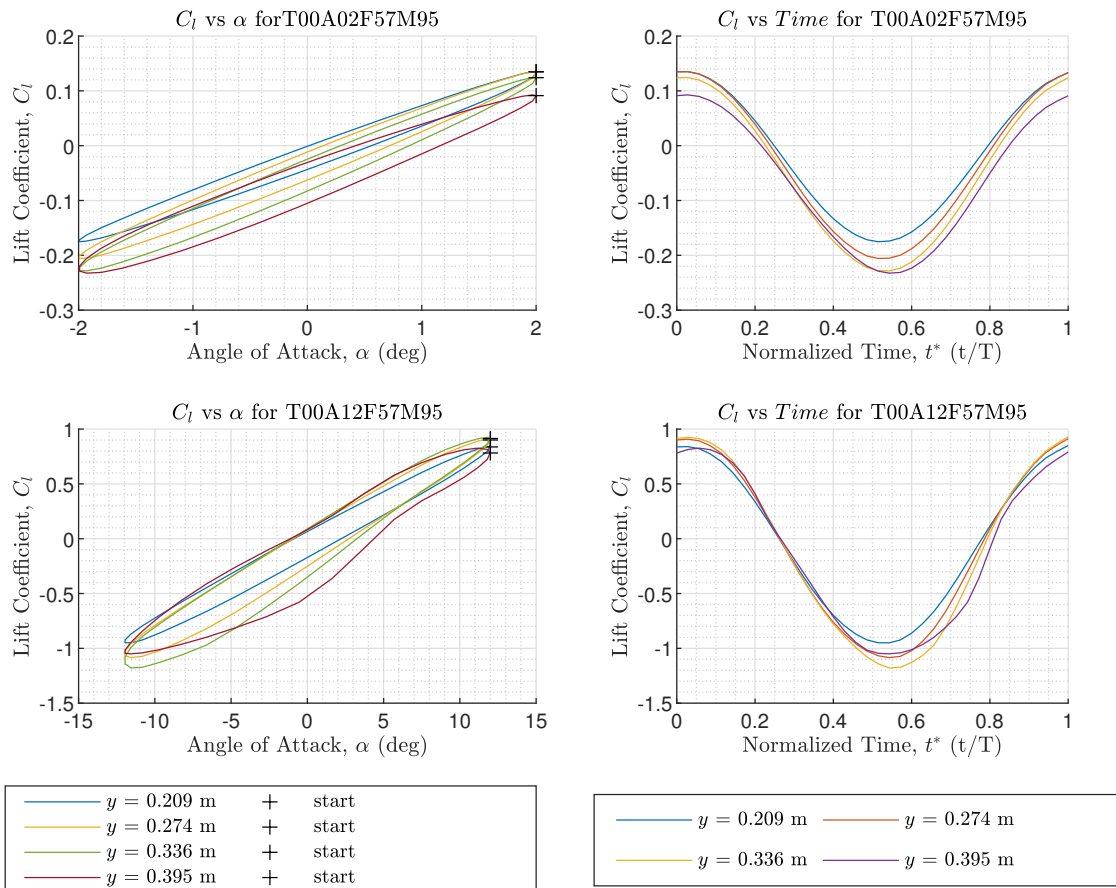


Figure F.19: Lift time histories at Mach number 0.95. Frequency = 5.7 Hz, trim = 0° , amplitude = 2° & 12°

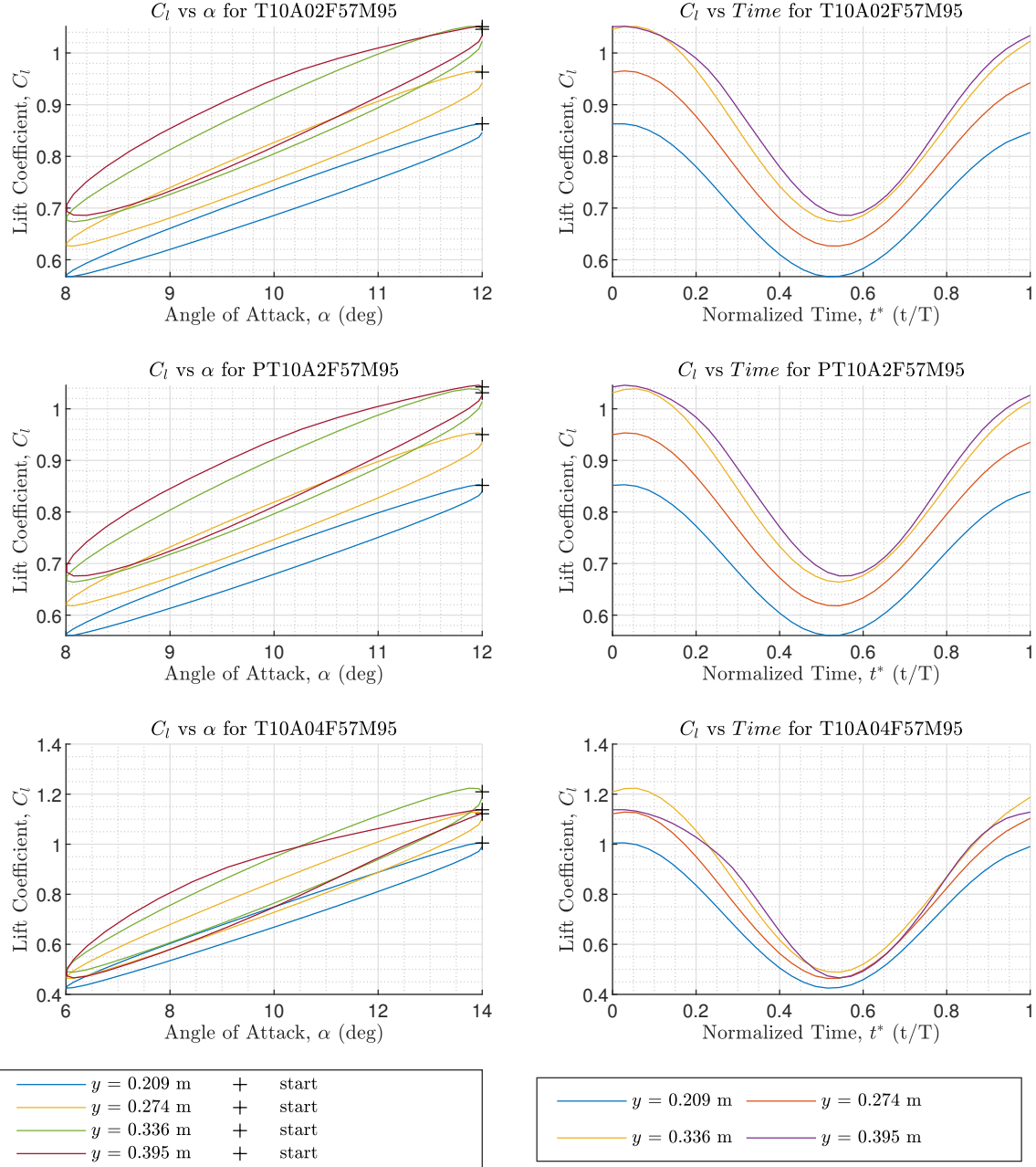


Figure F.20: Lift time histories at Mach number 0.95. Frequency = 5.7 Hz, trim = 10° , amplitude = 2° , 2° , & 4° . Middle plots used a +cosine function.

Bibliography

1. Administration, Federal Aviation. *Airplane Flying Handbook*. U.S. Government Printing Office, Washington D.C., 2004.
2. Anderson, John D. Jr. *Fundamentals of Aerodynamics*. McGraw Hill Education, New York NY, fifth edition, 2010.
3. Bendiksen, Oddvar O. “Review of Unsteady Transonic Aerodynamics: Theory and Applications”. *Progress in Aerospace Sciences*, (47 135-167), 2010. doi:10.1016/j.paerosci.2010.07.001.
4. den Boer, R.G. and A.M. Jr. Cunningham. “Low Speed Unsteady Aerodynamics of a Pitching Straked Wing at High Incidence”. *Journal of Aircraft*, 27:22–30, 1990. doi:10.2514/3.56824.
5. Bunton, Robert W. and Charles M. Denegri, Jr. “Limit Cycle Oscillation Characteristics of Fighter Aircraft”. *Journal of Aircraft*, 37(5):916–918, Sep 2000. doi:10.2514/2.2690.
6. Chen, P.C. and Denegri C.M. Jr. “Influence of External Store Aerodynamics on Flutter/LCO of a Fighter Aircraft”. *43rd AIAA/ASME/ASCE/AHS/ASC Structures, Structural Dynamics, and Materials Conference*, (AIAA 2002-1410), 2002. doi:10.2514/6.2002-1410.
7. Cunningham, A. M. *The Role of Shock Induced Trailing-Edge Separation In Limit Cycle Oscillations*. Technical report, General Dynamics, 1989.
8. Cunningham, A. M. and den Boer R.G. *Overview of Unsteady Transonic Wing Tunnel Test on a Semispan Straked Delta Wing Oscillating in Pitch*. Technical report, Lockheed Fort Worth Company and Nation Aerospace Laboratory, 1994.
9. Cunningham, A. M. and den Boer R.G. *Unsteady Transonic Wing Tunnel Test on a Semispan Straked Delta Wing Oscillating in Pitch, Part 1*. Technical report, Lockheed Fort Worth Company and Nation Aerospace Laboratory, 1994.
10. Cunningham, A. M. and Evert G.M. Geurts. *Transonic Pressure, Force, and Flow-Visualization Measurements on a Pitching Straked Delta Wing at High Alpha*. Technical report, Lockheed Martin Aeronautics Company and Nation Aerospace Laboratory, 2003.
11. Cunningham, A.M. Jr. and R.G. den Boer. *Unsteady Low Speed Wind Tunnel Test of a Straked Delta Wing, Oscillating in Pitch*. Technical Report AFWAL-TR-87-3098.
12. Denegri, Charles M., Jr. “Limit Cycle Oscillation Flight Test Results of a Fighter with External Stores”. *Journal of Aircraft*, 37(5):761–769, September 2000. doi:10.2514/2.2696.

13. Denegri, Charles M., Jr., James A. Dubben, and Daniel L. Maxwell. "In-Flight Wing Deformation Characteristics During Limit-Cycle Oscillations". *Journal of Aircraft*, 42(2):500–508, March 2005. doi:10.2514/6.2003-1426.
14. Dowell, E.H., J.P. Thomas, and K.C. Hall. "Theoretical Predictions of F-16 Fighter Limit Cycle Oscillations for Flight Flutter Testing". *Journal of Aircraft*, 46(5):1667–1672, 2009. doi:10.2514/1.42352.
15. Elsenaar, A. *Separation in transonic flow: a shocking experience*. Technical Report TP 97151, National Aerospace Laboratory NLR, Amsterdam, The Netherlands, 1997.
16. Ferguson, Iain D.M. et al. *Limited Evaluation of the Effects of Different AIM-9 Missile Variants on F-16D (Block 30) LCO Characteristics Project "LCOcho"*. *Limited Evaluation of the Effects of Different AIM-9 Missile Variants on F-16D (Block 30) LCO Characteristics: Project "LCOcho"*. Final Technical Information Memorandum AFFTC-TIM-08-10, Air Force Flight Test Center, Edwards AFB CA, December 2008.
17. Gabbard, Mark D. *Modeling the Effects of Underwing Missile Canards on F-16 Limit Cycle Oscillations*. Master's thesis, Air Force Institute of Technology, 2014. doi:10.2514/1.c033301.
18. Hanson, Colin Q. *Effect of Underwing Missile Fins and Canards on F-16 Limit Cycle Oscillations*. Master's thesis, Air Force Institute of Technology, 2013.
19. Hodges, Dewey H. and G. Alvin Pierce. *Introduction to Structural Dynamics and Aeroelasticity*. Cambridge University Press, New York NY, second edition, 2002. doi:10.1017/cbo9780511997112.005.
20. Hope, Dylan N. *An Efficient Euler Method to Predict Shock Migration on an Oscillating Straked Delta Wing Design*. Master's thesis, Air Force Institute of Technology, 2018.
21. Houghton, E. L. and P. W. Carpenter. *Aerodynamics for Engineering Students*. Butterworth-Heinemann, Jordan Hill, Oxford, fifth edition, 2003.
22. Massett, Anthony P. *AIM-9 Control Surface Effects on Subsonic LCO Analysis for F-16 Store Configuration Clearance*. Thesis AFIT/GAE/ENY/11-M19, Air Force Institute of Technology, Wright-Patterson AFB OH, March 2011.
23. Maxwell, Daniel L., Jr. Charles M. Denegri, Kenneth S. Dawson, and James Dubben. "Effect of Underwing Store Aerodynamics on Analytically Predicted F-16 Aeroelastic Instability". 48th AIAA/ASME/ASCE/AHS/ASC Structures, Structural Dynamics, and Materials Conference, Honolulu HI, April 2007. doi:10.2514/6.2007-2366.
24. Meijer, J. J. and Jr. A. M. Cunningham. *Understanding and Development of a Prediction Method of Transonic Limit Cycle Oscillation Characteristics of Fighter Aircraft*. Technical Report ICAS-92.6.4.3, 1992. doi:10.2514/6.1992-4501.

25. Melville, Reid. “Aeroelastic Instability of Tactical Aircraft in Nonlinear Flow Regimes”. 32nd AIAA Fluid Dynamics Conference, St. Louis MO, June 2002. doi:10.2514/6.2002-2970.
26. Mignolet, M.P. and D.D. Liu. “On the Nonlinear Structural Damping Mechanism of the Wing/Store Limit Cycle Oscillation”. *AIAA Archive Set 709*, 2148–2161, January. doi:10.2514/6.1999-1459.
27. Parker, Gregory H., Raymond C. Maple, and Philip S. Beran. “Analysis of Store Effects on Limit-Cycle Oscillation”. 47th AIAA/ASME/ASCE/AHS/ASC Structures, Structural Dynamics and Materials Conference, Newport RI, May 2006. doi:10.2514/6.2006-1846.
28. Pung, Justin A. *Tracking Shock Movement on the Surface of an Oscillating, Straked Semispan Delta Wing*. Master’s thesis, Air Force Institute of Technology, 2019.
29. Tauer, Thomas M. *Identifying Non-linear Aerodynamic Phenomena Contributing to F-16 Limit Cycle Oscillation*. Master’s thesis, Air Force Institute of Technology, 2015.
30. Thomas, Jeffrey P., Earl H. Dowell, and Kenneth C. Hall. “Further Investigation of Modeling Limit Cycle Oscillation Behavior of the F-16 Fighter Using a Harmonic Balance Approach”. *American Institute of Aeronautics and Astronautics*, (AIAA 2005-1917), 2005. doi:10.2514/6.2005-1917.
31. Tijdeman, H. and R. Seebass. “Transonic Flow Past Oscillating Airfoils”. *Annual Review of Fluid Mechanics*, 12(8157):181–222, 1980. doi:10.1146/annurev.fl.12.010180.001145.
32. Toth, Raymond G., Robert A. Canfield, and Reid Melville. “Non-Linear Transonic Flutter Analysis for F-16 Stores Configuration Clearance”. 43rd AIAA/ASME/ASCE/AHS/ASC Structures, Structural Dynamics, and Materials Conference, Denver CO, April 2002. doi:10.2514/6.2002-1212.
33. ZONA Technology, Inc., 9489 E. Ironwood Square Drive, Scottsdale, AZ 85258-4578. *ZEUS Version 3.9 User’s Manual*, 4 edition, February 2015.

Vita

Lt Alexander Brown was born in Wisconsin and raised in Stafford, VA. He graduated from Mountain View High School in 2008 and subsequently attended the Virginia Polytechnic Institute and State University where he earned a Bachelor of Science degree in Mechanical Engineering in 2013. Out of college, Lt Brown began a career in manufacturing engineering before commissioning into the USAF in 2017. Following Lt Brown's commission, he worked 2 years at Holloman AFB as a rocket sled test engineer before moving to Dayton, OH to pursue a master's degree at AFIT in the fall of 2019; this thesis completes his degree requirements to earn a Master of Science degree in Aeronautical Engineering.

Permanent address: 2950 Hobson Way
Air Force Institute of Technology
Wright-Patterson AFB, OH 45433